UNIVERSITY OF CALIFORNIA
RIVERSIDE

Fourier Transform Infrared Difference Spectroscopy Studies of Residue Roles at the Mn_4Ca Cluster and the Hydrogen Bonding Network in Photosystem II

A Dissertation submitted in partial satisfaction
of the requirements for the degree of

Doctor of Philosophy

in

Biochemistry and Molecular Biology

by

Rachel Jae Service

June 2011

Dissertation Committee:
Dr. Richard J Debus, Chairperson
Dr. Russ Hille
Dr. Li Fan

The Dissertation of Rachel Jae Service is approved:

_____

_____

_____
Committee Chairperson

University of California, Riverside

ACKNOWLEDGEMENTS

I would like to express my deep gratitude to Dr. Richard J. Debus for his patience and determination in mentoring and teaching me how to succeed in biophysical study of photosynthetic research. Additionally, I would like to express my sincere thanks to Anh P. Nguyen for carefully maintaining the lab and lending a hand any time.

Thanks all around to my committee, Dr. Russ Hille and Dr. Li Fan for their difficult questions and genuine interest in my work, which would not have proceeded as well without their involvement. Also, to the multi-talented Dr. Warrick Hillier who contributes ideas as well as invaluable skill in instrument upkeep and functionality. In addition, I am grateful to my collaborators Dr. Junko Yano, Dr. David Britt, and Dr. Robert Burnap for expanding the scope of this project.

Finally, I would like to express how absolutely grateful I am to my father James, my mother Karen, and my brother Jordan for their complete support throughout this process. I could never have made it to the end without their encouragement and devotion.

The text of this dissertation, in part, is a reprint of the material as it appears in:

(1) Service, R., Hillier, W., Debus, R. (2010) Evidence from FTIR Difference Spectroscopy of an Extensive Network of Hydrogen Bonds near the Oxygen-Evolving Mn_4Ca Cluster of Photosystem II Involving D1-Glu65, D2-Glu312, and D1-Glu329, *Biochemistry 49*, 6655-6669

(2) Service, R., Yano, J., McConnell, I., Hwang, H.J., Niks, S., Hille, R., Wydrzynski, T., Burnap, R., Hillier, W., Debus, R. (2011) Participation of Glutamate-354 of the CP43 Polypeptide in the Ligation of Manganese and the Binding of Substrate Water in Photosystem II, *Biochemistry 50*, 63-81

The co-author, Richard J. Debus, listed in these papers was director and supervisor to the research done. Other co-authors listed provided methodological and technical expertise.

ABSTRACT OF THE DISSERTATION

Fourier Transform Infrared Difference Spectroscopy Studies of Residue Roles at the Mn_4Ca Cluster and the Hydrogen Bonding Network in Photosystem II

by

Rachel Jae Service

Doctor of Philosophy, Graduate Program in Biochemistry and Molecular Biology
University of California, Riverside, June 2011
Dr. Richard J. Debus, Chairperson

Photosystem II (PSII) from both plants and cyanobacteria is a multiprotein, intramembrane complex responsible for the intricate processes of water oxidation and oxygen evolution. The oxygen evolving complex (OEC) of the active site is a four manganese and calcium (Mn_4Ca) cluster coordinated by carboxylate and histidine residues along with four water molecules. The OEC accumulates oxidizing equivalents in discrete one-electron steps during the catalytic cycle called storage states, or S-states, resulting in proton and electron transfer, and ultimately generation of dioxygen, which is then released from the active site through a channel in the protein. Identifying the amino acid residues directly involved in this process as well as those which stabilize the intermediate states of the catalytic cycle through a series of hydrogen bonds is important in understanding the mechanism as a whole. Spectroscopic methods such as Fourier transform infrared (FTIR) difference spectroscopy can probe the dynamic nature of bond creation/destruction that occurs in the structural rearrangements taking place in the OEC during catalysis. FTIR spectroscopy reproducibly shows many vibrational modes for each S-state throughout the cycle, indicating an arranged routine by residues during the catalytic cycle that is best viewed in the midfrequency region for amide I stretching, amide II bending,

symmetric/asymmetric carboxylate stretching, and carbonyl of carboxylic acid stretching. FTIR difference spectra show changes in vibrational modes, positive/negative peaks, that result from differences between S_{n+1}-*minus*-S_n states. FTIR difference spectra can compare S-state transitions of an amino acid mutant to that of wild-type to observe the effect of mutation on PSII.

Data have been collected for two ligands to the Mn_4Ca cluster, Glu354 of subunit CP43 and Glu333 of subunit D1, characterizing the former as a ligand that does not change its coordination mode transition from the S_1 to the S_2 state, and suggesting ligation to the Mn3 and Mn4 ions of the OEC. The latter residue plays an integral role in structure reinforcement as well as dynamic interactions, though its specific role is not yet clear. Two different channels, an oxygen channel (large) and water/proton egress channel (broad) are seen in the crystal structure of PSII. CP43-Glu354 and D1-Glu329 are in the large channel and D1-Glu65, D2-Glu312, D1-Glu333, D2-Glu323, and D2-Lys317 are in the broad channel. FTIR of a CP43-E354Q mutant gave evidence that Glu354 has some effect on the hydrogen-bonding network at the large channel, but did not directly engage the OEC as D1-Glu329 does. In the broad channel, only D1-Glu65 and D2-Glu312 showed clear signs of participating in the network. D1-Glu333 and D2-Lys317 showed evidence of being involved in stabilizing the structure of the OEC, a likely situation considering their proximity to an essential chloride ion. This study shows the complex and sensitive nature of the structure of PSII and not just localized to the OEC during the catalytic cycle.

Table of Contents

LIST OF FIGURES

CHAPTER 1

INTRODUCTION AND LITERATURE REVIEW

1.1 Introduction to Photosynthesis

Approximately 3 billion years ago, biology developed the ability to harness photons from sunlight to synthesize organic molecules and split water molecules for energy. This photosynthetic process of using light energy to convert water into protons, electrons, and molecular oxygen established an oxygenic atmosphere and ozone layer. Availability of oxygen allowed for more efficient metabolism, leading to evolution of eukaryotes and multicellular organisms. Though it is a fundamental mechanism to support life, not all photosynthetic reactions have been resolved. The process of photosynthesis is completed by two distinct reactions, Light Dependent and Light Independent. Light Independent reactions occur in the stroma of chloroplasts and do not require light energy to proceed. It is here that the carbon fixing Calvin cycle takes place, converting carbon dioxide and water into sugar while turning over one nicotinamide adenine dinucleotide phosphate (NADP+) and two adenine diphospate (ADP) molecules for the Light Dependent reaction. Light Dependent reactions occur in thylakoid membranes organized as grana in chloroplast organelles of leaf cells (Figure 1) and loose in cytoplasm near the plasma membrane of prokaryotic cells (Figure 2). In the Light Dependent processes, light is absorbed in antenna complexes which transfer excitation energy to chlorophyll *a* (P_{680}), exciting electrons to a higher energy state, P_{680}* (Figure 3). Following this is a charge separation and electron transfer series ultimately creating NADPH to be oxidized in the Calvin cycle and a proton gradient which drives the proton ATPase, creating ATP for use in two separate reactions in the Calvin cycle (Figure 4).

The antenna complex and location for water oxidation are in the thylakoid membrane protein Photosystem II (PSII). It is here that the Light Dependent reactions take place. During the four photon charge separation sequence, two water molecules held at the oxygen evolving complex (OEC) of PSII are split, reducing metals. The details of this process will be discussed further on. The result of this water splitting reaction at the OEC is four protons and dioxygen, an equation which can be written as:

$$2H_2O \text{ --}4h\nu\text{--> } O_2 + 4H^+$$

The precise mechanism of this reaction is presently unknown. However, the location of the OEC and its environment has been illustrated with x-ray crystallography. X-ray crystallography is a method for obtaining a three dimensional image for a molecule or protein. This technique uses x-ray diffraction to determine the arrangement of atoms within a protein crystal structure and builds structure information from the collected data. The resulting crystal structure data produces an overall structure of a protein and chemical bonds between atoms. Once the image has been created defining the structure, the function of a protein is more easily studied, especially when used in conjunction with spectroscopic techniques. When used together, these methods give a better understanding of the structure/function relationship of the protein.

1.2 Structure of Photosytem II

Photosystem II (PSII) crystal structures have been studied with x-ray crystallography, providing three-dimensional views of the protein as well as any active site and channels that exist within it. This is useful in isolating residues which surround the OEC and could be involved with water oxidation (Figure 5). Of those structures published, four are currently used with resolutions of 3.5, 3.0, 2.9, and 1.9 Å (1 - 4). The crystal structures of PSII collectively show a large polypeptide complex, about 650 kDa, consisting of 20 protein subunits and 77 cofactors per

monomer. There are 25 integrally bound lipids per monomer, approximately 0.7 lipids per transmembrane helix, which reside where monomers contact in the protein. This suggests the lipids are useful in providing a flexible interface for assembly/disassembly between the monomers, controlling overall dimer formation (3). Subunits comprising PSII are centrally located D1 and D2, flanked on either side by polypeptides CP43 and CP47 which function in transferring excitation energy from the antenna complex to D1 and D2. D1 and CP43 retain closest proximity to the active OEC. Outside these are 16 additional subunits (2, 3). The OEC of the PSII multisubunit complex can be seen in Figure 6. The transmembrane helix organization of these four main polypeptides has been compared in both plants and cyanobacteria. The x-ray crystallographic structures (Figure 7) show for D1, D2, CP43 and CP47, the formation and location within PSII are alike. Cyanobacteria shows an additional transmembrane helix at the periphery, but this does not interfere with the reaction center of PSII (5). Residues surrounding the OEC are conserved in both plants and cyanobacteria.

The OEC lies within the lumen near the surface of the thylakoid membrane and consists of a cluster of four manganese and one calcium. This Mn_4Ca cluster is the focal point of both the four electron water splitting catalytic cycle and the one electron photochemistry via Tyrosine-161 of the D1 subunit, often regarded as Y_Z, and quinones. The manganese atoms are held in formation through oxo bridges with five oxygen atoms which can be seen in Figure 8. Three of the four manganese, calcium, and four oxygens form a cubane structure where metals and oxygens occupy corners alternately while a fourth manganese juts out from the structure (4). The overall shape takes a distorted chair form. It is thought that oxygen-5 may exist as a hydroxide ion and could provide one of the substrates for dioxygen formation (4). For three x-ray crystallography structures, resolutions 3.5, 3.0, and 2.9 Å, there is a discrepancy of structure which can be attributed to x-ray radiation damage (1 – 3). This is caused by manganese III and

manganese IV reduction to manganese II, breaking the u-oxo-bridge structures and changing the structure surrounding the OEC. Only the recent x-ray crystallographic structure at 1.9 Å gives an accurate representation of ligating residues to the Mn_4Ca due to preparation and testing procedures which reduce or eliminate manganese reduction (4).

1.3 Electron Transfer and S-state Cycle

Absorption of photons within PSII by antennae complexes initiate the electron transfer process beginning with two water molecules, the electron source. Excitation energy absorbed by these pigments is transferred to the photosynthetic reaction center. The reaction center chlorophyll, P_{680}, absorbs energy from the other pigment molecules generating P_{680}*, the excited state of P_{680} and a strong reducing agent. P_{680}* reduces a pheophytin molecule (Pheo) in picoseconds resulting in $P_{680}^{\circ+}$ $Pheo^{\circ-}$ configuration. $Pheo^{\circ-}$ then reduces Q_A, the primary quinone, within a few hundred picoseconds creating $P_{680}^{\circ+}$ $PheoQ_A^-$. $P_{680}^{\circ+}$ oxidizes Y_Z to form Y_Z° radical in nanoseconds. Simultaneously, Q_A^- reduces a second quinone, Q_B, forming $Y_Z^{\circ}PheoQ_AQ_B$, and Y_Z° extracts an electron from manganese of the Mn_4Ca cluster. A second photon induces a duplicate reaction and produces Q_B^{2-} which is protonated and released from D1 to be oxidized by cytochrome b_6f complex. The Y_Z° oxidizes another manganese of the Mn_4Ca cluster as two more photons push the mechanism toward another Q_B^{2-}, further oxidizing the Mn_4Ca cluster, and ultimately splitting the two water molecules which release dioxygen (6). A diagram of this process can be seen in Figure 9. The stages of this process, often referred to as storage states, are cyclic beginning with the dark stable S_1 state. The first photon drives the cycle to the S_2 state and so on until S_4 rapidly degrades to S_0 with simultaneous release of dioxygen, proceeding again to dark stable S_1. This progressing cycle represents a charge separation process

that accumulates within the four manganese at the OEC (7). The time scale of the S-state cycle can be seen in Figure 10.

The positive charge accumulating on the manganese at the Mn_4Ca cluster is partially balanced by proton release (8 - 10). Proton release studies in PSII illustrate a 1:0:1:2 pattern in $S_0 \rightarrow S_1 \rightarrow S_2 \rightarrow S_3 \rightarrow S_0$ transitions, though the integers are an estimation of the results. Partial proton numbers of 1.1:0.3:1.0:1.6 for the S-state transitions, as seen experimentally, can be attributed not only to substrate water but titratable residues at or near the Mn_4Ca cluster (7, 11). Net charge changes of 0:+1:0:-1 previously detected is in agreement with this proton pattern seen for the four transitions (12). Effects of pH on transition show dependency in all but $S_1 \rightarrow S_2$, with inhibition occurring below 5 pH (13, 14). Previously, FTIR spectroscopy has been used to monitor proton release or shifts to strong hydrogen bonds, indicated by negative bands in the OH region, for the $S_2 \rightarrow S_3$, $S_3 \rightarrow S_0$, and $S_0 \rightarrow S_1$ transitions (15, 16). The $S_3 \rightarrow S_0$ transition gives double intensity in this region compared to the other bands, which suggests this transition accounts for two water OH bond reactions (8). The carbonyl of a carboxylic acid stretching region is another useful region to observe hydrogen bonding interactions. During S-state transitions, a band appears at 1747 cm^{-1}, either positive or negative depending on the S-state. This signifies a change in ν(C=O) region in response to the transition, representing a carboxylic acid's changing pK_a. It is likely that residues responsible for partial protonation in $S_1 \rightarrow S_2$ and reprotonation in $S_3 \rightarrow S_0$ are Asp, Glu, Arg, Lys, and/or Tyr (8).

The amino acids here mentioned can be found near the Mn_4Ca cluster and also in channel systems which run throughout the protein. Each channel is thought to aid in either water/proton or oxygen shuttling and has been designated broad or large respectively, seen in Figure 11 (1, 11, 17, 18). Methods testing solvent access channels via methanol (18), measurement of pK_a of titratable residues (11), and anomalous diffraction locating Ca^{2+} (19) or Xenon (17) have helped

to identify likely roles of channels. Some residues, which aid in proton exit or water entrance channels would likely have characteristics of those affecting proton release during the S-state transitions and would be of particular interest in the study of hydrogen bonding effects during the catalytic cycle.

1.4 Fourier Transform Infrared Spectroscopy in Photosystem II

As previously mentioned, different methods of spectroscopy are useful to further understand the implications of the structure illustrated through x-ray crystallography. Electron paramagnetic resonance, x-ray absorption near edge, x-ray absorption fine edge, and Fourier Transform Infrared (FTIR) spectroscopy are methods for examining dynamic and static interactions within an enzyme such as PSII. FTIR spectroscopy is a form of vibrational spectroscopy that monitors the vibration of atoms within molecules and their environment. Following applied radiation, in this case infrared light, chemical bonds vibrate characteristic to their group. The vibration occurs at a specific frequency and is used to identify the species. The midfrequency infrared region, 4000 - 400 cm^{-1}, is commonly observed in protein study. Here frequencies for bending groups such as amide II and stretching groups such as amide I, symmetric and asymmetric carboxylates, and carbonyl of the carboxylate can be viewed (Table 1). When examining a protein with FTIR spectroscopy such as PSII, the absorbance measured in the midfrequency region shows two very large amide peaks representative of the protein's peptide backbone. Small changes which occur as a result of the water splitting process would not be seen in this instance. However, the method of FTIR difference spectroscopy allows small changes in measured frequencies to be observed. Using PSII as an example, the protein's absorbance data for the dark stable S_1 state is measured followed by illumination of the sample which drives the S-state cycle to S_2 (Figure 11). Data for the S_2 state is collected and subtracted from the S_1 state. The resulting difference spectrum monitors bands that have disappeared, reappeared, or shifted

during the transition. Regions of band changes are identified by frequency and can be attributed to specific groups, identifying amino acids responsible for the changes seen. This data is useful in determining dynamic processes that occur during the water splitting reaction in PSII. Residues can be observed to coordinate the Mn_4Ca cluster based on changes in carboxylate stretching regions, to be involved in a carboxylic acid changing its pK_a in carboxylic acid stretching region, and to be necessary in maintaining structural integrity of PSII in amide stretching/bending region.

There are currently two general areas of activity in PSII under scrutiny. The first is the OEC of PSII, which has varying arrangement among the crystal structures (1 - 4). The second is a series of water channels, which guide the water molecules to or protons and oxygen away from the OEC during water oxidation (4, 17, 18). While the crystal structures for the OEC show multiple potential ligands, only one has been determined by FTIR difference spectroscopy to contribute a coordinate bond which changes its coordination mode in the S_1 to S_2 transition, Alanine-344 of the D1 polypeptide (20). FTIR difference spectroscopy has been used to monitor complex structure/restructure throughout the catalytic cycle induced by laser radiation. As previously described, this method follows changes between each storage state of the catalytic cycle. The changes observed can be attributed to residues' interactive role with the Mn_4Ca cluster, $Y_Z°$, and protons. Changing peaks in the midfrequency region observed during the S_{n+1}-*minus*-S_n transition in the spectra can be ascribed to bond creation, destruction, and strength, changing pK_a, environmental interactions, and polypeptide conformation (21).

Carboxylic acid stretching modes in the 2000 - 1000 cm^{-1} region are carefully studied for changes against wild-type spectra as these modes are a way of indicating interactions during the catalytic cycle. This is due to the carboxylic acid functional group which is capable of contributing coordinate bonds to the manganese, such as with the previously mentioned Alanine-344. After labeling PSII with ^{13}C alanine, D1-Ala344 showed a downshift in the symmetric

carboxylate stretching mode. The downshift in the symmetric carboxylate region is the only vibrational feature in any of the midfrequency S_{n+1}-*minus*-S_n FTIR difference spectra that has been identified as contributing a coordinate bond to a manganese (20). This method of following changes in identified vibrational modes helps to characterize structural changes or bonding during the catalytic cycle. Using the x-ray crystallographic structural models as a guide, residues which have likely roles in manganese ligation are chosen for examination. These residues are D1-Asp170, D1-Glu189, D1-Glu333, D1-Asp342, and CP43-Glu354 and can be seen in Figure 12. Site-directed mutagenesis studies are employed in conjunction with FTIR difference spectroscopy for studying residues individually. However, D1-Asp170, D1-Glu189, and D1-Asp342 have all been previously examined with this process and showed no evidence of coordinating a manganese that undergoes oxidation in S_0 through S_3 transitions at a resolution of 4 cm^{-1} (22, 23, 24). Site-directed mutagenesis of a single amino acid followed by FTIR spectroscopic studies isolates the function of that particular residue through examination of the resulting change of vibrational modes. Target amino acids are those shown by x-ray crystallographic structures to be possible ligands to the Mn_4Ca cluster, in the second coordination sphere, or possible hydrogen bond acceptors in channels. FTIR difference spectroscopy reveals changes that occur after residue mutation for S-state transitions, so the function of the residue in a particular environment can be recognized. The mutated residues each provide a portion of information for the entire system. Should a mutated carboxylate residue have an effect on a manganese with increasing charge, the resulting decrease of frequency within the symmetric or asymmetric carboxylate stretching modes as compared to wild-type spectra would be observed. The resulting frequency gives additional information on the nature of coordination, described in Figure 13. Mutants with no apparent change in the S_{n+1}-*minus*-S_n FTIR difference spectra suggest that the carboxylate group either does not ligate the Mn_4Ca cluster, or instead ligates a manganese ion that does not increase its

charge during the S_0 through S_3 transitions. Two residues which remain in question are Glu333 of the D1 polypeptide and Glu354 of the CP43 polypeptide (2). D1-Glu333 is represented in the 3.5 Å, 3.0 Å, 2.9 and 1.9 Å structural models as a bidentate ligand between Mn3 and Mn4. CP43-Glu354 is represented in the 3.5 Å structural model as a chelating ligand of Mn3 and in the 3.0 Å 2.9, and 1.9 Å structural models as a bidentate ligand between Mn2 and Mn3, one of which is the same Mn ion ligated by D1-Ala344 (1 - 4).

In conjunction with the water-splitting active site, water and proton channels within PSII could be contributing to the bands seen in the FTIR difference spectra. Both D1-Glu333 and CP43-Glu354 are located in the narrow water channel as potential H-bond acceptors contacting the channel wall. Additionally, CP43-Glu354 is located at the large water channel and D1-Glu333 is at the mouth of the broad channel, next to the chloride 1 ion, Cl^-1 (4, 18). In addition to these two, there are three carboxylate functional grouped residues near the Mn_4Ca cluster that are potential H-bond acceptors in channels. These are D1-Glu329 of the large channel and D2-Glu312 and D1-Glu65 of the broad channel. D1-Glu65 has an additional role as a "gate function" as it is one of four residues blocking free water access (18). The broad channel Cl^-1 contributes some amount of stability to the catalytic cycle, though specific function is not well understood. Surrounded by two water molecules, D1-Glu333, and D2-K317, it is also a matter of interest with respect to activity within the hydrogen bonding network and effect on the Mn_4Ca cluster (4, 25). As the control center for the water-splitting activity, understanding the role of specific residues and their impact on the Mn_4Ca cluster is imperative. The Mn_4Ca cluster actively regulates water oxidation while controlling oxidized intermediates thereby retaining structural integrity within the PSII active site and channels. This study focuses on Glu354 of the CP43 polypeptide, Glu329, Glu333, and Glu65 of the D1 polypeptide, and Glu312 and Lys317 of the D2 polypeptide.

1.5 References

1. Ferreira, K., Iverson, T., Maghlaoui, K., Barber, J., & Iwata, S. (2004) Architecture of the Photosynthetic Oxygen-Evolving Center, *Science 303*, 1831-1838.

2. Loll, B., Kern, J., Saenger, W., Zouni, A., Biesiadka, J. (2005) Towards Complete Cofactor Arrangement in the 3.0 Å Resolution Structure of Photosystem II, *Nature 438*: 1040-1044

3. Guskov, A., Kern, J., Gabdulkhakov, A., Broser, M., Zouni, A., and Saenger, W. (2009) Cyanobacterial Photosystem II at 2.9 Å Resolution and the Role of Quinones, Lipids, Channels and Chloride, *Nature Struct. & Mol. Biol*. *16*, 334-342

4. Umena, Y., Kawakami, K., Shen, J.R., Kamiya, N. (2011) Crystal Structure of the Oxygen-Evolving Photosystem II at a Resolution of 1.9 Å, *Nature 473* 55-61.

5. Barber, J. (2002) Photosystem II: A Multisubunit Membrane Protein that Oxidises Water Current Opinion in Structural Biology 12, 523-530

6. Biesiadka, J., Loll, B., Kern, J., Irrgang, K-D., & Zouni, A. (2004) Crystal Structure of Cyanobacterial Photosystem II at 3.2 Å Resolution: A Closer Look at the Mn-cluster, *Phys. Chem. Chem. Phys*. *6*, 4733-4736.

7. Barber, J. (2003) Photosystem II: The Engine of Life, *Quarterly Reviews of Biophysics*. *36*, 71-89.

8. Suzuki, H., Sugiura, M., Noguchi, T. (2009) Monitoring Proton Release during Photosynthetic Water Oxidation in Photosystem II by Means of Isotope-Edited Infrared Spectroscopy *J. Am. Chem. Soc 131*, 7849–7857.

9. Rappaport, F.; Lavergne, J. (2001) Coupling of Electron and Proton Transfer in the Photosynthetic Water Oxidase, *Biochim. Biophys. Acta 1503,* 246–259.

10. Schlodder, E.; Witt, H. T. (1999) Stoichiometry of Proton Release from the Catalytic Center in Photosynthetic Water Oxidation, Reexamination by a Glass Electrode Study at pH 5.5–7.2 *J. Biol. Chem. 274*, 30387–30392.

11. Ishikita, H., Saenger, W., Loll, B., Biesiadka, J., Knapp, E.W. (2006) Energetics of a Possible Proton Exit Pathway for Water Oxidation in Photosystem II, *Biochemistry 45*, 2063-2071.

12. Saygin, O., Witt, H. T. (1984) On the Change of the Charges in the Four Photo-Induced Oxidation Steps of the Water-splitting Enzyme System, *FEBS Lett. 176*, 83–87.

13. Berna´t, G.; Morvaridi, F.; Feyziyev, Y.; Styring, S. (2002) pH Dependence of the Four Individual Transitions in the Catalytic S-Cycle during Photosynthetic Oxygen Evolution *Biochemistry 41*, 5830–5843.

14. Suzuki, H.; Sugiura, M.; Noguchi, T. (2005) pH Dependence of the Flash-Induced S-State Transitions in the Oxygen-Evolving Center of Photosystem II from *Thermosynechoccocus elongatus* as Revealed by Fourier Transform Infrared Spectroscopy, *Biochemistry 44*, 1708–1718.

15. Noguchi, T.; Sugiura, M. (2000) Structure of an Active Water Molecule in the Water-Oxidizing Complex of Photosystem II As Studied by FTIR Spectroscopy *Biochemistry 39*, 10943–10949.

16. Noguchi, T.; Sugiura, M. (2002) FTIR Detection of Water Reactions during the Flash-Induced S-State Cycle of the Photosynthetic Water-Oxidizing Complex *Biochemistry 41*, 15706–15712

17. Murray, J.W., Barber, J. (2007) Structural Characteristics of Channels and Pathways in Photosystem II including the Identification of an Oxygen Channel, *J. Struct. Biol*. *159* 228–237.

18. Ho, F, Styring, S (2008) Access Channels and Methanol Binding Site to the $CaMn_4$ Cluster in Photosystem II Based on Solvent Accessibility Simulations, with Implications for Substrate Water Access, *Biochimica et Biophysica Acta 1777* 140–153

19. Murray, L,W., Barber, J., (2006) Identification of a Calcium-binding Site in the PsbO Protein of Photosystem II , *Biochemistry 45*, 4128-4130.

20. Chu, H-A., Hillier, W., & Debus, R.J. (2004) Evidence that the C-Terminus of the D1 Polypeptide of Photosystem II is Ligated to the Manganese Ion that Undergoes Oxidation During the S1 to S2 Transition, An Isotope-Edited FTIR Study, *Biochemistry 43*, 3152-3166.

21. Mantele, W. (1996) Infrared and Fourier-transform Infrared Spectroscopy, *Biophysical Techniques in Photosynthesis*. 137-160.

22. Strickler, M., Walker, L., Hillier, W., Britt, R., Debus, R. (2007) No evidence from FTIR Difference Spectroscopy that Aspartate-342 of the D1 polypeptide ligates a Mn ion that undergoes oxidation during the S_0 to S_1, S_1 to S_2, or S_2 to S_3 Transitions in Photosystem II, *Biochemistry 46*, 3151-3160.

23. Strickler, M., Hillier, W., Debus, R., (2006) No Evidence from FTIR Difference Spectroscopy that glutamate-189 of the D1 Polypeptide Ligates a Mn ion that Undergoes Oxidation During the S0 to S1, S1 to S2, or S2 to S3 Transitions in Photosystem II, *Biochemistry 45*, 8801-8811.

24. Debus, R., Strickler, M., Walker, L., Hillier, W., (2005) No Evidence from FTIR Difference Spectroscopy that aspartate-170 of the D1 Polypeptide Ligates a Mn ion that Undergoes Oxidation During the S0 to S1, S1 to S2, or S2 to S3 Transitions in Photosystem II, *Biochemistry 44*, 1367-1374.

25. Pokhrel, R., McConnell, I., Brudvig, G. (2011) Chloride Regulation of Enzyme Turnover: Application to the Role of Chloride in Photosystem II. *Biochemistry 50* 2725-2734.

Table 1. Infrared frequencies for symmetric and asymmetric carboxylate stretching, carbonyl of carboxylic acid stretching, amide stretching, and amide bending groups.

Group	Frequency
asymmetric carboxylate (stretching)	1570-1620
symmetric carboxylate (stretching)	1350-1450
amide I (stretching)	1620-1690
amide II (bending)	1540-1560
C=O carboxylic acid (stretching)	1710-1750

Table 1.1

Figure 1.1 Diagram showing the specific location of the oxygen evolving complex beginning with a leaf cell and ending with the OEC.

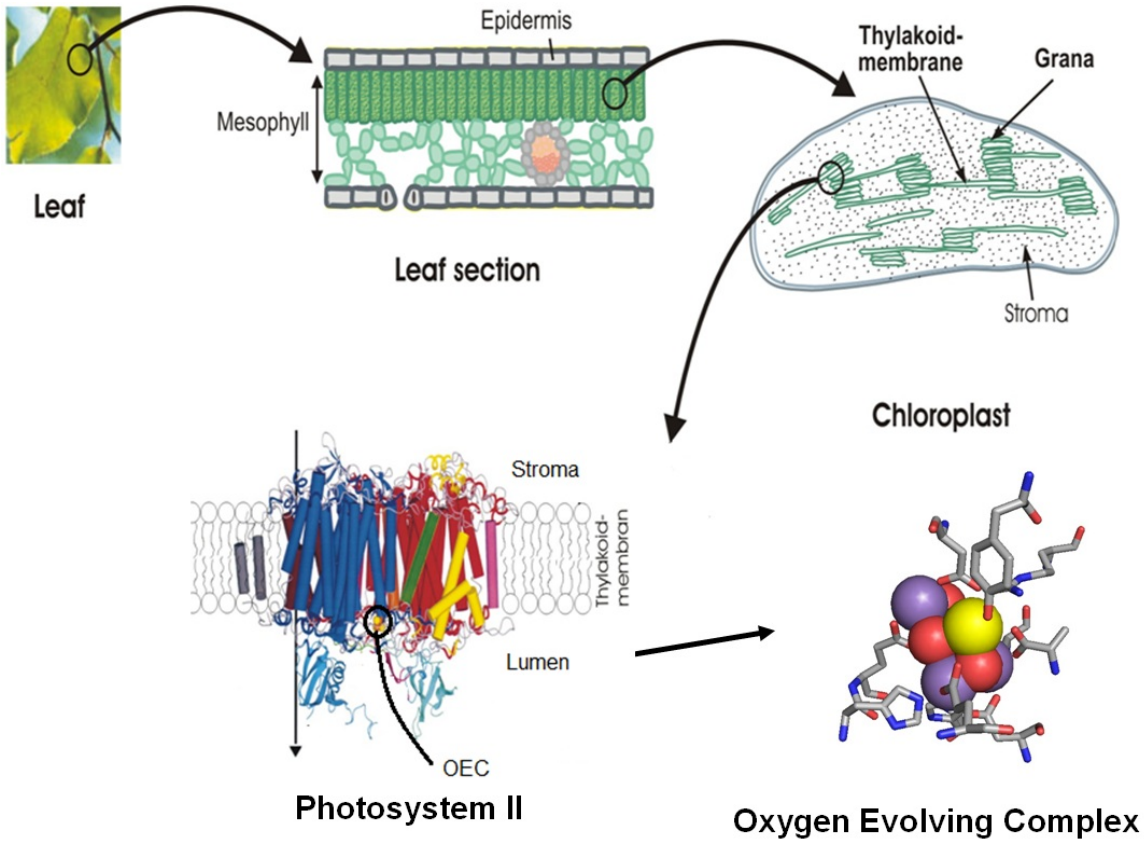
Leaf
Epidermis
Mesophyll
Leaf section
Thylakoid-membrane
Grana
Stroma
Chloroplast
Stroma
Thylakoid-membran
Lumen
OEC
Photosystem II
Oxygen Evolving Complex

Figure 1.1

Figure 1.2 Diagram showing the specific location of the oxygen evolving complex beginning with a cyanobacterial cell and ending with the OEC.

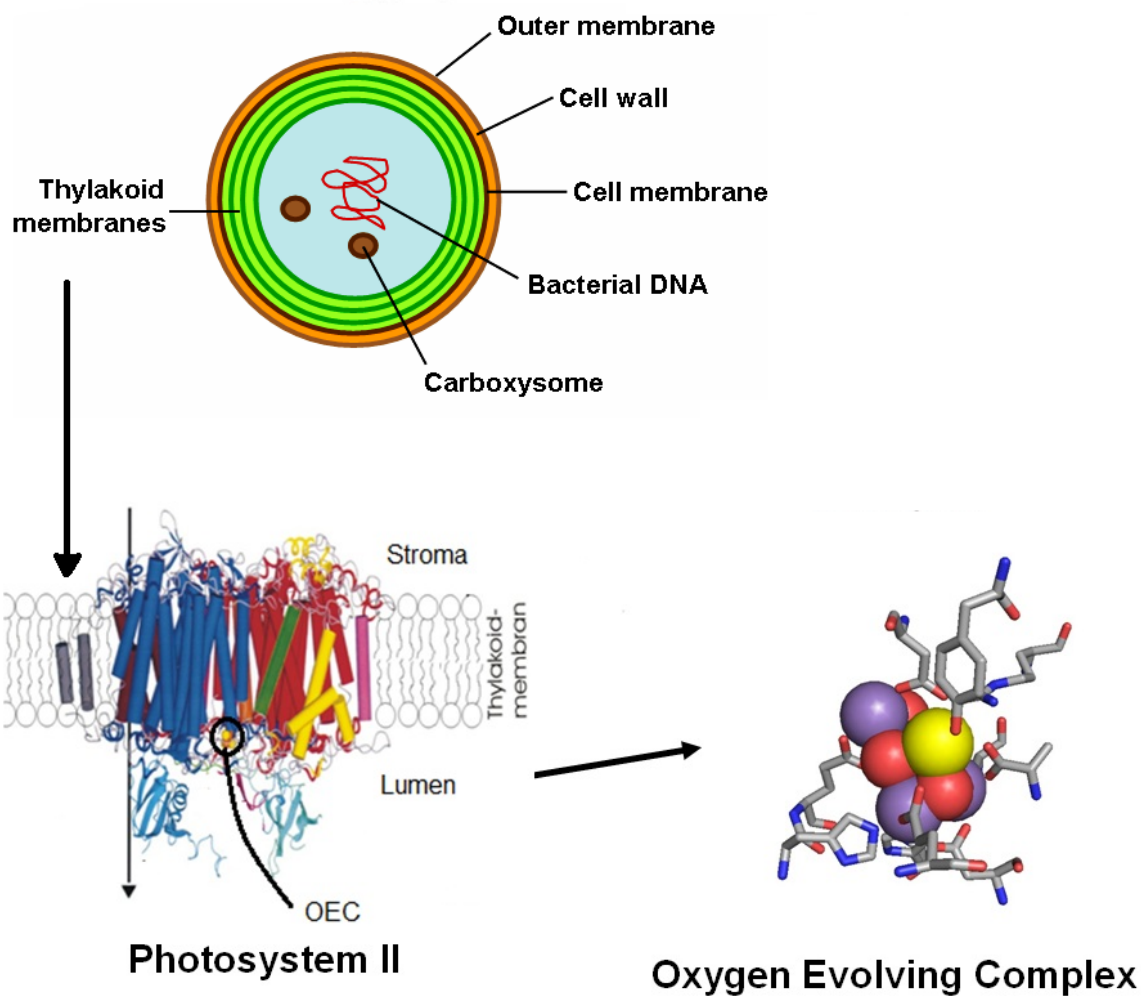
Outer membrane
Cell wall
Cell membrane
Thylakoid membranes
Bacterial DNA
Carboxysome
Stroma
Thylakoid-membran
Lumen
OEC
Photosystem II
Oxygen Evolving Complex

Figure 1.2

Figure 1.3 Antenna complex absorbs multiple wavelengths of light, transferring excitation energy to chlorophyll *a*, P_{680}.

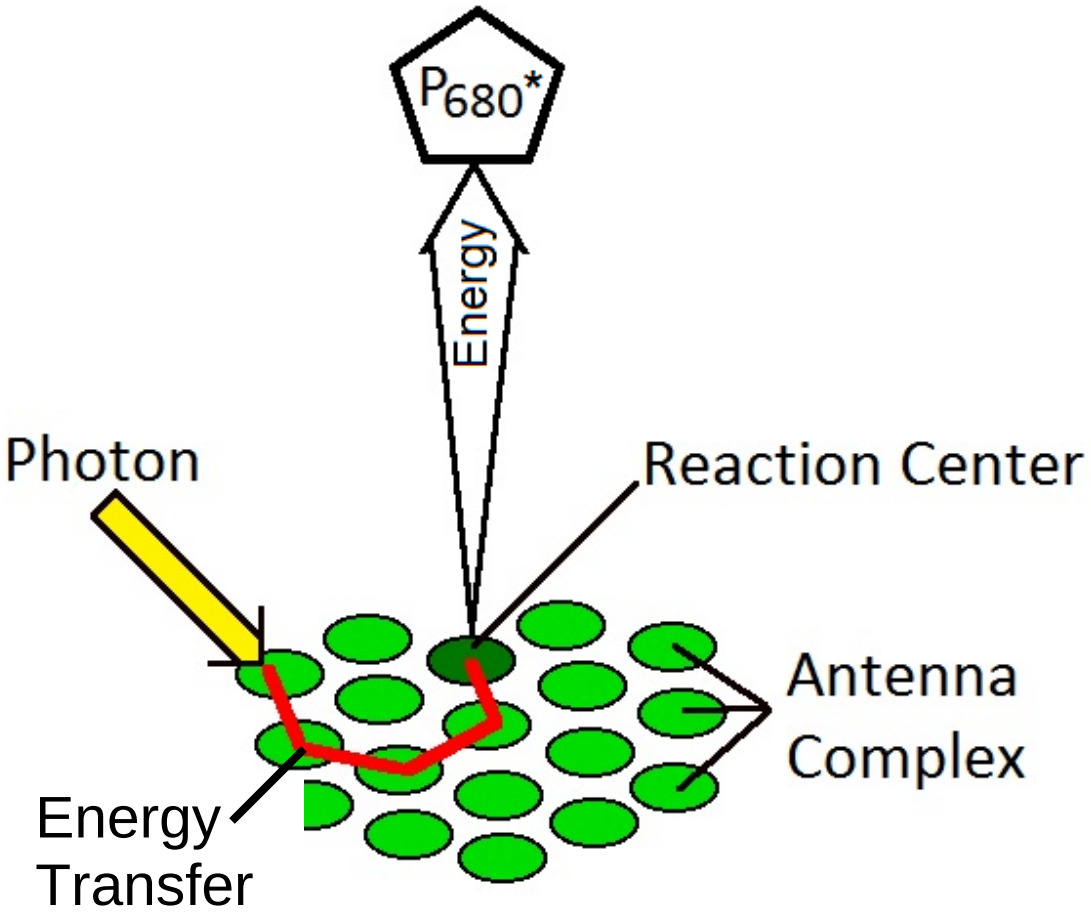
P680*
Energy
Photon
Reaction Center
Antenna
Complex
Energy
Transfer

Figure 1.3

Figure 1.4 Diagram of interactive nature of Light Dependent and Light Independent processes of photosynthesis.

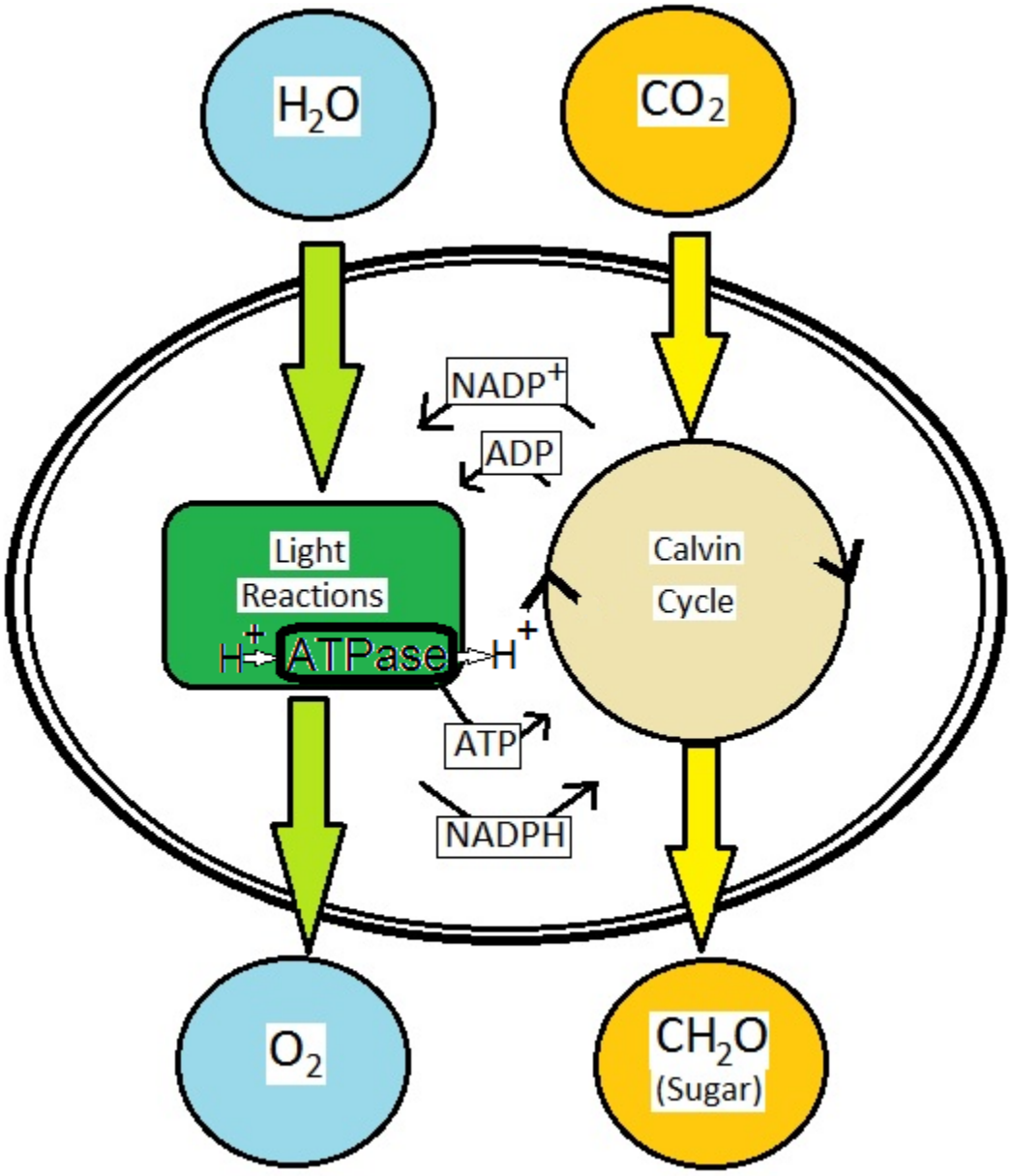
H_2O
CO_2
$NADP^+$
ADP
Light
Reactions
ATPase
H^+
H^+
Calvin
Cycle
ATP
NADPH
O_2
CH_2O
(Sugar)

Figure 1.4

Figure 1.5 Oxygen evolving complex (OEC) where water splitting occurs in Photosystem II. Mn_4Ca. Manganese in purple, calcium in yellow, and oxygen in red spheres. Residue environment in grey stick.

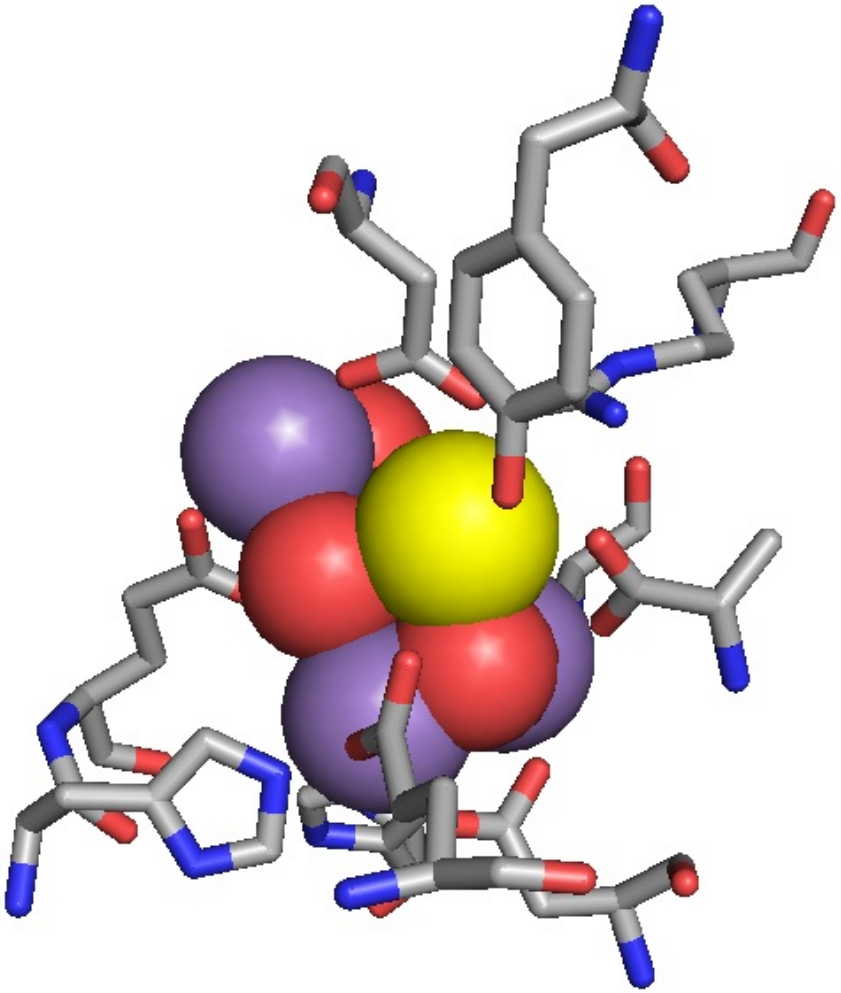

Figure 1.5

Figure 1.6 Photosystem II multisubunit complex with OEC. Subunits individually defined by color. Four polypeptides which surround the OEC D1 (light tan), CP43 (light pink), CP47 (dark peach), and D2 (turquoise). OEC circled in sphere cluster on lumenal side.

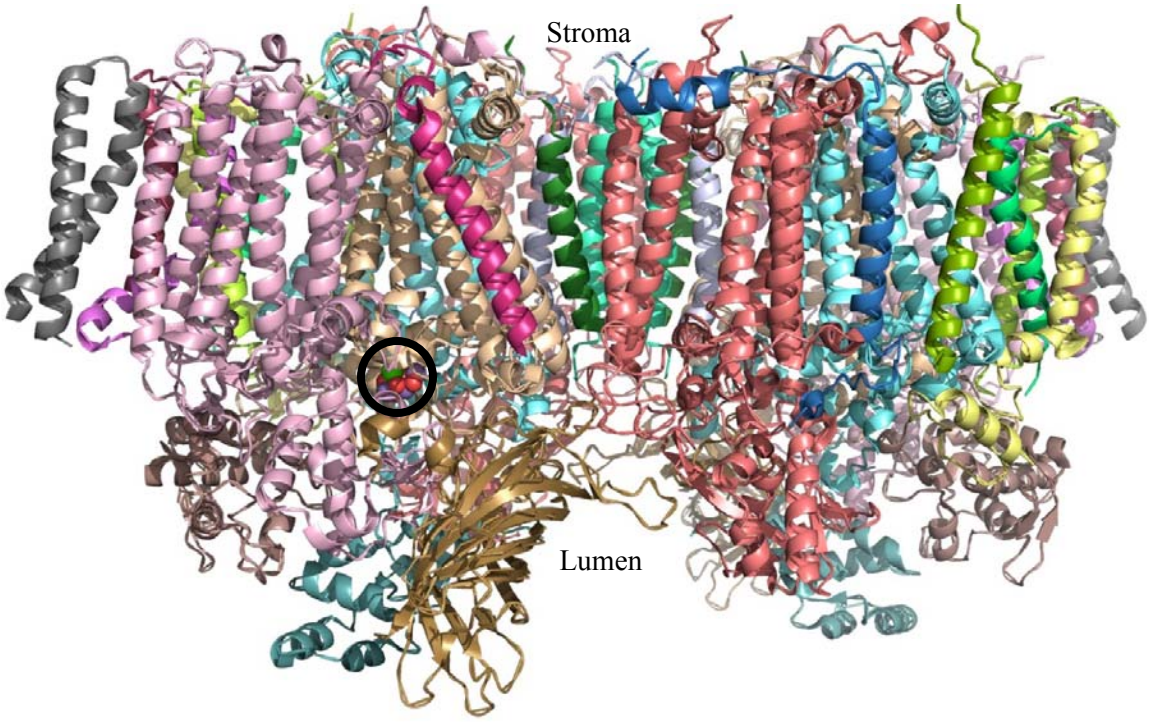

Figure 1.6

Figure 1.7 Comparison of transmembrane helix organization of PSII core dimers from cyanobacteria *Synechocystis elongatus* (left) and spinach (right). Difference in transmembrane helix area in white.

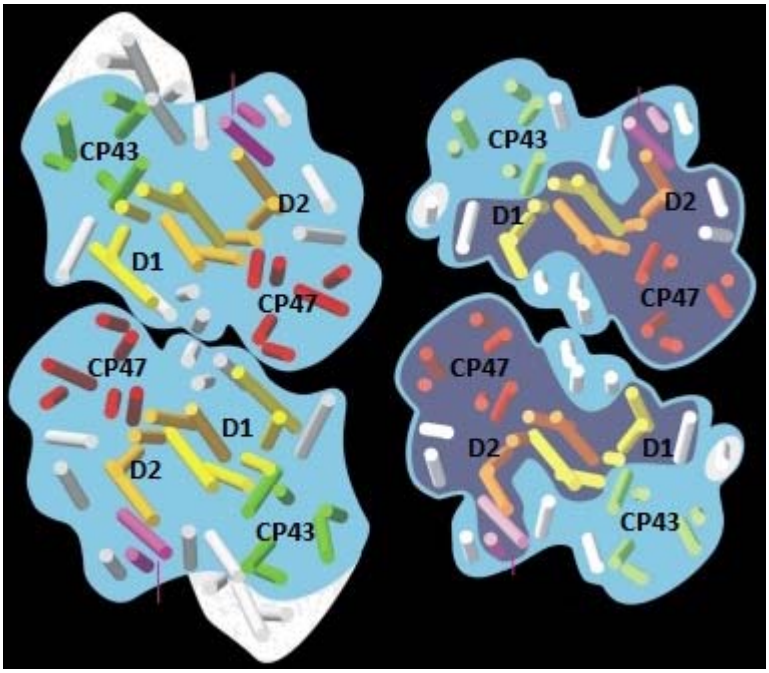

Figure 1.7

Figure 1.8 The cubane structure of the Mn_4O_5Ca cluster which takes an overall distorted chair form. Bond lengths in angstrom.

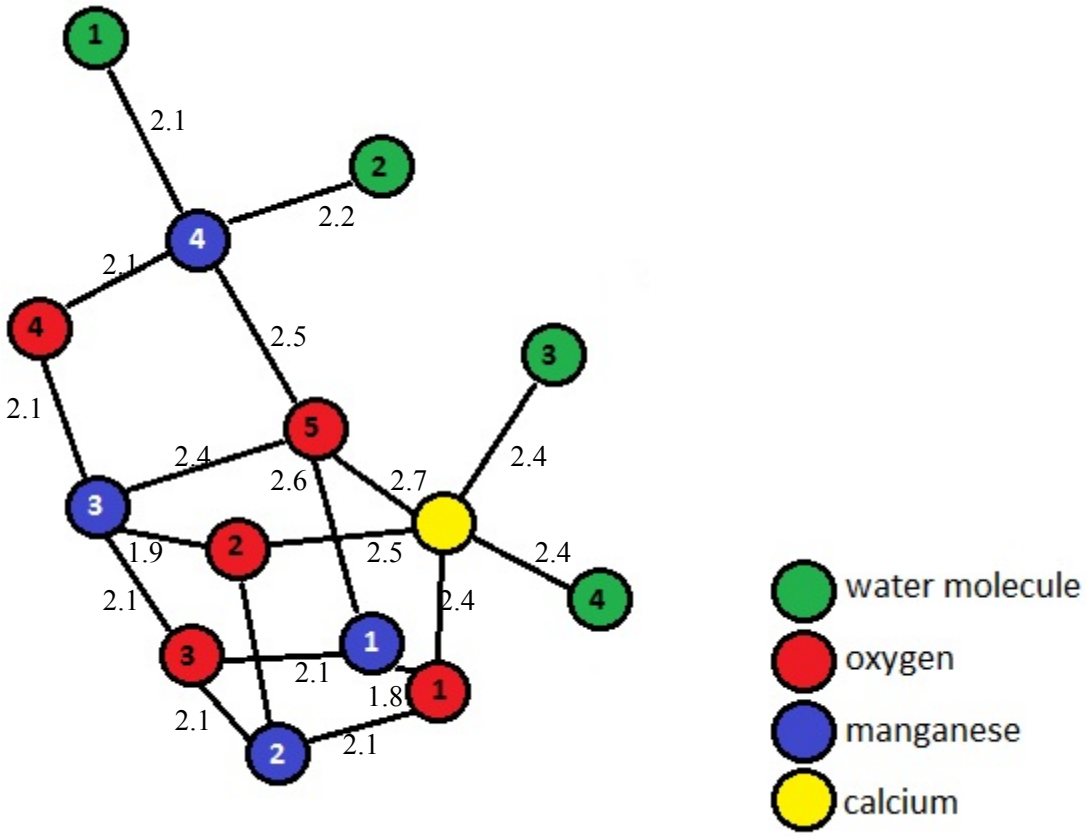
1
2.1
2
2.2
4
2.1
4
2.5
3
2.1
5
2.4
2.6
2.7
2.4
3
1.9
2
2.5
2.4
2.1
2.4
4
3
1
2.1
1.8
1
2.1
2
2.1
water molecule
oxygen
manganese
calcium

Figure 1.8

Figure 1.9 Complete pathway of electron transfer from oxidation at Mn_4Ca cluster to reduction and protonation of plastoquinone Q_B.

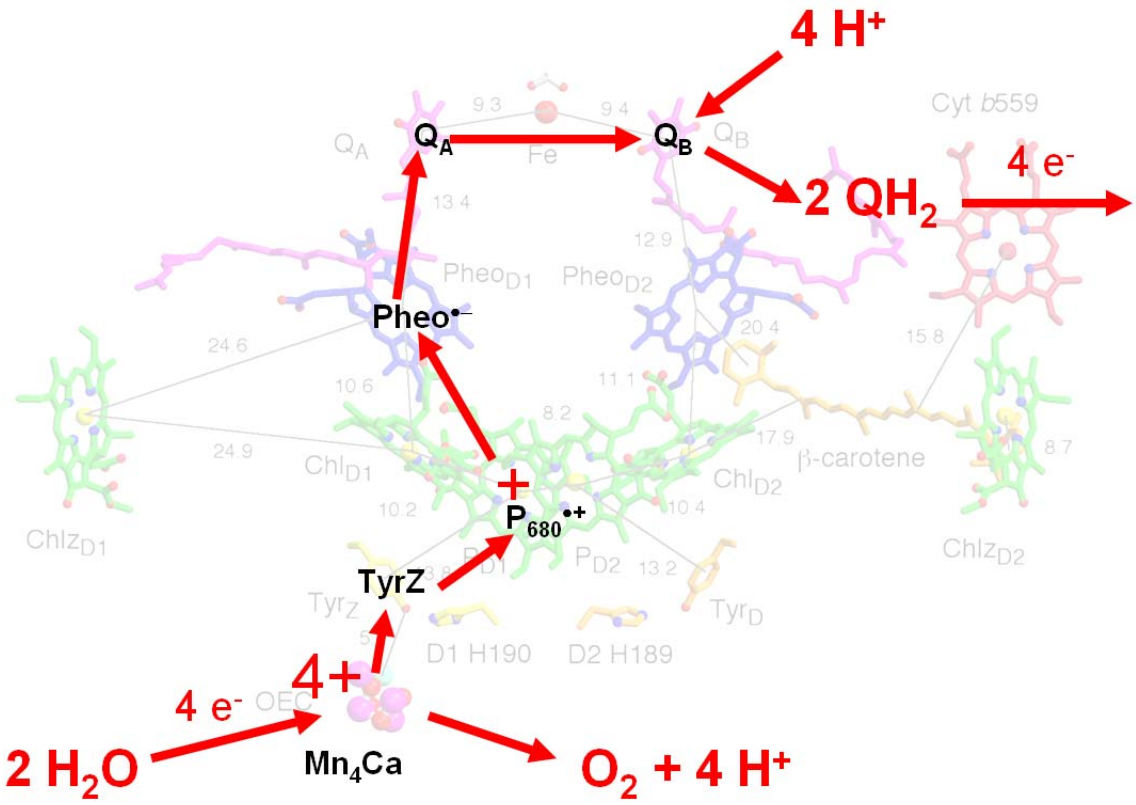
4 H+
Cyt b559
QA
QB
Fe
4 e-
2 QH2
Pheo•–
PheoD1
PheoD2
ChlD1
ChlD2
β-carotene
ChlzD1
ChlzD2
P680•+
TyrZ
TyrD
D1 H190
D2 H189
4+
4 e-
OEC
2 H2O
Mn4Ca
O2 + 4 H+

Figure 1.9

Figure 1.10 The storage state cycle with transition times between states.

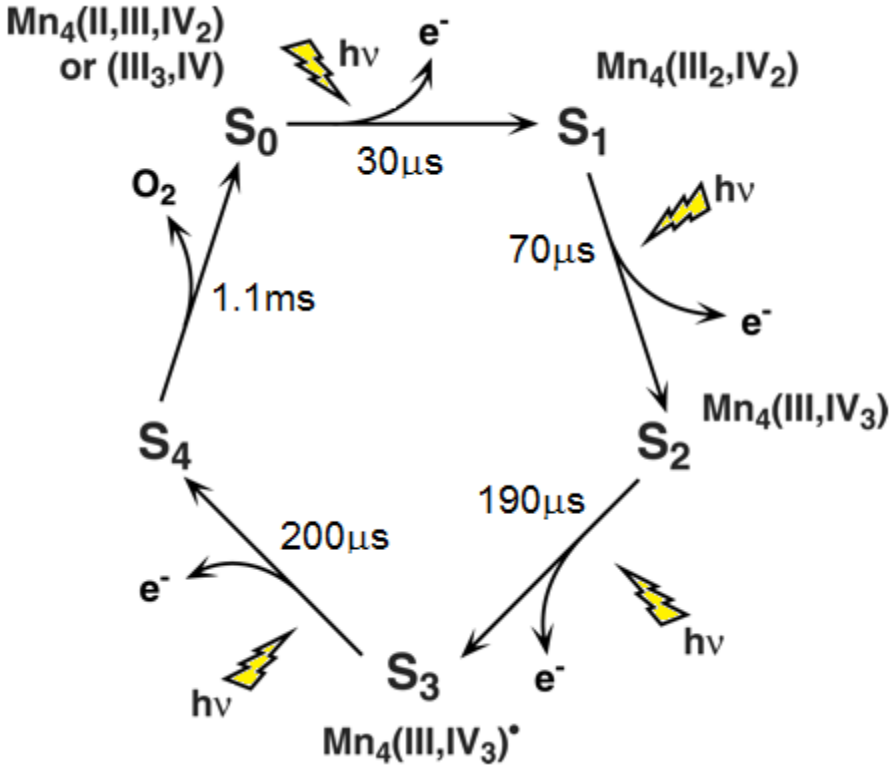
Mn4(II,III,IV2)
or (III3,IV)
hν
e-
Mn4(III2,IV2)
S0
30μs
S1
O2
hν
70μs
1.1ms
e-
Mn4(III,IV3)
S4
S2
190μs
200μs
e-
hν
hν
S3
e-
Mn4(III,IV3)•

Figure 1.10

Figure 1.11 Large and broad channels of PSII. OEC in sphere, protein backbone in grey ribbons, channel residues in yellow stick, water molecules in red dots. Two chloride ions in free, green spheres in large channel.

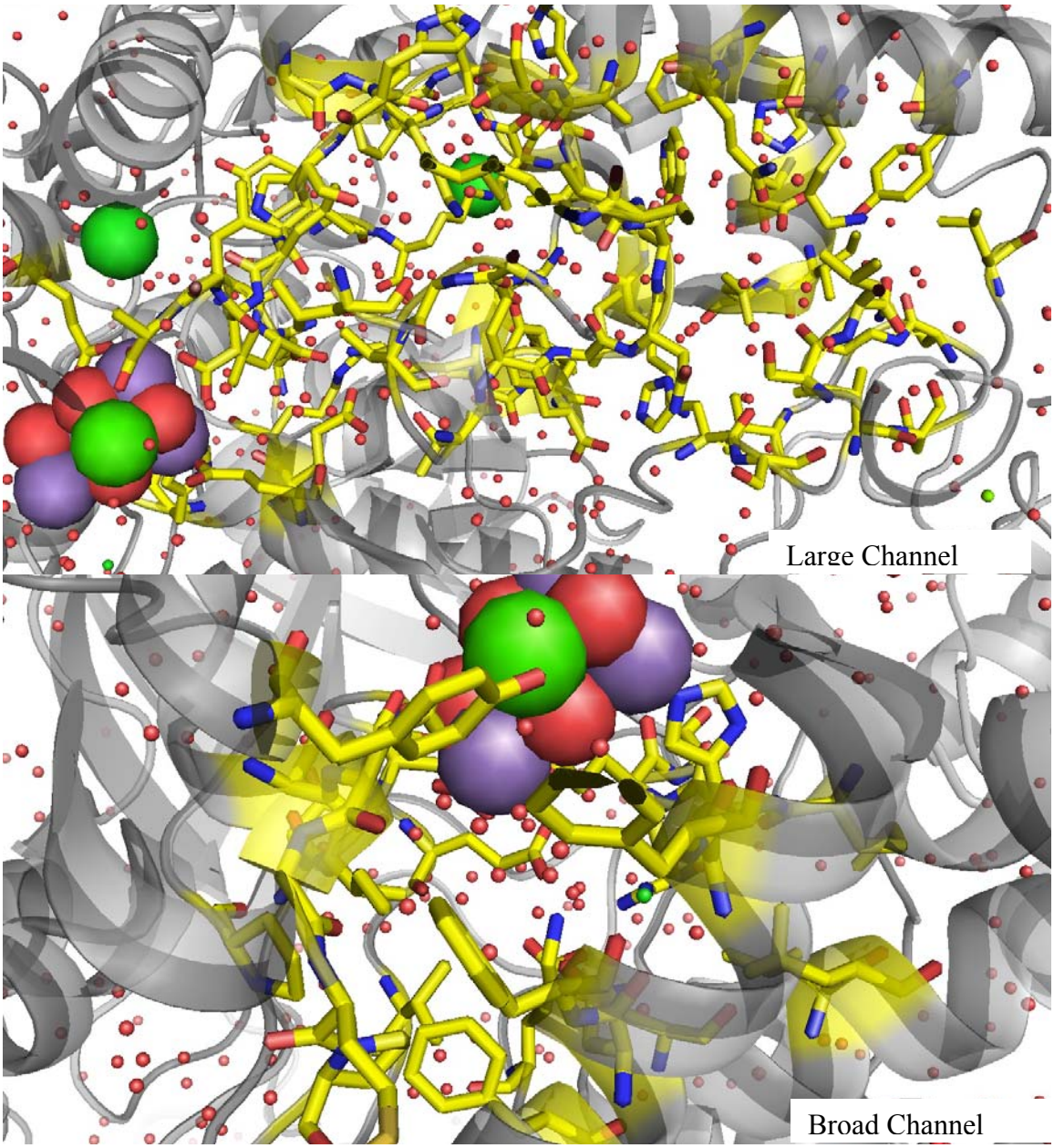
Large Channel
Broad Channel

Figure 1.12 FTIR difference spectra for PSII S_1 to S_2 transition. Difference is taken by subtracting S_2 from S_1.

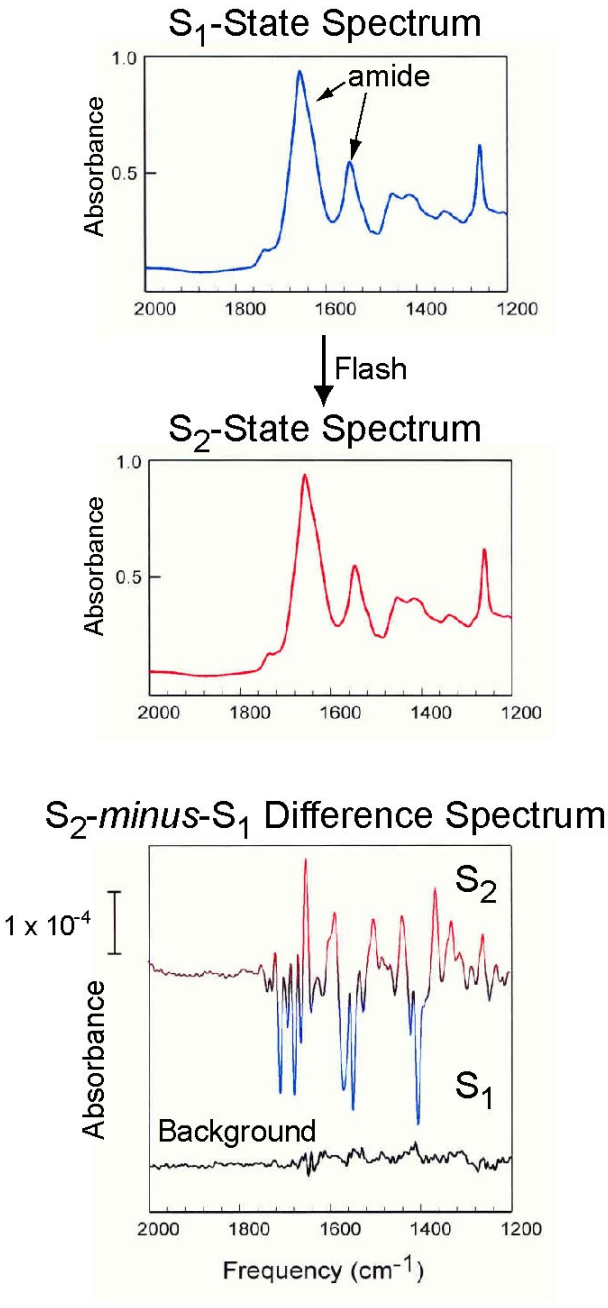
S1-State Spectrum
amide
Absorbance
1.0
0.5
2000
1800
1600
1400
1200
Flash
S2-State Spectrum
S2-minus-S1 Difference Spectrum
1 x 10-4
S2
S1
Background
Frequency (cm-1)

Figure 1.12

Figure 1.13 X-ray crystallographic described ligands to the OEC. Ligands in blue stick, manganese in purple sphere, calcium in yellow sphere, oxygen in red sphere.

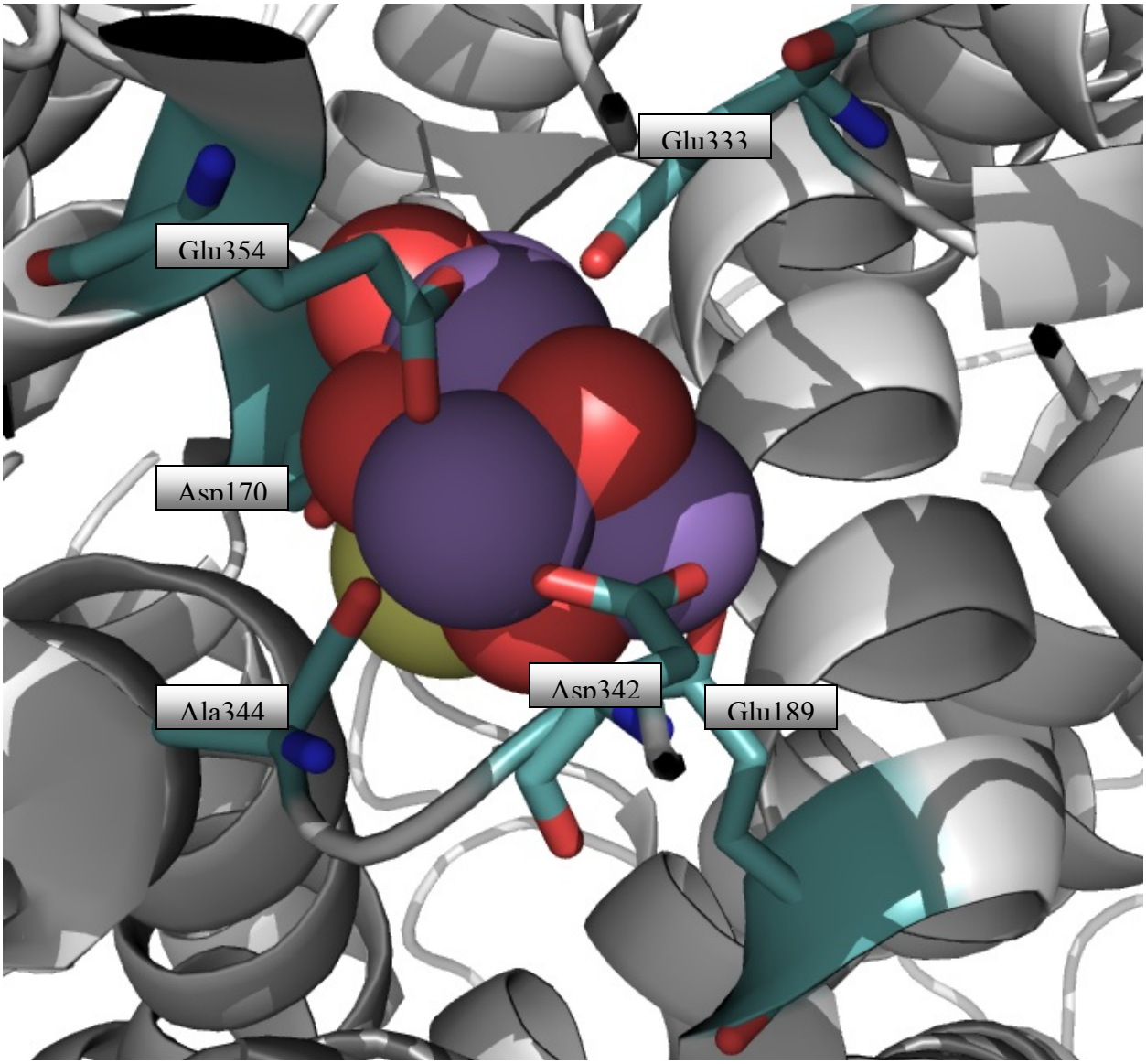

Figure 1.13

Figure 1.14 Infrared vibrational frequencies for asymmetric and symmetric carboxylate stretching coordination modes bridging, bidentate chelating, unidentate, and free ionic.

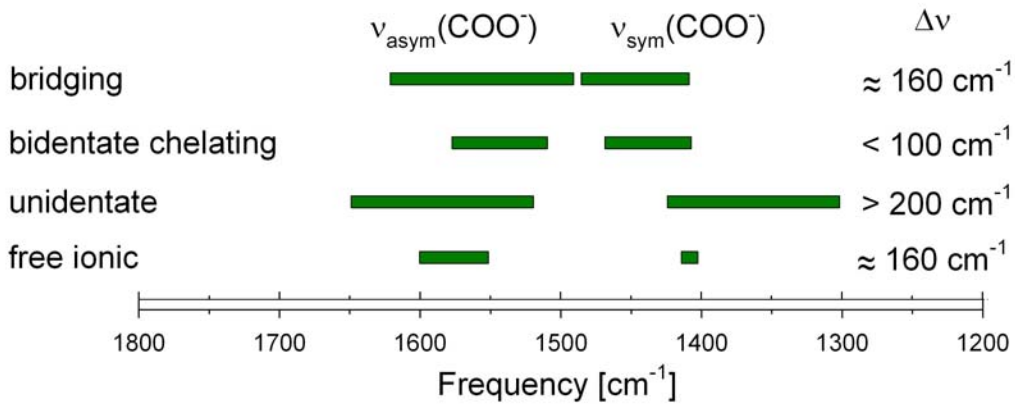
$\nu_{asym}(COO^-)$
$\nu_{sym}(COO^-)$
$\Delta\nu$
bridging
≈ 160 cm^{-1}
bidentate chelating
< 100 cm^{-1}
unidentate
> 200 cm^{-1}
free ionic
≈ 160 cm^{-1}
1800
1700
1600
1500
1400
1300
1200
Frequency [cm^{-1}]

Figure 1.14

CHAPTER 2

PARTICIPATION OF GLUTAMATE-354 OF THE CP43 POLYPEPTIDE IN THE LIGATION OF MN AND BINDING OF SUBSTRATE WATER IN PHOTOSYSTEM II

2.1 Abstract

In the current x-ray crystallographic structural models of photosystem II, Glu354 of the CP43 polypeptide is the only amino acid ligand of the oxygen-evolving Mn_4Ca cluster that is not provided by the D1 polypeptide. To further explore the influence of this structurally unique residue on the properties of the Mn_4Ca cluster, the CP43-E354Q mutant of the cyanobacterium *Synechocystis* sp. PCC 6803 was characterized with a variety of biophysical and spectroscopic methods, including polarography, EPR, x-ray Absorption, FTIR, and mass spectrometry. The kinetics of oxygen release in the mutant were essentially unchanged from those in wild-type. In addition, the oxygen flash-yields exhibited normal period-four oscillations having normal S-state parameters, although the yields were lower, correlating with the mutant's lower steady-state rate (approx. 20% compared to wild-type). Experiments conducted with $H_2{}^{18}O$ showed that the fast and slow phases of substrate water exchange in CP43-E354Q thylakoid membranes were accelerated 8.5- and 1.8-fold, respectively, in the S_3 state compared to wild-type. Purified oxygen-evolving CP43-E354Q PSII core complexes exhibited a slightly altered S_1 state Mn-EXAFS spectrum, a slightly altered S_2 state multiline EPR signal, a substantially altered S_2-*minus*-S_1 FTIR difference spectrum, and an unusually long lifetime for the S_2 state (> 10 hours) in a substantial fraction of reaction centers. In contrast, the S_2 state Mn-EXAFS spectrum was nearly indistinguishable from that of wild-type. The S_2-*minus*-S_1 FTIR difference spectrum showed alterations throughout the amide and carboxylate stretching regions. Global labeling with ^{15}N and specific labeling with L-[1-^{13}C]alanine revealed that the mutation perturbs both amide II and

carboxylate stretching modes and shifts the symmetric carboxylate stretching modes of the α-COO^- group of D1-Ala344 (the C-terminus of the D1 polypeptide) to higher frequencies by 3 – 4 cm^{-1} in both the S_1 and S_2 states. The EPR and FTIR data implied that 76 – 82 % of CP43-E354Q PSII centers can achieve the S_2 state and that most of these can achieve the S_3 state, but no evidence for advancement beyond the S_3 state was observed in the FTIR data, at least not in a majority of PSII centers. Although the x-ray absorption and EPR data showed that the CP43-E354Q mutation only subtly perturbs the structure and spin state of the Mn_4Ca cluster in the S_2 state, the FTIR and $H_2{}^{18}O$ exchange data show that the mutation strongly influences other properties of the Mn_4Ca cluster, altering the response of numerous carboxylate and amide groups to the increased positive charge that develops on the cluster during the S_1 to S_2 transition and weakening the binding of both substrate water molecules (or water derived ligands), especially the one that exchanges rapidly in the S_3 state. The FTIR data provide evidence that CP43-Glu354 coordinates to the Mn_4Ca cluster in the S_1 state as a bridging ligand between two metal ions, but provide no compelling evidence that this residue changes its coordination mode during the S_1 to S_2 transition. The $H_2{}^{18}O$ exchange data provide evidence that CP43-Glu354 interacts with the Mn ion that ligates the substrate water molecule (or water-derived ligand) that is in rapid exchange in the S_3 state.

2.2 Introduction

The light-driven oxidation of water in Photosystem II (PSII) [1] produces nearly all of the O_2 on Earth and drives the production of nearly all of its biomass. Photosystem II is an integral

[1] Abbreviations: Chl, chlorophyll; EDTA, ethylenediaminetetraacetic acid; EPR, electron paramagnetic resonance; EXAFS, extended X-ray absorption fine structure; FTIR, Fourier transform infrared; MES, 2-(N-morpholino)-ethanesulfonic acid; NTA, nitrilotriacetic acid; P_{680}, chlorophyll multimer that serves as the light-induced electron donor in PSII; Pheo, pheophytin; PSII, photosystem II; Q_A, primary plastoquinone electron acceptor; Q_B, secondary plastoquinone electron acceptor; RH, relative humidity; XANES, X-ray absorption near edge structure; Y_Z, tyrosine residue electron transfer mediary between the Mn_4Ca cluster and $P_{680}{}^{+\bullet}$, Y_D, second tyrosine residue that can reduce $P_{680}{}^{+\bullet}$ in PSII.

membrane protein complex that is located in the thylakoid membranes of plants, algae, and cyanobacteria. It is a homodimer *in vivo*, having a total molecular weight of over 700 kDa. Each monomer consists of at least 20 different subunits and contains over 60 organic and inorganic cofactors including 35 Chl *a* and 12 carotenoid molecules. Each monomer's primary subunits include the membrane spanning polypeptides CP47 (56 kDa), CP43 (52 kDa), D2 (39 kDa), and D1 (38 kDa), and the extrinsic polypeptide PsbO (26.8 kDa). The D1 and D2 polypeptides are homologous and together form a heterodimer at the core of each monomer. Within each monomer, the CP47 and CP43 polypeptides are located on either side of the D1/D2 heterodimer and serve to transfer excitation energy from the peripherally-located antenna complex to the D1/D2 heterodimer, and specifically to the photochemically active Chl *a* multimer known as P_{680} (*1-6*).

The O_2-evolving catalytic site consists of a pentanuclear metal cluster containing four Mn ions and one Ca ion. The Mn_4Ca cluster accumulates oxidizing equivalents in response to photochemical events within PSII and then catalyzes the oxidation of two molecules of water, releasing one molecule of O_2 as a by-product (*7-11*). The Mn_4Ca cluster serves as the interface between single-electron photochemistry and the four-electron process of water oxidation. The photochemical events that precede water oxidation take place in the D1/D2 heterodimer. These events are initiated by the transfer of excitation energy to P_{680} following capture of light energy by the antenna complex. Excitation of P_{680} results in the formation of the charge-separated state, $P_{680}^{\bullet+}Pheo^{\bullet-}$. This light-induced separation of charge is stabilized by the rapid oxidation of $Pheo^{\bullet-}$ by Q_A, the primary plastoquinone electron acceptor, and by the rapid reduction of $P_{680}^{\bullet+}$ by Y_Z, one of two redox-active tyrosine residues in PSII. The resulting $Y_Z^{\bullet}$ radical in turn oxidizes the Mn_4Ca cluster, while $Q_A^{\bullet-}$ reduces the secondary plastoquinone, Q_B. Subsequent charge-separations result in further oxidation of the Mn_4Ca cluster and in the two-electron reduction and

protonation of Q_B to form plastoquinol, which subsequently exchanges into the membrane-bound plastoquinone pool. During each catalytic cycle, two molecules of plastoquinol are produced at the Q_B site and the Mn_4Ca cluster cycles through five oxidation states termed S_n, where "n" denotes the number of oxidizing equivalents that are stored (n = 0 – 4). The S_1 state predominates in dark-adapted samples. Most interpretations of Mn-XANES and EPR data have concluded that the S_1 state consists of two Mn(III) and two Mn(IV) ions and that the S_2 state consists of one Mn(III) and three Mn(IV) ions (*11-14*). The S_4 state is a transient intermediate. Its formation triggers the rapid oxidation of the two substrate water molecules, the regeneration of the S_0 state, and the release of O_2.

Refined x-ray crystallographic structural models of PSII are available at 3.5 Å (*1*), 3.0 Å (*2*), and 2.9 Å (*5*). These models, plus less-complete models at somewhat lower resolutions (*15, 16*), provide views of the Mn_4Ca cluster and its ligation environment, including 1 – 2 catalytically-essential Cl^- ions that are located 6 – 7 Å distant. However, there are significant differences between these views. For example, in the 2.9 and 3.0 Å structural models, most of the carboxylate ligands are bidentate and the α-COO^- group of D1-Ala344 (the C-terminus of the D1 polypeptide) ligates the Mn_4Ca cluster, whereas in the 3.5 Å structural model, most of the carboxylate ligands are unidentate and the α-COO^- group of D1-Ala344 ligates *no* metal ion. One reason for these differences is that the resolutions of the diffraction data are limited. A second reason is that the Mn(III/IV) ions of the Mn_4Ca cluster were undoubtedly reduced by x-ray generated radicals to their Mn(II) oxidation states during collection of the x-ray diffraction data (*17, 18*). This reduction would have disrupted the cluster's Mn-O-Mn bridging moieties and altered Mn-ligand interactions. Consequently, the structures of the Mn_4Ca cluster depicted in the x-ray crystallographic models represent unknown superimpositions of native and disrupted Mn_4Ca clusters, with the metal ions in the latter being retained in the vicinity of their native

positions by virtue of the crystals being kept frozen at 100 K during data collection. Importantly, none of the crystallographic structural models is fully compatible with polarized EXAFS studies of single crystals of PSII that were conducted with low x-ray fluxes that minimize photoreduction of the Mn ions (*19*) [2]. Nevertheless, the existing crystallographic studies agree with each other, and with the earlier mutagenesis studies (*20*), on the identity of most of the Mn_4Ca cluster's amino acid ligands. Furthermore, the structure of PSII outside the immediate environment of the Mn_4Ca cluster should be largely unaffected by the radiation-induced reduction of the cluster's Mn ions. Consequently, the existing crystallographic structural models are serving as valuable guides for spectroscopic studies designed to provide insight into the structure, dynamics, and mechanism of the Mn_4Ca cluster throughout its catalytic cycle.

To satisfy the very severe energetic and mechanistic constraints of oxidizing water, the Mn_4Ca cluster's reactivity in each of its oxidation states is tightly controlled by its protein environment. The amino acid residues in this environment choreograph the proton and electron reactions associated with water oxidation and play important roles in the delivery of substrate water and the release of O_2 and protons. In particular, these residues minimize the energetic requirements for water oxidation by coupling the requisite proton and electron extraction reactions (*7, 13, 21, 22*), minimize deleterious side-reactions by preventing unregulated access of water to the Mn_4Ca catalyst (*23*), and minimize oxidative damage by promoting rapid egress of newly formed O_2 (*24*). Understanding the influence on the Mn_4Ca cluster of specific residues in this environment is crucial to understanding the mechanism of water oxidation in PSII.

---

[2] An x-ray crystallographic structural model of PSII at 1.9 Å was recently reported at the 15th International Congress of Photosythesis in Beijing, China by J.-R. Shen, Y. Umena, K. Kawakami, and N. Kamiya (poster PS6.5). In addition to being obtained at much higher resolution than in previous studies, the diffraction data were obtained with much lower x-ray fluxes in order to minimize radiation-induced reduction of the Mn(III/IV) ions. To a large extent, the coordination modes of the ligating amino acid residues in this model appear to resemble those in the 3.0 Å and 2.9 Å structural models, but the new model's compatibility with the polarized EXAFS studies of single crystals is not known as of this writing.

This study focuses on Glu354 of the CP43 polypeptide [3]. In all of the current x-ray crystallographic structural models, this residue is depicted as being a ligand to the Mn_4Ca cluster and is the only amino acid ligand of the cluster that is not provided by the D1 polypeptide. In the 3.5 Å model, this residue is a bidentate ligand of a single Mn ion [Mn(3)]. In the 3.0 Å and 2.9 Å models, this residue bridges two Mn ions [Mn(2) and Mn(3)], including the Mn ion that is ligated (in these models) by the α-COO^- group of D1-Ala344, the C-terminus of the D1 polypeptide [Mn(2) in these models]. The CP43-E354Q mutation severely impedes the photoautotropic growth of the cyanobacterium *Synechocystis* sp. PCC 6803 and sharply diminishes its O_2 evolving activity (*26-28*). To better understand the role of CP43-Glu354 in influencing the reactivity of the Mn_4Ca cluster, we have characterized the CP43-E354Q mutant with a variety of biophysical and spectroscopic methods including polarography, EPR, FTIR, XANES, EXAFS, and mass spectrometry, the latter to measure the exchange rates of the two substrate water molecules in the S_3 state. Our results provide evidence that CP43-Glu354 coordinates to the Mn_4Ca cluster as a bridging ligand between two metal ions, in agreement with the 2.9 and 3.0 Å x-ray crystallographic structural models (*2, 5*) and with a recent FTIR study of the same mutant (*28*). However, our FTIR data provide no compelling evidence that this residue changes its coordination mode during the S_1 to S_2 transition, contrary to one of the conclusions of the earlier FTIR study (*28*). Our results also provide evidence that CP43-Glu354 interacts with the Mn ion that ligates the substrate water molecule or water-derived ligand that is in rapid exchange in the S_3 state. A preliminary account of this work has been presented (*27*).

[3] Multiple numbering systems are in use for CP43 (*25*). The different numbering systems arise because *psbC* (the gene encoding CP43) has an unusual start codon, because CP43 is post-translationally processed at its amino terminus, and because, in *Synechocystis* sp. PCC 6803, there is a deletion of one residue at position 7 compared to the amino acid sequences of CP43 in other organisms. The numbering system used in this study is the same as that used in the X-ray crystallographic studies (*1, 2, 5*).

2.3 Materials and Methods

Construction of Mutant and Propagation of Cultures.

The CP43-E354Q mutation was constructed in the *psbC* gene of *Synechocystis* sp. PCC 6803 and transformed into a host strain of *Synechocystis* that lacks the large extrinsic loop of CP43 and contains a hexahistidine-tag (His-tag) fused to the C-terminus of CP47 [the cloned *psbC* gene was the kind gift of W. F. J. Vermaas (Arizona State University); our strategy for introducing mutations into the large extrinsic loop of CP43 is similar to that described in Ref. *29*; the addition of a His-tag to CP47 has been described previously (*30*)]. The wild-type strain was constructed in an identical manner as the mutant strain except that the transforming plasmid carried no site-directed mutation. Single colonies were selected for ability to grow on solid media containing 5 μg/mL kanamycin monosulfate. Solid media contained 5 mM glucose and 10 μM DCMU. The DCMU and antibiotic were omitted from the liquid cultures. Large-scale liquid cultures (each consisting of three 7 L cultures held in glass carboys) were propagated as described previously (*31*). For the purification of PSII core complexes that had been uniformly labeled with ^{15}N, liquid cultures were propagated in the presence of 10 mM $Na^{15}NO_3$ as the sole nitrogen source (98% ^{15}N enrichment, Cambridge Isotope Laboratories, Andover, MA) (*32*). For the purification of L-[1-^{13}C]alanine-labeled PSII core complexes, liquid cultures were propagated in the presence of 0.5 mM L-[1-^{13}C]alanine (99% ^{13}C enrichment, Cambridge Isotope Laboratories, Andover, MA) (*31, 33, 34*). To verify the integrity of the mutant cultures that were harvested for the purification of thylakoid membranes and PSII core complexes, an aliquot of each culture was set aside and the sequence of the portion of the *psbC* gene that encodes the large extrinsic loop of CP43 was obtained after PCR amplification of genomic DNA (*35*). No trace of the wild-type codon was detected in any of the mutant cultures.

Purification of Thylakoid Membranes.

Thylakoid membranes were isolated under dim green light at 4 °C with a procedure (*34*) that was modified from that of Tang & Diner (*36*). Harvested cells were concentrated and suspended in a buffer containing 1.2 M betaine, 10% (v/v) glycerol, 50 mM MES-NaOH (pH 6.0), 5 mM $CaCl_2$, 5 mM $MgCl_2$, 1 mM benzamidine, 1 mM ε-amino-n-caproic acid, 1 mM phenymethylsulfonyl fluoride, and 0.05 mg/mL DNAse I, then broken by nine cycles of (5 s on/15 min off) in a glass bead homogenizer (Bead-Beater, BioSpec Products, Bartlesville, OK). After separation of unbroken cells and debris by low speed centrifugation, the resulting thylakoid membranes were concentrated by ultracentrifugation (20 min at 40,000 rpm in a Beckman Ti45 rotor) and suspended to a concentration of 1.0–1.5 mg of Chl/mL in a buffer containing 1.2 M betaine, 10% (v/v) glycerol, 50 mM MES-NaOH (pH 6.0), 20 mM $CaCl_2$, 5 mM $MgCl_2$. The concentrated thylakoid membranes were either flash-frozen as 1 mL aliquots in liquid nitrogen and stored at -80 °C, or used immediately for the purification of PSII core complexes.

Purification of PSII core complexes.

Isolated oxygen-evolving PSII core complexes were purified under dim green light at 4 °C with Ni-NTA superflow affinity resin (Qiagen, Valentia, CA) as described previously (*34*). For most of the experiments, the purification buffer consisted of 1.2 M betaine, 10% (v/v) glycerol, 50 mM MES-NaOH (pH 6.0), 20 mM $CaCl_2$, 5 mM $MgCl_2$, 50 mM histidine, 1 mM EDTA, and 0.03% (w/v) *n*-dodecyl *β*-D-maltoside. For some of the FTIR experiments described in Figure 8, the betaine was omitted from the cell and thylakoid membrane suspension buffers and from the purification buffer and the concentration of glycerol was increased to 25% (v/v). The purified PSII core complexes were concentrated to ~ 1.0 mg of Chl/mL by ultrafiltration, frozen in liquid N_2, and stored at −196 °C (vapor phase nitrogen).

Flash O_2 Yield and Kinetic Measurements.

Measurements were performed with a bare platinum electrode that permits the centrifugal deposition of samples onto the electrode surface (*37*). Before deposition, thylakoid membranes were concentrated by centrifugation and suspended at ~ 0.8 mg of Chl/mL in 50 mM HEPES-NaOH (pH 7.2), 5 mM $CaCl_2$, 10 mM $MgCl_2$, and 1 M sucrose (*38*). For each measurement, 3.2 µg of Chl were deposited on the platinum surface of the platinum electrode by being centrifuged at 18,000 x g for 10 min in a Sorvall HB-4 swing-out rotor. Samples were given a series of 20 preflashes and then dark-adapted for 10 min prior to the initiation of the measuring flash sequence. Flashes were provided by a xenon flash lamp (6 µs FWHM). The preflash sequence was applied to oxidize PSII centers that may populate the "super-reduced" S_{-1} and S_{-2} states. The 10 min dark-adaptation period was incorporated to allow PSII centers to relax to the S_1 and S_0 states. Polarization of the electrode (0.73 V) was initiated 10 s before the initiation of data acquisition and the measuring flash sequence (15 flashes at a frequency of 4 Hz) was initiated 333 ms after that. Numerical extraction of the S-state parameters was performed assuming a four-state model (*39, 40*). The kinetics of O_2 release was estimated from the rising portion of the O_2 signal using the exponential method (*41*).

Preparation of EPR and X-ray Absorption Samples.

For the experiments of Figures 3A and 4, samples were concentrated to 7 – 8 mg of Chl/mL with Centricon-100 concentrators, transferred into standard quartz 4 mm OD EPR tubes (Wilmad LabGlass, Buena, NJ), dark adapted for 18 hours at 4 °C, then frozen in liquid nitrogen. For the experiments of Figure 3A, condensed O_2 was purged from the EPR tubes immediately prior to measurement by warming the tubes to 198 K (in dry ice and methanol) and directing a stream of Ar gas over the sample for 10 min in absolute darkness followed by rapid freezing in liquid N_2 (*42*). For the EPR experiments of Figure 3B and for the x-ray absorption measurements

(Figures 5 and 6), samples were transferred to a buffer containing 1.2 M betaine, 40% (v/v) glycerol, 50 mM MES-NaOH (pH 6.0), 20 mM $CaCl_2$, 5 mM $MgCl_2$, and 0.03% (w/v) *n*-dodecyl *β*-D-maltoside by concentrating them to ~ 9 mg of Chl/mL with Centricon-100 concentrators, diluting them 20-fold with a buffer containing 42% (v/v) glycerol, then concentrating them to ~ 11 mg of Chl/mL. The concentrated samples were transferred to lucite sample holders that were designed to fit in both EPR and x-ray cryostats (*43*), dark-adapted for 12 hours at 4 °C followed by six hours at room temperature, then frozen in liquid N_2. For the experiments of Figures 3B and 4, the S_2 state was generated by illuminating samples for 5 min in a non-silvered Dewar at 198 K (dry ice/ethanol) with a focused, heat-filtered, 350-Watt Radiac light source. The samples were then immediately frozen in liquid nitrogen.

EPR Measurements.

For the experiments of Figures 3A and 4, continuous-wave EPR spectra were recorded with a Bruker ER 300 EPR spectrometer (Bruker BioSpin Corporation, Billerica, MA) equipped with either a Bruker ER 4116 DM dual mode cavity (parallel mode experiments) or a Bruker ER 4102 ST standard cavity (perpendicular mode experiments) . For these experiments, the sample temperature was controlled with an Oxford ESR900 liquid helium cryostat (Oxford Instruments, Oxfordshire, United Kingdom). For the experiments of Figure 3B, continuous-wave EPR spectra were recorded with a Varian E-109 EPR spectrometer equipped with a standard TE102 cavity. For these experiments, the sample temperature was controlled with a Heli-tran liquid helium cryostat (Air Products, Allentown, PA). Sample manipulations were conducted under dim green light at 4 °C.

Preparation of FTIR Samples.

All manipulations were conducted under dim green light at 4 °C. Samples (approx. 70 μg of Chl *a*) were exchanged into FTIR analysis buffer [40 mM sucrose, 10 mM MES-NaOH (pH

6.0), 5 mM $CaCl_2$, 5 mM NaCl, 0.06% (w/v) *n*-dodecyl β-D-maltoside (*32, 44*)] by passage through a centrifugal gel filtration column at 27 x g (*45*). Concentrated samples (approx. 10 μL in volume) were mixed with 1/10 volume of fresh 100 mM potassium ferricyanide (dissolved in water) to serve as the electron acceptor, spread to a diameter of about 10 mm on a 15 mm diameter BaF_2 window, then dried lightly (until tacky) under a stream of dry nitrogen gas. For experiments in which only the S_2-*minus*-S_1 FTIR difference spectrum was recorded (Figures 8B-8D, 9, and 11), samples were placed in a controlled humidity chamber at 95% RH for 10 min. For experiments in which four successive flashes were applied (Figure 7), 1 μL of 20% (v/v) glycerol (in water) was spotted onto the window, adjacent to the sample, but not touching it to maintain the humidity of the sample in the FTIR cryostat at 99% RH (*46*). A second IR window with a Teflon spacer (0.5 mm thick) was placed over the first and sealed in place with silicon-free high-vacuum grease. The sample was loaded immediately into the FTIR cryostat at 273.0 K or 250.0 K and allowed to equilibrate in darkness for 2 h or 18 h, depending on the experiment. Sample concentrations and thicknesses were adjusted so that the absolute absorbance of the amide I band at 1657 cm^{-1} was 0.7 – 1.1.

Measurement of FTIR Spectra.

Midfrequency FTIR spectra were recorded with a Bruker Equinox 55 spectrometer (Bruker Optics, Billerica, MA) at a spectral resolution of 4 cm^{-1} as described previously (*31, 34, 44, 45, 47*). Flash illumination (~ 20 mJ/flash, ~ 7 ns fwhm) was provided by a frequency-doubled Q-switched Nd:YAG laser [Surelite I (Continuum, Santa Clara, CA)]. After dark adaptation, either four successive flashes were applied with an interval of 96 sec between each (Figure 7) or a single flash was applied (Figures 8, 9, and 11). Two single beam spectra were recorded before the first flash and one single-beam spectrum was recorded starting 0.33 sec after the first and subsequent flashes (for the experiments of Figure 7, 8B, 9, and 11, each single beam

spectrum consisted of 800 scans; for the experiments of Figures 8C and 8D, each single beam spectrum consisted of 200 scans). The 0.33 sec delay was incorporated to allow for the oxidation of $Q_A^{\bullet-}$ by the ferricyanide. Difference spectra were obtained by dividing the single-beam spectrum that was recorded after the *n*th flash by the single-beam spectrum that was recorded immediately before the *n*th flash and the ratio was converted to units of absorption. Each sample was subjected to a single set of four flashes (Figure 7), a single flash (Figures 8B, 9, and 11), or to single flashes spaced by 30 min (Figures 8C and 8D). To improve the signal-to-noise ratio, the difference spectra recorded with multiple samples were averaged.

Measurement of Mn XANES and EXAFS Spectra.

X-ray absorption spectroscopy (XAS) was performed at the Stanford Synchrotron Radiation Laboratory (SSRL) on beamline 9-3 and 7-3 at an electron energy of 3.0 GeV with an average current of 85-100 mA. The radiation was monochromatized by a Si(220) double-crystal monochromator. The intensity of the incident x-ray beam was monitored by a N_2-filled ion chamber (I_0) in front of the sample. The monochromator energy was calibrated using a pre-edge peak of $KMnO_4$ (6543.3 eV). These standards were placed between two N_2-filled ionization chambers (I_1 and I_2) after the sample. The x-ray flux at 6.6 keV was at 1 x 10^{13} photons $s^{-1}mm^{-2}$. The monochromator was detuned at 6600 eV to 50% of maximal flux to attenuate the x-ray 2nd harmonic. Samples were kept at a temperature of 10 K in a liquid helium flow cryostat to minimize radiation damage. The procedures for data reduction have been described previously (*48*).

Measurement of Substrate Water Exchange Rates by Mass Spectrometry

Frozen thylakoid samples were thawed and diluted to 0.25 mg/mL Chl in 40 mM MES (pH 6.5), 15 mM $MgCl_2$, 15 mM $CaCl_2$, 10% glycerol, and 1.2 M betaine, with potassium ferricyanide added to 0.5 mM to serve as the electron acceptor. Immediately before measurement,

individual samples were prepared in total darkness (visualized by IR goggles) and subjected to a one pre-flash, 10 min dark adaptation period to maximize the concentration of PSII centers in the S_1 state. Flashes were provided with a xenon flash lamp (FWHM = 5.2 μs). The rapid mixing sample chamber that is interfaced to the spectrometer has been described previously (*49*). Two saturating flashes were applied to poise the sample in the S_3 state, then 25 μL of 95% $H_2{}^{18}O$ was injected rapidly (mixing rate, k_{inj} = 175 s^{-1}) to produce a final ^{18}O enrichment of 12.0 ± 0.5%. A third saturating flash (the turnover flash) was then applied at varying delay times (Δt) after $H_2{}^{18}O$ injection to induce O_2 evolution. Measurements of O_2 evolved (Y_C) as a function of Δt were made at *m/e* = 34 for the mixed labeled $^{16,18}O_2$ using an in line mass spectrometer (Vacuum Generation MM6, Winford, UK). The biphasic plots of Y_C versus Δt at *m/e* = 34 were analyzed as the sum of two exponential functions using the following equation (*50*), revealing fast phase k_2 and slow phase k_1 rate constants for substrate water exchange according to the expression,

$$Y_C = 0.57(1 - \exp(-k_2 t)) + 0.43(1 - \exp(-k_1 t))$$

Further details of the data analysis procedures are provided in ref. *49*. No data were recorded at *m/e* = 36 for the double labeled $^{18,18}O_2$ because of the low ^{18}O enrichment and small oxygen signals in the mutant samples.

2.4 Results

The light-saturated, steady-state O_2 evolving activity of CP43-E354Q cells was 90 – 100 μmol O_2 (mg of Chl)$^{-1}$ h^{-1} compared to 480 – 500 μmol O_2 (μg of Chl)$^{-1}$ h^{-1} for wild-type cells. The lower rate in mutant cells (18 – 20% compared to wild-type) is consistent with earlier reports (*26, 28*). The light-saturated O_2 evolving activity of purified CP43-E354Q PSII core complexes was 0.52 – 0.70 mmol O_2 (mg of Chl)$^{-1}$ h^{-1} compared to 5.1 – 5.5 mmol O_2 (mg of Chl)$^{-1}$ h^{-1} for wild-type PSII core complexes. The lower activity of the purified mutant PSII core complexes

(10 – 14% compared to wild-type) suggests that the Mn_4Ca cluster in the *Synechocystis* CP43-E354Q mutant is somewhat labile.

O_2 Flash Yields and Kinetics of O_2 Release.

To further investigate the lower rates of O_2 evolution that are caused by the CP43-E354Q mutation, wild-type and mutant thylakoid membranes were isolated and examined with a bare platinum electrode that permits the centrifugal deposition of samples upon the electrode surface. The pattern of O_2 yields that are produced by the individual flashes in a series of saturating single-turnover flashes provides a measure of the efficiency of the individual S-state transitions. The pattern of O_2 flash yields in CP43-E354Q thylakoid membranes (Figure 1) showed the same period-four oscillations that are observed in wild-type membranes, although the amplitudes were much smaller, consistent with the lower steady-state rates of O_2 evolution observed in the mutant cells and PSII core complexes. Analysis of these data revealed that the parameters that describe the factors that contribute to the damping of the oscillations (*i.e.*, the parameters that describe misses, double-hits, and the deactivations that occur in the dark intervals between flashes) are virtually the same in the mutant as in the wild-type control (Table 1). This analysis also revealed that, after a 10 min period of dark-adaptation, the distribution of S-states in the mutant thylakoid membranes was only slightly different from that in wild-type: the percentages of PSII centers in the S_1 and S_2 states increased (the latter from 2% to 6%), whereas the percentage in the S_0 state decreased. The kinetics of O_2 release in CP43-E354Q thylakoid membranes in comparison with wild-type are presented in Figure 2. Analysis of these data showed that the kinetics of O_2 release are virtually the same in the mutant as in the wild-type, being characterized by half-times of approximately 1.2 ms.

EPR Spectra.

A parallel polarization multiline EPR signal was observed in extensively dark adapted CP43-E354Q PSII core complexes (Figure 3A, lower trace). Between 375 G and 650G, the signal resembled the S_1 state multiline EPR signal observed in wild-type PSII core complexes (upper trace), in terms of both peak positions and spacings. However, the intensity of the spectrum was low and the features below 375 G and above 650 G could not be obtained reproducibly. A perpendicular polarization multiline EPR signal was observed in extensively dark-adapted CP43-E354Q PSII core complexes after illumination at 195 K (Figure 3B, lower trace). This signal was originally observed *before* illumination in mutant PSII core complexes that had been dark adapted for only 2 h. Further investigation revealed that the signal decayed very slowly at 4 °C (Figure 4), with about 60% of the signal decaying with a half-time of about 2.5 h and the remainder decaying with a half time greater than 20 hours (Figure 4). For the data shown in Figure 3B, the mutant core complexes were dark adapted 12 hours at 4 °C followed by 6 h at room temperature to fully relax the S_2 state before illumination. In terms of peak positions and spacing, this signal resembles the S_2 state multiline EPR signal that is observed in wild-type PSII core complexes (Figure 3B, upper trace). We assign this signal to the S_2 state and conclude that the S_2 state is unusually stable in CP43-E354Q PSII core complexes. The signal's superfine structure is different from that in wild-type, especially above 3500 G, and the peaks in the mutant spectrum are shifted 10 – 20 G to lower field compared to their positions in the wild-type spectrum. No features were evident between 600 and 2000 G in the mutant spectrum (Figure 3B, insert); the broad features observed in this region in the wild-type spectrum may correspond to cytochrome heme groups.

The integrated area of the seven peaks indicated in the mutant S_2 state multiline EPR spectrum (asterisks in the lower trace of Figure 3B) was approximately 76% of the integrated area

of the corresponding peaks in the wild-type spectrum (asterisks in the upper trace of Figure 3). Accordingly, approximately 76% of the CP43-E354Q PSII core complexes were estimated to contain photooxidizable Mn_4Ca clusters on the basis of the EPR data.

To determine if the mutant reaction centers are able to advance beyond the S_2 state, extensively dark-adapted CP43-E354Q PSII core complexes were illuminated at 0ºC in the presence of 0.5 mM phenyl-1,4-benzoquinone as electron acceptor before being rapidly frozen in liquid nitrogen. The illuminated samples exhibited no "split" EPR signal characteristic of the $S_2Y_Z^{\bullet}$ state in PSII preparations that are unable to advance to the S_3 state (*51-54*) (data not shown). This observation implies that a majority of CP43-E354Q PSII core complexes *are* able to advance beyond the S_2 state to the S_3 state.

X-ray Absorption Data.

The Mn K-edge XANES spectra of CP43-E354Q PSII core complexes poised in the S_1 and S_2 states were compared with the corresponding spectra of wild-type PSII core complexes (Figure 5). In the mutant core complexes, the S_1 state was prepared by dark-adapting samples for 12 hours at 4 °C followed by six hours at room temperature. The Mn XANES spectra of the mutant core complex in both the S_1 and S_2 states, including the pre-edge features (inserts in Figure 5A and 5B) were similar to those of wild-type. In particular, the S_2 state XANES spectrum of the mutant was identical to that of wild-type. The similarity of the wild-type and CP43-E354Q spectra is most clearly shown by the similarity of the second derivative spectra (Figures 5C and 5D for the S_1 and S_2 states, respectively).

The Mn K-edge EXAFS spectra of CP43-E354Q PSII core complexes poised in the S_1 and S_2 states were also compared with the corresponding spectra of wild-type PSII core complexes (Figure 6). The wild-type and mutant Mn EXAFS spectra in the S_2 state were nearly indistinguishable, whereas small differences were apparent in the EXAFS spectra of the S_1 state.

FTIR Data.

The unusual stability of the S_2 state multiline EPR signal in CP43-E354Q PSII core complexes led us to investigate the stability of the S_2 state with FTIR difference spectroscopy. The spectrum induced by a single flash given to dark-adapted PSII core complexes corresponds predominantly to the S_2-*minus*-S_1 FTIR difference spectrum (*55-58*). In CP43-E354Q PSII core complexes, the difference spectrum that was generated by a single saturating flash given after 18 h of dark adaptation at 273 K could only be fully regenerated by a subsequent flash after a lengthy dark recovery period of at least 10 hours at 273 K. However, most of the features in the difference spectrum were evident after 30 min of dark recovery (data not shown). Slowest to recover were features in the $\nu_{sym}(COO^-)$ region, particularly the positive band at 1363 cm^{-1}. Consequently, the unusually stability of the S_2 state observed in the EPR experiments, and its multiphasic decay, were confirmed with FTIR, although the rates of decay were slower in the EPR samples than in the FTIR samples. Accordingly, most of the FTIR data were collected by dark adapting samples for 18 h at 273 K and subjecting each sample to single set of four excitation flashes. The samples were then discarded. To increase the signal-to-noise ratio of the recorded spectra, 800 scans were recorded after each measuring flash instead of the 100 scans that we employed previously (*31, 44, 45*). Consequently, the time spacing between flashes was 96 s instead of the 10 – 12 s that has been used in most previous FTIR studies of S-state turnovers [*e.g.*, (*32, 44, 46*)].

The FTIR difference spectra induced by four successive flashes given to wild-type and CP43-E354Q PSII core complexes at 273 K after 18 h of dark adaptation are compared in Figure 7. As noted in the previous paragraph, the spectra that are induced by the first flash should correspond predominantly to S_2-*minus*-S_1 FTIR difference spectra. When the overall amplitudes of the S_2-*minus*-S_1 FTIR difference spectra were normalized to the extent of flash-induced charge

separation in the samples (accomplished by normalizing the mutant and wild-type spectra to the peak-to-peak amplitudes of the negative ferricyanide peak at 2115 cm^{-1} and the positive ferrocyanide peak at 2038 cm^{-1} produced by the oxidation of $Q_A^{\bullet -}$ by the ferricyanide), the amplitude of the mutant spectrum was found to be approximately 82% of the amplitude of the wild-type spectrum. Accordingly, approximately 82% of the CP43-E354Q PSII core complexes were estimated to contain photooxidizable Mn_4Ca clusters on the basis of the FTIR data.

Because of the long time intervals between flashes (96 s), it was expected that significant fractions of wild-type PSII centers would relax between flashes (from the S_2 state to the S_1 state or from the S_3 state to the S_2 and S_1 states). Consequently, it was expected that the difference spectra induced by the second, third, and fourth flashes applied to wild-type PSII core complexes would represent mixtures of S-state transitions. In support of this expectation, the fourth-flash difference spectrum of wild-type resembles the S_0-*minus*-S_3 FTIR difference spectrum that has been observed in previous studies after the *third* flash [*e.g.*, (*32, 44, 46*)], although its amplitude is smaller. Evidently, the long time interval between flashes dampened the period-four oscillations of the wild-type FTIR difference spectra sufficiently that the S_0-*minus*-S_3 FTIR difference spectrum dominates after the fourth flash. Note especially the features at 1544(+) and 1510(-) cm^{-1} and the features between 1440 and 1350 cm^{-1} in the fourth flash spectrum. These features, typically observed in S_0-*minus*-S_3 FTIR difference spectra (*56-58*), partly reverse spectral features that are present in the S_2-*minus*-S_1 and S_3-*minus*-S_2 FTIR difference spectra. In CP43-E354Q PSII core complexes, because of the unusual stability of the S_2 state, the long time intervals between flashes should cause less damping of the FTIR difference spectra. In this regard, it is noteworthy that the second-flash spectrum of CP43-E354Q PSII core particles generally resembles the second-flash spectrum of wild-type and that the third- and fourth-flash

difference spectra of the mutant show no hint of spectral features reversing sign from those present in the first- and second-flash spectra.

The features in the third- and fourth-flash spectra of the CP43-E354Q PSII core particles differ from those in the first-flash spectrum. In particular, note the presence of the positive feature at 1586 cm^{-1} in the first-flash spectrum and its absence in the third- and fourth-flash spectra, the change in appearance of the spectra between 1460 and 1380 cm^{-1} between the first- and third-flash spectra, and the appearance of features at 1375(-), 1362(+), and 1346(-) cm^{-1} in the third-flash spectra. These spectral changes provide evidence that the majority of CP43-E354Q PSII core complexes advance beyond the S_2 state, in agreement with the EPR data described earlier. Importantly, because the third- and fourth-flash difference spectra show no hint of spectral features reversing sign from those present in the first- and second-flash spectra, these data provide no evidence for S-state advancement beyond the S_3 state in a majority of CP43-E354Q PSII core particles, although advancement beyond S_3 in a minority of reaction centers (*i.e.*, the approximately 20% that evolve O_2 with normal flash yields and kinetics) would likely escape detection.

Because the second-, third-, and fourth-flash difference spectra represented mixtures of S oxidation states, we focused our attention on the features of the first-flash difference spectra. Because the wild-type and mutant samples were not given a preflash, the first-flash spectra may contain contributions from Y_D•-*minus*-Y_D (*33*). One of the largest features in the Y_D•-*minus*-Y_D FTIR difference spectrum is a negative band at 1703 cm^{-1} (*32, 33, 59, 60*). Because the negative feature at 1704 cm^{-1} in the wild-type first-flash spectrum is not significantly larger than the feature that is usually observed near this frequency in wild-type S_2-*minus*-S_1 FTIR difference spectra (*55-58*), the spectral features of Y_D•-*minus*-Y_D probably make only small contributions to the wild-type and CP43-E354Q first-flash spectra that are shown in Figure 7. However, the first-

flash spectrum of the CP43-E354Q PSII core complexes should contain contributions from Y_Z•-*minus*-Y_Z (*31*) because only 76 – 82% of the mutant complexes contain photooxidizable Mn_4Ca clusters on the basis of our EPR and FTIR data (see above). The larger negative bands at 1702-1703 cm^{-1} in the CP43-E354Q FTIR difference spectra compared to wild-type probably reflect the flash-induced formation of $Y_Z^{\bullet}$ in the fraction of CP43-E354Q PSII reaction centers that lack Mn_4Ca clusters. However, the features of the Y_Z•-*minus*-Y_Z FTIR difference spectrum are relatively small except for positive bands at 1699, 1550, and 1512 cm^{-1} (*31, 61*). Therefore, we conclude that first-flash spectra are dominated by the wild-type and mutant S_2-*minus*-S_1 FTIR difference spectra and that differences between the wild-type and mutant spectra can be attributed to the CP43-E354Q mutation and not to contaminating features of Y_Z•-*minus*-Y_Z.

The S_2-*minus*-S_1 FTIR difference spectra of wild-type and CP43-E354Q PSII core complexes show many differences, especially throughout the symmetric carboxylate stretching [$\nu_{sym}(COO^-)$] region and the overlapping amide II and asymmetric carboxylate stretching [$\nu_{asym}(COO^-)$] regions (Figure 7, top set of traces). The largest differences include substantially diminished negative features at 1747, 1543, and 1522 cm^{-1}, a substantially diminished positive feature at 1504 cm^{-1}, the appearance of large positive features at 1667 cm^{-1} and 1528 cm^{-1}, the appearance of a negative feature at 1570 cm^{-1}, and a variety of peak shifts and/or amplitude changes between 1450 cm^{-1} and 1380 cm^{-1} in the mutant spectrum. These mutation-induced changes are substantially larger than those that are induced by mutations of other residues that have been assigned as Mn ligands in the current x-ray crystallographic structural models [*e.g.*, D1-D170H (*44, 62*), D1-E189Q (*45, 63*), D1-D342N (*31*), and D1-A344G (*33, 64-66*)].

While this work was originally being prepared for submission, another study of the same mutant constructed independently in the same organism was published (*28*). The S_2-*minus*-S_1 FTIR difference spectrum of CP43-E354Q reported in this study differs in many respects from

ours. In particular, the mutant spectrum more closely resembles that of wild-type, showing no significant differences near 1747 or 1543 cm^{-1} and fewer differences in the symmetric carboxylate stretching region between 1450 and 1380 cm^{-1} [see Figure 4 of ref. *28*]. In comparing the two studies, we noticed three procedural differences that stood out. First, we had purified our PSII core complexes in the presence of 1.2 M betaine and 10% (v/v) glycerol, whereas they employed no betaine, instead using 25% (v/v) glycerol. Second, our samples had been dark-adapted for 18 hours, whereas theirs were dark adapted for only 20 min. Third, our samples had been subjected to a single set of illuminating flashes, whereas theirs were flash-illuminated repeatedly, with a 20 min period of dark adaptation between illuminations. Accordingly, we set out to acquire more FTIR data with samples that had been purified in the presence of 25% (v/v) glycerol (and no betaine), with samples that had been subjected to shorter periods of dark adaptation, and with samples that had been illuminated repeatedly after a suitable period of dark adaptation.

We first determined that S_2 state was similarly stabilized in CP43-E354Q PSII core complexes whether they had been purified in the presence of 25% (v/v) glycerol or 1.2 M betaine and 10% (v/v) glycerol. This determination was made by comparing the decay of the S_2 state multiline EPR signal in mutant PSII core complexes purified in the two types of buffer (data not shown). We also determined that the S_2-*minus*-S_1 FTIR difference spectrum of mutant PSII core complexes purified in the presence of 25% (v/v) glycerol appeared to exhibit the same FTIR difference spectra as those purified in the presence of 1.2 M betaine and 10% (v/v) glycerol when examined under the conditions of Figure 7 (*i.e.*, an 18 hour dark adaptation time followed by a single set of flashes, data not shown). Accordingly, we examined the effect of shorter dark adaptation times.

The S_2-*minus*-S_1 FTIR difference spectra of wild-type and CP43-E354Q PSII core complexes recorded under a variety of conditions are compared in Figure 8. A comparison of

wild-type and mutant PSII core complexes that had been purified in the presence of 25% (v/v) glycerol, dark adapted for only two hours, then given a single flash is shown in Figure 8B (the same number of scans were accumulated after the flash as in Figure 7; to obtain a stable dark-*minus*-dark baseline after only two hours of dark adaptation required recording these data at 250 K instead of at 273 K). These data closely resemble the data acquired after an 18 h adaptation (top pair of traces in Figure 7, reproduced in Figure 8A to facilitate comparison). The primary differences are that the large positive feature at 1668 cm^{-1} in the mutant is less prominent and the positive feature at 1509 cm^{-1} is diminished to a larger extent. The other mutation-induced changes to the features at 1747 cm^{-1}, 1569 cm^{-1}, 1543 cm^{-1}, 1528 cm^{-1}, 1522 cm^{-1}, and between 1450 cm^{-1} and 1380 cm^{-1} noted earlier were still evident.

Next, we investigated the effect of repeatedly illuminating samples. For this purpose, wild-type and mutant PSII core complexes were compared after a 2 h dark adaptation time followed by 16 single flashes spaced by 30 min. For these experiments, PSII core complexes were purified in the presence of either 25% (v/v) glycerol (Figure 8C) or 1.2 M betaine and 10% (v/v) glycerol (Figure 8D). The data shown in Figures 8C and 8D closely resemble each other, again showing that the features of the spectra are not determined by the sample purification buffer. These data also closely resemble the data shown in Figure 8B: the positive feature at 1667 cm^{-1} is less prevalent and the positive feature at 1507 cm^{-1} is diminished to a greater extent than in samples dark adapted for 18 h (Figure 8A). The primary difference between the data of Figured 8C and 8D and the samples not subjected to repeated illuminations (Figures 8A and 8B) is a loss of positive intensity at 1364 cm^{-1} and the appearance of a derivative feature at 1370(+)/1359(-) cm^{-1} in the mutant difference spectra. As noted earlier, the 1364 cm^{-1} feature required ~ 10 h of dark adaptation for full recovery between flashes. We observed that the 1370(+)/1359(-) cm^{-1} derivative feature became increasingly prominent as the flash illuminations increased (data not

shown). Consequently, only 16 illuminations were accumulated for the data shown in Figures 8C and 8D.

The data of Figure 8 show that, regardless of sample purification buffer, time of dark adaptation, or whether samples were illuminated once or multiple times, we obtained essentially the same spectral features in the S_2-*minus*-S_1 FTIR difference spectra of wild-type and CP43-E354Q PSII core complexes. Consequently, the reasons for the different features of the spectra in ref. *28* remain unknown. To determine if the features between 1650 and 1450 cm^{-1} correspond to amide or $\nu_{asym}(COO^-)$ modes, both wild-type and CP43-E354Q PSII core particles were uniformly labeled with ^{15}N. A comparison of the midfrequency S_2-*minus*-S_1 FTIR difference spectra of unlabeled and ^{15}N-labeled wild-type and CP43-E354Q PSII core complexes is shown in Figure 9. The difference spectrum of ^{15}N-labeled wild-type PSII core complexes (Figure 9A, blue trace) closely resembles spectra reported previously for ^{15}N-labeled PSII preparations from spinach (*67*), *Thermosynechococcus elongatus* (*68*) and *Synechocystis* sp. PCC 6803 (*32, 69*). In particular, the bands at 1552(+), 1543(–), 1531(+), and 1522(–) cm^{-1} have previously been identified as amide II modes because all four bands downshift appreciably after global incorporation of either ^{15}N (*32, 68, 69*) or ^{13}C (*32, 68-70*). The large positive band at 1587 cm^{-1} was previously assigned to a $\nu_{asym}(COO^-)$ mode because it is largely insensitive to the global incorporation of ^{15}N (*32, 68, 69*), but downshifts by 30 – 35 cm^{-1} after global incorporation of ^{13}C (*32, 68-70*). Of particular importance to this study, the large positive band at 1509 cm^{-1} appears to consist of overlapping amide II and $\nu_{asym}(COO^-)$ modes (*32, 68, 69*). Similar ^{15}N-induced shifts are observed in CP43-E354Q PSII core complexes (Figure 9B). In particular, the global incorporation of ^{15}N downshifts the 1667 cm^{-1} feature to 1666 cm^{-1} and downshifts the positive feature at 1551 cm^{-1} to 1537 cm^{-1}. The magnitudes of these shifts (1 cm^{-1} and 14 cm^{-1},

respectively) are consistent with the 1667 and 1551 cm^{-1} features corresponding to amide I and amide II modes, respectively (*32, 68, 69*).

To isolate the vibrational modes altered by the CP43-E354Q mutation and to display them more clearly, wild-type-*minus*-mutant double difference spectra were calculated for the four experimental conditions shown in Figure 8. Included with these double difference spectra (shown in Figure 10) are double difference spectra calculated with ^{15}N-labeled wild-type and mutant PSII core complexes that were examined under two of the experimental conditions (blue traces in Figures 10A and 10C). As shown previously (Figs. 7 and 8), the CP43-E354Q mutation substantially diminishes the negative feature at 1747 cm^{-1}. This feature has recently been assigned to the carbonyl stretching vibration (C=O) of a carboxylic acid residue whose pK_A decreases in response to the S_1 to S_2 transition (*47*). Of particular interest to this study is the large negative band near 1524 cm^{-1} that appears in all of the double difference spectra. Because this band is largely unaltered by the global incorporation of ^{15}N (Figs. 10A and 10C), it must correspond to the $\nu_{asym}(COO^-)$ mode of a carboxylate residue that appears near 1524 cm^{-1} in the S_1 state in wild-type PSII preparations, but that is eliminated by the CP43-E354Q mutation. If the mutation eliminates this mode from the S_1 state, then the mutation must also eliminate it from the S_2 state. Consequently, there should be a corresponding positive peak in the double difference spectrum. It would be tempting to assign the positive feature near 1508 cm^{-1} in the double difference spectra to the $\nu_{asym}(COO^-)$ mode in the S_2 state. Indeed, this assignment was made by the authors of ref. *28*. However, the global incorporation of ^{15}N causes the 1508 cm^{-1} mode to downshift by 13 – 15 cm^{-1} (Figures 10A, C), showing that, although both amide II and $\nu_{asym}(COO^-)$ modes contribute to the 1504 – 1509 feature in the wild-type S_2-*minus*-S_1 FTIR difference spectra, it is the amide II mode that is altered by the CP43-E354Q mutation, causing it to appear in the double difference spectrum. Nevertheless, because the 1506 – 1508 cm^{-1} feature in the double difference spectra is

quite broad, we cannot exclude the possibility that the $\nu_{asym}(COO^-)$ mode of CP43-Glu354 also appears at 1506 – 1508 cm^{-1} in the double difference spectra of the ^{15}N-labeled samples (*e.g.*, see Figure 10C, blue trace at this frequency).

The large number of features present in the double difference spectra (Figure 10) shows that the CP43-E354Q mutation perturbs multiple carboxylate residues. To determine if the mutation perturbs the α-COO^- group of D1-Ala344 at the C-terminus of the D1 polypeptide, the frequency of this mode was determined by specifically labeling wild-type and CP43-E354Q PSII core complexes with L-[1-^{13}C]alanine (*31, 33, 34, 66*). A comparison of the unlabeled and L-[1-^{13}C]alanine-labeled S_2-*minus*-S_1 FTIR difference spectra of wild-type and CP43-E354Q PSII core complexes is shown in Figures 11A and 11B. The positive feature at 1600 cm^{-1} in the L-[1-^{13}C]alanine-labeled CP43-E354Q PSII core particles (Figure 11B) is characteristic of Mn-depleted PSII (*33*) and is consistent with our conclusions that only 76 – 82% of the mutant PSII core complexes contain photooxidizable Mn_4Ca clusters (see above). In Mn-depleted PSII core complexes, the incorporation of [1-^{13}C]alanine produces no changes in the light-*minus*-dark FTIR difference spectrum between 1450 and 1200 cm^{-1} (*33*). Consequently, the [1-^{13}C]alanine-induced changes that are apparent in the $\nu_{sym}(COO^-)$ region of the S_2-*minus*-S_1 FTIR difference spectrum of CP43-E354Q PSII core complexes (Figure 11B) can be attributed to mutant PSII complexes that *contain* Mn_4Ca clusters, and not to PSII complexes that *lack* Mn_4Ca clusters.

To isolate the L-[1-^{13}C]alanine-shifted $\nu_{sym}(COO^-)$ modes and to display them more clearly, the ^{12}C-*minus*-^{13}C double difference spectra of the region between 1380 and 1280 cm^{-1} in the wild-type and mutant samples are presented in Figure 11C. The data show that the positions of the L-[1-^{13}C]alanine-shifted modes are shifted 3 – 6 cm^{-1} to higher frequency in both the S_1 and S_2 states in CP43-E354Q PSII core complexes compared to their positions in wild-type, showing

that the α-COO^- group of D1-Ala344 is perturbed by the CP43-E354Q mutation [4].

Substrate water exchange data

The results of ^{18}O exchange measurements conducted with wild-type and CP43-E354Q thylakoid membranes poised in the S_3 state are shown in Figure 12. The data revealed the biphasic kinetics that have been observed in all other PSII preparations and that are characteristic of the two substrate water binding sites (*49, 71-75*). The wild-type (black circles) and CP43-E354Q (red circles) data are presented in Figure 12 along with the exchange kinetics, fit according to Equation 1 and depicted with solid lines. The extracted rate constants are listed in Table 2. The inset to Figure 12 shows a shorter time scale to better compare the kinetics of the fast phase. The exchange rate constants for the wild-type thylakoids were $k_1 = 0.47 \pm 0.04$ s^{-1} and $k_2 = 19.7 \pm 1.3$ s^{-1} for the slow and fast phases, respectively. The exchange rates for the CP43-E354Q thylakoids were $k_1 = 0.86 \pm 0.35$ s^{-1} and $k_2 = 167 \pm 38$ s^{-1} for the slow and fast phases, respectively. The most striking impact of the CP43-E354Q mutation is its profound acceleration of the fast exchange rate. The CP43-E354Q mutation accelerated the fast phase of substrate water exchange, k_2, by a factor of 8.5 ± 2.0 and accelerated the slow phase, k_1, by a factor of 1.8 ± 0.8. Evidently, both substrate-binding sites are perturbed by the mutation and both interact more weakly with substrate water in the mutant in the S_3 state compared to wild-type. However, the profound acceleration in the fast phase underlies a far more significant perturbation to the substrate water site that is in rapid exchange.

2.5 Discussion

Our observation that CP43-E354Q thylakoid membranes evolve O_2 with normal S-state parameters and release kinetics shows that, in at least a fraction of CP43-E354Q PSII reaction

[4] Specific L-[1-^{13}C]alanine-labeling of PSII shifts the $\nu_{sym}(COO^-)$ mode of the α-COO^- group of D1-Ala344 by either ~ 19 or ~ 36 cm^{-1} (*31, 33, 34, 66*). It is not yet possible to distinguish between these two possibilities.

centers, the S-state transitions proceed normally. This fraction was estimated to be about 20% on the basis of the steady state rate of O_2 evolution in CP43-E354Q cells and the amplitudes of the O_2 flash yields in CP43-E354Q thylakoid membranes. In contrast, between 76% and 82% of the purified CP43-E354Q PSII core complexes contain photooxidizable Mn_4Ca clusters, as estimated on the basis of the amplitude of the mutant S_2 state multiline EPR signal and the amplitude of the mutant S_2-*minus*-S_1 FTIR difference spectrum. Although both the EPR and FTIR data provide evidence that a majority of CP43-E354Q PSII reaction centers advance beyond the S_2 state, the FTIR data provide no evidence that a substantial fraction advances beyond the S_3 state. We conclude that the CP43-E354Q PSII reaction centers are heterogeneous, with a minority able to evolve O_2 with normal S-state parameters and O_2 release kinetics and a majority capable of achieving the S_3 state, but unable to advance beyond the S_3 state. Evidence for heterogeneity was also provided by the decay kinetics of the S_2 state. In the EPR samples, the S_2 state multiline EPR signal decayed with approximate half-times of ~ 2.5 h and > 20 h, respectively. In the FTIR samples, the decay times were much faster, with the S_2 state decaying within 30 min in most PSII reaction centers, but requiring up to 10 hours in others. We presume that the difference in decay kinetics in the EPR and FTIR samples reflects differences in the illumination protocols employed for generating the S_2 state and/or differences in the buffers employed for the two sets of measurements. It should be noted that a recent study of an independently constructed CP43-E354Q mutation in *Synechocystis* sp. PCC 6803 reported no apparent heterogeneity (*28*). However, the characterizations reported in that study did not include measurements of O_2 flash yields and is unclear if the delayed luminescence data would have been sensitive to a small (~ 20%) fraction of Mn_4Ca clusters that evolve O_2 with normal S-state parameters.

What could be the reason for the heterogeneity our CP43-E354Q PSII reaction centers? Proton-coupled electron transfer processes are believed to provide the driving force for oxidizing

the Mn_4Ca cluster in its higher oxidation states (*7-10*). Recent models postulate that CP43-Arg357 (or D1-Asp61) serves as a redox-activated catalytic base that facilitates the oxidation of the Mn_4Ca cluster during the S_2 to S_3 and S_3 to S_4 transitions (*7, 13, 21, 22, 76-79*). In these models, the formation of $Y_Z^{\bullet}$ when the Mn_4Ca cluster is in its S_2 or S_3 states triggers the deprotonation of CP43-Arg357 (or D1-Asp61) to the thylakoid lumen. Deprotonation to the lumen is necessary from energetic considerations (*80*) and takes place via a network of protonatable amino acid side chains and water molecules such as those envisaged to exist in the potential proton egress channels that have been identified in the x-ray crystallographic structural models (*1, 5, 81-84*). Kinetically efficient proton transfer through these channels requires finely tuned pK_a differences between key residues and transient formation of clusters of water molecules (*80, 85-87*). An alteration of these pK_a values may slow oxidation of the Mn_4Ca cluster in the same manner that mutations that impair proton uptake also slow the transfer of an electron from $Q_A^{\bullet -}$ to $Q_B^{\bullet -}$ in reaction centers of *Rhodobacter sphaeroides* (*88-90*) and the reduction of O_2 to H_2O in cytochrome *c* oxidase (*91-93*). The heterogeneity of CP43-E354Q may arise from a mutation-induced alteration of the pK_a value(s) of one or more key residues that alters the static or dynamic properties of a network of hydrogen bonds that comprises part of a dominant proton egress channel.

A mutation-induced alteration of a network of hydrogen bonds in the vicinity of the Mn_4Ca cluster is evident from the S_2-*minus*-S_1 FTIR difference spectrum of CP43-E354Q PSII core complexes. The data, obtained under a variety of conditions (Figure 10), show that the mutation substantially diminishes or eliminates the negative feature at 1747 cm^{-1} that was recently assigned to a carboxylate group whose pK_a decreases during the S_1 to S_2 transition (*47*). This carboxylate group participates in a network of hydrogen bonds that extends at least 20 Å across the lumenal face of the Mn_4Ca cluster and includes D1-Asp61, D1-Glu65, D1-Glu329, and D2-

Glu312, and presumably also includes the Cl ion that is coordinated by D2-Lys317 (*47*). The near or complete elimination of the negative feature at 1747 cm^{-1} suggests that CP43-Glu354 participates in the same network and shows that the CP43-E354Q mutation disrupts the network sufficiently that, in at least a majority of PSII reaction centers, the structural perturbations associated with the S_1 to S_2 transition are no longer transmitted to the carboxylate group that gives rise to the 1747 cm^{-1} band.

An unusually stable S_2 state is also characteristic of PSII preparations that have been depleted of Ca in the presence of the flexible poly-carboxylic acids EDTA, EGTA, or citrate (*94-97*). The inability of these Ca-depleted PSII preparations to advance beyond the $S_2Y_Z^{\bullet}$ state, and the unusual stability of the S_2 state in these preparations, has been attributed to the participation of the Ca ion in the network of hydrogen bonds that facilitates the oxidation of the Mn_4Ca cluster in its higher oxidation states (*98, 99*). Consequently, the unusually stability of the S_2 state in CP43-E354Q PSII core complexes may also reflect a mutation-induced alteration to the pK_a values of residues involved in the deprotonation reactions that facilitate oxidation of the Mn_4Ca cluster in its higher oxidation states.

The small differences between the wild-type and mutant Mn-XANES and Mn-EXAFS spectra show that the geometric structure and electronic characteristics of the Mn_4Ca cluster are only subtly perturbed by the CP43-E354Q mutation. The light-driven assembly of the Mn_4Ca cluster involves the binding and photooxidation of a single Mn(II) ion to Mn(III), followed by protein structural rearrangements that create or increase the affinity of the binding sites for the additional Mn(II) ions and the Ca ion (*100, 101*). After these ions bind, the Mn ions are photooxidized to their Mn(III/IV) oxidation states characteristic of the physiological S-states. Evidently, the elimination of a negatively charged glutamate residue at position 354 of the CP43 polypeptide has little effect on the cluster's ability to assemble and to achieve its native

conformation, at least in the S_1 and S_2 states. In contrast, the D1-H332E mutation of *Synechocystis* sp. PCC 6803 substantially alters both the geometric structure and electronic characteristics of the Mn_4Ca cluster, shifting the Mn K-edge energy to a lower energy and elongating the Mn-Mn and Mn-ligand interactions to a far greater extent than are caused by any biochemical treatment (*e.g*, removal of Ca, exchange of Sr for Ca, or inhibition with NH_3) (*102*). In the case of the D1-H332E mutation, these substantial alterations were interpreted in terms of a negatively charged carboxylate oxygen replacing the τ histidyl nitrogen of D1-His332 as a ligand to a Mn(III) or Mn(IV) ion (*102*). In the case of the CP43-E354Q mutation, because of the insensitivity of the Mn-XANES and Mn-EXAFS to the mutation, it remains an open question whether the carboxylate oxygen(s) of Glu354 is(are) replaced by the carbonyl oxygen and/or amine nitrogen of Gln or by one (or two) small molecule(s) (*e.g*., water), or if the Mn ion(s) become(s) coordination deficient in the mutant.

The similarity of the S_2 state multiline EPR signals of wild-type and CP43-E354Q PSII core complexes also shows that the mutation has little effect on the structure or electronic properties of the Mn_4Ca cluster in the S_2 state. The small differences between the appearance of the wild-type and mutant spectra show that the magnetic interactions that give rise to the S_2 state multiline EPR signal (*103-105*) are only subtly altered by the CP43-E354Q mutation. In contrast, both the *Synechocystis* D1-H332E mutation (*30, 106*) and the substitution of Sr for Ca (*e.g*., refs. *34* and *107*) substantially perturb these interactions and substantially alter the appearance of the S_2 state multiline EPR signal. The spectral features of the mutant S_1 state multiline EPR signal below 375 G and above 650 G could not be obtained reproducibly. Consequently, it cannot be concluded that the signal is the same as in wild-type. Nevertheless, the similarity of the wild-type and mutant spectra between 375 and 650 G in terms of both peak positions and spacings suggests

that the magnetic interactions that give rise to this signal are also only subtly altered by the CP43-E354Q mutation.

Our FTIR data show that the CP43-E354Q mutation introduces far more perturbations into the environment of the Mn_4Ca cluster that than are introduced by mutations that have been constructed at other putative cluster ligands such as D1-Asp170 (*44, 62*), D1-Glu189 (*45, 63*), D1-Asp342 (*31*), and the α-COO^- group of D1-Ala344 (*33, 64-66*). In particular, the S_2-*minus*-S_1 FTIR difference spectrum of CP43-E354Q PSII core complexes showed alterations throughout the amide II, $\nu_{asym}(COO^-)$ and $\nu_{sym}(COO^-)$ regions. This was true whether the PSII core complexes were purified in the presence of 1.2 M betaine or 25% (v/v) glycerol, whether the samples were dark adapted for 18 h or 2 h, or whether the samples were illuminated only once or repeatedly with 30 min of dark adaptation between flashes. Global labeling with ^{15}N showed that the CP43-E354Q mutation perturbs both amide II and carboxylate stretching modes. Specific labeling with L-[1-^{13}C]alanine showed that the CP43-E354Q mutation shifts the $\nu_{sym}(COO^-)$ mode of the α-COO^- group of D1-Ala344 to higher frequencies by 3 – 6 cm^{-1} in both the S_1 and S_2 states. These data are an indication that the CP43-E354Q mutation perturbs multiple carboxylate groups in the vicinity of the Mn_4Ca cluster. Because the $\nu_{sym}(COO^-)$ mode of the α-COO^- group of D1-Ala344 downshifts in frequency during the S_1 to S_2 transition to approximately the same extent in both wild-type and CP43-E354Q PSII core complexes, these data also show that the same Mn ion undergoes oxidation during the S_1 to S_2 transition in the mutant as in wild-type [5].

[5] The spectrum reported in a preliminary version of this study (*27*) as corresponding to the S_2-*minus*-S_1 FTIR difference spectrum in CP43-E354Q PSII core complexes actually corresponds most closely to the S_3-*minus*-S_2 FTIR difference spectrum. The error arose because of the unusual stability of the S_2 state in the mutant and because the samples examined in ref. *27* were given a pre-flash 5 min before measurement. Consequently, two conclusionS-stated in ref. *27*, namely that a different Mn ion undergoes oxidation during

As noted earlier, the S_2-*minus*-S_1 FTIR difference spectrum of CP43-E354Q PSII core complexes that was published recently by Shimada et al. (*28*) has fewer differences with wild-type than our mutant spectrum. Because our wild-type and mutant S_2-*minus*-S_1 FTIR difference spectra were essentially the same regardless of sample purification buffer, time of dark adaptation, or whether the samples were illuminated once or multiple times, the reasons for the differences between the spectra presented in ref. (*28*) and the current study remain unknown. In ref. *28*, the four largest features in the wild-type-*minus*-mutant double difference spectrum were assigned to the $\nu_{asym}(COO^-)$ and $\nu_{sym}(COO^-)$ modes of CP43-E354Q on the basis of their insensitivity to D_2O/H_2O exchange (*28*). In that study, the negative features at 1525 cm^{-1} and 1394 cm^{-1} were assigned to the $\nu_{asym}(COO^-)$ and $\nu_{sym}(COO^-)$ modes of CP43-E354Q in the S_1 state, respectively, and the positive features at 1502 cm^{-1} and 1431 cm^{-1} were assigned to the $\nu_{asym}(COO^-)$ and $\nu_{sym}(COO^-)$ modes of CP43-E354Q in the S_2 state, respectively (*28*). On the basis of these assignments, CP43-Glu354 was proposed to bridge two Mn ions in the S_1 state and shift to chelating bidentate coordination of a single Mn ion in the S_2 state (*28*).

However, we consistently observed more features in the $\nu_{sym}(COO^-)$ region of our double difference spectra than the authors of ref. *28*. In particular, our double difference spectra contain an extra pair of bands at 1406(+) and 1416(–) cm^{-1} that are as intense as those at 1429(+) and 1395(–) cm^{-1}. Consequently, we were unable to uniquely assign a particular $\nu_{sym}(COO^-)$ mode to CP43-Glu354 in either the S_1 or S_2 states. In addition, we could not identify the $\nu_{asym}(COO^-)$ mode of CP43-Glu354 in the S_2 state. Although the authors of ref. *28* assigned a positive feature at 1502 cm^{-1} to this mode, we observed that the corresponding feature in our double difference spectra (appearing at 1506 – 1508 cm^{-1}) downshifted by 14 – 15 cm^{-1} after global labeling with

---

the S_1 to S_2 transition in the mutant and that different functional groups necessarily give rise to the 1400(–) cm^{-1} and 1588(+) cm^{-1} bands in the wild-type S_2-*minus*-S_1 FTIR difference spectrum, are invalid.

^{15}N, consistent with the assignment of this feature to an amide II mode but incompatible with the assignment of this feature to a carboxylate mode. Because the 1506 – 1508 cm^{-1} feature is quite broad, we cannot exclude the possibility that the $\nu_{asym}(COO^-)$ mode of CP43-Glu354 appears at this frequency and underlies the amide II mode in the double difference spectrum of the ^{15}N-labeled samples. However, a more straightforward interpretation of our ^{15}N data is that the positive feature at 1506 – 1508 cm^{-1} in our double difference spectrum corresponds solely to an amide II mode. This would imply that the $\nu_{asym}(COO^-)$ mode of CP43-Glu354 in the S_2 state appears elsewhere in the spectrum and is obscured by the amide II or $\nu_{asym}(COO^-)$ mode of another residue that is perturbed by the mutation.

Our data show that the CP43-E354Q mutation eliminates a $\nu_{asym}(COO^-)$ mode at 1524 cm^{-1} from the wild-type S_2-*minus*-S_1 FTIR difference spectrum. We assign this mode to the $\nu_{asym}(COO^-)$ mode of CP43-Glu354 in the S_1 state, in agreement with the authors of ref. *28*. The presence of this mode in the S_2-*minus*-S_1 FTIR difference spectrum of wild-type shows that the carboxylate group of CP43-Glu354 is perturbed by the electrostatic influences that arise from the positive charge that develops on the Mn_4Ca cluster during the S_1 to S_2 transition. The elimination of this mode by the CP43-E354Q mutation is consistent with ligation of the Mn_4Ca cluster by CP43-Glu354. This conclusion is in agreement with the authors of ref. *28* and supports a recent prediction made on the basis of QM/MM calculations that CP43-Glu354 ligates along the Jahn-Teller axis of a Mn(III) ion and that its $\nu_{asym}(COO^-)$ mode shifts during the S_1 to S_2 transition (*22, 78*).

The frequencies of the $\nu_{asym}(COO^-)$ and $\nu_{sym}(COO^-)$ modes in metal–carboxylate complexes, and the difference in frequency between them, $\Delta\nu$, vary significantly with the metal ion and the type of carboxylate coordination (*108-112*). The $\nu_{sym}(COO^-)$ and $\nu_{asym}(COO^-)$ modes of free ionic Glu and Asp residues generally appear near 1402 – 1404 cm^{-1} and between 1556 and

1579 cm^{-1}, respectively, corresponding to $\Delta\nu$ = 152 – 177 cm^{-1} (*113-116*). Indeed, having $\Delta\nu \approx$ 160 cm^{-1} is typical of free ionic carboxylates. Unidentate ligation of a metal ion generally shifts the $\nu_{sym}(COO^-)$ and $\nu_{asym}(COO^-)$ modes to lower and higher frequencies, respectively, increasing $\Delta\nu$ to more than 200 cm^{-1} (*108-112*). Bidentate chelating coordination (characterized by both carboxylate oxygens ligating a single metal ion) generally shifts the $\nu_{sym}(COO^-)$ and $\nu_{asym}(COO^-)$ modes to *higher* and *lower* frequencies, respectively, resulting in $\Delta\nu$ < 100 cm^{-1} (*108-112*). Bidentate bridging ligation (characterized by the carboxylate group bridging two metal ions) can shift the $\nu_{sym}(COO^-)$ and $\nu_{asym}(COO^-)$ modes in either direction and typically results in $\Delta\nu$ being similar to the values found in free ionic carboxylates (*108-112*). Because the $\nu_{asym}(COO^-)$ mode of CP43-Glu354 appears at ~ 1524 cm^{-1} in the S_1 state, a frequency much lower than that of free ionic Asp and Glu residues, our data are inconsistent with unidentate coordination of CP43-Glu354 to a single metal ion, at least in the S_1 state. If the $\nu_{sym}(COO^-)$ of CP43-Glu354 in the S_1 state corresponds to one of the negative bands observed at 1416, 1395, or 1351 cm^{-1} in our wild-type-*minus*-mutant double difference spectra, then our data would be most consistent with CP43-Glu354 bridging two metal ions, such as depicted in the 3.0 and 2.9 Å crystallographic structural models (and in the recently announced 1.9 Å structural model – see footnote 2). Consequently, our data support the conclusion of ref. *28* that CP43-Glu354 serves a as a bridging ligand between two Mn ions. However, because we cannot attribute the positive feature at 1506 – 1508 cm^{-1} in our double difference spectra to the $\nu_{asym}(COO^-)$ mode of CP43-Glu354 in the S_2 state and cannot uniquely assign specific $\nu_{sym}(COO^-)$ modes to CP43-Glu354, we cannot confirm another conclusion of ref. *28*, that CP43-Glu354 residue changes its coordination mode during the S_1 to S_2 transition. We would note that ^{15}N labeling is more reliable than D_2O/H_2O exchange for differentiating amide II from $\nu_{asym}(COO^-)$ modes because ^{15}N labeling does not rely on D_2O replacing H_2O in all regions of an assembled protein complex.

One of the most striking results of the FTIR studies on PSII to date is the stunning insensitivity of the individual FTIR difference spectra to the mutation of at least three of the Mn_4Ca cluster's six putative carboxylate ligands. Not only do mutations of D1-Asp170 (*44, 62*), D1-Glu189 (*45, 63*), and D1-Asp342 (*31*) fail to eliminate any carboxylate vibrational stretching modes, they fail to produce significant changes in polypeptide backbone conformations as shown by the lack of significant mutation-induced alterations to the amide I and amide II regions of the spectra. Whereas some of the features in the S_{n+1}-*minus*-S_n FTIR difference spectra of PSII clearly correspond to first coordination sphere ligands (*i.e.*, CP43-Glu354 and the α-COO^- group of D1-Ala344), the majority of these features evidently correspond to residues in the cluster's second coordination sphere and beyond and reflect the response of the protein to the positive charge that develops on the Mn_4Ca cluster during the S_1 to S_2 transition [*e.g.*, see ref. *47*] and to the structural changes that are associated with the S_2 to S_3, S_3 to S_0, and S_0 to S_1 transitions.

The exchange rates of the rapidly exchanging and slowly exchanging substrate water molecules in the S_3 state were increased 8.5-fold and 1.8-fold in CP43-E354Q thylakoid membranes, respectively. These results show that the CP43-E354Q mutation weakens the binding of both substrate water molecules to their respective binding sites in the S_3 state, especially that of the more rapidly exchanging substrate water molecule. The 8.5-fold acceleration is the largest perturbation to the rapid exchange rate yet observed in any system. In earlier work, we considered whether the substrate water molecule in fast exchange was kinetically limited by (i) substrate diffusion into/out of the catalytic site, or (ii) metal ligand exchange (*49, 50, 75, 117*). Either possibility would be kinetically tenable, with the former possibility implying rapid ligand exchange followed by kinetically limiting substrate accessibility. Conversely, the substrate water molecule in slow exchange was argued to be kinetically limited by metal ligand exchange. Recent molecular dynamics simulations of water diffusion in PSII provide evidence that substrate entry

takes place many orders of magnitude faster than the measured rates of substrate water exchange (*118*). Consequently, the measured exchange rates for both substrate water molecules must reflect metal-ligand oxygen exchange rates. The rates of metal ligand exchange depend on many factors including the charge and ionic radius of the metal ion, the electronic occupancy of the *d* orbitals, the degree of protonation of the bound water molecule, and the degree of protonation of neighboring ligands (*75, 117*). Despite our limited knowledge of these factors with respect to the Mn_4Ca cluster in PSII, the fact that the CP43-E354Q mutation substantially perturbs the exchange rate of the rapidly exchanging substrate water molecule provides strong evidence that CP43-Glu354 interacts with a substrate water-derived ligand in the S_3 state. Whether this interaction is direct or indirect remains unclear. If the interaction is direct (*i.e.*, if CP43-Glu354 coordinates to the Mn ion that binds the substrate water that is in fast exchange), then the Mn-oxygen bond must be weakened by the change in Mn ligation produced by the CP43-E354Q mutation. If the interaction is indirect, (*i.e.*, if CP43-Glu354 interacts with a substrate water molecule on a different metal ion via one or more hydrogen bonds), then the metal-oxygen bond must be weakened because of changes to the hydrogen bonds that connect the water molecule to CP43-Glu354. Both possibilities are potentially feasible and both imply a close association of the substrate water-derived oxygen ligand with CP43-Glu354. On the basis of earlier estimates of substrate water-metal bond strengths derived from an analysis of Arrhenius parameters with transition state theory (*50*), the 8.5-fold increase in exchange rate corresponds to an approximately 5.3 kJ/mol decrease in the barrier to ligand exchange, corresponding to a 14% decrease in the total predicted bond enthalpy. A change in predicted bond enthalpy of this magnitude can readily be accommodated by a change in the first coordination sphere of a metal ion; for example, replacing Glu with Gln could produce either *cis* or *trans* ligand effects on a substrate water molecule or water-derived ligand such as a μ-oxo bridge (*75, 119*). It might also

be accommodated by a change in the second coordination sphere (*i.e.*, to the hydrogen bonds that interact with the substrate water molecule), but we are unaware of any documented examples of this in the inorganic literature.

The identification of water molecules coordinated to Mn or Ca in high resolution x-ray crystallographic structural models of PSII (*e.g.*, see footnote 2) would be highly significant because two of these water molecules may ultimately provide the substrate oxygen atoms for the O-O bond. Mass spectrometry studies of $H_2{}^{18}O$-exchange have shown that both substrate water molecules are already bound in the S_2 state and that these are bound in different chemical forms or environments (*e.g.*, to different metal ions) (*50, 120*). However, the precise chemical nature of this water molecule (*i.e.*, whether it corresponds to a terminal water molecule, to a water-derived metal ligand such as a terminal hydroxo or oxo species, or to a μ-oxo bridge between two metal ions) remains to be established, although a terminal species has been advocated on the basis of rate constants and activation energies (*50, 75*). The final unresolved question central to the chemistry of water oxidation is whether both substrate oxygen atoms correspond to the terminal water molecules detected in FTIR studies (*121-123*), or if at least one corresponds to a μ-oxo bridge between two Mn ions, as proposed on the basis of pulsed EPR studies employing ^{17}O and ^{2}H (*124, 125*).

Our discovery, that the CP43-E354Q mutation perturbs the substrate water molecule (or water-derived ligand) that is in fast exchange complements the data presented in the recent FTIR study of Shimada et al. (*28*). The authors of this study examined the weakly H-bonded O-H stretching region of the S_2-*minus*-S_1 FTIR difference spectrum of wild-type and CP43-E354Q PSII particles and concluded that a water molecule binds to same Mn ion that is ligated by CP43-Glu354, although an indirect interaction via hydrogen bonds was not excluded. Our mass spectrometry data are consistent with these results and additionally show that the water molecule

detected in ref. *28* and in earlier FTIR studies (*120, 121*) corresponds to a substrate water molecule. One interesting aspect of our ^{18}O exchange measurements is that the substantially accelerated rates of substrate water exchange in the S_3 state have no apparent effect on the S-state parameters or O_2 release kinetics that were measured polarographically. This lack of correlation implies that the binding affinities of the substrate water molecules in the S_3 state do not factor in the rate limiting step of O-O bond formation.

Summary and Conclusion

Mutant CP43-E354Q PSII reaction centers are heterogeneous, with a minority able to evolve O_2 with normal S-state parameters and O_2 release kinetics and a majority capable of achieving the S_3 state, but unable to advance beyond the S_3 state. Although both EPR and x-ray absorption data show that the CP43-E354Q mutation only subtly perturbs the structure and electronic properties of the Mn_4Ca cluster in the S_1 and S_2 states, FTIR and $H_2{}^{18}O$ exchange data show that CP43-Glu354 interacts with the Mn_4Ca cluster sufficiently that the CP43-E354Q mutation perturbs numerous amide and carboxylate stretching modes and weakens the binding of both substrate water molecules, especially the one that exchanges rapidly. Our FTIR data provide evidence that CP43-Glu354 coordinates to the Mn_4Ca cluster in the S_1 state as a bridging ligand between two metal ions, but provide no compelling evidence that this residue changes its coordination mode during the S_1 to S_2 transition. Our $H_2{}^{18}O$ exchange data additionally provide evidence that CP43-Glu354 interacts with the Mn ion that ligates the substrate water molecule (or water-derived ligand) that undergoes rapid exchange in the S_3 state.

2.8 References

1. Ferreira, K. N., Iverson, T. M., Maghlaoui, K., Barber, J., and Iwata, S. (2004) Architecture of the Photosynthetic Oxygen-Evolving Center, *Science 303*, 1831-1838.

2. Loll, B., Kern, J., Saenger, W., Zouni, A., and Biesiadka, J. (2005) Towards Complete Cofactor Arrangement in the 3.0 Å Resolution Structure of Photosystem II, *Nature 438*, 1040-1044.

3. Kern, J., Biesiadka, J., Loll, B., Saenger, W., and Zouni, A. (2007) Structure of the Mn_4-Ca Cluster as Derived from X-ray Diffraction, *Photosyn. Res. 92*, 389-405.

4. Barber, J. (2008) Crystal Structure of the Oxygen-Evolving Complex of Photosystem II, *Inorg. Chem. 47*, 1700-1710.

5. Guskov, A., Kern, J., Gabdulkhakov, A., Broser, M., Zouni, A., and Saenger, W. (2009) Cyanobacterial Photosystem II at 2.9-Å Resolution and the Role of Quinones, Lipids, Channels, and Chloride, *Nature Struct. & Mol. Biol. 16*, 334-342.

6. Guskov, A., Gabdulkhakov, A., Broser, M., Glöckner, C., Hellmich, J., Kern, J., Frank, J., Müh, F., Saenger, W., and Zouni, A. (2010) Recent Progress in the Crystallographic Studies of Photosystem II, *ChemPhysChem 11*, 1160-1171.

7. McEvoy, J. P. and Brudvig, G. W. (2006) Water-Splitting Chemistry of Photosystem II, *Chem. Rev. 106*, 4455-4483.

8. McCarrick, R. M. and Britt, R. D. (2008) Current Models and Mechanism of Water Splitting, in *Photosynthetic Protein Complexes* (Fromme, P., Ed.) pp 107-136, Wiley-VCH Verlag GmbH & Co. KGaA, Weinheim, Germany.

9. Rappaport, F. and Diner, B. A. (2008) Primary Photochemistry and Energetics Leading to the Oxidation of the $(Mn)_4Ca$ Cluster and to the Evolution of Molecular Oxygen in Photosystem II, *Coord. Chem. Rev. 252*, 259-272.

10. Renger, G. and Renger, T. (2008) Photosystem II: The Machinery of Photosynthetic Water Splitting, *Photosynth. Res. 98*, 53-80.

11. Yano, J. and Yachandra, V. K. (2008) Where Water is Oxidized to Dioxygen: Structure of the Photosynthetic Mn_4Ca Cluster from X-ray Spectroscopy, *Inorg. Chem. 47*, 1711-1726.

12. Yano, J. and Yachandra, V. K. (2007) Oxidation State Changes of the Mn_4Ca Cluster in Photosystem II, *Photosynth. Res. 92*, 289-303.

13. Dau, H. and Haumann, M. (2008) The Manganese Complex of Photosystem II in its Reaction Cycle - Basic Framework and Possible Realization at the Atomic Level, *Coord. Chem. Rev. 252*, 273-295.

14. Sauer, K., Yano, J., and Yachandra, V. K. (2008) X-ray Spectrsocopy of the Photosynthetic Oxygen-Evolving Complex, *Coord. Chem. Rev. 252*, 318-335.

15. Murray, J. W., Maghlaoui, K., Kargul, J., Ishida, N., Lai, T.-L., Rutherford, A. W., Sugiura, M., Boussac, A., and Barber, J. (2008) X-ray Crystallography Identifies two Chloride Binding Sites in the Oxygen Evolving Centre of Photosystem II, *Energy Environ. Sci. 1*, 161-166.

16. Kawakami, K., Umena, Y., Kamiya, N., and Shen, J.-R. (2009) Location of Chloride and its Possible Functions in Oxygen-Evolving Photosystem II Revealed by X-ray Crystallography, *Proc. Natl. Acad. Sci. USA 106*, 8567-8572.

17. Yano, J., Kern, J., Irrgang, K.-D., Latimer, M. J., Bergmann, U., Glatzel, P., Pushkar, Y., Biesiadka, J., Loll, B., Sauer, K., Messinger, J., Zouni, A., and Yachandra, V. K. (2005) X-ray Damage to the Mn_4Ca Complex in Single Crystals of Photosystem II: A Case Study for Metalloprotein Crystallography, *Proc. Natl. Acad. Sci. USA 102*, 12047-12052.

18. Grabolle, M., Haumann, M., Müller, C., Liebisch, P., and Dau, H. (2006) Rapid Loss of Structural Motifs in the Manganese Complex of Oxygenic Photosynthesis by X-ray Irradiation at 10-300 K, *J. Biol. Chem. 281*, 4580-4588.

19. Yano, J., Kern, J., Sauer, K., Latimer, M. J., Pushkar, Y., Biesiadka, J., Loll, B., Saenger, W., Messinger, J., Zouni, A., and Yachandra, V. K. (2006) Where Water is Oxidized to Dioxygen: Structure of the Photosynthetic Mn_4Ca Cluster, *Science 314*, 821-825.

20. Debus, R. J. (2008) Protein Ligation of the Photosynthetic Oxygen-Evolving Center, *Coord. Chem. Rev. 252*, 244-258.

21. Dau, H. and Haumann, M. (2007) Time Resolved X-ray Spectroscopy Leads to an Extension of the Classical S-State Cycle Model of Photosynthetic Oxygen Evolution, *Photosynth. Res. 92*, 327-343.

22. Sproviero, E. M., Gascón, J. A., McEvoy, J. P., Brudvig, G. W., and Batista, V. S. (2008) Computation Studies of the O_2-Evolving Complex of Photosystem II and Biomimetic Oxomanganese Complexes, *Coord. Chem. Rev. 252*, 395-415.

23. Wydrzynski, T., Hillier, W., and Messinger, J. (1996) On the Functional Significance of Substrate Accessibility in the Photosynthetic Water Oxidation Mechanism, *Physiol. Plant. 96*, 342-350.

24. Anderson, J. M. (2001) Does Functional Photosystem II Complex have an Oxygen Channel?, *FEBS Lett. 488*, 1-4.

25. Bricker, T. M. and Frankel, L. K. (2002) The structure and function of CP47 and CP43 in Photosystem II, *Photosynth. Res. 72*, 131-146.

26. Rosenberg, C., Christian, J., Bricker, T. M., and Putnam-Evans, C. (1999) Site-directed mutagenesis of glutamate residues in the large extrinsic loop of the photosystem II protein CP 43 affects oxygen-evolving activity and PSII assembly, *Biochemistry 38*, 15994-16000.

27. Strickler, M. A., Hwang, H. J., Burnap, R. L., Yano, J., Walker, L. M., Service, R. J., Britt, R. D., Hillier, W., and Debus, R. J. (2008) Glutamate-354 of the CP43 Polypeptide Interacts with the Oxygen-Evolving Mn_4Ca Cluster of Photosystem II: A Preliminary Characterization of the Glu354Gln Mutant, *Phil. Trans. R. Soc. London, Ser. B 363*, 1179-1188.

28. Shimada, Y., Suzuki, H., Tsuchiya, T., Tomo, T., Noguchi, T., and Mimuro, M. (2009) Effect of a Single-Amino Acid Substitution of the 43 kDa Chlorophyll Protein on the Oxygen-Evolving Reaction of the Cyanobacterium *Synechocystis* sp. PCC 6803: Analysis of the Glu354Gln Mutation., *Biochemistry 48*, 6095-6103.

29. Goldfarb, N., Knoepfle, N., and Putnam-Evans, C. (1997) Contruction of a *psbC* Deletion Strain in *Synechocystis* 6803, *SAAS Bull. Biochem. Biotechnol. 10*, 1-6.

30. Debus, R. J., Campbell, K. A., Gregor, W., Li, Z.-L., Burnap, R. L., and Britt, R. D. (2001) Does Histidine 332 of the D1 Polypeptide Ligate the Manganese Cluster in Photosystem II? An Electron Spin Echo Envelope Modulation Study, *Biochemistry 40*, 3690-3699.

31. Strickler, M. A., Walker, L. M., Hillier, W., Britt, R. D., and Debus, R. J. (2007) No Evidence from FTIR Difference Spectroscopy That Aspartate-342 of the D1 Polypeptide Ligates a Mn Ion That Undergoes Oxidation during the S_0 to S_1, S_1 to S_2, or S_2 to S_3 Transitions in Photosystem II, *Biochemistry 46*, 3151-3160.

32. Yamanari, T., Kimura, Y., Mizusawa, N., Ishii, A., and Ono, T.-A. (2004) Mid- to Low-Frequency Fourier Transform Infrared Spectra of S-State Cycle for Photosynthetic Water Oxidation in *Synechocystis* sp. PCC 6803, *Biochemistry 43*, 7479-7490.

33. Chu, H.-A., Hillier, W., and Debus, R. J. (2004) Evidence that the C-Terminus of the D1 Polypeptide is Ligated to the Manganese Ion that Undergoes Oxidation During the S_1 to S_2 Transition: An Isotope-Edited FTIR Study, *Biochemistry 43*, 3152-3166.

34. Strickler, M. A., Walker, L. M., Hillier, W., and Debus, R. J. (2005) Evidence from Biosynthetically Incorporated Strontium and FTIR Difference Spectroscopy that the C-Terminus of the D1 Polypeptide of Photosystem II Does Not Ligate Calcium, *Biochemistry 44*, 8571-8577.

35. Chu, H.-A., Nguyen, A. P., and Debus, R. J. (1994) Site-Directed Photosystem II Mutants with Perturbed Oxygen Evolving Properties: 1. Instability or Inefficient Assembly of the Manganese Cluster *In Vivo*, *Biochemistry 33*, 6137-6149.

36. Tang, X.-S. and Diner, B. A. (1994) Biochemical and Spectroscopic Characterization of a New Oxygen-Evolving Photosystem II Core Complex from the Cyanobacterium *Synechocystis* sp. PCC 6803, *Biochemistry 33*, 4594-4603.

37. Burnap, R. L., Qian, M., and Pierce, C. (1996) The Manganese-Stabilizing Protein of Photosystem II Modifies the *in vivo* Deactivation Kinetics of the H_2O Oxidation Complex in *Synechocystis* sp. PCC 6803, *Biochemistry 35*, 874-882.

38. Qian, M., Dao, L., Debus, R. J., and Burnap, R. L. (1999) Impact of Mutations within the Putative Ca^{2+}-Binding Lumenal Interhelical a-b Loop of the Photosystem II D1 Protein on the Kinetics of Photoactivation and H_2O-Oxidation in *Synechocystis* sp. PCC 6803, *Biochemistry 38*, 6070-6081.

39. Lavorel, J. (1976) Matrix Analysis of the Oxygen Evolving System of Photosynthesis, *J. Theor. Biol. 57*, 171-185.

40. Meunier, P. C., Burnap, R. L., and Sherman, L. A. (1996) Improved 5-step Modeling of the Photosystem II S-state Mechanism in Cyanobacteria, *Photosynth. Res. 47*, 61-76.

41. Jursinic, P. A. and Dennenberg, R. J. (1990) Oxygen Release Time in Leaf Discs and Thylakoids of Peas and Photosystem II Membrane Fragments of Spinach, *Biochim. Biophys. Acta 1020*, 195-206.

42. Debus, R. J., Aznar, C., Campbell, K. A., Gregor, W., Diner, B. A., and Britt, R. D. (2003) Does Aspartate 170 of the D1 Polypeptide Ligate the Manganese Cluster in Photosystem II? An EPR and ESEEM Study, *Biochemistry 42*, 10600-10608.

43. Yano, J., Pushkar, Y., Glatzel, P., Lewis, A., Sauer, K., Messinger, J., Bergmann, U., and Yachandra, V. K. (2005) High-Resolution Mn EXAFS of the Oxygen-Evovling Complex in Photosystem II: Structural Implications for the Mn_4Ca Cluster, *J. Am. Chem. Soc.* 14974-14975.

44. Debus, R. J., Strickler, M. A., Walker, L. M., and Hillier, W. (2005) No Evidence from FTIR Difference Spectroscopy That Aspartate-170 of the D1 Polypeptide Ligates a Manganese Ion That Undergoes Oxidation during the S_0 to S_1, S_1 to S_2, or S_2 to S_3 Transitions in Photosystem II, *Biochemistry 44*, 1367-1374.

45. Strickler, M. A., Hillier, W., and Debus, R. J. (2006) No Evidence from FTIR Difference Spectroscopy that Glutamate-189 of the D1 Polypeptide Ligates a Mn Ion that Undergoes Oxidation During the S_0 to S_1, S_1 to S_2, or S_2 to S_3 Transitions in Photosystem II, *Biochemistry 45*, 8801-8811.

46. Noguchi, T. and Sugiura, M. (2002) Flash-Induced FTIR Difference Spectra of the Water Oxidizing Complex in Moderately Hydrated Photosystem II Core Films: Effect of Hydration Extent on S-State Transitions, *Biochemistry 41*, 2322-2330.

47. Service, R. J., Hillier, W., and Debus, R. J. (2010) Evidence from FTIR Difference Spectroscopy of an Extensive Network of Hydrogen Bonds near the Oxygen-Evolving Mn_4Ca Cluster of PhotosystemII Involving D1-Glu65, D2-Glu312, and D1-Glu329, *Biochemistry 49*, 6655-6669.

48. Robblee, J. H., Messinger, J., Cinco, R. M., McFarlane, K. L., Fernandez, C., Pizarro, S. A., Sauer, K., and Yachandra, V. K. (2002) The Mn Cluster in the S0 State of the Oxygen-Evolving Complex of Photosystem II Studied by EXAFS Spectroscopy: Are

There Three Di-μ-oxo-bridged Mn_2 Moieties in the Tetranuclear Mn Complex?, *J. Am. Chem. Soc. 124*, 7459-7471.

49. Singh, S., Debus, R. J., Wydrzynski, T., and Hillier, W. (2008) Investigation of Substrate Water Interactions at the High-Affinity Mn Site in the Photosystem II Oxygen-Evolving Complex, *Phil. Trans. R. Soc. London, Ser. B 363*, 1229-1235.

50. Hillier, W. and Wydrzynski, T. (2004) Substrate Water Interactions within the Photosystem II Oxygen Evolving Complex, *Phys. Chem. Chem. Phys. 6*, 4882-4889.

51. Gilchrist, M. L., Jr., Ball, J. A., Randall, D. W., and Britt, R. D. (1995) Proximity of the Manganese Cluster of Photosystem II to the Redox Active Tyrosine Y_Z, *Proc. Natl. Acad. Sci. USA 92*, 9545-9549.

52. Peloquin, J. M., Campbell, K. A., and Britt, R. D. (1998) ^{55}Mn Pulsed ENDOR Demonstrates that the Photosystem II "Split" EPR Signal Arises from a Magnetically-Coupled Mangano-Tyrosyl Complex, *J. Am. Chem. Soc. 120*, 6840-6841.

53. Lakshmi, K. V., Eaton, S. S., Eaton, G. R., Frank, H. A., and Brudvig, G. W. (1998) Analysis of Dipolar and Exchange Interactions between Manganese and Tyrosine Z in the S2YZdot State of Acetate-Inhibited Photosystem II via EPR Spectral Simulations at X- and Q- bands, *J. Phys. Chem. B 102*, 8327-8335.

54. Dorlet, P., Boussac, A., Rutherford, A. W., and Un, S. (1999) Multifrequency High-Field EPR Study of the Interaction between the Tyrosyl Z Radical and the Manganese Cluster in Plant Photosystem II, *J. Phys. Chem. B 103*, 10945-10954.

55. Chu, H.-A., Hillier, W., Law, N. A., and Babcock, G. T. (2001) Vibrational Spectroscopy of the Oxygen-Evolving Complex and of Manganese Model Compounds, *Biochim. Biophys. Acta 1503*, 69-82.

56. Noguchi, T. and Berthomieu, C. (2005) Molecular Analysis by Vibrational Spectroscopy, in *Photosystem II: The Light-Driven Water:Plastoquinone Oxidoreductase* (Wydrzynski, T. and Satoh, Ki., Eds.) pp 367-387, Springer, Dordrecht, The Netherlands.

57. Noguchi, T. (2007) Light-Induced FTIR Difference Spectroscopy as a Powerful Tool Toward Understanding the Molecular Mechanism of Photosynthetic Oxygen Evolution, *Photosyn. Res. 91*, 59-69.

58. Noguchi, T. (2008) Fourier Transform Infrared Analysis of the Photosynthetic Oxygen-Evolving Center, *Coord. Chem. Rev. 251*, 336-346.

59. Hienerwadel, R., Boussac, A., Breton, J., Diner, B. A., and Berthomieu, C. (1997) Fourier Transform Infrared Difference Spectroscopy of Photosystem II Tyrosine D using Site-Directed Mutagenesis and Specific Isotope Labeling, *Biochemistry 36*, 14712-14723.

60. Noguchi, T., Inoue, Y., and Tang, X. S. (1997) Structural coupling between the oxygen-evolving Mn cluster and a tyrosine residue in photosystem II as revealed by Fourier transform infrared spectroscopy, *Biochemistry 36*, 14705-14711.

61. Berthomieu, C., Hienerwadel, R., Boussac, A., Breton, J., and Diner, B. A. (1998) Hydrogen-Bonding of Redox-Active Tyrosine Z of Photosystem II Probed by FTIR Difference Spectroscopy, *Biochemistry 37*, 10547-10554.

62. Chu, H.-A., Debus, R. J., and Babcock, G. T. (2001) D1-Asp170 is Structurally Coupled to the Oxygen Evolving Complex in Photosystem II as Revealed by Light-Induced Fourier Transform Infrared Difference Spectroscopy, *Biochemistry 40*, 2312-2316.

63. Kimura, Y., Mizusawa, N., Ishii, A., Nakazawa, S., and Ono, T.-A. (2005) Changes in Structural and Functional Properties of Oxygen-Evolving Complex Induced by Replacement of D1-Glutamate 189 with Glutamine in Photosystem II: Ligation of Glutamate 189 Carboxylate to the Manganese Cluster, *J. Biol. Chem. 280*, 37895-37900.

64. Mizusawa, N., Kimura, Y., Ishii, A., Yamanari, T., Nakazawa, S., Teramoto, H., and Ono, T.-A. (2004) Impact of Replacement of D1 C-terminal Alanine with Glycine on Structure and Function of Photosynthetic Oxygen-Evolving Complex, *J. Biol. Chem. 279*, 29622-29627.

65. Mizusawa, N., Yamanari, T., Kimura, Y., Ishii, A., Nakazawa, S., and Ono, T.-A. (2004) Changes in the Functional and Structural Properties of the Mn Cluster Induced by Replacing the Side Group of the C-Terminus of the D1 Protein of Photosystem II, *Biochemistry 43*, 14644-14652.

66. Kimura, Y., Mizusawa, N., Yamanari, T., Ishii, A., and Ono, T.-A. (2005) Structural Changes of D1 C-terminal α-Carboxylate during S-state Cycling of Photosynthetic Oxygen Evolution, *J. Biol. Chem. 280*, 2078-2083.

67. Noguchi, T., Ono, T.-A., and Inoue, Y. (1995) Direct Detection of a Carboxylate Bridge Between Mn and Ca^{2+} in the Photosynthetic Oxygen-Evolving Center by Means of Fourier Transform Infrared Spectroscopy, *Biochim. Biophys. Acta 1228*, 189-200.

68. Noguchi, T. and Sugiura, M. (2003) Analysis of Flash-Induced FTIR Difference Spectra of the S-State Cycle in the Photosynthetic Water-Oxidizing Complex by Uniform ^{15}N and ^{13}C Isotope Labeling, *Biochemistry 42*, 6035-6042.

69. Kimura, Y., Mizusawa, N., Ishii, A., Yamanari, T., and Ono, T.-A. (2003) Changes of Low-Frequency Vibrational Modes Induced by Universal ^{15}N- and ^{13}C-Isotope Labeling in S_2/S_1 FTIR Difference Spectrum of Oxygen-Evolving Complex, *Biochemistry 42*, 13170-13177.

70. Noguchi, T., Sugiura, M., and Inoue, Y. (1999) FTIR Studies on the Amino-Acid Ligands of the Photosynthetic Oxygen-Evolving Mn-Cluster, in *Fourier Transform Spectroscopy: Twelfth International Conference* (Itoh, K. and Tasumi, M., Eds.) pp 459-460, Waseda University Press, Tokyo, Japan.

71. Messinger, J., Badger, M., and Wydrzynski, T. (1995) Detection of *one* Slowly Exchanging Substrate Water Molecule in the S_3 state of Photosystem II, *Proc. Natl. Acad. Sci. USA 92*, 3209-3213.

72. Hillier, W., Messinger, J., and Wydrzynski, T. (1998) Kinetic Determination of the Fast Exchanging Substrate Water Molecule in the S_3 State of Photosystem II, *Biochemistry 37*, 16908-16914.

73. Hillier, W., Hendry, G., Burnap, R. L., and Wydrzynski, T. (2001) Substrate Water Exchange in Photosystem II Depends on the Peripheral Proteins, *J. Biol. Chem. 276*, 46917-46924.

74. Konermann, L., Messinger, J., and Hillier, W. (2008) Mass Spectrometry-Based Methods for Studying Kinetics and Dynamics in Biological Systems, in *Biophysical Techniques in Photosynthesis II* (Aartsma, T. J. and Matysik, J., Eds.) pp 167-190, Springer, Dordrecht, The Netherlands.

75. Hillier, W. and Wydrzynski, T. (2008) ^{18}O-Water Exchange in Photosystem II: Substrate Binding and Intermediates of the Water Splitting Cycle, *Coord. Chem. Rev. 252*, 306-317.

76. McEvoy, J. P. and Brudvig, G. W. (2004) Structure-Based Mechanism of Photosynthetic Water Oxidation, *Phys. Chem. Chem. Phys. 6*, 4754-4763.

77. Haumann, M., Liebisch, P., Müller, C., Barra, M., Grabolle, M., and Dau, H. (2005) Photosynthetic O_2 Formation Tracked by Time-Resolved X-ray Experiments, *Science 310*, 1019-1021.

78. Sproviero, E. M., Gascón, J. A., McEvoy, J. P., Brudvig, G. W., and Batista, V. S. (2008) Quantum Mechanics/Molecular Mechanics Study of the Catalytic Cycle of Water Splitting In Photosystem II, *J. Am. Chem. Soc. 130*, 3428-3442.

79. Sproviero, E. M., McEvoy, J. P., Gascón, J. A., Brudvig, G. W., and Batista, V. S. (2008) Computational Insights into the O2-Evolving Complex of Photosystem II, *Photosynth. Res. 97*, 91-114.

80. Tommos, C. and Babcock, G. T. (2000) Proton and Hydrogen Currents in Photosynthetic Water Oxidation, *Biochim. Biophys. Acta 1458*, 199-219.

81. Ishikita, H., Saenger, W., Loll, B., Biesiadka, J., and Knapp, E.-W. (2006) Energetics of a Possible Proton Exit Pathway for Water Oxidation in Photosystem II, *Biochemistry 45*, 2063-2071.

82. Murray, J. W. and Barber, J. (2007) Structural Characteristics of Channels and Pathways in Photosystem II Including the Identification of an Oxygen Channel, *J. Struct. Biol. 159*, 228-237.

83. Ho, F. M. and Styring, S. (2008) Access Channels and Methanol Binding Site to the $CaMn_4$ Cluster in Photosystem II based on Solvent Accessibility Simulation, with Implications for Substrate Water Access, *Biochim. Biophys. Acta 1777*, 140-153.

84. Gabdulkhakov, A., Guskov, A., Broser, M., Kern, J., Müh, F., Saenger, W., and Zouni, A. (2009) Probing the Accessibility of the Mn_4Ca Cluster in Photosystem II: Channels Calculation, Noble Gas Derivatization, and Cocrystallization with DMSO, *Structure 17*, 1223-1234.

85. Wraight, C. A. (2006) Chance and Design - Proton Transfer in Water, Channels and Bioenergetic Proteins, *Biochim. Biophys. Acta 1757*, 886-912.

86. Silverman, D. N. and McKenna, R. (2007) Solvent-Mediated Proton Transfer in Catalysis by Carbonic Anhydrase, *Acc. Chem. Res. 40*, 669-675.

87. Mikulski, R. L. and Silverman, D. N. (2010) Proton Transfer in Catalysis and the Role of Proton Shuttles in Carbonic Anhydrase, *Biochim. Biophys. Acta 1804*, 422-426.

88. Okamura, M. Y., Paddock, M. L., Graige, M. S., and Feher, G. (2000) Proton and electron transfer in bacterial reaction centers, *Biochim. Biophys. Acta 1458*, 148-163.

89. Paddock, M. L., Feher, G., and Okamura, M. Y. (2003) Proton Transfer Pathways and Mechanism in Bacterial Reaction Centers, *FEBS Lett. 555*, 45-50.

90. Wraight, C. A. (2005) Intraprotein Proton Transfer - Concepts and Realities from the Bacterial Photosynthetic Reaction Center, in *Biophysical and Structural Aspects of Bioenergetics* (Wikström, M., Ed.) pp 273-313, RSC Publishing, Cambridge, UK.

91. Hosler, J. P., Ferguson-Miller, S., and Mills, D. A. (2006) Energy Transduction: Proton Transfer Through the Respiratory Complexes, *Annu. Rev. Biochem. 75*, 165-187.

92. Wikström, M. and Verkhovsky, M. I. (2007) Mechanism and Energetics of Proton Translocation by the Respiratory Heme-Copper Oxidases, *Biochim. Biophys. Acta 1767*, 1200-1214.

93. Brzezinski, P. and Gennis, R. B. (2008) Cytochrome *c* Oxidase: Exciting Progress and Remaining Mysteries, *J. Bioenerg. Biomemb. 40*, 521-531.

94. Boussac, A., Zimmermann, J.-L., and Rutherford, A. W. (1989) EPR Signals from Modified Charge Accumulation States of the Oxygen Evolving Enzyme in Ca^{2+}-Deficient Photosystem II, *Biochemistry 28*, 8984-8989.

95. Sivaraja, M., Tso, J., and Dismukes, G. C. (1989) A Calcium-Specific Site Influences the Structure and Activity of the Manganese Cluster Responsible for Photosynthetic Water Oxidation, *Biochemistry 28*, 9459-9464.

96. Ono, T.-A. and Inoue, Y. (1989) Removal of Ca by pH 3.0 Treatment Inhibits S_2 to S_3 Transition in Photosynthetic Oxygen Evolution System, *Biochim. Biophys. Acta 973*, 443-449.

97. Boussac, A., Zimmermann, J.-L., and Rutherford, A. W. (1990) Factors Influencing the Formation of Modified S_2 EPR Signal and the S_3 EPR Signal in Ca^{2+}-Depleted Photosystem II, *FEBS Lett. 277*, 69-74.

98. Haumann, M. and Junge, W. (1999) Evidence for Impaired Hydrogen-Bonding of Tyrosine Y_Z in Calcium-Depleted Photosystem II, *Biochim. Biophys. Acta 1411*, 121-133.

99. Styring, S., Feyziyev, Y., Mamedov, F., Hillier, W., and Babcock, G. T. (2003) pH Dependence of the Donor Side Reactions in Ca^{2+}-Depleted Photosystem II, *Biochemistry 42*, 6185-6192.

100. Burnap, R. L. (2004) D1 Protein Processing and Mn Cluster Assembly in Light of the Emerging Photosystem II Structure, *Phys. Chem. Chem. Phys. 6*, 4803-4809.

101. DasGupta, J., Ananyev, G., and Dismukes, G. C. (2008) Photoassembly of the Water-Oxidizing Complex in Photosystem II, *Coord. Chem. Rev. 252*, 347-360.

102. Yano, J., Walker, L. M., Yachandra, V. K., and Debus, R. J. (2010) Altered Structure of the Mn_4Ca Cluster in the Oxygen Evolving Complex of Photosystem II in a Cyanobacteria Mutant (*submitted*).

103. Peloquin, J. M., Campbell, K. A., Randall, D. W., Evanchik, M. A., Pecoraro, V. L., Armstrong, W. H., and Britt, R. D. (2000) ^{55}Mn ENDOR of the S_2-state Multiline EPR Signal of Photosystem II: Implications on the Structure of the Tetranuclear Mn Cluster, *J. Am. Chem. Soc. 122*, 10926-10942.

104. Kulik, L., Epel, B., Lubitz, W., and Messinger, J. (2005) ^{55}Mn Pulse ENDOR at 34 GHz of the S_0 and S_2 States of the Oxygen-Evolving Complex in Photosystem II, *J. Am. Chem. Soc. 127*, 2392-2393.

105. Kulik, L., Epel, B., Lubitz, W., and Messinger, J. (2007) Electronic Structure of the Mn_4O_xCa Cluster in the S_0 and S_2 States of the Oxygen-Evolving Complex of Photosystem II Based on Pulse ^{55}Mn-ENDOR and EPR Spectroscopy, *J. Am. Chem. Soc. 129*, 13421-13435.

106. Debus, R. J., Campbell, K. A., Peloquin, J. M., Pham, D. P., and Britt, R. D. (2000) Histidine 332 of the D1 Polypeptide Modulates the Magnetic and Redox Properties of the Manganese Cluster and Tyrosine Y_Z in Photosystem II, *Biochemistry 39*, 470-478.

107. Boussac, A., Rappaport, F., Carrier, P., Verbavatz, J.-M., Gobin, R., Kirilovsky, D., Rutherford, A. W., and Sugiura, M. (2004) Biosynthetic Ca^{2+}/Sr^{2+} Exchange in the Photosystem II Oxygen-Evolving Enzyme of *Thermosynechococcus elongatus*, *J. Biol. Chem. 279*, 22809-22819.

108. Mehrotra, R. C. and Bohra, R. (1983) *Metal Carboxylates* Academic Press, London, UK.

109. Deacon, G. B. and Phillips, R. J. (1980) Relationships between the Carbon-Oxygen Stretching Frequencies of Carboxylato Complexes and the Type of Carboxylate Coordination, *Coord. Chem. Rev. 33*, 227-250.

110. Tackett, J. E. (1989) FT-IR Characterization of Metal Acetates in Aqueous Solution, *Appl. Spectrosc. 43*, 483-489.

111. Nakamoto, K. (1997) Infrared and Raman Spectra of Inorganic and Coordination Compounds, Part B: Applications in Coordination, Organometallic, and Bioinorganic Chemistry, 5th ed., John Wiley & Sons, New York, NY.

112. Nara, M., Torii, H., and Tasumi, M. (1996) Correlation between the Vibrational Frequencies of the Carboxylate Group and Types of its Coordination to a Metal Ion: An *ab Initio* Molecular Orbital Study, *J. Phys. Chem. 100*, 19812-19817.

113. Venyaminov, S. Yu. and Kalnin, N. N. (1990) Quantitative IR Spectrophotometry of Peptide Compounds in Water (H_2O) Solutions. 1. Spectral Parameters of Amino Acid Residue Absorption Bands, *Biopolymers 30*, 1243-1257.

114. Rahmelow, K., Hübner, W., and Ackermann, Th. (1998) Infrared Absorbances of Protein Side Chains, *Anal. Biochem. 257*, 1-11.

115. Barth, A. (2000) The Infrared Absorption of Amino Acid Side Chains, *Prog. Biophys. Molec. Biol. 74*, 141-173.

116. Barth, A. and Zscherp, C. (2002) What Vibrations Tell Us About Proteins, *Q. Rev. Biophys. 35*, 369-430.

117. Hillier, W. and Wydrzynski, T. (2001) Oxygen Ligand Exchange at Metal sites - Implications for the O_2 Evolving Mechanism of Photosystem II, *Biochim. Biophys. Acta 1503*, 197-209.

118. Vassiliev, S., Comte, P., Mahboob, A., and Bruce, D. (2010) Tracking the Flow of Water through Photosystem II Using Molecular Dynamics and Streamline Tracing, *Biochemistry 49*, 1873-1881.

119. Richens, D. T. (2005) Ligand Substitution Reactions at Inorganic Centers, *Chem. Rev. 105*, 1961-2002.

120. Hendry, G. and Wydrzynski, T. (2002) The Two Substrate-Water molecules are Already Bound to the Oxygen-Evolving Complex in the S_2 State of Photosystem II, *Biochemistry 41*, 13328-13334.

121. Noguchi, T. and Sugiura, M. (2000) Structure of an Active Water Molecule in the Water-Oxidizing Complex of Photosystem II As Studied by FTIR Spectroscopy, *Biochemistry 39*, 10943-10949.

122. Noguchi, T. and Sugiura, M. (2002) FTIR Detection of Water Reactions During the Flash-Induced S-State Cycle of the Photosynthetic Water-Oxidizing Complex, *Biochemistry 41*, 15706-15712.

123. Suzuki, H., Sugiura, M., and Noguchi, T. (2008) Monitoring Water Reactions during the S-State Cycle of the Photosynthetic Water-Oxidizing Center: Detection of the DOD Bending Vibrations by Means of Fourier Transform Infrared Spectroscopy, *Biochemistry 47*, 11024-11030.

124. Su, J.-H., Lubitz, W., and Messinger, J. (2008) Probing Mode and Site of Substrate Water Binding to the Oxygen-Evolving Complex in the S_2 State of Photosystem II by ^{17}O-HYSCORE Spectroscopy, *J. Am. Chem. Soc. 130*, 786-787.

125. Su, J.-H. and Messinger, J. (2010) Is Mn-Bound Substrate Water Protonated in the S_2 State of Photosystem II?, *Appl. Magn. Reson. 37*, 123-136.

2.8 Tables and Figures

Table 2.1 Membranes were given a series of 20 pre-flashes followed by a 10 min dark-adaptation period prior to the initiation of the measuring flash sequence. Numerical analysis of the O_2 flash-yield amplitudes was performed assuming a four-state model as described previously (*39, 40*).

Table 1. S-state decay cycling parameters of CP43-E354Q membranes

Strain	S-state distribution: S_0:S_1:S_2:S_3 (%)	Misses α (%)	Hits β (%)	Double hits γ (%)	Deactivations δ (%)
Wild-Type	36:62:2:0	9	86	3	2
CP43-E354Q	31:63:6:0	9	84	4	3

Table 2.1

Table 2.2 Buffer solution medium: 40 mM MES, pH 6.5, 15 mM $MgCl_2$, 15 mM $CaCl_2$, 10% glycerol, 1.2 M betaine.

Table 2: Rate constants for ^{18}O exchange in the S_3 state of Wild-type and CP43-E354Q thylakoid membranes from *Synechocystis* sp. PCC 6803

Sample	k_1 (s^{-1})	k_2 (s^{-1})
WT	0.47±0.04	19.7±1.3
CP43-E354Q	0.86±0.35	167±38

Table 2.2

Figure 2.1 Comparison of the flash O_2 yield patterns of wild-type (A) and CP43-E354Q (B) thylakoid membranes in response to 15 saturating xenon flashes applied at a frequency of 4 Hz. Equivalent amounts of thylakoid membranes were deposited centrifugally on the surface of a bare-platinum electrode, subjected to 20 preflashes, then dark-adapted for ten minutes before the sequence of measuring flashes was initiated.

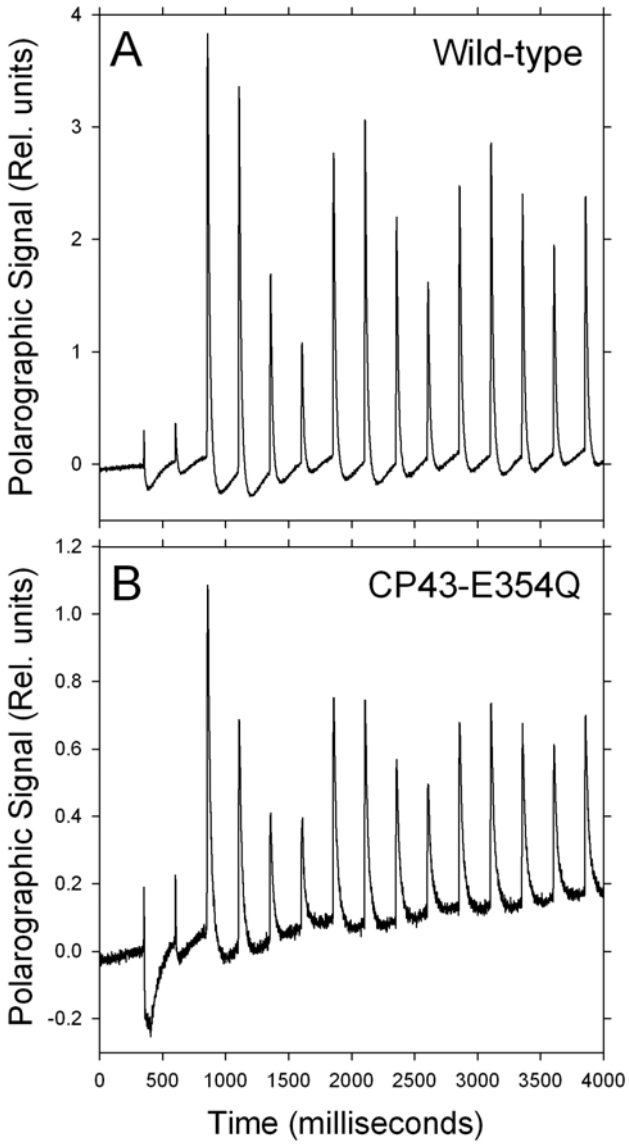
A
Wild-type
Polarographic Signal (Rel. units)
4
3
2
1
0
B
CP43-E354Q
Polarographic Signal (Rel. units)
1.2
1.0
0.8
0.6
0.4
0.2
0.0
-0.2
0
500
1000
1500
2000
2500
3000
3500
4000
Time (milliseconds)

Figure 2.1

Figure 2.2 Comparison of the flash-induced O_2 signals of wild-type (black traces) and CP43-E354Q (red traces) thylakoid membranes plotted on (A) linear and (B) logarithmic time scales. The traces have been normalized to facilitate comparison (the data of the mutant was multiplied vertically by a factor of 3.6). Equivalent amounts of thylakoid membranes were deposited centrifugally on the surface of a bare-platinum electrode and given a sequence of 100 saturating xenon flashes at 4 Hz. The data show the averages from each set of 100 kinetic traces.

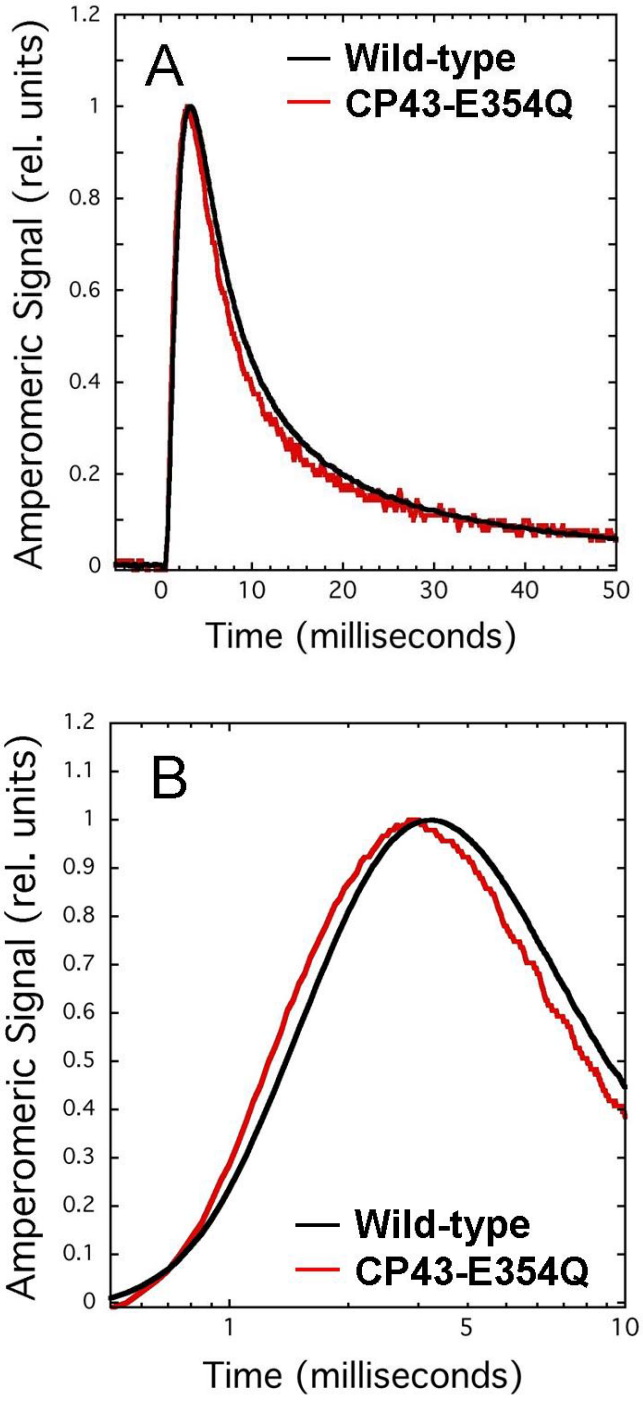
A
Wild-type
CP43-E354Q
Amperomeric Signal (rel. units)
Time (milliseconds)
B
Wild-type
CP43-E354Q
Amperomeric Signal (rel. units)
Time (milliseconds)

Figure 2.2

Figure 2.3 Comparison of the parallel polarization S_1 state (A) and light-*minus*-dark perpendicular polarization S_2 state (B) multiline EPR signals of wild-type (black) and CP43-E354Q (red) PSII core complexes. The wild-type and mutant samples in (A) contained 125 μL of 6.7 mg of Chl/mL and 8.1 mg of Chl/mL, respectively and were deaerated prior to measurement to remove condensed O_2. To facilitate comparison, the mutant spectrum has been multiplied vertically by a factor of 4. Features below 375 G or above 650 G in the mutant spectrum were not reproducible. The sample buffer in (A) consisted of 1.2 M betaine, 10% (v/v) glycerol, 10 mM MES-NaOH (pH 6.0), 10 mM $CaCl_2$, 5 mM $MgCl_2$, 50 mM histidine, 1 mM EDTA, and 0.03% (w/v) *n*-dodecyl β-D-maltoside. The wild-type and mutant samples in (B) contained 100 μL of 11.0 mg of Chl/mL and 60 μL of 10.9 mg of Chl/mL, respectively. The sample buffer consisted of 1.2 M betaine, 40% (v/v) glycerol, 10 mM MES-NaOH (pH 6.0), 10 mM $CaCl_2$, 5 mM $MgCl_2$, and 0.03% (w/v) *n*-dodecyl β-D-maltoside. The data in (A) were recorded at 4.7 K with a microwave frequency of 9.3822 GHz, a microwave power of 50 mW, a modulation amplitude of 9 G, a modulation frequency of 100 GHz, a time constant of 81 ms, and a scan time of 170 s/1100 G. The wild-type and mutant spectra represent the averages of 25 and 100 scans, respectively. The data in (B) were recorded at 9 K with a microwave frequency of 9.2579 GHz, a microwave power of 5 mW, a modulation amplitude of 8 G, a modulation frequency of 100 kHz, a time constant of 250 ms, and a scan time of 4 min/3300 G. To generate the S_2 state in (B), samples were illuminated for 5 min at 195 K before being flash-frozen in liquid nitrogen. Both spectra in (B) have had the large signal of $Y_D^{\bullet}$ at $g = 2$ excised for clarity. Each spectrum in (B) represents the average of 60 scans. To correct for the lower amount of Chl in the mutant sample, the mutant spectrum in (B) has been multiplied vertically by a factor of 1.67. Asterisks denote peaks used to estimate the relative amplitudes of the signals (see text). The insert in (B) shows light-*minus*-dark scans between 600 and 3800 G.

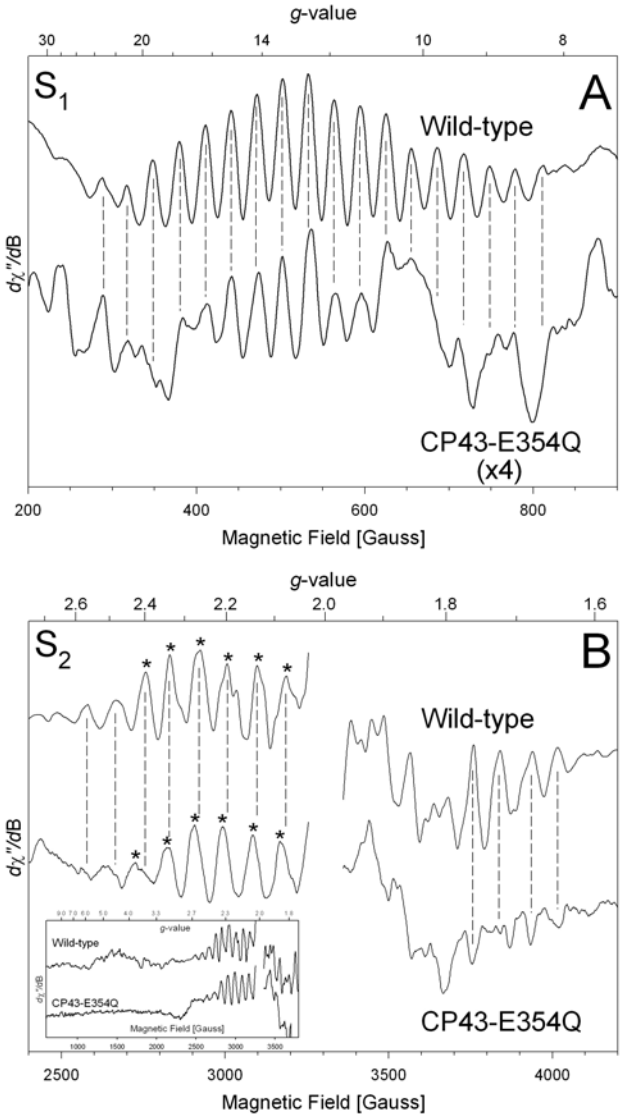
g-value
30
20
14
10
8
S1
A
Wild-type
dχ''/dB
CP43-E354Q
(x4)
200
400
600
800
Magnetic Field [Gauss]
g-value
2.6
2.4
2.2
2.0
1.8
1.6
S2
B
Wild-type
dχ''/dB
CP43-E354Q
2500
3000
3500
4000
Magnetic Field [Gauss]

Figure 2.3

Figure 2.4 The decay of the S_2 state in CP43-E354Q PSII core complexes as measured from the decay of the S_2 state multiline EPR signal at 4°C. The signal amplitude was estimated from the area under the six low-field lines shown as asterisks in Figure 3.

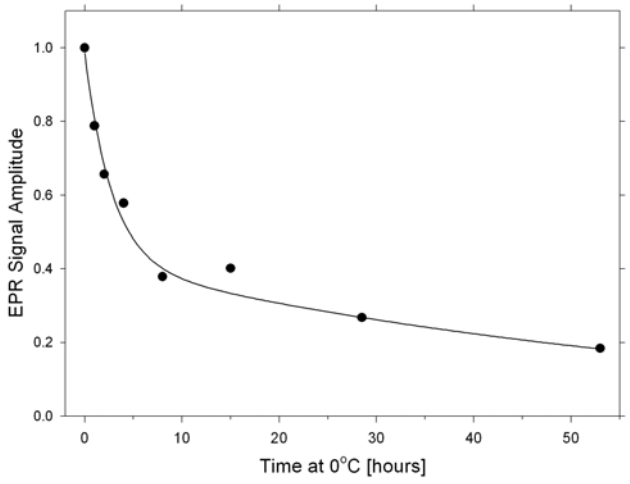
EPR Signal Amplitude
1.0
0.8
0.6
0.4
0.2
0.0
0
10
20
30
40
50
Time at 0°C [hours]

Figure 2.4

Figure 2.5 Comparison of the Mn K-edge XANES spectra of wild-type (blue traces) and CP43-E354Q (red traces) in PSII core complexes poised in the S_1 state by extensive dark-adaptation (A) and in the S_2 state after illumination (B). The corresponding second derivatives of the data in (A) and (B) are shown in (C) and (D), respectively.

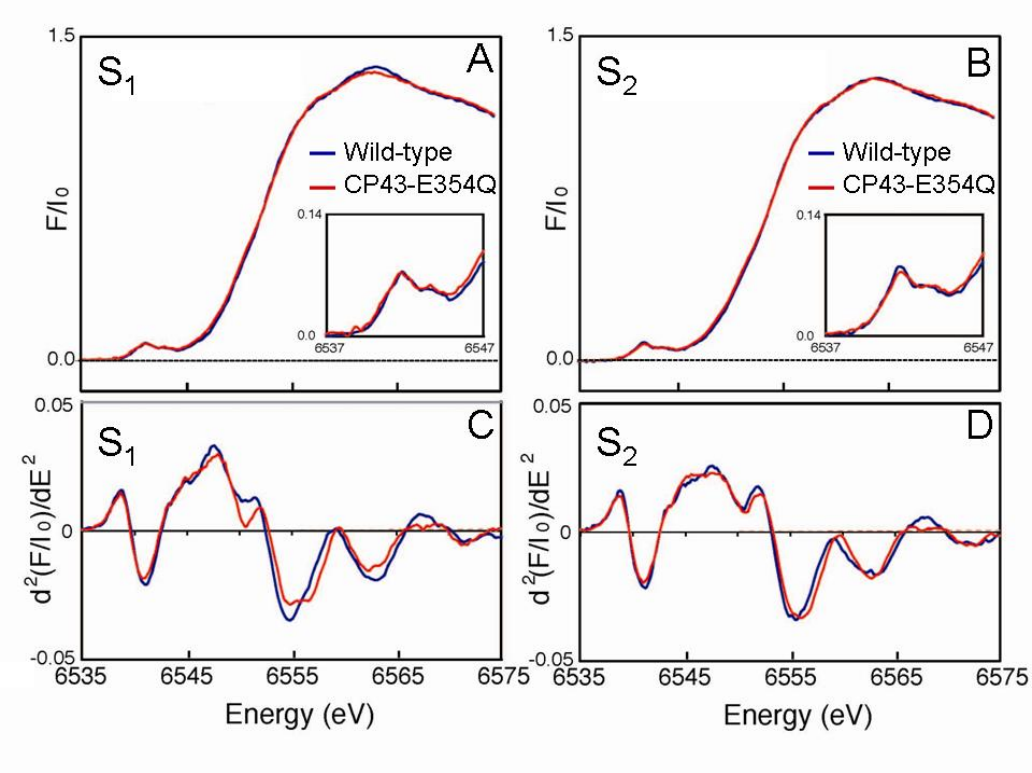
S1
A
Wild-type
CP43-E354Q
F/I0
1.5
0.0
0.14
0.0
6537
6547
S2
B
C
D
d2(F/I0)/dE2
0.05
0
-0.05
6535
6545
6555
6565
6575
Energy (eV)

Figure 2.5

Figure 2.6 Comparison of the Fourier transforms of k^3-weighted Mn-EXAFS of wild-type (A) and CP43-E354Q (B) PSII core complexes poised in the S_1 (blue traces) and S_2 traces (red traces). The wild-type spectra from (A) are reproduced in (B) in grey.

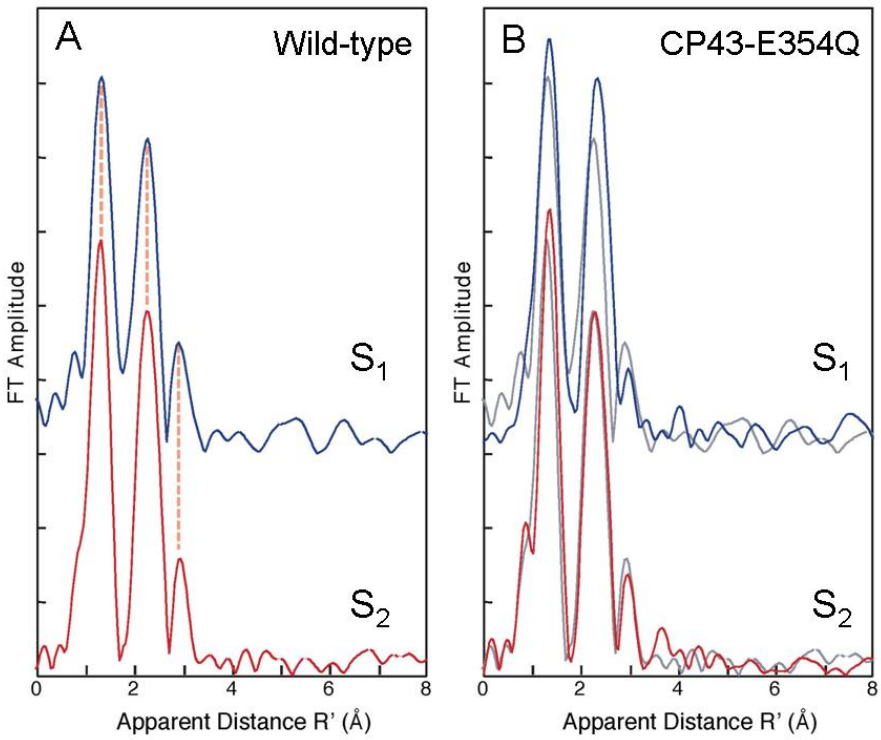
A
Wild-type
B
CP43-E354Q
FT Amplitude
FT Amplitude
S1
S2
S1
S2
0
2
4
6
8
0
2
4
6
8
Apparent Distance R' (Å)
Apparent Distance R' (Å)

Figure 2.6

Figure 2.7 Comparison of the midfrequency FTIR difference spectra of wild-type (black traces) and CP43-E354Q (red traces) PSII core complexes in response to four successive flash illuminations applied at 273 K and spaced by 96 s. The spectra were normalized to the peak-to-peak amplitudes of the negative ferricyanide peak at 2115 cm^{-1} and the positive ferrocyanide peak at 2038 cm^{-1} (these peaks reflect the reduction of the ferricyanide electron acceptor by $Q_A^{\bullet-}$). The wild-type spectra represent the averages of seven samples (5,600 scans). The CP43-E354Q spectra represent the averages of nine samples (7,200 scans). Samples were given a single set of four flashes at 273 K after having been dark adapted for 18 hours at the same temperature. The data recorded after the 1st flash are dominated by the S_1 to S_2 transition and represent S_2-*minus*-S_1 FTIR difference spectra. Dark-*minus*-dark control spectra are included to show the noise level (lower traces).

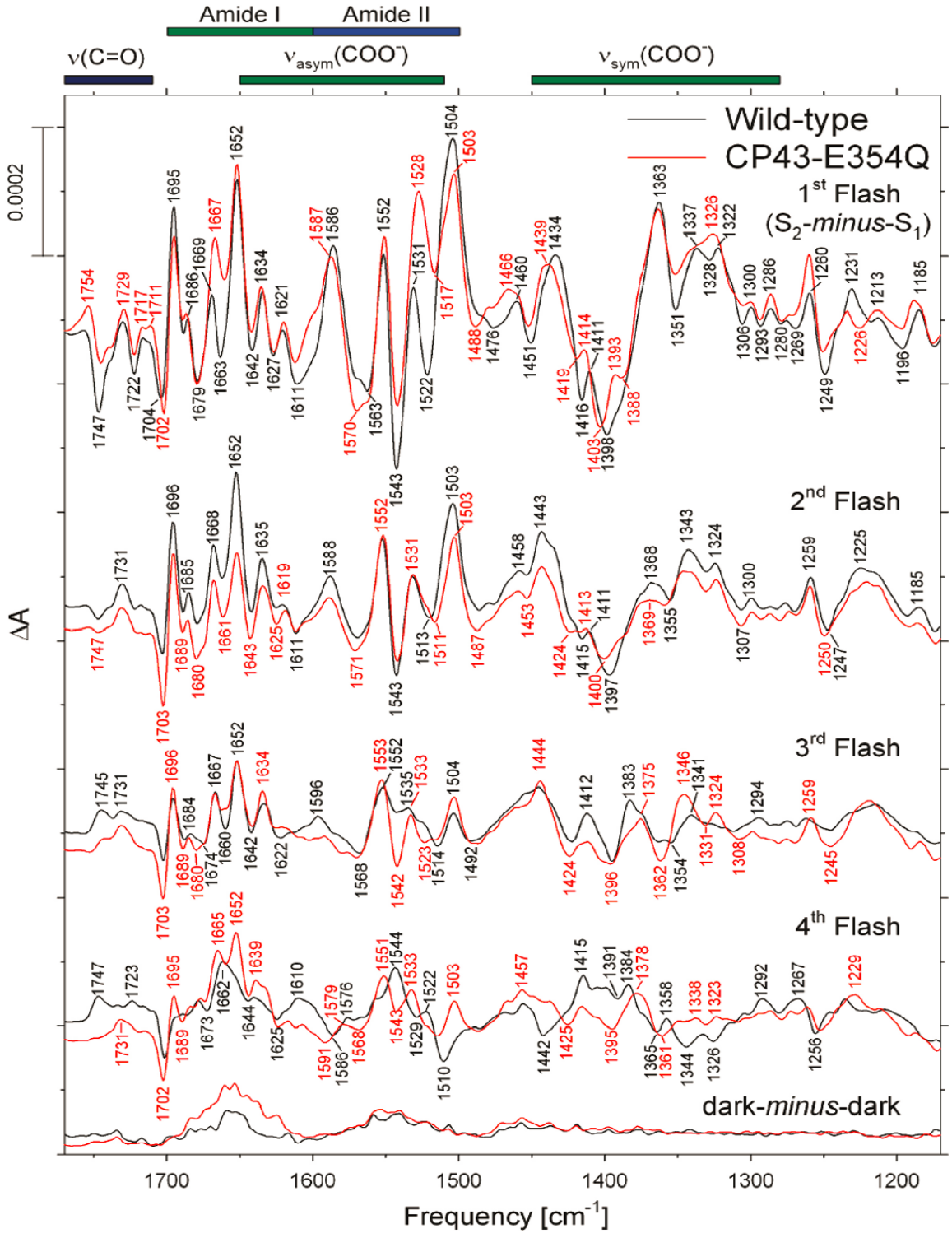
Amide I
Amide II
ν(C=O)
ν_asym(COO⁻)
ν_sym(COO⁻)
Wild-type
CP43-E354Q
1st Flash
(S2-minus-S1)
2nd Flash
3rd Flash
4th Flash
dark-minus-dark
0.0002
ΔA
1700
1600
1500
1400
1300
1200
Frequency [cm-1]

Figure 2.7

Figure 2.8 Comparison of the midfrequency S_2-*minus*-S_1 FTIR difference spectra of wild-type (black traces) and CP43-E354Q (red traces) PSII core complexes purified and examined under a variety of conditions. In panel (A), samples were purified in the presence of 1.2 M betaine and 10% (v/v) glycerol, dark adapted for 18 hr, then subjected to a single set of flashes at 273 K (data reproduced from Figure 8, top set of traces). In panel (B), samples were purified in the presence of 25% (v/v) glycerol, dark adapted 2 h, then given a single flash at 250 K [the wild-type and mutant samples correspond to the averages of three samples (2,400 scans) and four samples (3,200 scans), respectively]. In panel (C), samples were purified in the presence of 25% (v/v) glycerol, dark adapted 2 h, then given 16 flashes spaced 30 min apart at 273 K [the wild-type and mutant samples correspond to the averages of four samples each (12,800 scans each). In panel (D), samples were purified in the presence of 1.2 M betaine and 10% (v/v) glycerol, dark adapted 2 h, then given 16 flashes spaced 30 min apart at 273 K [the wild-type and mutant samples correspond to the averages of four samples each (12,800 scans each). Within each panel, the spectra were normalized to the peak-to-peak amplitudes of the negative ferricyanide peak at 2115 cm^{-1} and the positive ferrocyanide peak at 2038 cm^{-1}.

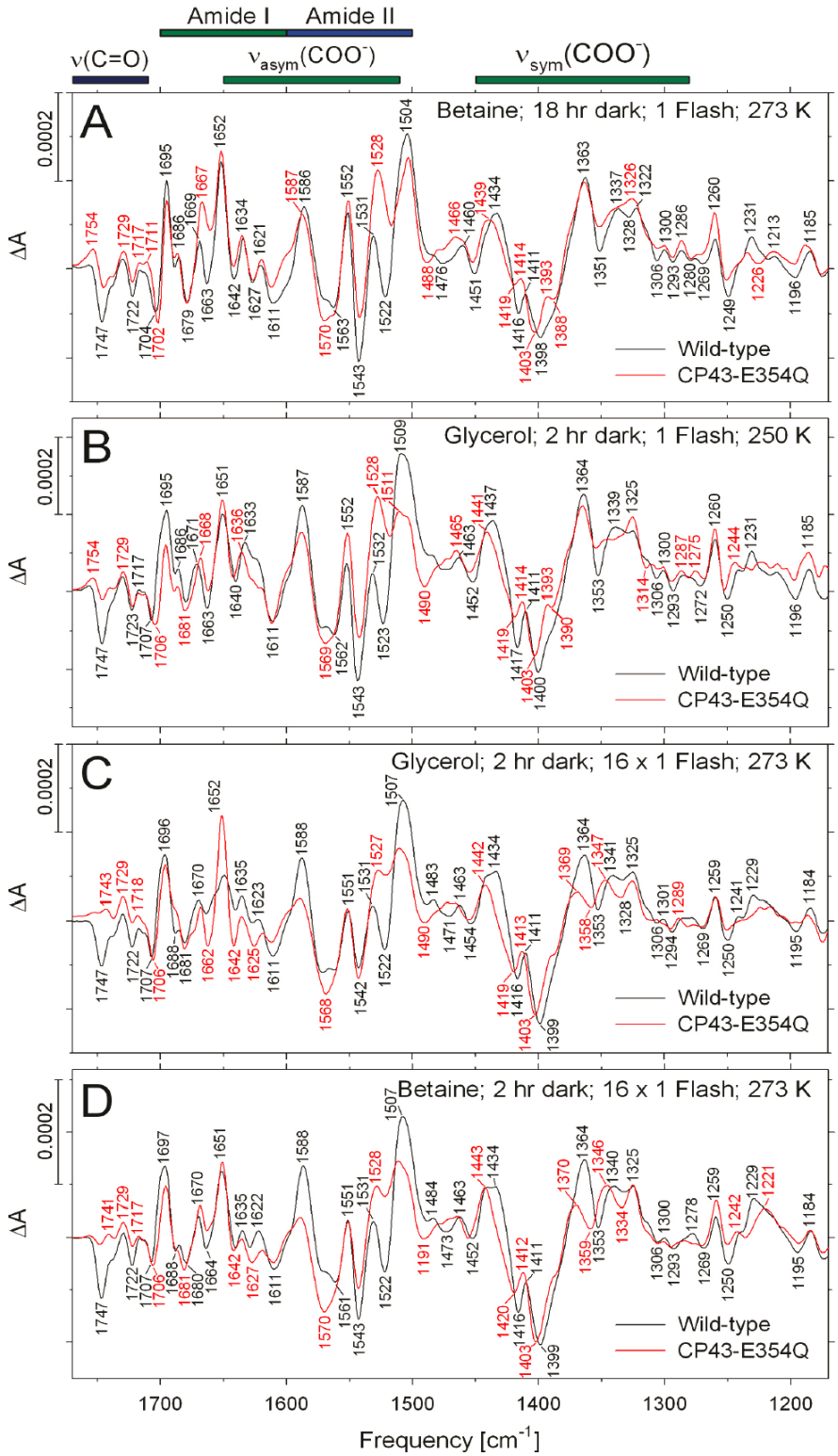
Amide I
Amide II
ν(C=O)
ν_asym(COO⁻)
ν_sym(COO⁻)
A
Betaine; 18 hr dark; 1 Flash; 273 K
B
Glycerol; 2 hr dark; 1 Flash; 250 K
C
Glycerol; 2 hr dark; 16 x 1 Flash; 273 K
D
Betaine; 2 hr dark; 16 x 1 Flash; 273 K
0.0002
ΔA
Wild-type
CP43-E354Q
1700
1600
1500
1400
1300
1200
Frequency [cm⁻¹]

Figure 2.8

Figure 2.9 Comparison of the midfrequency S_2-*minus*-S_1 FTIR difference spectra of unlabeled (black traces) and ^{15}N-globally-labeled (blue traces) wild-type (A) and CP43-E354Q (B) PSII core complexes in response to a single flash applied at 273 K. The unlabeled spectra in (A) and (B) are reproduced from Figure 7, top traces (black and red, respectively). The ^{15}N-labeled wild-type and CP43-E354Q spectra represents the averages of nine (7,200 scans) and eight samples (6,400 scans), respectively. Samples were given a single flash at 273 K after having been dark adapted for 18 hours at the same temperature.

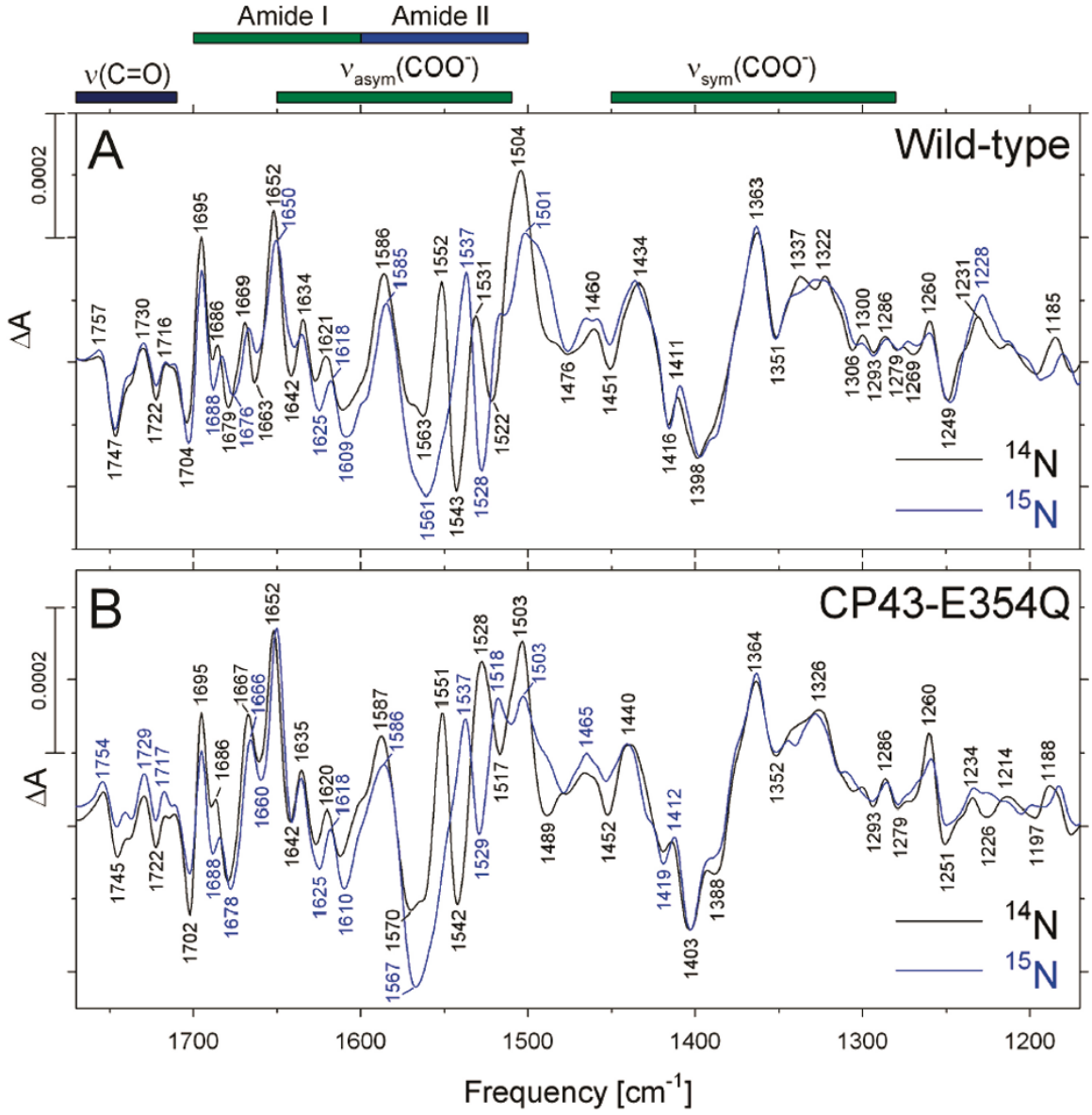
Amide I
Amide II
ν(C=O)
ν_asym(COO⁻)
ν_sym(COO⁻)
A
Wild-type
B
CP43-E354Q
0.0002
ΔA
14N
15N
Frequency [cm-1]
1700
1600
1500
1400
1300
1200

Figure 2.9

Figure 2.10 Comparison of the double difference spectra (wild-type-*minus*-mutant) that were obtained by subtracting the S_2-*minus*-S_1 FTIR difference spectrum of unlabeled or ^{15}N-labeled CP43-E354Q PSII core complexes from the S_2-*minus*-S_1 FTIR difference spectrum of unlabeled or ^{15}N-labeled wild-type PSII complexes recorded under each of the conditions shown in Figure 9. Double difference spectra obtained by subtracting the spectra of unlabeled samples are shown with black lines. Double difference spectra obtained by subtracting the spectra of ^{15}N-labeled samples are shown with blue lines. The unlabeled double difference spectra in panels (A), (B), (C), and (D) were obtained by directly subtracting the data of Figure 9A, 9B, 9C, and 9D, respectively. The ^{15}N-labeled double difference spectrum in panel (A) was obtained by subtracting the ^{15}N-labeled spectra shown in Figure 8.

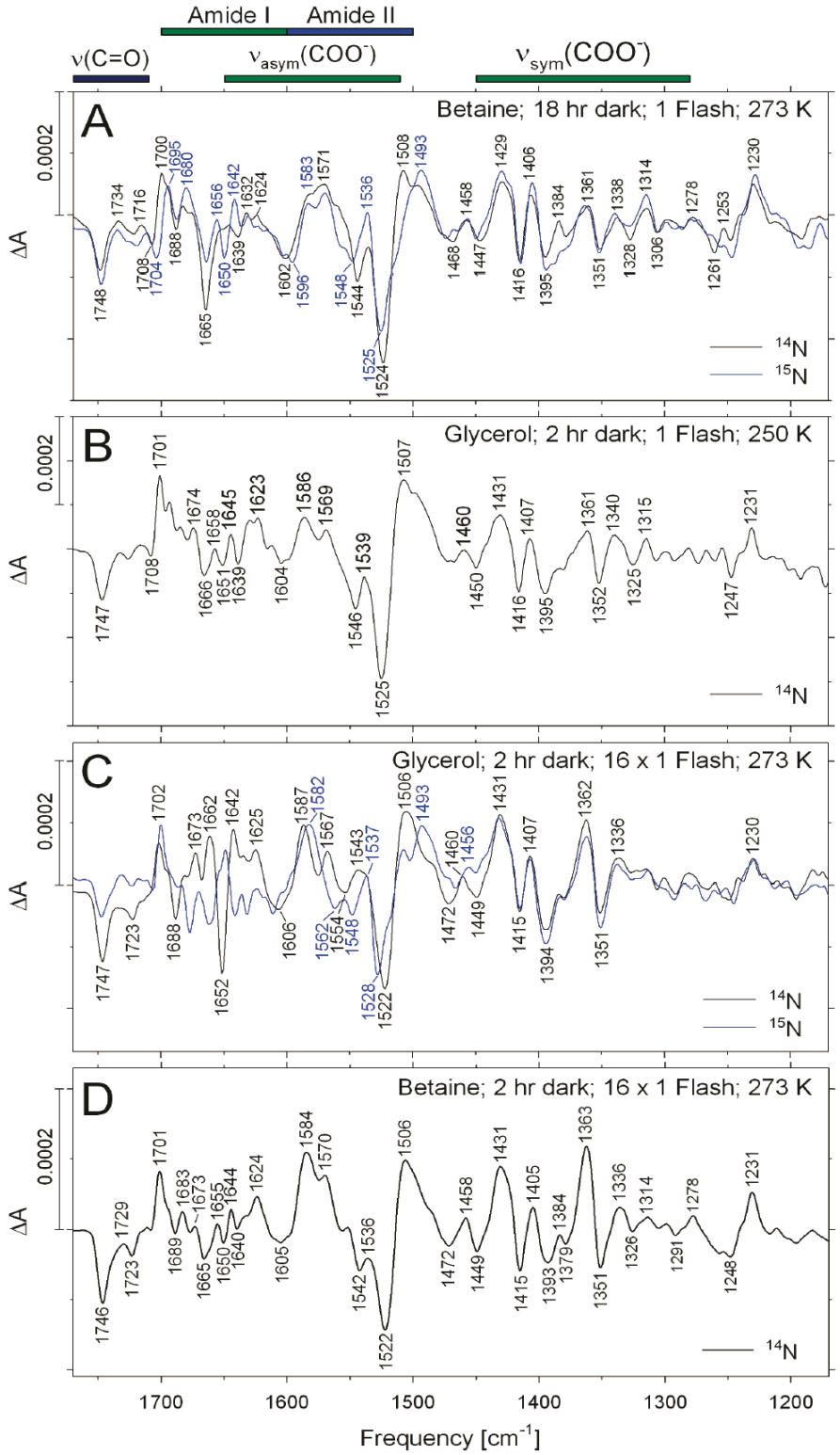
Amide I
Amide II
ν(C=O)
ν_asym(COO⁻)
ν_sym(COO⁻)
A
Betaine; 18 hr dark; 1 Flash; 273 K
B
Glycerol; 2 hr dark; 1 Flash; 250 K
C
Glycerol; 2 hr dark; 16 x 1 Flash; 273 K
D
Betaine; 2 hr dark; 16 x 1 Flash; 273 K
ΔA
0.0002
14N
15N
1700
1600
1500
1400
1300
1200
Frequency [cm-1]

Figure 2.10

Figure 2.11 Comparison of the midfrequency S_2-*minus*-S_1 FTIR difference spectra of unlabeled (black traces) and L-[1-^{13}C]alanine-labeled (red traces) wild-type (A) or CP43-E354Q (B) PSII core complexes. Each sample was given a single flash at 273 K after having been dark-adapted for 18 hours at the same temperature. The spectra of the unlabeled wild-type and CP43-E354Q PSII core complexes have been normalized to the peak-to-peak amplitudes of the negative ferricyanide peak at 2115 cm^{-1} and the positive ferrocyanide peak at 2038 cm^{-1}. The unlabeled and L-[1-^{13}C]alanine-labeled wild-type spectra in (A) represent the averages of seven samples (5,600 scans) and eight samples (6,400 scans), respectively. The unlabeled and L-[1-^{13}C]alanine-labeled CP43-E354Q spectra in (B) each represent the averages of nine samples (7,200 scans). Within each panel, the spectra have been normalized to maximize their overlap between 1500 and 1350 cm^{-1}. Panel (C) shows the double difference spectra, ^{12}C-*minus*-^{13}C, of wild-type (black trace) and CP43-E354Q (red trace) PSII core complexes that were obtained by subtracting the S_2-*minus*-S_1 FTIR difference spectra of the L-[1-^{13}C]alanine-labeled core complexes from the S_2-*minus*-S_1 FTIR difference spectra of the unlabeled core complexes (the spectra shown in Figures 11A and 11B were subtracted directly). Only the regions between 1380 and 1280 cm^{-1} are shown.

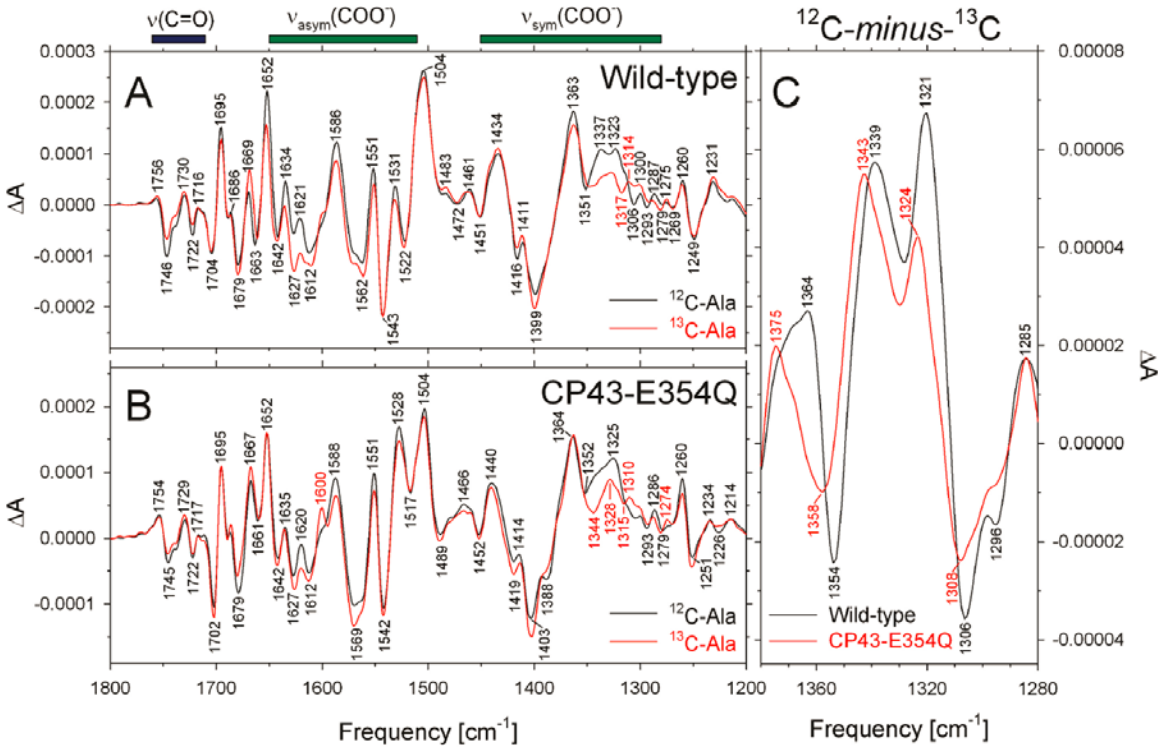
ν(C=O)
νasym(COO-)
νsym(COO-)
12C-minus-13C
A
Wild-type
B
CP43-E354Q
C
12C-Ala
13C-Ala
Wild-type
CP43-E354Q
ΔA
Frequency [cm-1]

Figure 2.11

Figure 2.12 ^{18}O exchange measurements in the S_3 state of wild-type (black circles and line) and CP43-E354Q (red circles and line) thylakoid membranes. The data are shown as filled circles with the kinetic fit shown by a line. The inset shows the same data plotted a shorter expanded time scale to show the fast phase of exchange.

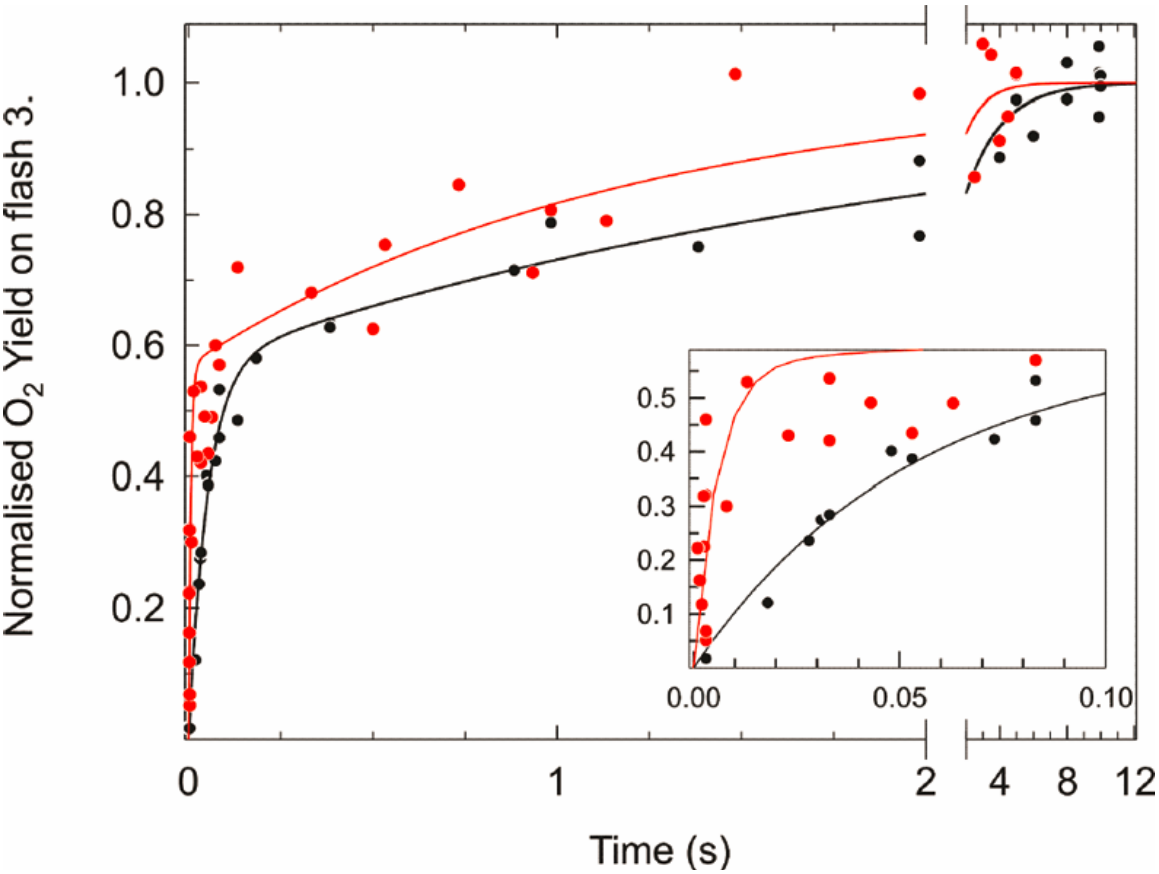
Normalised O_2 Yield on flash 3.
1.0
0.8
0.6
0.4
0.2
0
1
2
4
8
12
Time (s)
0.5
0.4
0.3
0.2
0.1
0.00
0.05
0.10

Figure 2.12

CHAPTER 3

EVIDENCE FROM FTIR DIFFERENCE SPECTROSCOPY OF AN EXTENSIVE NETWORK OF HYDROGEN BONDS NEAR THE OXYGEN-EVOLVING MN_4CA CLUSTER OF PHOTOSYSTEM II INVOLVING D1-GLU65, D2-GLU312, AND D1-GLU329

3.1 Abstract

Analyses of the refined x-ray crystallographic structures of photosystem II (PSII) at 2.9−3.5 Å have revealed the presence of possible channels for the removal of protons from the catalytic Mn_4Ca cluster during the water-splitting reaction. As an initial attempt to verify these channels experimentally, the presence of a network of hydrogen bonds near the Mn_4Ca cluster was probed with FTIR difference spectroscopy in a spectral region sensitive to the protonation states of carboxylate residues and, in particular, with a negative band at 1747 cm^{-1} that is often observed in the S_2-*minus*-S_1 FTIR difference spectrum of PSII from the cyanobacterium Synechocystis sp. PCC 6803. On the basis of its 4 cm^{-1} downshift in D_2O, this band was assigned to the carbonyl stretching vibration (C═O) of a protonated carboxylate group whose pK_a decreases during the S_1 to S_2 transition. The positive charge that forms on the Mn_4Ca cluster during the S_1 to S_2 transition presumably causes structural perturbations that are transmitted to this carboxylate group via electrostatic interactions and/or an extended network of hydrogen bonds. In an attempt to identify the carboxylate group that gives rise to this band, the FTIR difference spectra of PSII core complexes from the mutants D1-Asp61Ala, D1-Glu65Ala, D1-Glu329Gln, and D2-Glu312Ala were examined. In the x-ray crystallographic models, these are the closest carboxylate residues to the Mn_4Ca cluster that do not ligate Mn or Ca and all are highly conserved. The 1747 cm^{-1} band is present in the S_2-*minus*-S_1 FTIR difference spectrum of

D1-Asp61Ala but absent from the corresponding spectra of D1-Glu65Ala, D2-Glu312Ala, and D1-Glu329Gln. The band is also sharply diminished in magnitude in the wild type when samples are maintained at a relative humidity of ≤85%. It is proposed that D1-Glu65, D2-Glu312, and D1-Glu329 participate in a common network of hydrogen bonds that includes water molecules and the carboxylate group that gives rise to the 1747 cm^{-1} band. It is further proposed that the mutation of any of these three residues, or partial dehydration caused by maintaining samples at a relative humidity of ≤85%, disrupts the network sufficiently that the structural perturbations associated with the S_1 to S_2 transition are no longer transmitted to the carboxylate group that gives rise to the 1747 cm^{-1} band. Because D1-Glu329 is located approximately 20 Å from D1-Glu65 and D2-Glu312, the postulated network of hydrogen bonds must extend for at least 20 Å across the lumenal face of the Mn_4Ca cluster. The D1-Asp61Ala, D1-Glu65Ala, and D2-Glu312Ala mutations also appear to substantially decrease the fraction of PSII reaction centers that undergo the S_3 to S_0 transition in response to a saturating flash. This behavior is consistent with D1-Asp61, D1-Glu65, and D2-Glu312 participating in a dominant proton egress channel that links the Mn_4Ca cluster with the thylakoid lumen.

3.2 Introduction

The light-driven oxidation of water in photosystem II (PSII)[1] produces nearly all of the O_2 on Earth and drives the production of nearly all of its biomass. Photosystem II is an integral membrane protein complex that is located in the thylakoid membranes of plants, algae, and

[1] Abbreviations: Chl, chlorophyll; EDTA, ethylenediaminetetraacetic acid; EPR, electron paramagnetic resonance; EXAFS, extended x-ray absorption fine structure; FTIR, Fourier transform infrared; MES, 2-(N-morpholino)ethanesulfonic acide; NTA, nitrolotriacetic acide; P680, chlorophyll multimer that serves as the light-indunced electron donor in PSII; Pheo, pheophytin; PSII, photosystem II; Q_A, primary plastoquinone electron acceptor; Q_B secondary plastoquinone electron acceptor; RH, relative humidity; XANES, x-ray absorption near edge structure; Y_Z, tyrosine residue that mediates electron transfer between the Mn_4Ca cluster and $P^{680+\bullet}$; Y_D, second tyrosine residue that can reduce $P^{680+\bullet}$ in PSII.

cyanobacteria. It is a homodimer in vivo, having a total molecular mass of >700 kDa. Each monomer consists of at least 20 different subunits and contains more than 60 organic and inorganic cofactors, including 35 Chl a and 12 carotenoid molecules. Each monomer's primary subunits include the membrane spanning polypeptides CP47 (56 kDa), CP43 (52 kDa), D2 (39 kDa), and D1 (38 kDa) and the extrinsic polypeptide PsbO (26.8 kDa). The D1 and D2 polypeptides are homologous and together form a heterodimer at the core of each monomer. Within each monomer, the CP47 and CP43 polypeptides are located on either side of the D1−D2 heterodimer and serve to transfer excitation energy from the peripherally located antenna complex to the D1−D2 heterodimer, and specifically to the photochemically active Chl a multimer known as P_{680} (1-6).

The O_2-evolving catalytic site consists of a pentanuclear metal cluster containing four Mn ions and one Ca ion. The Mn_4Ca cluster accumulates oxidizing equivalents in response to photochemical events within PSII and then catalyzes the oxidation of two molecules of water, releasing one molecule of O_2 as a byproduct (7-11). The Mn_4Ca cluster serves as the interface between single-electron photochemistry and the four-electron process of water oxidation. The photochemical events that precede water oxidation take place in the D1−D2 heterodimer. These events are initiated by the transfer of excitation energy to P_{680} following capture of light energy by the antenna complex. Excitation of P_{680} results in the formation of the charge-separated state, $P_{680}^{\bullet+}Pheo^{\bullet-}$. This light-induced separation of charge is stabilized by the rapid oxidation of $Pheo^{\bullet-}$ by Q_A, the primary plastoquinone electron acceptor, and by the rapid reduction of $P_{680}^{\bullet+}$ by Y_Z, one of two redox-active tyrosine residues in PSII. The resulting $Y_Z^{\bullet}$ radical in turn oxidizes the Mn_4Ca cluster, while $Q_A^{\bullet-}$ reduces the secondary plastoquinone, Q_B. Subsequent charge separations result in further oxidation of the Mn_4Ca cluster and in the two-electron reduction and protonation of Q_B to form plastoquinol, which subsequently exchanges into the membrane-bound

plastoquinone pool. During each catalytic cycle, two molecules of plastoquinol are produced at the Q_B site and the Mn_4Ca cluster cycles through five oxidation states termed S_n, where n denotes the number of oxidizing equivalents that are stored (n = 0−4). The S_1 state predominates in dark-adapted samples. Most interpretations of Mn-XANES data have concluded that the S_1 state consists of two Mn(III) and two Mn(IV) ions and that the S_2 state consists of one Mn(III) and three Mn(IV) ions (11-14). The S_4 state is a transient intermediate. Its formation triggers the rapid oxidation of the two substrate water molecules, the regeneration of the S_0 state, and the release of O_2.

Refined x-ray crystallographic structural models of PSII are available at 3.5 (1), 3.0 (2), and 2.9 Å (5) (although the 2.9 Å structural model was developed by reprocessing the data used for the 3.0 Å model). These models, and less complete models at somewhat lower resolutions (15, 16), provide views of the Mn_4Ca cluster and its ligation environment, including one or two catalytically essential Cl^- ions that are located 6−7 Å distant. However, there are significant differences between these views. For example, in the 2.9 and 3.0 Å structural models, most carboxylate ligands are bidentate and the α-COO^- group of D1-Ala344 (the C-terminus of the D1 polypeptide) ligates the Mn_4Ca cluster, whereas in the 3.5 Å structural model, most carboxylate ligands are unidentate and the α-COO^- group of D1-Ala344 ligates no metal ion. One reason for these differences is that the resolutions of the diffraction data are limited. A second reason is that the Mn(III/IV) ions of the Mn_4Ca cluster were undoubtedly reduced by x-ray-generated radicals to their fully reduced Mn(II) oxidation states during collection of the x-ray diffraction data (17, 18). This reduction would have disrupted the cluster's Mn−O−Mn bridging moieties and altered Mn−ligand interactions. Consequently, the structures of the Mn_4Ca cluster depicted in the s-ray crystallographic models represent unknown superimpositions of native and disrupted Mn_4Ca clusters, with the metal ions in the latter being retained in the vicinity of their native positions by

virtue of the crystals being kept frozen at 100 K during data collection. Importantly, none of the crystallographic structural models is fully compatible with polarized EXAFS studies of single crystals of PSII that were conducted with low x-ray fluxes that minimize photoreduction of the Mn ions (19). The low-radiation flux studies must be reconciled with future x-ray crystallographic studies. Nevertheless, the existing crystallographic studies agree with each other, and with the earlier mutagenesis studies (20), on the identity of most of the Mn_4Ca cluster's amino acid ligands. Furthermore, the structure of PSII outside the immediate environment of the Mn_4Ca cluster should be largely unaffected by the radiation-induced reduction of the cluster's Mn ions. Consequently, the existing crystallographic structural models are serving as valuable guides for spectroscopic studies designed to provide insight into the structure, dynamics, and mechanism of the Mn_4Ca cluster throughout its catalytic cycle.

To satisfy the very severe energetic and mechanistic constraints of oxidizing water, the Mn_4Ca cluster's reactivity in each of its oxidation states is tightly controlled by its protein environment. The amino acid residues in this environment choreograph the proton and electron reactions associated with water oxidation and play important roles in the delivery of substrate water and the release of O_2 and protons. In particular, these residues minimize the energetic requirements for water oxidation by coupling the requisite proton and electron extraction reactions (7, 13, 21, 22), minimize deleterious side reactions by preventing unregulated access of water to the Mn_4Ca catalyst (23), and minimize oxidative damage by promoting rapid egress of newly formed O_2 (24). For example, the deprotonation of CP43-Arg357 or D1-Asp61 to the thylakoid lumen has been proposed to provide the thermodynamic driving force for oxidizing the Mn_4Ca cluster in its higher oxidation states (7, 13, 21, 22, 25-28). Deprotonation is envisioned to take place via one or more proton egress pathways or "channels". Several possible channels for water access, O_2 egress, and proton egress have been identified in the current crystallographic

structural models on the basis of visual examinations (1, 29-31), electrostatic calculations (32), solvent accessibility simulations (33), cavity searching algorithms (5, 34, 35), and molecular dynamics simulations of water diffusion (36). In the 2.9 Å structural model, nine discrete channels have been identified on the basis of cavity searching algorithms, including four attributed to water access or O_2 egress channels and five attributed to proton egress channels (5, 35). These predicted channels are presumably dynamic in nature and presumably contain extensive networks of hydrogen-bonded amino acid side chains and water molecules. Our goal is to employ FTIR difference spectroscopy to further delineate the proton egress pathways leading from the Mn_4Ca cluster to the lumen and to determine if multiple pathways are active or if a single pathway dominates. Such a situation prevails in reaction centers of Rhodobacter sphaeroides, where a single proton entry point and a single proton access channel dominate the transfer of protons to the Q_B site (37-39).

FTIR difference spectroscopy is an extremely sensitive tool for characterizing the dynamic structural changes that occur during an enzyme's catalytic cycle (40-44). It is particularly suited for analyzing protonation−deprotonation reactions, pK_a shifts, and changes in hydrogen-bonded structures in proteins. The carbonyl stretching mode [ν(C═O)] of a protonated carboxylate residue appears between 1770 and 1700 cm^{-1}, a region where no other protein bands occur. The actual frequency of this mode depends on the number and strengths of hydrogen bonds involving this group (45-49). The O−H stretching frequency of weakly hydrogen bonded O−H groups appears between 3700 and 3500 cm^{-1} (50-52), the O−D stretching frequency of weakly deuteron-bonded O−D groups between 2600 and 2200 cm^{-1} (51), and the D−O−D bending region of D_2O molecules between 1250 and 1150 cm^{-1} (53, 54), also in a region mostly devoid of other protein vibrational modes. This mode is also sensitive to hydrogen (deuteron) bonding and disappears upon deprotonation, making it particularly suitable for monitoring proton release

reactions. Changes in the hydrogen bonding status of amino acid residues and water molecules participating in putative water access or proton egress pathways can be monitored at these easily accessible frequencies.

In PSII, numerous vibrational modes are altered in frequency as the Mn_4Ca cluster is oxidized through the S-state cycle, including many modes that can be attributed to carboxylate residues and hydrogen-bonded water molecules (55-57). In this study, on the basis of the presence or absence of the ν(C═O) mode of a protonated carboxylate group in the S_2-*minus*-S_1 FTIR difference spectrum, we present evidence that residues D1-Glu65, D1-Glu329, and D2-Glu312 participate in a hydrogen-bonded network that extends at least 20 Å across the lumenal face of the Mn_4Ca cluster. This network presumably also includes D1-Asp61. The D1-D61A, D1-E65A, and D2-E312A mutations were also found to substantially decrease the fraction of PSII reaction centers that undergo the S_3 to S_0 transition in response to a saturating flash. Consequently, the hydrogen-bonded network that includes D1-Asp61, D1-Glu65, D2-Glu312, and D1-Glu329 may comprise part of a dominant proton egress pathway leading from the Mn_4Ca cluster to the thylakoid lumen. The participation of D1-Asp61, D1-Glu65, and D2-Glu312 in such a pathway has been proposed previously (1, 5, 32-35), but the participation of D1-Glu329 in the same network is unexpected because it is located far from any proposed proton egress channel.

3.3 Materials and Methods

Construction of Mutants and Propagation of Cultures

The D1-D61A, D1-E65A, and D1-E329Q mutations were constructed in the psbA-2 gene of Synechocystis sp. PCC 6803 (58) and transformed into a host strain of Synechocystis that lacks all three psbA genes and contains a hexahistidine tag (His tag) fused to the C-terminus of CP47 (59). Single colonies were selected for their ability to grow on solid media containing 5 μg/mL

kanamycin monosulfate. The D2-E312A mutation was constructed in the psbD-1 gene of Synechocystis sp. PCC 6803 (60) and transformed into a host strain of Synechocystis that lacks both psbD genes and contains a hexahistidine tag (His tag) fused to the C-terminus of CP47 (59). Single colonies were also selected for their ability to grow on solid media containing 5 μg/mL kanamycin monosulfate. Solid media contained 5 mM glucose and 10 μM DCMU. The DCMU and antibiotic were omitted from the liquid cultures. Large-scale liquid cultures (each consisting of three 7 L cultures held in glass carboys) were propagated as described previously (61). To verify the integrity of the mutant cultures that were harvested for the purification of PSII core complexes, an aliquot of each culture was set aside and the sequence of the relevant portions of the psbA-2 or psbD-1 gene was obtained after PCR amplification of genomic DNA (58).

Purification of PSII Core Complexes

Oxygen-evolving PSII core complexes were purified under dim green light at 4 °C with Ni-NTA superflow affinity resin (Qiagen, Valencia, CA) as described previously (62). The purification buffer consisted of 1.2 M betaine, 10% (v/v) glycerol, 50 mM MES-NaOH (pH 6.0), 20 mM $CaCl_2$, 5 mM $MgCl_2$, 50 mM histidine, 1 mM EDTA, and 0.03% (w/v) n-dodecyl β-d-maltoside. The purified PSII core complexes were concentrated to ~1.0 mg of Chl/mL by ultrafiltration, frozen in liquid N_2, and stored at −196 °C (vapor phase nitrogen).

Preparation of FTIR Samples

All manipulations were conducted under dim green light at 4 °C. Samples (approximately 70 μg of Chl a) were exchanged into FTIR analysis buffer [40 mM sucrose, 10 mM MES-NaOH (pH 6.0), 5 mM $CaCl_2$, 5 mM NaCl, and 0.06% (w/v) n-dodecyl β-d-maltoside (63, 64)] by passage through a centrifugal gel filtration column at 27g (65). Concentrated samples (approximately 10 μL in volume) were mixed with $^1/_{10}$ volume of fresh 100 mM potassium ferricyanide (dissolved in water), spread to a diameter of ~10 mm on a 15 mm diameter BaF_2

window, and then dried lightly (until tacky) under a stream of dry nitrogen gas. To maintain the humidity of the sample in the FTIR cryostat, 1 μL of a solution of glycerol in water was spotted onto the window, adjacent to the sample, but not touching it (66). For most experiments, 1 μL of 20% (v/v) glycerol was employed to maintain the samples at 99% RH. For the experiments depicted in Figure 1A, lower relative humidities were obtained with an increase in the concentration of glycerol in the 1 μL droplet [e.g., 40, 50, and 60% (v/v) glycerol for 95, 85, and 73% RH, respectively (66)]. A second IR window with a Teflon spacer (0.5 mm thick) was placed over the first and sealed in place with silicon-free high-vacuum grease. The sample was immediately loaded into the FTIR cryostat and allowed to equilibrate to 273.0 K in darkness for 2 h. Sample concentrations and thicknesses were adjusted so that the absolute absorbance of the amide I band at 1657 cm^{-1} was 0.8−1.2. For the experiments depicted in Figure 1B, the FTIR analysis buffer and the potassium ferricyanide and glycerol solutions were prepared with D_2O (99.9% enrichment, Cambridge Isotope Laboratories, Andover, MA). The pD of the FTIR analysis buffer prepared in D_2O was adjusted with freshly opened NaOD (99.5% enrichment, Cambridge Isotope Laboratories). The pD value was obtained by addition of 0.40 to the pH meter reading (67, 68).

Measurement of FTIR Spectra

Midfrequency FTIR spectra were recorded with a Bruker Equinox 55 spectrometer (Bruker Optics, Billerica, MA) at a spectral resolution of 4 cm^{-1} as described previously (61, 64, 65). Flash illumination (~20 mJ/flash, ~7 ns fwhm) was provided by a frequency-doubled Q-switched Nd:YAG laser [Surelite I (Continuum, Santa Clara, CA)]. For the experiments depicted in Figure 1, a single flash was applied after dark adaptation. Two single-beam spectra were recorded before the flash, and one single-beam spectrum was recorded starting 0.33 s after the flash (each single-beam spectrum consisted of 200 scans). The 0.33 s delay was incorporated to

allow for the oxidation of $Q_A^{\bullet-}$ by the ferricyanide. To obtain a difference spectrum, the spectrum that was recorded after the flash was divided by the spectrum that was recorded immediately before the flash and the ratio was converted to units of absorption. To estimate the background noise level, the second preflash spectrum was divided by the first and the ratio was converted to units of absorption. The sample was dark-adapted for 30 min, and then the measurement cycle was repeated. Each sample was subjected to a total of 16−18 measurement cycles. The difference spectra recorded with several samples were averaged. For the experiments depicted in Figures 2−6, one preflash was applied after dark adaptation and followed by dark adaptation for an additional 5 min. This treatment was employed to oxidize Y_D and to maximize the proportion of PSII reaction centers in the S_1 state. Six successive flashes then were applied with an interval of 12.2 s between each. Two single-beam spectra were recorded before the first flash, and one single-beam spectrum was recorded starting 0.33 s after the first and subsequent flashes (each single-beam spectrum consisted of 100 scans). To obtain difference spectra corresponding to successive S-state transitions, the spectrum that was recorded after the nth flash was divided by the spectrum that was recorded immediately before the nth flash and the ratio was converted to units of absorption. To estimate the background noise level, the second preflash spectrum was divided by the first and the ratio was converted to units of absorption. The sample was dark-adapted for 30 min, and then the entire cycle was repeated, including the preflash and the 5 min additional dark adaptation period. The entire cycle was repeated 12 times for each sample, and the difference spectra recorded for several samples were averaged.

Other Procedures

Chlorophyll concentrations and light-saturated, steady state rates of O_2 evolution were measured as described previously (69).

3.4 Results

Wild-type PSII core complexes from the cyanobacterium Synechocystis sp. PCC 6803 frequently exhibit a negative band at 1747 cm^{-1} in the S_2-*minus*-S_1 FTIR difference spectrum (61, 64, 65, 70, 71) (Figure 1A, black trace). In this study, this band was altered or eliminated by a number of mutations of highly conserved carboxylate residues in the D1 and D2 polypeptides of Synechocystis 6803. The 1790−1710 cm^{-1} region contains the C═O carbonyl stretching mode [ν(C═O)] of protonated carboxylate residues (42, 43, 72) and also the keto and ester C═O vibrations of chlorophyll, pheophytin, heme, and lipids (73). In carboxylic acids, the C═O stretching and C−O−H bending modes of the COOH group are weakly coupled. This coupling is removed by deuteration, causing the ν(C═O) mode to downshift by 4−20 cm^{-1} (45, 47-49, 72). Accordingly, to test whether the 1747 cm^{-1} band corresponds to the ν(C═O) mode of a protonated carboxylate residue, the S_2-*minus*-S_1 FTIR difference spectra of wild-type PSII core complexes was obtained after exchange into buffer containing D_2O (Figure 1B). In D_2O, the 1747 cm^{-1} mode appeared at 1743 cm^{-1}, a downshift of 4 cm^{-1}. Therefore, we attribute it to the ν(C═O) mode of a protonated carboxylate residue whose environment changes during the S_1 to S_2 transition (see Discussion).

The negative (C═O) band at 1747 cm^{-1} is not observed in PSII core complexes from Thermosynechococcus elongatus (51, 66, 74-76) or PSII membranes from spinach (77-80). Nevertheless, we observe this feature consistently in PSII core complexes from Synechocystis sp. PCC 6803 when the samples are maintained at relative humidities of 99% (61, 62, 64, 65, 69) (Figure 1A, black trace) or 95% (not shown). The band has also been observed by others in PSII core complexes purified from the same organism (70). In this study, the amplitude of the 1747 cm^{-1} band was diminished substantially at relative humidities of 85% (Figure 1A, blue trace),

73% (not shown), or lower [i.e., when a dry film was placed in the sample cell (Figure 1A, red trace)]. Evidently, the degree of sample hydration is an important factor in the manifestation of this band. Interestingly, whereas other bands in the S_2-*minus*-S_1 FTIR difference spectrum are sensitive to the degree of sample hydration, none is altered as dramatically at the 1747 cm^{-1} band and many are relatively unperturbed by changes in the sample's relative humidity (see below).

Exchange into D_2O induced additional alterations to the wild-type S_2-*minus*-S_1 FTIR difference spectrum (Figure 1B). The D_2O-induced alterations between 1700 and 1500 cm^{-1} resemble those reported previously in PSII membranes from spinach (78) and PSII core complexes from T. elongatus (51). The apparent upshift of a negative band from 1561 to 1578 cm^{-1} was previously attributed to a D_2O-induced shift of the $\nu_{asym}(COO^-)$ mode of a carboxylate residue that accepts a strong hydrogen bond from a Mn-bound water molecule (78). The D_2O-induced alterations to the amide I region, including the appearance of a positive band at 1636 cm^{-1}, were previously attributed to D_2O-induced changes in stretches of polypeptide having random coil conformations (78). The apparent upshift of the large positive feature from 1587 to 1593 cm^{-1} is consistent with the D_2O-induced upshift of the $\nu_{asym}(COO^-)$ mode of another hydrogen-bonded carboxylate residue (78). The feature has been assigned to a $\nu_{asym}(COO^-)$ mode because it downshifts by 30−35 cm^{-1} after global incorporation of ^{13}C (63, 74, 81, 82) but is largely insensitive to global incorporation of ^{15}N (63, 74, 82).

When the samples were maintained at a relative humidity of ≤85%, spectral alterations were present throughout the overlapping amide II/$\nu_{asym}(COO^-)$ region and in the amide I region, whereas few alterations were present elsewhere (except near 1747 cm^{-1}, as described earlier). Some of the largest alterations were to the 1551(+), 1543(−), 1531(+), and 1522(−) cm^{-1} bands, whose amplitudes decreased substantially. The 1551(+) and 1543(−) cm^{-1} bands were assigned previously to amide II modes because both downshift by 11−20 cm^{-1} after global incorporation of

^{13}C or ^{15}N (63, 74, 78, 81, 82). The 1531(+) and 1522(−) cm^{-1} bands downshift similarly (63, 74, 78, 81, 82) and presumably can also be assigned to amide II modes. The magnitude of a positive band at 1622 cm^{-1} also diminished substantially. This band downshifts significantly after global incorporation of ^{13}C (63, 82), but not appreciably after global incorporation of ^{15}N (63, 82), thereby identifying it as an amide I mode.

The D1-E239Q (83) and D2-E312A mutants examined in this study were photoautotrophic, whereas the D1-D61A and D1-E65A cells (84) were only weakly so. The O_2 evolving activity of D2-E312A cells was 330−380 μmol of O_2 (mg of Chl)$^{-1}$ h^{-1} compared to 500−580 μmol of O_2 (μg of Chl)$^{-1}$ h^{-1} for wild-type cells (i.e., 60−70% compared to that of the wild type). The O_2 evolving activities of D1-D61A, D1-E65A, and D1-E329Q cells have been reported previously to be ~19, ~21, and ~100% of the wild-type value, respectively (83, 84). The O_2 evolving activities of the D1-D61A, D1-E65A, D1-E329Q, and D2-E312A PSII core particles examined in this study were ~870, ~730, ~3340, and ~1380 μmol of O_2 (mg of Chl)$^{-1}$ h^{-1}, respectively, compared to 4900−5400 μmol of O_2 (mg of Chl)$^{-1}$ h^{-1} for the wild type. The O_2 evolving activity of the D1-D61A PSII core complexes (~17% of that of the wild type) correlated with the lower O_2 evolving activity of D1-D61A cells, but the O_2 evolving activities of the D1-E65A, D1-E329Q, and D2-E312A PSII core complexes (~14, ~65, and ~27%, respectively, of that of the wild type) were lower than in intact cells, suggesting either that the Mn_4Ca clusters in D1-E65A, D1-E329Q, and D2-E312A cells are less stable than those in the wild type or that the S-state transitions proceed less efficiently in PSII core complexes purified from these mutants than in intact cells.

The midfrequency FTIR difference spectra of wild-type and D1-D61A PSII core complexes that were induced by four successive flashes are compared in Figure 2 (black and red spectra, respectively). The spectra that were induced by the first, second, third, and fourth flashes

given to the wild-type PSII core complexes correspond predominantly to the S_2-*minus*-S_1, S_3-*minus*-S_2, S_0-*minus*-S_3, and S_1-*minus*-S_0 FTIR difference spectra, respectively. These spectra closely resemble the S_{n+1}-*minus*-S_n difference spectra that have been reported previously for wild-type PSII core complexes from Synechocystis sp. PCC 6803 (61, 63-65, 85). The S_2-*minus*-S_1 FTIR difference spectrum of D1-D61A PSII core complexes (top red trace in Figure 2) showed substantial differences from the wild-type spectrum throughout the overlapping amide II/$\nu_{asym}(COO^-)$ region. As was the case with partly dehydrated samples (Figure 1A), the magnitudes of the bands at 1552(+), 1543(−), 1531(+), and 1522(−) cm^{-1} were diminished substantially. The magnitudes of positive bands at 1635, 1622, 1587, and 1509 cm^{-1} were also diminished substantially, with the 1587 cm^{-1} band being downshifted to 1583 cm^{-1} and the 1509 cm^{-1} band being upshifted to 1512 cm^{-1}. The 1635 and 1622 cm^{-1} bands can be identified as amide I modes because both downshift significantly after global incorporation of ^{13}C (63, 82), but not appreciably after global incorporation of ^{15}N (63, 82). The 1552(+), 1543(−), 1531(+), and 1522(−) cm^{-1} bands can be identified as amide II modes because all four bands downshift appreciably after global incorporation of ^{13}C (63, 74, 81, 82) or ^{15}N (63, 74, 82). Similarly, the 1587 cm^{-1} band was previously assigned to a $\nu_{asym}(COO^-)$ mode because it downshifts by 30−35 cm^{-1} after global incorporation of ^{13}C (63, 74, 81, 82) but is largely insensitive to the global incorporation of ^{15}N (63, 74, 82). The 1509 cm^{-1} band appears to consist of overlapping amide II and $\nu_{asym}(COO^-)$ modes (63, 74, 82). Of particular importance to this study is the fact that the negative band at 1747 cm^{-1} was unaffected by the D1-D61A mutation.

The FTIR difference spectrum induced by the second flash applied to D1-D61A PSII core complexes contained some of the features that are present in the S_2-*minus*-S_1 FTIR difference spectra of the wild type (compare the top two sets of black and red traces in Figure 2). These include bands at 1543(−), 1510(+), 1399(−), and 1365(+) cm^{-1}. The presence of these

bands shows that a significant fraction of D1-D61A PSII reaction centers failed to undergo the S_2 to S_3 transition following the second flash.

The FTIR difference spectra induced by the third and fourth flashes applied to D1-D61A PSII core complexes were practically devoid of features (bottom two red traces in Figure 2). Typically, spectral features that appear during the S_1 to S_2 and S_2 to S_3 transitions in wild-type PSII are reversed during the S_3 to S_0 and S_0 to S_1 transitions (55-57). If large fractions of PSII reaction centers fail to advance between S-states in response to saturating flashes, PSII reaction centers that undergo the S_3 to S_0 or S_0 to S_1 transition after the third or fourth flash, respectively, may have their spectral features canceled by PSII reaction centers undergoing the S_1 to S_2 or S_2 to S_3 transition after these flashes. The absence of clear, distinct peaks after the third and fourth flashes in D1-D61A PSII core complexes shows that a large fraction of D1-D61A PSII core complexes failed to advance beyond the S_3 state in response to the these flashes.

The midfrequency FTIR difference spectra of wild-type and D1-E65A PSII core complexes that were induced by four successive flash illuminations are compared in Figure 3 (black and red spectra, respectively). The S_2-*minus*-S_1 FTIR difference spectrum of D1-E65A PSII core complexes (top red trace in Figure 3) showed substantial differences from the wild-type spectrum throughout the overlapping amide II/$\nu_{asym}(COO^-)$ region. As was the case with D1-D61A PSII core complexes, the magnitudes of the positive bands at 1622 and 1552 cm^{-1} and the negative band at 1543 cm^{-1} were diminished substantially. As noted above, the 1622 cm^{-1} band corresponds to an amide I mode and the 1552 and 1543 cm^{-1} bands correspond to amide II modes. Of particular importance to this study is the fact that the negative band at 1747 cm^{-1} in the S_2-*minus*-S_1 FTIR difference spectrum of wild-type PSII core complexes was eliminated by the D1-E65A mutation (compare the top traces in Figure 3).

The FTIR difference spectrum induced by the second flash applied to D1-E65A PSII core complexes contained some of the features present in the S_2-*minus*-S_1 FTIR difference spectra of the wild type (compare the top two sets of black and red traces in Figure 3). These include bands at 1544(−), 1506(+), 1398(−), and 1373(+) cm^{-1}. The presence of these bands shows that a significant fraction of D1-E65A PSII reaction centers failed to undergo the S_2 to S_3 transition following the second flash. As was observed with D1-D61A, the spectra induced by the third and fourth flashes applied to D1-E65A PSII core complexes are nearly devoid of features (bottom two red traces in Figure 3). Evidently, as was the case with D1-D61A, a large fraction of D1-E65A PSII core complexes fail to advance beyond the S_3 state in response to saturating flashes.

The midfrequency FTIR difference spectrum of D2-E312A PSII core complexes that was induced by the first of six successive flash illuminations is shown in Figure 4 (red spectrum). The presence of a large derivative feature at 1706(−)/1699(+) cm^{-1} suggests that the D2-E312A PSII core complexes contain a significant fraction of PSII reaction centers that lack Mn_4Ca clusters (61). The spectrum of Mn-depleted wild-type PSII core complexes obtained under conditions identical to those described in ref 61 is shown for comparison (Figure 4, black trace). This spectrum corresponds to the $Y_Z^{\bullet}$-*minus*-Y_Z FTIR difference spectrum in Synechocystis sp. PCC 6803, whose primary features are positive peaks at 1699, 1677, 1651, 1550, 1521, and 1512 cm^{-1} and negative peaks at 1706, 1624, 1453, and 1250 cm^{-1} (86). To estimate the fraction of Mn-depleted PSII reaction centers in the D2-E312A PSII core complexes, the amplitudes of the negative 1706 cm^{-1} band in intact wild-type, Mn-depleted wild-type, and D2-E312A PSII core complexes were compared after normalization of all three spectra to the peak to peak amplitudes of the negative ferricyanide band at 2115 cm^{-1} and the positive ferrocyanide band at 2038 cm^{-1} (i.e., the spectra were normalized to the extent of flash-induced charge separation in each sample, as determined from the reduction of ferricyanide to ferricyanide by $Q_A^{\bullet-}$). On this basis, assuming

that 0% of intact and 100% of Mn-depleted wild-type PSII core complexes lack Mn_4Ca clusters, we estimated that ≈31% of D2-E312A PSII core complexes lack Mn_4Ca clusters (presumably the Mn_4Ca clusters in D2-E312A cells are less stable than those in wild-type cells, despite the cluster's distance from D2-Glu312). Accordingly, we corrected the first flash spectrum of the D2-E312A PSII core complexes by subtracting from it 31% of the spectrum of Mn-depleted wild-type PSII (61). No correction was applied to the second, third, or fourth flash spectra because Mn-depleted PSII makes no significant contribution to these spectra (61).

The midfrequency FTIR difference spectra of wild-type and D2-E312A PSII core complexes that were induced by four successive flash illuminations are compared in Figure 5 (black and red spectra, respectively). The corrected S_2-*minus*-S_1 FTIR difference spectrum of D1-E312A PSII core complexes (top red trace in Figure 5) showed substantial differences from the wild-type spectrum throughout the overlapping amide II/$\nu_{asym}(COO^-)$ region. As was the case with D1-D61A PSII core complexes, the magnitudes of the bands at 1543(−), 1532(+), and 1523(−) cm^{-1} were diminished substantially. As noted earlier, the 1543(−) and 1532(+) cm^{-1} bands can be identified as amide II modes on the basis of global labeling experiments. Other changes include increased amplitudes of bands at 1674, 1652, and 1637 cm^{-1} in the amide I region, a slight downshift of the positive band at 1622 cm^{-1} [assigned to an amide I mode (see above)], and changes to amplitudes of bands in the symmetric carboxylate stretching region, including decreased amplitudes of positive bands at 1442, 1366, and 1342 cm^{-1} and an increased amplitude of the negative band at 1400 cm^{-1}. Of particular importance to this study is the fact that the negative band at 1747 cm^{-1} in the S_2-*minus*-S_1 FTIR difference spectrum of wild-type PSII core complexes was eliminated by the D1-E312A mutation (compare the top traces in Figure 5).

The FTIR difference spectrum induced by the second flash applied to D2-E312A PSII core complexes contained some of the features present in the S_2-*minus*-S_1 FTIR difference spectra

of the wild type (compare the top two sets of black and red traces in Figure 5). These include bands at 1542(−), 1510(+), 1397(−), and 1372(+) cm^{-1}. The presence of these bands shows that a significant fraction of D2-E312A PSII reaction centers failed to undergo the S_2 to S_3 transition following the second flash. As was the case with D1-D61A and D1-E65A, the spectra induced by the third and fourth flashes applied to D1-E312A PSII core complexes were nearly devoid of features (bottom two red traces in Figure 5). Evidently, as was the case with D1-D61A and D1-E65A, a large fraction of D2-E312A PSII core complexes failed to advance beyond the S_3 state in response to these flashes.

The midfrequency FTIR difference spectra of wild-type and D1-E329Q PSII core complexes that were induced by four successive flash illuminations are compared in Figure 6 (black and red spectra, respectively). The S_2-*minus*-S_1 FTIR difference spectrum of D1-E329Q PSII core complexes (top red trace in Figure 6) showed many fewer differences from the wild-type spectrum than the other mutants. The differences included decreased amplitudes of bands at 1543(−), 1442(+), 1342(+), and 1220(+) cm^{-1} and increased amplitudes of bands at 1651(+), 1635(+), 1398(−), and 1364(+) cm^{-1}. As indicated previously, the 1543(−) and 1635(+) cm^{-1} bands correspond to amide II and amide I modes, respectively. The 1442(+), 1364(+), and 1342(+) cm^{-1} bands correspond to $\nu_{sym}(COO^-)$ modes because they downshift by 20−45 cm^{-1} after global incorporation of ^{13}C (63, 74, 81, 82) but are largely insensitive to the global incorporation of ^{15}N (63, 74, 82).

The FTIR difference spectrum induced by the second flash given to D1-E329Q PSII core complexes contained some of the features present in the S_2-*minus*-S_1 FTIR difference spectra of wild-type PSII (compare the top two sets of black and red traces in Figure 6). These include bands at 1546(−), 1397(−), and 1373(+) cm^{-1}. The presence of these bands shows that a significant fraction of D1-E329Q PSII reaction centers failed to undergo the S_2 to S_3 transition

following the second flash. However, in contrast to the other mutants examined in this study, the FTIR difference spectra induced by the third and fourth flashes resembled those of wild-type PSII core complexes. The primary differences were the slightly diminished amplitudes of the 1544(+) and 1509(−) cm^{-1} bands in the S_0-*minus*-S_3 FTIR difference spectrum and the minor changes between 1667 and 1538 cm^{-1} in the S_1-*minus*-S_0 FTIR difference spectrum. Note the similarities between the S_0-*minus*-S_3 and S_1-*minus*-S_0 FTIR difference spectra of wild-type and D1-E329Q PSII core complexes between 1450 and 1350 cm^{-1} (compare the bottom two pairs of black and red traces in Figure 6). Evidently, D1-E329Q PSII core complexes advance relatively efficiently between S-states in response to saturating laser flashes, in marked contrast to the PSII core complexes of D1-D61A, D1-E65A, and D2-E312A. Of particular importance to this study is the fact that the negative band at 1747 cm^{-1} in the S_2-*minus*-S_1 FTIR difference spectrum of wild-type PSII core complexes was eliminated by the D1-E329Q mutation (compare the top traces in Figure 6).

It is noteworthy that the second flash spectra of D1-D61A, D1-E65A, D2-E312A, and D1-E329Q PSII core complexes resemble one another (Figures 2, 3, 5, and 6). All four mutant spectra show similar deviations from the wild-type S_3-*minus*-S_2 FTIR difference spectrum, including negative features at 1546−1542 and 1399−1397 cm^{-1} and positive features at 1510−1506 and 1373−1365 cm^{-1}. The similarities between the second flash spectra of all four mutants suggest that all four mutations decrease the efficiency of the S_2 to S_3 transition to similar extents. In contrast, the essentially featureless third and fourth flash spectra of D1-D61A, D1-E65A, and D2-E312A PSII core complexes show no resemblance to the third or fourth flash spectra of wild-type or D1-E329Q PSII core particles. Evidently, the D1-D61A, D1-E65A, and D2-E312A mutations decrease the efficiency of the S_3 to S_0 transition far more substantially than they decrease the efficiency of the S_2 to S_3 transition.

3.5 Discussion

One of the most striking results of the FTIR studies on PSII to date is the stunning insensitivity of the individual FTIR difference spectra to the mutation of at least three of the Mn_4Ca cluster's six putative carboxylate ligands. Not only do mutations of D1-Asp170 (64, 87), D1-Glu189 (65, 88), and D1-Asp342 (61) fail to eliminate any carboxylate vibrational stretching modes, they fail to produce significant changes in polypeptide backbone conformations as shown by the lack of significant mutation-induced alterations to the amide I and amide II regions of the spectra. This result was entirely unexpected. The individual FTIR difference spectra of wild-type PSII core complexes contain a wealth of spectral features. It had long been assumed that most of these features would correspond to amino acid residues that ligate the Mn_4Ca cluster. Whereas some of these features clearly correspond to first coordination sphere ligands [i.e., CP43-Glu354 (71, 85) and the α-COO^- group of D1-Ala344 (62, 69, 89)], the majority of these features evidently correspond to residues in the cluster's second coordination sphere and beyond. These features must reflect the response of the protein to the electrostatic influences that arise from the positive charge that develops on the Mn_4Ca cluster during the S_1 to S_2 transition and to the structural changes that are associated with the S_2 to S_3, S_3 to S_0, and S_0 to S_1 transitions.

The simplest explanation for the insensitivity of the S_2-*minus*-S_1 FTIR difference spectrum to the individual mutation of most the cluster's putative carboxylate ligands is that the positive charge that develops on the Mn_4Ca cluster during this transition is highly delocalized at ambient temperatures. There is ample precedent for such delocalization in mixed-valence inorganic metal complexes (90-92). Such delocalization would be consistent with a comparative inelastic x-ray scattering (RIXS) study of Mn oxides, Mn coordination complexes, and spinach PSII membranes (93). The authors of this study concluded that the electron that leaves the Mn_4Ca

cluster during the S_1 to S_2 transition originates from a highly delocalized orbital (93). Delocalization would also be consistent with QM/MM analyses that have been based on the 3.5 Å x-ray crystallographic structural model (7, 22, 27, 94). The authors of these studies concluded that the oxidation of the Mn_4Ca cluster during the S_1 to S_2 transition would cause little increase in the electrostatic charge of the individual Mn ions. In their analyses, the greatest increase in electrostatic charge during this transition is actually on the Ca ion. These authors also proposed that the α-COO^- group of D1-Ala344 is a unidentate ligand of Ca. However, a recent ^{13}C ENDOR study shows that this group ligates Mn (95) (ligation of both Mn and Ca is possible), consistent with the 3.0 and 2.9 Å crystallographic structural models (2, 5) and with an earlier FTIR study involving the replacement of Ca with Sr (62). The QM/MM analyses also predict that CP43-Glu354 ligates along the Jahn−Teller axis of a Mn(III) ion (7, 22, 27, 94). On the basis of recent FTIR studies, it has been proposed that CP43-Glu354 changes its coordination mode during the S_1 to S_2 transition (85) (but see ref 71) and that D1-Ala344 significantly changes its orientation (96). Consequently, the reason that both the $\nu_{sym}(COO^-)$ mode of D1-Ala344 (62, 69, 89) and the $\nu_{asym}(COO^-)$ mode of CP43-Glu354 (71, 85) shift during the S_1 to S_2 transition may be that the carboxylate group of one ligates along the Jahn−Teller axis of the Mn(III) ion that undergoes oxidation and the carboxylate group of the other changes its coordination mode or orientation.

Most of the Mn_4Ca cluster's putative carboxylate ligands appear to facilitate the cluster's assembly (97, 98) rather than regulate its function: D1-Asp170, D1-Glu189, and D1-Asp342 each can be replaced by at least one other amino acid that supports significant O_2 producing activity (20, 99-101). In contrast, residues in the Mn_4Ca cluster's second coordination sphere and beyond are postulated to play key roles in providing the driving force for oxidizing the cluster in its higher oxidation states and in regulating the access of substrate water. In particular, recent models postulate that CP43-Arg357 (or D1-Asp61) serves as a redox-activated catalytic base that

facilitates the oxidation of the Mn_4Ca cluster during the S_2 to S_3 and S_3 to S_4 transitions (7, 13, 21, 22, 25-28). In these models, when the Mn_4Ca cluster is in its S_2 or S_3 state, the formation of $Y_Z^{\bullet}$ triggers the deprotonation of CP43-Arg357 (or D1-Asp61) to the thylakoid lumen. Protonation to the lumen is necessary from energetic considerations (102). The subsequent oxidation of the Mn_4Ca cluster involves the simultaneous transfer of a proton from the Mn_4Ca cluster to the now deprotonated CP43-Arg357 (or D1-Asp61). In these models, the pK_a of CP43-Arg357 (or D1-Asp61) is decreased substantially by the presence of the positive charge on the $Y_Z^{\bullet}$/D1-His190 pair (hence, the formation of $Y_Z^{\bullet}$ triggers the residue's deprotonation). The pK_a value is restored when the charge on the $Y_Z^{\bullet}$/D1-His190 pair is neutralized by the transfer of an electron from the Mn_4Ca cluster to $Y_Z^{\bullet}$. Hence, the reprotonation of CP43-Arg357 (or D1-Asp61) is highly favored and provides a strong thermodynamic driving force for oxidizing the Mn_4Ca cluster in its higher oxidation states. The initial, $Y_Z^{\bullet}$-induced deprotonation of CP43-Arg357 (or D1-Asp61) requires its deprotonation to the lumen via a network of protonatable amino acid side chains and water molecules such as those envisaged to exist in the potential proton egress channels that have been identified in the x-ray crystallographic structural models (1, 5, 32-35). Kinetically efficient proton transfer through these channels requires finely tuned pK_a differences between key residues and transient formation of clusters of water molecules (102-105). Consequently, mutation of key residues in a dominant proton egress pathway would be expected to slow oxidation of the Mn_4Ca cluster in the same manner that mutations that impair proton uptake slow the transfer of an electron from $Q_A^{\bullet-}$ to $Q_B^{\bullet-}$ in reaction centers of Rhodobacter sphaeroides (37-39) and the reduction of O_2 to H_2O in cytochrome c oxidase (106-108). In support of their proposed roles in proton transfer, mutations of D1-Asp61 (109-111) and CP43-Arg357 (112, 113) slow oxidation of the Mn_4Ca cluster substantially during one or more of the S-state transitions.

As an initial attempt to verify the proposed proton egress channels in PSII experimentally, we have used the negative band at 1747 cm^{-1} in the wild-type S_2-*minus*-S_1 FTIR difference spectrum to probe for the presence of a network of hydrogen bonds near the Mn_4Ca cluster. Residues D1-Asp61, D1-Glu65, D2-Glu312, and D1-Glu329 are highly conserved and are the closest carboxylate residues to the Mn_4Ca cluster that do not ligate Mn or Ca (1, 2, 5). In the 2.9 Å crystallographic structural model, these residues are located 4.6, 10.8, 11.3, and 7.5 Å from the nearest Mn ion, respectively (5) (Figure 7). The peptide carbonyl of D1-Glu329 accepts a hydrogen bond from D1-His332, a putative Mn ligand. The side chain of D1-Glu329 has been proposed to participate in an O_2 egress channel (5, 35), while the side chains of D1-Asp61, D1-Glu65, and D2-Glu312 have been proposed to participate in a proton egress channel (1, 5, 32-35) with D1-Glu65 located at the channel's narrowest point (5, 35).

Our data show that the D1-D61A, D1-E65A, and D2-E312A mutations perturb the properties of the Mn_4Ca cluster far more than do mutations of the putative Mn ligands D1-Asp170, D1-Glu189, and D1-Asp342. The fraction of PSII reaction centers that advance through the S-state cycle in response to saturating flashes is substantially diminished in PSII core complexes from all three mutants (Figures 2, 3, and 5). In all three mutants, the efficiency of the S_2 to S_3 transition is lower than in the wild type and the efficiency of the S_3 to S_0 transition appears to be substantially lower. The latter point is best illustrated via comparison of the second and third flash spectra of D1-E329Q with the corresponding data of D1-D61A, D1-E65A, and D2-E312A. Whereas the efficiency of the S_2 to S_3 transition appears to be decreased to similar extents in all four mutants, the efficiency of the S_3 to S_0 transition is much lower in D1-D61A, D1-E65A, and D2-E312A than in D1-E329Q. In contrast, D1-D170H, D1-E189Q, D1-E189R, and D1-D342N PSII core complexes advance efficiently through the S-state cycle, with no apparent decrease in the efficiency of any S-state transition (61, 64, 65). A substantially

decreased efficiency for the S_3 to S_0 transition in D1-D61A PSII core complexes would be consistent with earlier data showing that the rate of O_2 release is slowed 8-fold in D1-D61A cells (109). The D1-D61N mutation also decreases the efficiency of the S-state transitions and slows the rate of O_2 release 10-fold (109). In D1-D61N PSII core complexes, the S_1 to S_2 and S_2 to S_3 transitions are slowed 2-fold (109) and the S_3 to S_0 transition is slowed 10-fold (110). A similar slowing of the S-state transitions is likely to occur in D1-D61A PSII core complexes and, by inference, in D1-E65A and D2-E312A PSII core complexes. Slowed oxidation of the Mn_4Ca cluster during the S-state transitions would be consistent with a role for all three residues in a dominant postulated proton egress pathway linking the Mn_4Ca cluster with the thylakoid lumen, such as those identified in analyses of the existing x-ray crystallographic structural models (1, 5, 32-35).

The S_2-*minus*-S_1 FTIR difference spectra of D1-D61A, D1-E65A, D2-E312A, and D1-E329Q PSII core complexes are altered far more than the corresponding spectra of D1-D170H, D1-E189Q, and D1-D342N PSII core complexes. Several amide II modes are altered substantially in the S_2-*minus*-S_1 FTIR difference spectra of D1-D61A, D1-E65A, and D2-E312A. These alterations show that these mutations alter the conformational rearrangements of the polypeptide backbone that normally accompany the S_1 to S_2 transition. Evidently, the D1-D61A, D1-E65A, and D2-E312A mutations substantially alter part of the protein's structural response to the increased charge that develops on the Mn_4Ca cluster during this transition. The D1-E329Q mutation evidently alters this response to a much lesser extent because only the negative amide II mode at 1543 cm^{-1} is affected significantly.

The primary focus of this study is on the negative band at 1747 cm^{-1}. This band is observed in the S_2-*minus*-S_1 FTIR difference spectrum of moderately hydrated wild-type PSII core complexes (Figure 8). This band is eliminated by partial dehydration (Figure 8A). It is also

eliminated by the D1-E65A, D2-E312A, and D1-E329Q mutations (Figure 8D−F). In contrast, it is unaltered by the D1-D61A mutation (Figure 8C). The elimination of this mode does not correlate with substantial changes in the protein's structural response to the S_1 to S_2 transition because it is present in D1-D61A and absent in D1-E329Q. In carboxylic acids, deuteration removes the weak coupling that exists between the C═O stretching and C−O−H bending modes of the COOH group, causing the ν(C═O) mode to downshift by 4−20 cm^{-1} (45, 47-49, 72). This D_2O-induced downshift is diagnostic for the ν(C═O) mode of protonated carboxylate residues and has been used as such in many systems, including bacteriorhodopsin (45, 114-117), rhodopsin (118, 119), bacterial reaction centers (120-123), heme-copper oxidases (124-127), and photoactive yellow protein (128). Exchange of wild-type PSII core complexes into buffer containing D_2O downshifted the 1747 cm^{-1} band by 4 cm^{-1} (Figure 8B). Deuteration-induced downshifts of 4 cm^{-1} have been reported previously for the ν(C═O) mode of Asp212 in bacteriorhodopsin (117), Glu L212 in bacterial reaction centers (121), and Glu278 in cytochrome c oxidase from Paracoccus denitrificans (124, 126) (also see ref 125). On the basis of its downshift in D_2O, we attribute the negative 1747 cm^{-1} band to the ν(C═O) mode of a protonated carboxylate residue whose environment changes during the S_1 to S_2 transition.

The frequency of the ν(C═O) mode of a carboxylic acid residue depends on the numbers and strengths of hydrogen bonds involving the C═O and O−H groups (45, 47-49, 72). Its appearance at 1747 cm^{-1} in wild-type PSII core complexes suggests that it participates in a single hydrogen bond that involves the C═O group (48, 49), although participation in two hydrogen bonds, with one involving the C−O−H oxygen, cannot be excluded (49). In an FTIR difference spectrum, the peak corresponding to the ν(C═O) mode of a carboxylic acid residue can change in a number of ways. Partial protonation (deprotonation) of an Asp or Glu residue gives rise to a single positive (negative) absorption band. Proton transfer between two Asp/Glu residues gives

rise to positive and negative bands of approximately equal amplitudes [assuming that the two ν(C═O) modes are well separated]. A change in the environment of a carboxylic acid causes the band to shift and gives rise to a differential band. The shape of the negative 1747 cm^{-1} peak in wild-type PSII core complexes suggests that a carboxylate residue partly deprotonates (i.e., its pK_a decreases) in response to the S_1 to S_2 transition. The partial depronation of this residue should increase the amplitudes of the $\nu_{asym}(COO^-)$ and $\nu_{sym}(COO^-)$ modes of the same residue in its carboxylate form. These modes should appear near 1580−1560 and 1400 cm^{-1}, respectively (72). Consequently, the loss of the negative peak at 1747 cm^{-1} should correlate with a loss of positive spectral features (or the increase in negative spectral features) near 1580−1560 and 1400 cm^{-1}. Although a decreased positive amplitude at 1587 cm^{-1} is observed in the S_2-*minus*-S_1 FTIR difference spectrum of partly dehydrated wild-type PSII (blue and red traces in Figure 1A), the same change is not observed in D1-E65A, D2-E312A, or D1-E329Q (top traces in Figures 3, 5, and 6, respectively). Similarly, while an increased negative amplitude near 1400 cm^{-1} is observed in the S_2-*minus*-S_1 FTIR difference spectra of D1-E65A, D2-E312A, and D1-E329Q (Figures 3, 5, and 6), the same change is not observed in the partly dehydrated wild type (Figure 1A). We presume that the expected changes to the $\nu_{asym}(COO^-)$ and $\nu_{sym}(COO^-)$ modes are masked by other mutation-induced or dehydration-induced structural changes in these regions.

The structural response of PSII to the development of charge on the Mn_4Ca cluster during the S_1 to S_2 transition presumably is propagated both electrostatically and through networks of hydrogen bonds involving amino acid residues and water molecules. We propose that this propagated structural response alters the environment of the carboxylate group responsible for the 1747 cm^{-1} band, decreasing this group's pK_a value. We also propose that D1-Glu65, D2-Glu312, and D1-Glu329 participate in the same network of hydrogen bonds as the carboxylate group responsible for this band. Finally, we propose that the mutation of any of these three residues to a

nonprotonatable residue, or the partial dehydration caused by maintaining samples at a relative humidity of ≤85%, disrupts the network sufficiently that the structural perturbations associated with the S_1 to S_2 transition are no longer transmitted to this carboxylate, thereby eliminating the 1747 cm^{-1} band from the spectrum. The carboxylate group that corresponds to the 1747 cm^{-1} band could be the side chain of D1-Glu65, D2-Glu312, or D1-Glu329. Alternatively, it could belong to another carboxylate residue located in the same proposed network of hydrogen-bonded side chains and water molecules. Because the side chain of D1-Glu329 is located ~20 Å from D1-Glu65 and D2-Glu312 in the 2.9 Å crystallographic structural model (5), the extended network of hydrogen bonds identified in this study must extend for at least 20 Å across the lumenal face of the Mn_4Ca cluster and probably includes the chloride ion identified in this model. The existence of extensive networks of hydrogen bonds in the lumenal domains of PSII was predicted recently on the basis of a molecular dynamics study (36). Because mutations of D1-Asp61, D1-Glu65, and D2-Glu312 substantially decrease the fraction of PSII reaction centers that undergo the S_3 to S_0 transition in response to a saturating flash, the hydrogen-bonded network that includes these residues may form part of a dominant proton egress pathway leading from the Mn_4Ca cluster to the thylakoid lumen. In is noteworthy that D1-Glu329 does not form part of the same putative access/egress channel as D1-Asp61, D1-Glu65, and D2-Glu312 in recent analyses of static PSII structures (1, 5, 32-35). It is an open question whether features of this network, particularly the apparent connection between D1-Glu329 and the other three residues, exist permanently or fleetingly, like the networks of hydrogen bonds that transiently connect hydrophilic pockets in the recent molecular dynamics study (36).

In the 2.9 Å crystallographic structural model, the side chain of D1-Asp61 is located only 4.8 Å from the side chain of D1-Glu65 and only 6.4 Å from the side chain of D2-Glu312 (5). Furthermore, D1-Asp61 is located between the Mn_4Ca cluster and both of these residues.

Consequently, it seems likely that D1-Asp61 participates in the same network of hydrogen bonds as D1-Glu65, D2-Glu312, and D1-Glu329. Nevertheless, the 1747 cm^{-1} band is unaltered by the mutation of D1-Asp61 to Ala. This lack of an effect provides a constraint on attempts to identify the source of the 1747 cm^{-1} band and suggests that the carboxylate residue that gives rise to this band is located closer to D1-Glu65, D2-Glu312, or D1-Glu329 than to D1-Asp61. Possible candidates include D2-Glu302, D2-Glu308, D2-Glu310, D2-Glu323, PsbO-Asp184, and PsbO-Asp250.

Comparison of the individual FTIR difference spectra of wild-type PSII core particles (e.g., Figure 2, black traces) shows that the negative band at 1747 cm^{-1} in the S_2-*minus*-S_1 spectrum appears to correlate with a positive band at 1747 cm^{-1} in the S_0-*minus*-S_3 spectrum and that a positive band at 1745 cm^{-1} in the S_3-*minus*-S_2 spectrum appears to correlate with a negative band at 1745 cm^{-1} in the S_1-*minus*-S_0 spectrum. It is tempting to speculate that the structural perturbations responsible for the negative 1747 cm^{-1} band during the S_1 to S_2 transition are reversed during the S_3 to S_0 transition and that another carboxylate group has its pK_a increased during the S_2 to S_3 transition and restored during the S_0 to S_1 transition. It is interesting to note that the 1745 cm^{-1} band was eliminated by all four mutants examined in this study. However, conclusions regarding the reversibility of the 1747 cm^{-1} band and the nature of the 1745 cm^{-1} band must await D_2O exchange analysis of the S_3-*minus*-S_2, S_0-*minus*-S_3, and S_1-*minus*-S_0 transitions in wild-type PSII core complexes.

In PSII core complexes from the cyanobacterium T. elongatus, the S_2-*minus*-S_1 FTIR difference spectrum contains no large negative features at 1747 cm^{-1} (51, 66, 74-76). Furthermore, the exchange of T. elongatus PSII core complexes into D_2O produces no downshift of any mode in the ν(C=O) region (51). The band is also absent from the S_2-*minus*-S_1 FTIR difference spectrum of spinach PSII membranes (77-80), although a positive band at 1747 cm^{-1}

was reported in spinach PSII core complexes (129). Exchange of spinach PSII membranes into D_2O also produces no downshift of any mode in the ν(C═O) region (78). One possible explanation for the lack of this band in T. elongatus and spinach PSII preparations derives from the slight differences between the amino acid sequences of the PSII polypeptides of spinach, T. elongatus, and Synechocystis sp. PCC 6803. Because the sequences differ, the orientations of side chains and water molecules in the extended network of hydrogen bonds are likely to differ. Perhaps these networks differ to the extent that the structural perturbations associated with the S_1 to S_2 transition in T. elongatus and spinach are not transmitted to the carboxylate group that is responsible for the 1747 cm^{-1} band in Synechocystis sp. PCC 6803. The sensitivity of this band to the extent of sample hydration and to the mutation of selected single amino acid residues shows the sensitivity of the corresponding carboxylate group to minor changes in the protein environment. Alternatively, this carboxylate residue may not be conserved in all organisms. However, a third explanation is that the observation of this band is preparation-dependent. For example, this band has been reported previously in some PSII preparations from Synechocystis sp. PCC 6803 (61, 62, 64, 65, 69, 70), but not in others (85, 87-89, 130). Nevertheless, we have observed it under a variety of conditions, including in PSII core complexes that have been purified in the presence of 25% (v/v) glycerol instead of 1.2 M betaine.

Concluding Remarks

On the basis of the presence or absence of the ν(C═O) mode of a protonated carboxylate group in the S_2-*minus*-S_1 FTIR difference spectrum, we conclude that residues D1-Glu65, D1-Glu329, and D2-Glu312 participate in a hydrogen-bonded network that extends at least 20 Å across the lumenal face of the Mn_4Ca cluster. This network presumably also includes D1-Asp61. The D1-D61A, D1-E65A, and D2-E312A mutations appear to substantially decrease the fraction of PSII reaction centers that undergo the S_3 to S_0 transition in response to a saturating flash.

Consequently, elements of the hydrogen-bonded network that includes D1-Asp61, D1-Glu65, D2-Glu312, and D1-Glu329 may comprise part of a dominant proton egress pathway leading from the Mn_4Ca cluster to the thylakoid lumen.

3.6 References

1. Ferreira, K. N., Iverson, T. M., Maghlaoui, K., Barber, J., and Iwata, S. (2004) Architecture of the Photosynthetic Oxygen-Evolving Center *Science 303*, 1831– 1838.

2. Loll, B., Kern, J., Saenger, W., Zouni, A., and Biesiadka, J. (2005) Towards Complete Cofactor Arrangement in the 3.0 Å Resolution Structure of Photosystem II *Nature 438*, 1040– 1044.

3. Kern, J., Biesiadka, J., Loll, B., Saenger, W., and Zouni, A. (2007) Structure of the Mn_4-Ca Cluster as Derived from X-ray Diffraction *Photosynth. Res. 92*, 389– 405.

4. Barber, J. (2008) Crystal Structure of the Oxygen-Evolving Complex of Photosystem II *Inorg. Chem. 47*, 1700– 1710.

5. Guskov, A., Kern, J., Gabdulkhakov, A., Broser, M., Zouni, A., and Saenger, W. (2009) Cyanobacterial Photosystem II at 2.9-Å Resolution and the Role of Quinones, Lipids, Channels, and Chloride *Nat. Struct. Mol. Biol. 16*, 334– 342.

6. Guskov, A., Gabdulkhakov, A., Broser, M., Gl□ckner, C., Hellmich, J., Kern, J., Frank, J., M□h, F., Saenger, W., and Zouni, A. (2010) Recent Progress in the Crystallographic Studies of Photosystem II *Chem Phys Chem 11*, 1160– 1171.

7. McEvoy, J. P. and Brudvig, G. W. (2006) Water-Splitting Chemistry of Photosystem II *Chem. Rev. 106*, 4455– 4483.

8. McCarrick, R. M. and Britt, R. D. (2008) Current Models and Mechanism of Water Splitting. In Photosynthetic Protein Complexes (Fromme, P., Ed.) pp 107− 136, Wiley-VCH Verlag GmbH & Co. KGaA, Weinheim, Germany.

9. Rappaport, F. and Diner, B. A. (2008) Primary Photochemistry and Energetics Leading to the Oxidation of the $(Mn)_4Ca$ Cluster and to the Evolution of Molecular Oxygen in Photosystem II *Coord. Chem. Rev. 252*, 259– 272.

10. Renger, G. and Renger, T. (2008) Photosystem II: The Machinery of Photosynthetic Water Splitting *Photosynth. Res. 98*, 53– 80.

11. Yano, J. and Yachandra, V. K. (2008) Where Water is Oxidized to Dioxygen: Structure of the Photosynthetic Mn_4Ca Cluster from X-ray Spectroscopy *Inorg. Chem. 47*, 1711– 1726.

12. Yano, J. and Yachandra, V. K. (2007) Oxidation State Changes of the Mn_4Ca Cluster in Photosystem II *Photosynth. Res. 92*, 289– 303.

13. Dau, H. and Haumann, M. (2008) The Manganese Complex of Photosystem II in its Reaction Cycle: Basic Framework and Possible Realization at the Atomic Level *Coord. Chem. Rev. 252*, 273– 295.

14. Sauer, K., Yano, J., and Yachandra, V. K. (2008) X-ray Spectrsocopy of the Photosynthetic Oxygen-Evolving Complex *Coord. Chem. Rev. 252*, 318– 335.

15. Murray, J. W., Maghlaoui, K., Kargul, J., Ishida, N., Lai, T.-L., Rutherford, A. W., Sugiura, M., Boussac, A., and Barber, J. (2008) X-ray Crystallography Identifies two Chloride Binding Sites in the Oxygen Evolving Centre of Photosystem II Energy *Environ. Sci. 1*, 161– 166.

16. Kawakami, K., Umena, Y., Kamiya, N., and Shen, J.-R. (2009) Location of Chloride and its Possible Functions in Oxygen-Evolving Photosystem II Revealed by X-ray Crystallography *Proc. Natl. Acad. Sci. U.S.A. 106*, 8567– 8572.

17. Yano, J., Kern, J., Irrgang, K.-D., Latimer, M. J., Bergmann, U., Glatzel, P., Pushkar, Y., Biesiadka, J., Loll, B., Sauer, K., Messinger, J., Zouni, A., and Yachandra, V. K. (2005) X-ray Damage to the Mn_4Ca Complex in Single Crystals of Photosystem II: A e Study for Metalloprotein Crystallography *Proc. Natl. Acad. Sci. U.S.A. 102*, 12047– 12052.

18. Grabolle, M., Haumann, M., M□ller, C., Liebisch, P., and Dau, H. (2006) Rapid Loss of Structural Motifs in the Manganese Complex of Oxygenic Photosynthesis by X-ray Irradiation at 10−300 K *J. Biol. Chem. 281*, 4580– 4588.

19. Yano, J., Kern, J., Sauer, K., Latimer, M. J., Pushkar, Y., Biesiadka, J., Loll, B., Saenger, W., Messinger, J., Zouni, A., and Yachandra, V. K. (2006) Where Water is Oxidized to Dioxygen: Structure of the Photosynthetic Mn_4Ca Cluster *Science 314*, 821– 825.

20. Debus, R. J. (2008) Protein Ligation of the Photosynthetic Oxygen-Evolving Center *Coord. Chem. Rev. 252*, 244– 258.

21. Dau, H. and Haumann, M. (2007) Time Resolved X-ray Spectroscopy Leads to an Extension of the Classical S-State Cycle Model of Photosynthetic Oxygen Evolution *Photosynth. Res. 92*, 327– 343.

22. Sproviero, E. M., Gasc□n, J. A., McEvoy, J. P., Brudvig, G. W., and Batista, V. S. (2008) Computation Studies of the O_2-Evolving Complex of Photosystem II and Biomimetic Oxomanganese Complexes *Coord. Chem. Rev. 252*, 395– 415.

23. Wydrzynski, T., Hillier, W., and Messinger, J. (1996) On the Functional Significance of Substrate Accessibility in the Photosynthetic Water Oxidation Mechanism *Physiol. Plant. 96*, 342– 350.

24. Anderson, J. M. (2001) Does Functional Photosystem II Complex have an Oxygen Channel? *FEBS Lett. 488*, 1– 4.

25. McEvoy, J. P. and Brudvig, G. W. (2004) Structure-Based Mechanism of Photosynthetic Water Oxidation *Phys. Chem. Chem. Phys. 6*, 4754– 4763.

26. Haumann, M., Liebisch, P., Müller, C., Barra, M., Grabolle, M., and Dau, H. (2005) Photosynthetic O_2 Formation Tracked by Time-Resolved X-ray Experiments *Science 310*, 1019– 1021.

27. Sproviero, E. M., Gascón, J. A., McEvoy, J. P., Brudvig, G. W., and Batista, V. S. (2008) Quantum Mechanics/Molecular Mechanics Study of the Catalytic Cycle of Water Splitting In Photosystem II *J. Am. Chem. Soc. 130*, 3428– 3442.

28. Sproviero, E. M., McEvoy, J. P., Gascón, J. A., Brudvig, G. W., and Batista, V. S. (2008) Computational Insights into the O_2-Evolving Complex of Photosystem II *Photosynth. Res. 97*, 91– 114.

29. Barber, J., Ferreira, K. N., Maghlaoui, K., and Iwata, S. (2004) Structural Model of the Oxygen-Evolving Centre of Photosystem II with Mechanistic Implications *Phys. Chem. Chem. Phys. 6*, 4737– 4742.

30. De Las Rivas, J. and Barber, J. (2004) Analysis of the Structure of the PsbO Protein and Its Implications *Photosynth. Res. 81*, 329– 343.

31. Shutova, T., Klimov, V. V., Andersson, B., and Samuelsson, G. (2007) A Cluster of Carboxylic Groups in PsbO Protein is Involved in Proton Transfer from the Water Oxidizing Complex of Photosystem II *Biochim. Biophys. Acta 1767*, 434– 440.

32. Ishikita, H., Saenger, W., Loll, B., Biesiadka, J., and Knapp, E.-W. (2006) Energetics of a Possible Proton Exit Pathway for Water Oxidation in Photosystem II *Biochemistry 45*, 2063– 2071.

33. Ho, F. M. and Styring, S. (2008) Access Channels and Methanol Binding Site to the $CaMn_4$ Cluster in Photosystem II based on Solvent Accessibility Simulation, with Implications for Substrate Water Access *Biochim. Biophys. Acta 1777*, 140– 153.

34. Murray, J. W. and Barber, J. (2007) Structural Characteristics of Channels and Pathways in Photosystem II Including the Identification of an Oxygen Channel *J. Struct. Biol. 159*, 228– 237.

35. Gabdulkhakov, A., Guskov, A., Broser, M., Kern, J., Müh, F., Saenger, W., and Zouni, A. (2009) Probing the Accessibility of the Mn_4Ca Cluster in Photosystem II: Channels Calculation, Noble Gas Derivatization, and Cocrystallization with DMSO *Structure 17*, 1223– 1234.

36. Vassiliev, S., Comte, P., Mahboob, A., and Bruce, D. (2010) Tracking the Flow of Water through Photosystem II Using Molecular Dynamics and Streamline Tracing *Biochemistry 49*, 1873– 1881.

37. Okamura, M. Y., Paddock, M. L., Graige, M. S., and Feher, G. (2000) Proton and electron transfer in bacterial reaction centers *Biochim. Biophys. Acta 1458*, 148– 163.

38. Paddock, M. L., Feher, G., and Okamura, M. Y. (2003) Proton Transfer Pathways and Mechanism in Bacterial Reaction Centers *FEBS Lett. 555*, 45– 50.

39. Wraight, C. A. (2005) Intraprotein Proton Transfer: Concepts and Realities from the Bacterial Photosynthetic Reaction Center. In Biophysical and Structural Aspects of Bioenergetics (Wikstr□m, M., Ed.) pp 273− 313, Royal Society of Chemistry, Cambridge, U.K.

40. Zscherp, C. and Barth, A. (2001) Reaction-Induced Infrared Difference Spectroscopy for the Study of Protein Reaction Mechanisms *Biochemistry 40*, 1875– 1883.

41. Barth, A. and Zscherp, C. (2002) What Vibrations Tell Us About Proteins *Q. Rev. Biophys. 35*, 369– 430.

42. Rich, P. R. and Iwaki, M. (2005) Infrared Protein Spectroscopy as a Tool to Study Protonation Reactions Within Proteins. In Biopysical and Structural Aspects of Bioenergetics (Wikstr□m, M., Ed.) pp 314− 333, Royal Society of Chemistry, Cambridge, U.K.

43. Barth, A. (2007) Infrared Spectroscopy of Proteins *Biochim. Biophys. Acta 1767*, 1073– 1101.

44. Berthomieu, C. and Hienerwadel, R. (2009) Fourier Transform Infrared (FTIR) Spectroscopy *Photosynth. Res. 101*, 157– 170.

45. Maeda, A., Sasaki, J., Shichida, Y., Yoshizawa, Y., Chang, M., Ni, B., Needleman, R., and Lanyi, J. K. (1992) Structures of Aspartic Acid-96 in the L and N Intermediates of Bacteriorhodopsin: Analysis by Fourier Transform Infrared Spectroscopy *Biochemistry 31*, 4684– 4690.

46. Dioumaev, A. K. and Braiman, M. S. (1995) Modeling Vibrational Spectra of Amino Acid Side Chains in Proteins: The Carbonyl Stretch Frequency of Buried Carboxylic Side Chains *J. Am. Chem. Soc. 117*, 10572– 10574.

47. Dioumaev, A. K. (2001) Infrared Methods for Monitoring the Protonation State of Carboxylic Amino Acids in the Photocycle of Bacteriorhodopsin *Biochemistry (Moscow, Russ. Fed.) 66*, 1269– 1276.

48. Nie, B., Stutzman, J., and Xie, A. (2005) A Vibrational Spectral Marker for Probing the Hydrogen-Bonding Status of Protonated Asp and Glu Residues *Biophys. J. 88*, 2833– 2847.

49. Takei, K.-I., Takahashi, R., and Noguchi, T. (2008) Correlation Between the Hydrogen-Bond Structures and the C═O Stretching Frequencies of Carboxylic Acids as Studied by Density Functional Theory Calculations: Theoretical Basis for Interpretation of Infrared Bands of Carboxylic Groups in Proteins *J. Phys. Chem. B 112*, 6725– 6731.

50. Noguchi, T. and Sugiura, M. (2000) Structure of an Active Water Molecule in the Water-Oxidizing Complex of Photosystem II as Studied by FTIR Spectroscopy *Biochemistry 39*, 10943– 10949.

51. Noguchi, T. and Sugiura, M. (2002) FTIR Detection of Water Reactions During the Flash-Induced S-State Cycle of the Photosynthetic Water-Oxidizing Complex *Biochemistry 41*, 15706– 15712.

52. Noguchi, T. (2007) FTIR Detection of Water Reactions in the Oxygen-Evolving Center of Photosystem II *Philos. Trans. R. Soc. London, Ser. B 363*, 1189– 1195.

53. Venyaminov, S. Yu. and Prendergast, F. G. (1997) Water (H_2O and D_2O) Molar Aborptivity in the 1000−4000 cm^{-1} Range and Quantitative Infrared Spectroscpy of Aqueous Solutions *Anal. Biochem. 248*, 234– 245.

54. Suzuki, H., Sugiura, M., and Noguchi, T. (2008) Monitoring Water Reactions during the S-State Cycle of the Photosynthetic Water-Oxidizing Center: Detection of the DOD Bending Vibrations by Means of Fourier Transform Infrared Spectroscopy *Biochemistry 47*, 11024– 11030.

55. Noguchi, T. and Berthomieu, C. (2005) Molecular Analysis by Vibrational Spectroscopy. In Photosystem II: The Light-Driven Water:Plastoquinone Oxidoreductase (Wydrzynski, T. and Satoh, K., Eds.) pp 367− 387, Springer, Dordrecht, The Netherlands.

56. Noguchi, T. (2007) Light-Induced FTIR Difference Spectroscopy as a Powerful Tool Toward Understanding the Molecular Mechanism of Photosynthetic Oxygen Evolution *Photosynth. Res. 91*, 59– 69.

57. Noguchi, T. (2008) Fourier Transform Infrared Analysis of the Photosynthetic Oxygen-Evolving Center *Coord. Chem. Rev. 251*, 336– 346.

58. Chu, H.-A., Nguyen, A. P., and Debus, R. J. (1994) Site-Directed Photosystem II Mutants with Perturbed Oxygen Evolving Properties: 1. Instability or Inefficient Assembly of the Manganese Cluster *In Vivo Biochemistry 33*, 6137– 6149.

59. Debus, R. J., Campbell, K. A., Gregor, W., Li, Z.-L., Burnap, R. L., and Britt, R. D. (2001) Does Histidine 332 of the D1 Polypeptide Ligate the Manganese Cluster in Photosystem II? An Electron Spin Echo Envelope Modulation Study *Biochemistry 40*, 3690– 3699.

60. Faller, P., Rutherford, A. W., and Debus, R. J. (2002) Tyrosine D Oxidation at Cryogenic Temperature in Photosystem II *Biochemistry 41*, 12914– 12920.

61. Strickler, M. A., Walker, L. M., Hillier, W., Britt, R. D., and Debus, R. J. (2007) No Evidence from FTIR Difference Spectroscopy That Aspartate-342 of the D1 Polypeptide

Ligates a Mn Ion That Undergoes Oxidation during the S_0 to S_1, S_1 to S_2, or S_2 to S_3 Transitions in Photosystem II *Biochemistry 46*, 3151– 3160.

62. Strickler, M. A., Walker, L. M., Hillier, W., and Debus, R. J. (2005) Evidence from Biosynthetically Incorporated Strontium and FTIR Difference Spectroscopy that the C-Terminus of the D1 Polypeptide of Photosystem II Does Not Ligate Calcium *Biochemistry 44*, 8571– 8577.

63. Yamanari, T., Kimura, Y., Mizusawa, N., Ishii, A., and Ono, T.-A. (2004) Mid- to Low-Frequency Fourier Transform Infrared Spectra of S-State Cycle for Photosynthetic Water Oxidation in *Synechocystis* sp. PCC 6803 *Biochemistry 43*, 7479– 7490.

64. Debus, R. J., Strickler, M. A., Walker, L. M., and Hillier, W. (2005) No Evidence from FTIR Difference Spectroscopy That Aspartate-170 of the D1 Polypeptide Ligates a Manganese Ion That Undergoes Oxidation during the S_0 to S_1, S_1 to S_2, or S_2 to S_3 Transitions in Photosystem II *Biochemistry 44*, 1367– 1374.

65. Strickler, M. A., Hillier, W., and Debus, R. J. (2006) No Evidence from FTIR Difference Spectroscopy that Glutamate-189 of the D1 Polypeptide Ligates a Mn Ion that Undergoes Oxidation During the S_0 to S_1, S_1 to S_2, or S_2 to S_3 Transitions in Photosystem II *Biochemistry 45*, 8801– 8811.

66. Noguchi, T. and Sugiura, M. (2002) Flash-Induced FTIR Difference Spectra of the Water Oxidizing Complex in Moderately Hydrated Photosystem II Core Films: Effect of Hydration Extent on S-State Transitions *Biochemistry 41*, 2322– 2330.

67. Glasoe, P. K. and Long, F. A. (1960) Use of Glass Electrodes to Measure Acidities in Deuterium Oxide *J. Phys. Chem. 64*, 188– 191.

68. Salomaa, P., Schaleger, L. L., and Long, F. A. (1964) Solvent Deuterium Isotope Effects on Acid-Base Equilibria *J. Am. Chem. Soc. 86*, 1– 7.

69. Chu, H.-A., Hillier, W., and Debus, R. J. (2004) Evidence that the C-Terminus of the D1 Polypeptide is Ligated to the Manganese Ion that Undergoes Oxidation During the S_1 to S_2 Transition: An Isotope-Edited FTIR Study *Biochemistry 43*, 3152– 3166.

70. Noguchi, T., Inoue, Y., and Tang, X. S. (1997) Structural coupling between the oxygen-evolving Mn cluster and a tyrosine residue in photosystem II as revealed by Fourier transform infrared spectroscopy *Biochemistry 36*, 14705– 14711.

71. Strickler, M. A., Hwang, H. J., Burnap, R. L., Yano, J., Walker, L. M., Service, R. J., Britt, R. D., Hillier, W., and Debus, R. J. (2008) Glutamate-354 of the CP43 Polypeptide Interacts with the Oxygen-Evolving Mn_4Ca Cluster of Photosystem II: A Preliminary Characterization of the Glu354Gln Mutant *Philos. Trans. R. Soc. London, Ser. B 363*, 1179– 1188.

72. Barth, A. (2000) The Infrared Absorption of Amino Acid Side Chains *Prog. Biophys. Mol. Biol. 74*, 141– 173.

73. Socrates, G. (2001) Infrared Characteristic Group Frequencies: Tables and Charts, 3rd ed., John Wiley & Sons, Chichester, U.K..

74. Noguchi, T. and Sugiura, M. (2003) Analysis of Flash-Induced FTIR Difference Spectra of the S-State Cycle in the Photosynthetic Water-Oxidizing Complex by Uniform ^{15}N and ^{13}C Isotope Labeling *Biochemistry 42*, 6035– 6042.

75. Suzuki, H., Sugiura, M., and Noguchi, T. (2005) pH Dependence of the Flash-Induced S-State Transitions in the Oxygen-Evolving Center of Photosystem II from *Thermosynechococcus elongatus* as Revealed by Fourier Transform Infrared Spectroscopy *Biochemistry 44*, 1708– 1718.

76. Suzuki, H., Sugiura, M., and Noguchi, T. (2009) Monitoring Proton Release during Photosynthetic Water Oxidation in Photosystem II by Means of Isotope-Edited Infrared Spectroscopy *J. Am. Chem. Soc. 131*, 7849– 7857.

77. Noguchi, T., Ono, T.-A., and Inoue, Y. (1995) Direct Detection of a Carboxylate Bridge Between Mn and Ca^{2+} in the Photosynthetic Oxygen-Evolving Center by Means of Fourier Transform Infrared Spectroscopy *Biochim. Biophys. Acta 1228*, 189– 200.

78. Noguchi, T., Ono, T.-A., and Inoue, Y. (1995) A Carboxylate Ligand Interacting with Water in the Oxygen-Evolving Center of Photosystem II as Revealed by Fourier Transform Infrared Spectroscopy *Biochim. Biophys. Acta 1232*, 59– 66.

79. Onoda, K., Mino, H., Inoue, Y., and Noguchi, T. (2000) An FTIR study on the structure of the oxygen-evolving Mn-cluster of Photosystem II in different spin forms of the S_2 state *Photosynth. Res. 63*, 47– 57.

80. Kimura, Y., Hasegawa, K., Yamanari, T., and Ono, T.-A. (2005) Studies on Photosynthetic Oxygen-Evolving Complex by Means of Fourier Transform Infrared Spectroscopy: Calcium and Chloride Cofactors *Photosynth. Res. 84*, 245– 250.

81. Noguchi, T., Sugiura, M., and Inoue, Y. (1999) FTIR Studies on the Amino-Acid Ligands of the Photosynthetic Oxygen-Evolving Mn-Cluster. In Fourier Transform Spectroscopy: Twelfth International Conference (Itoh, K., and and Tasumi, M., Eds.) pp 459− 460, Waseda University Press, Tokyo.

82. Kimura, Y., Mizusawa, N., Ishii, A., Yamanari, T., and Ono, T.-A. (2003) Changes of Low-Frequency Vibrational Modes Induced by Universal ^{15}N- and ^{13}C-Isotope Labeling in S2/S1 FTIR Difference Spectrum of Oxygen-Evolving Complex *Biochemistry 42*, 13170– 13177.

83. Chu, H.-A., Nguyen, A. P., and Debus, R. J. (1995) Amino Acid Residues that Influence the Binding of Manganese or Calcium to Photosystem II. 2. The Carboxy-terminal Domain of the D1 Polypeptide *Biochemistry 34*, 5859– 5882.

84. Chu, H.-A., Nguyen, A. P., and Debus, R. J. (1995) Amino Acid Residues that Influence the Binding of Manganese or Calcium to Photosystem II. 1. The Lumenal Inter-Helical Domains of the D1 Polypeptide *Biochemistry 34*, 5839– 5858.

85. Shimada, Y., Suzuki, H., Tsuchiya, T., Tomo, T., Noguchi, T., and Mimuro, M. (2009) Effect of a Single-Amino Acid Substitution of the 43 kDa Chlorophyll Protein on the Oxygen-Evolving Reaction of the Cyanobacterium *Synechocystis* sp. PCC 6803: Analysis of the Glu354Gln Mutation *Biochemistry 48*, 6095– 6103.

86. Berthomieu, C., Hienerwadel, R., Boussac, A., Breton, J., and Diner, B. A. (1998) Hydrogen-Bonding of Redox-Active Tyrosine Z of Photosystem II Probed by FTIR Difference Spectroscopy *Biochemistry 37*, 10547– 10554.

87. Chu, H.-A., Debus, R. J., and Babcock, G. T. (2001) D1-Asp170 is Structurally Coupled to the Oxygen Evolving Complex in Photosystem II as Revealed by Light-Induced Fourier Transform Infrared Difference Spectroscopy *Biochemistry 40*, 2312– 2316.

88. Kimura, Y., Mizusawa, N., Ishii, A., Nakazawa, S., and Ono, T.-A. (2005) Changes in Structural and Functional Properties of Oxygen-Evolving Complex Induced by Replacement of D1-Glutamate 189 with Glutamine in Photosystem II: Ligation of Glutamate 189 Carboxylate to the Manganese Cluster *J. Biol. Chem. 280*, 37895– 37900.

89. Kimura, Y., Mizusawa, N., Yamanari, T., Ishii, A., and Ono, T.-A. (2005) Structural Changes of D1 C-terminal α-Carboxylate during S-state Cycling of Photosynthetic Oxygen Evolution *J. Biol. Chem. 280*, 2078– 2083.

90. Londergan, C. H. and Kubiak, C. P. (2003) Electron Transfer and Dynamic Infrared-Band Coalescence: It looks like Dynamic NMR Spectroscopy, but a Billion Times Faster *Chem. Eur. J. 9*, 5962– 5969.

91. Glover, S. D., Goeltz, J. C., Lear, B. J., and Kubiak, C. P. (2009) Mixed Valency at the Nearly Delocalized Limit: Fundamentals and Forecast *Eur. J. Inorg. Chem. 5*, 585– 594.

92. Goeltz, J. C., Hanson, C. J., and Kubiak, C. P. (2009) Rates of Electron Self-Exchange Reactions between Oxo-Centered Ruthenium Clusters are Determined by Orbital Overlap *Inorg. Chem. 48*, 4763– 4767.

93. Glatzel, P., Bergmann, U., Yano, J., Visser, H., Robblee, J. H., Gu, W., De Groot, F. M. F., Christou, G., Pecoraro, V. L., Cramer, S. P., and Yachandra, V. K. (2004) The Electronic Structure of Mn in Oxides, Coordination Complexes, and the Oxygen-Evolving Complex of Photosystem II Studied by Resonant Inelastic X-ray Scattering *J. Am. Chem. Soc. 126*, 9946– 9959.

94. Sproviero, E. M., Gasc☌n, J. A., McEvoy, J. P., Brudvig, G. W., and Batista, V. S. (2006) QM/MM Models of the O_2-Evolving Complex of Photosystem II *J. Chem. Theory Comput. 2*, 1119– 1134.

95. Stull, J. A., Stich, T. A., Service, R. J., Debus, R. J., Mandal, S. K., Armstrong, W. H., and Britt, R. D. (2010) ^{13}C ENDOR Reveals that the D1 Polypeptide C-Terminus is Directly Bound to Mn in the Photosystem II Oxygen Evolving Complex *J. Am. Chem. Soc. 132*, 446– 447.

96. Iizasa, M., Suzuki, H., and Noguchi, T. (2010) Orientations of Carboxylate Groups Coupled to the Mn Cluster in the Photosynthetic Oxygen-Evolving Center as Studied by Polarized ATR-FTIR Spectroscopy *Biochemistry 49*, 3074– 3082.

97. Cohen, R. O., Nixon, P. J., and Diner, B. A. (2007) Participation of the C-terminal Region of the D1-Polypeptide in the First Steps in the Assembly of the Mn_4Ca Cluser of Photosystem II *J. Biol. Chem. 282*, 7209– 7218.

98. Hwang, H. J., McLain, A., Debus, R. J., and Burnap, R. L. (2007) Photoassembly of the Manganese Cluster in Mutants Perturbed in the High Affinity Mn-Binding Site of the H_2O-Oxidation Complex of Photosystem II *Biochemistry 46*, 13648– 13657.

99. Debus, R. J. (2001) Amino Acid Residues that Modulate the Properties of Tyrosine Y_Z and the Manganese Cluster in the Water Oxidizing Complex of Photosystem II *Biochim. Biophys. Acta 1503*, 164– 186.

100. Diner, B. A. (2001) Amino Acid Residues Involved in the Coordination and Assembly of the Manganese Cluster of Photosystem II. Proton-Coupled Electron Transport of the Redox-Active Tyrosines and Its Relationship to Water Oxidation *Biochim. Biophys. Acta 1503*, 147– 163.

101. Debus, R. J. (2005) The Catalytic Manganese Cluster: Protein Ligation. In Photosystem II: The Light-Driven Water:Plastoquinone Oxidoreductase (Wydrzynski, T. and Satoh, K., Eds.) pp 261− 284, Springer, Dordrecht, The Netherlands.

102. Tommos, C. and Babcock, G. T. (2000) Proton and Hydrogen Currents in Photosynthetic Water Oxidation *Biochim. Biophys. Acta 1458*, 199– 219.

103. Wraight, C. A. (2006) Chance and Design: Proton Transfer in Water, Channels and Bioenergetic Proteins *Biochim. Biophys. Acta 1757*, 886– 912.

104. Silverman, D. N. and McKenna, R. (2007) Solvent-Mediated Proton Transfer in Catalysis by Carbonic Anhydrase *Acc. Chem. Res. 40*, 669– 675.

105. Mikulski, R. L. and Silverman, D. N. (2010) Proton Transfer in Catalysis and the Role of Proton Shuttles in Carbonic Anhydrase *Biochim. Biophys. Acta 1804*, 422– 426.

106. Hosler, J. P., Ferguson-Miller, S., and Mills, D. A. (2006) Energy Transduction: Proton Transfer Through the Respiratory Complexes Annu. Rev. *Biochem. 75*, 165– 187.

107. Wikstr$\ddot{o}$m, M. and Verkhovsky, M. I. (2007) Mechanism and Energetics of Proton Translocation by the Respiratory Heme-Copper Oxidases *Biochim. Biophys. Acta 1767*, 1200– 1214.

108. Brzezinski, P. and Gennis, R. B. (2008) Cytochrome c Oxidase: Exciting Progress and Remaining Mysteries *J. Bioenerg. Biomembr. 40*, 521– 531.

109. Hundelt, M., Hays, A.-M. A., Debus, R. J., and Junge, W. (1998) Oxygenic Photosystem II: The Mutation D1-D61N in *Synechocystis* sp. PCC 6803 Retards S-State Transitions without Affecting Electron Transfer from Y_Z to P_{680}^+ *Biochemistry 37*, 14450– 14456.

110. Hundelt, M., Hays, A.-M. A., Debus, R. J., and Junge, W. (1998) The Mutation D1-D61N in PSII of *Synechocystis*: Retardation of ET from OEC→Y_Z^{ox} and No Effect on Y_Z→P_{680}^+. In Photosynthesis: Mechanisms and Effects (Garab, G., Ed.) Vol. II, pp 1387− 1390, Kluwer Academic Publishers, Dordrecht, The Netherlands.

111. Qian, M., Dao, L., Debus, R. J., and Burnap, R. L. (1999) Impact of Mutations within the Putative Ca^{2+}-Binding Lumenal Interhelical a-b Loop of the Photosystem II D1 Protein on the Kinetics of Photoactivation and H_2O-Oxidation in *Synechocystis* sp. PCC 6803 *Biochemistry 38*, 6070– 6081.

112. Ananyev, G., Nguyen, T., Putnam-Evans, C., and Dismukes, G. C. (2005) Mutagenesis of CP43-Arginine-357 to Serine Reveals New Evidence for (Bi)Carbonate Functioning in the Water Oxidizing Complex of Photosystem II *Photochem. Photobiol. Sci. 4*, 991– 998.

113. Hwang, H. J., Dilbeck, P., Debus, R. J., and Burnap, R. L. (2007) Mutation of Arginine 357 of the CP43 Protein of Photosystem II Severely Impairs the Catalytic S-State Cycle of the H_2O Oxidation Complex *Biochemistry 46*, 11987– 11997.

114. Siebert, F., Mäntele, W., and Kreutz, W. (1982) Evidence for the Protonation of Two Internal Carboxylic Groups During the Photocycle of Bacteriorhodopsin *FEBS Lett. 141*, 82– 87.

115. Engelhard, M., Gerwert, K., Hess, B., Kreutz, W., and Siebert, F. (1985) Light-Driven Protonation Changes of Internal Aspartic Acids of Bacteriorhodopsin: An Investigation by Static and Time-Resolved Infrared Difference Spectroscopy Using [4-^{13}C]Aspartic Acid Labeled Purple Membrane *Biochemistry 24*, 400– 407.

116. Dioumaev, A. K., Richter, H. T., Brown, L. S., Tanio, M., Tuzi, S., Saito, H., Kimura, Y., Needleman, R., and Lanyi, J. K. (1998) Existence of a proton transfer chain in bacteriorhodopsin: Participation of Glu-194 in the release of protons to the extracellular surface *Biochemistry 37*, 2496– 2506.

117. Dioumaev, A. K., Brown, L. S., Needleman, R., and Lanyi, J. K. (1999) Fourier-Transform Infrared Spectra of a Late Intermediate of the Bacteriorhodopsin Photocycle Suggest Transient Protonation of Asp-212 *Biochemistry 38*, 10070– 10078.

118. de Grip, W. J., Gillespie, J., and Rothschild, K. J. (1985) Carboxyl Group Involvement in the Meta I and Meta II Stages in Rhodopsin Bleaching: A Fourier Transform Infrared Spectroscopic Study *Biochim. Biophys. Acta 809*, 97– 106.

119. Ganter, U. M., Gärtner, W., and Siebert, F. (1988) Rhodopsin-Lumirhodopsin Phototransition of Bovine Rhodopsin Investigated by Fourier Transform Infrared Difference Spectroscopy *Biochemistry 27*, 7480– 7488.

120. Nabedryk, E., Breton, J., Hienerwadel, R., Fogel, C., Mäntele, W., Paddock, M. L., and Okamura, M. Y. (1995) Fourier Transform Infrared Difference Spectroscopy of Secondary Quinone Acceptor Photoreduction in Proton Transfer Mutants of *Rhodobacter sphaeroides Biochemistry 34*, 14722– 14732.

121. Hienerwadel, R., Grzybek, S., Fogel, C., Kreutz, W., Okamura, M. Y., Paddock, M. L., Breton, J., Nabedryk, E., and Mäntele, W. (1995) Protonation of Glu L212 Following Q_B^- Formation in the Photosynthetic Reaction Center of *Rhodobacter sphaeroides*: Evidence from Time-Resolved Infrared Spectroscopy *Biochemistry 34*, 2832– 2843.

122. Nabedryk, E., Breton, J., Okamura, M. Y., and Paddock, M. L. (1998) Proton Uptake by Carboxylic Acid Groups upon Photoreduction of the Secondary Quinone (Q_B) in Bacterial Reaction Centers from *Rhodobacter sphaeroides*: FTIR Studies on the Effects of Replacing Glu H173 *Biochemistry 37*, 14457– 14462.

123. Nabedryk, E., Breton, J., Okamura, M. Y., and Paddock, M. L. (1998) Direct Evidence of Structural Changes in Reaction Centers of *Rb. sphaeroides* Containing Suppressor Mutations for AspL213→Asn: A FTIR Study of Q_B Photoreduction *Photosynth. Res. 55*, 293– 299.

124. Hellwig, P., Rost, B., Kaiser, U., Ostermeier, C., Michel, H., and Mäntele, W. (1996) Carboxyl Group Protonation upon Reduction of the *Paracoccus denitrificans* Cytochrome *c* Oxidase: Direct Evidence by FTIR Spectroscopy *FEBS Lett. 385*, 53– 57.

125. Lübben, M. and Gerwert, K. (1996) Redox FTIR Difference Spectroscopy Using Caged Electrons Reveals Contributions of Carboxyl Groups to the Catalytic Mechanism of Haem-Copper Oxidases *FEBS Lett. 397*, 303– 307.

126. Hellwig, P., Behr, J., Ostermeier, C., Richter, O. M., Pfitzner, U., Odenwald, A., Ludwig, B., Michel, H., and Mäntele, W. (1998) Involvement of Glutamic Acid 278 in the Redox Reaction of the Cytochrome *c* Oxidase from *Paracoccus denitrificans* Investigated by FTIR Spectroscopy *Biochemistry 37*, 7390– 7399.

127. Lübben, M., Prutsch, A., Mamat, B., and Gerwert, K. (1999) Electron Transfer Induces Side-Chain Conformational Changes of Gluamate-286 from Cytochrome bo_3 *Biochemistry 38*, 2048– 2056.

128. Xie, A., Hoff, W. D., Kroon, A. R., and Hellingwerf, K. J. (1996) Glu46 Donates a Proton to the 4-Hydroxycinnamate Anion Chromophore During the Photocycle of Photoactive Yellow Protein *Biochemistry 35*, 14671– 14678.

129. Hillier, W. and Babcock, G. T. (2001) S-State Dependent FTIR Difference Spectra for the Photosystem II Oxygen Evolving Complex *Biochemistry 40*, 1503– 1509.

130. Mizusawa, N., Kimura, Y., Ishii, A., Yamanari, T., Nakazawa, S., Teramoto, H., and Ono, T.-A. (2004) Impact of Replacement of D1 C-terminal Alanine with Glycine on Structure and Function of Photosynthetic Oxygen-Evolving Complex *J. Biol. Chem. 279*, 29622– 29627.

3.7 Figures

Figure 3.1 Comparison of the midfrequency S_2-*minus*-S_1 FTIR difference spectra of wild-type PSII core complexes (A) maintained at a relative humidity of 99% (black) or 85% (blue) or as a dry film in the sample cell (red) or (B) exchanged into FTIR buffer containing H_2O (black) or D_2O (red) and maintained at a relative humidity of 99% (in an atmosphere of H_2O or D_2O, respectively). In panel A, the spectra have been normalized to the peak to peak amplitudes of the negative ferricyanide peak at 2115 cm^{-1} and the positive ferrocyanide peak at 2038 cm^{-1}. In panel B, the spectra have been normalized to maximize overlap between 1450 and 1350 cm^{-1}. The black, blue, and red traces in panel A represent the averages of four, seven, and four samples, respectively, and consist of 13800, 24200, and 13400 scans, respectively. The black and red traces in panel B each represent the average of four samples and consist of 13800 and 13600 scans, respectively. The sample temperature was 273 K.

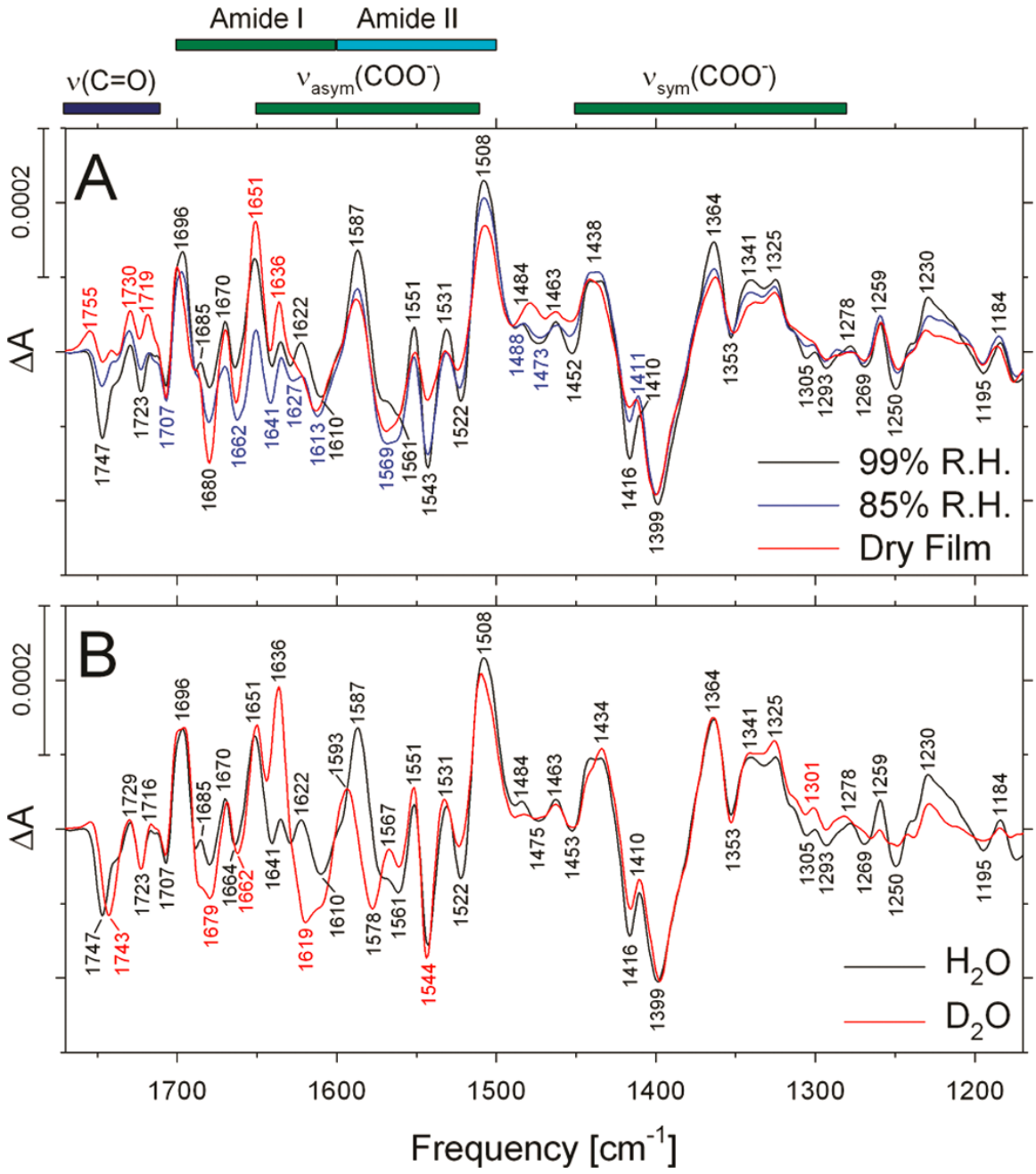
Amide I
Amide II
ν(C=O)
ν_asym(COO⁻)
ν_sym(COO⁻)
A
0.0002
ΔA
99% R.H.
85% R.H.
Dry Film
B
H2O
D2O
Frequency [cm⁻¹]

Figure 3.1

Figure 3.2 Comparison of the midfrequency FTIR difference spectra of wild-type (black) and D1-D61A (red) PSII core complexes in response to four successive flash illuminations applied at 273 K. The wild-type spectra correspond predominantly to the S_2-*minus*-S_1, S_3-*minus*-S_2, S_0-*minus*-S_3, and S_1-*minus*-S_0 FTIR difference spectra, respectively. The data (plotted from 1770 to 1170 cm^{-1}) represent the averages of nine wild-type and eight D61A samples (10800 and 9600 scans, respectively). To facilitate comparisons, the mutant spectra have been multiplied by factors of ~1.1 after normalization to the peak to peak amplitudes of the negative ferricyanide peak at 2115 cm^{-1} and the positive ferrocyanide peak at 2038 cm^{-1} to maximize overlap with the wild-type spectra. Dark-*minus*-dark control traces are included to show the noise level (bottom traces).

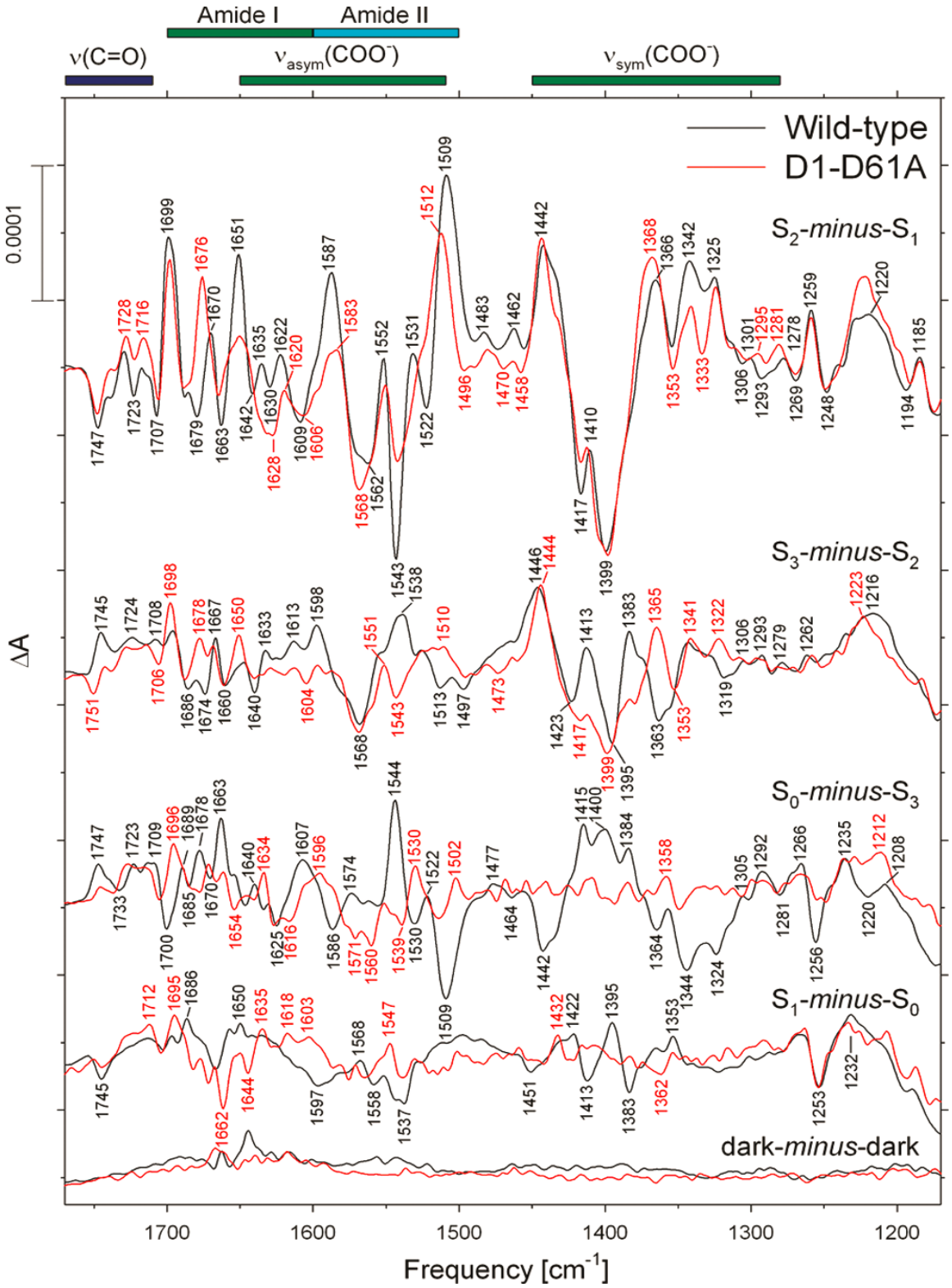
Amide I
Amide II
ν(C=O)
ν_asym(COO⁻)
ν_sym(COO⁻)
Wild-type
D1-D61A
0.0001
S2-minus-S1
S3-minus-S2
S0-minus-S3
S1-minus-S0
dark-minus-dark
ΔA
Frequency [cm⁻¹]
1700
1600
1500
1400
1300
1200

Figure 3.2

Figure 3.3 Comparison of the midfrequency FTIR difference spectra of wild-type (black) and D1-E65A (red) PSII core complexes in response to four successive flash illuminations applied at 273 K. The data (plotted from 1770 to 1170 cm^{-1}) represent the averages of nine wild-type and 12 D1-D61A samples (10800 and 14400 scans, respectively). To facilitate comparisons, the mutant spectra have been multiplied by factors of ~0.83 after normalization to the peak to peak amplitudes of the negative ferricyanide peak at 2115 cm^{-1} and the positive ferrocyanide peak at 2038 cm^{-1} to maximize overlap with the wild-type spectra. Dark-*minus*-dark control traces are included to show the noise level (bottom traces).

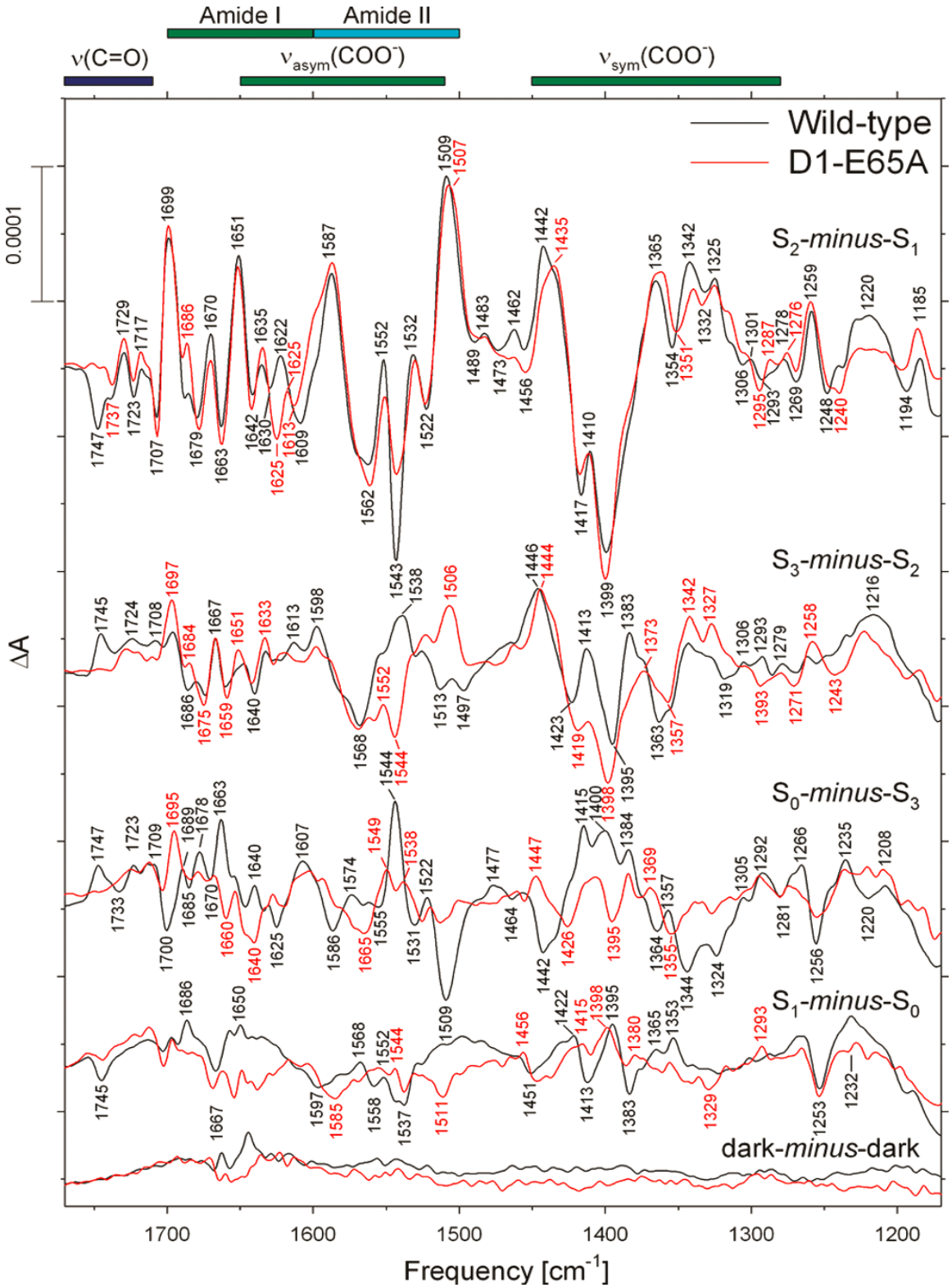
Amide I
Amide II
ν(C=O)
ν_asym(COO⁻)
ν_sym(COO⁻)
Wild-type
D1-E65A
0.0001
S2-minus-S1
S3-minus-S2
S0-minus-S3
S1-minus-S0
dark-minus-dark
ΔA
1700
1600
1500
1400
1300
1200
Frequency [cm-1]

Figure 3.3

Figure 3.4 Comparison of the midfrequency FTIR difference spectra of Mn-depleted wild-type (black) and intact D2-E312A (red) PSII core complexes in response to the first of six successive flash illuminations applied at 273 K. The data (plotted from 1770 to 1170 cm−1) represent the averages of nine Mn-depleted wild-type and nine D2-E312A samples (10800 scans each). The fraction of D2-E312A PSII reaction centers lacking Mn_4Ca clusters (0.31) was estimated from the amplitude of the negative peak at 1706 cm^{-1} (see the text for details). Accordingly, the spectrum of the Mn-depleted wild-type sample shown in this figure was multiplied by a factor of 0.31 after normalization to the peak to peak amplitudes of the negative ferricyanide peak at 2115 cm^{-1} and the positive ferrocyanide peak at 2038 cm^{-1}.

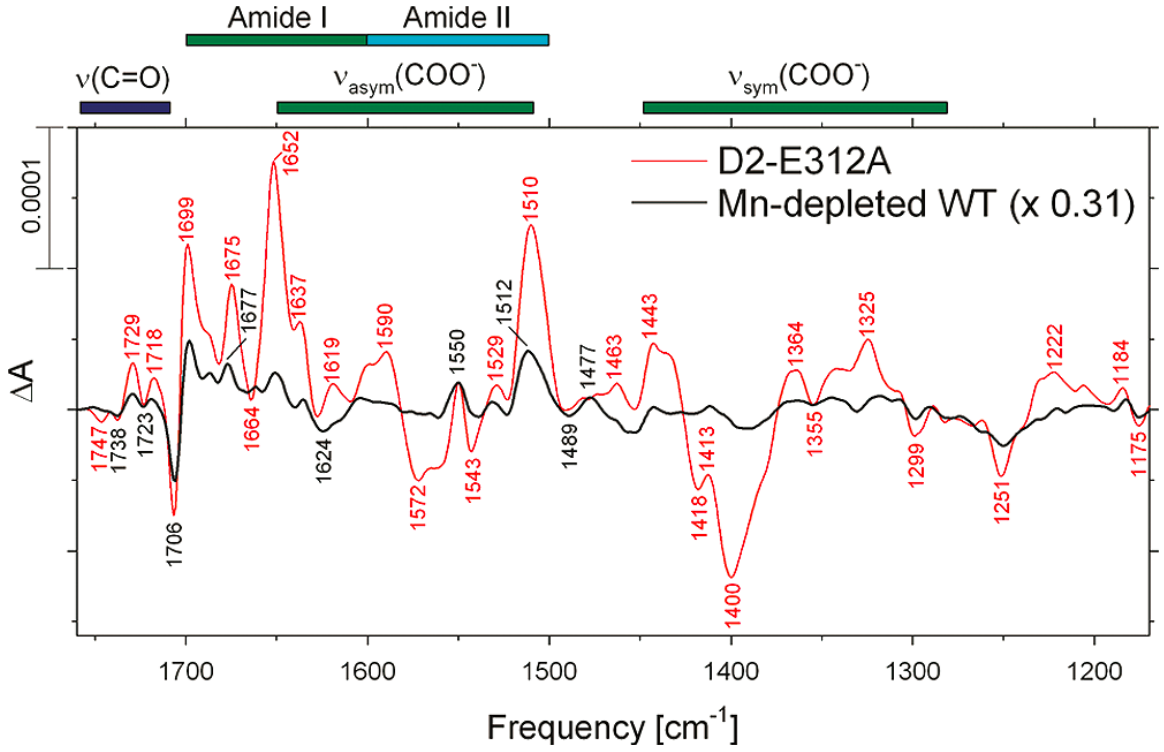
Amide I
Amide II
ν(C=O)
ν_asym(COO⁻)
ν_sym(COO⁻)
D2-E312A
Mn-depleted WT (x 0.31)
0.0001
ΔA
1747
1738
1729
1723
1718
1706
1699
1675
1677
1664
1652
1637
1624
1619
1590
1572
1550
1543
1529
1512
1510
1489
1477
1463
1443
1418
1413
1400
1364
1355
1325
1299
1251
1222
1184
1175
1700
1600
1500
1400
1300
1200
Frequency [cm⁻¹]

Figure 3.4

Figure 3.5 Comparison of the midfrequency FTIR difference spectra of wild-type (black) and D2-E312A (red) PSII core complexes in response to four successive flash illuminations applied at 273 K. The data (plotted from 1770 to 1170 cm^{-1}) represent the averages of nine wild-type and nine D2-E312A samples (10800 scans each). The S_2-*minus*-S_1 FTIR difference spectrum of D2-E312A was corrected for the presence of a significant population of Mn-depleted PSII reaction centers (see the text for details). To facilitate comparisons, the mutant spectra have been multiplied by factors of ~1.4 after normalization to the peak to peak amplitudes of the negative ferricyanide peak at 2115 cm^{-1} and the positive ferrocyanide peak at 2038 cm^{-1} to maximize overlap with the wild-type spectra. Dark-*minus*-dark control traces are included to show the noise level (bottom traces).

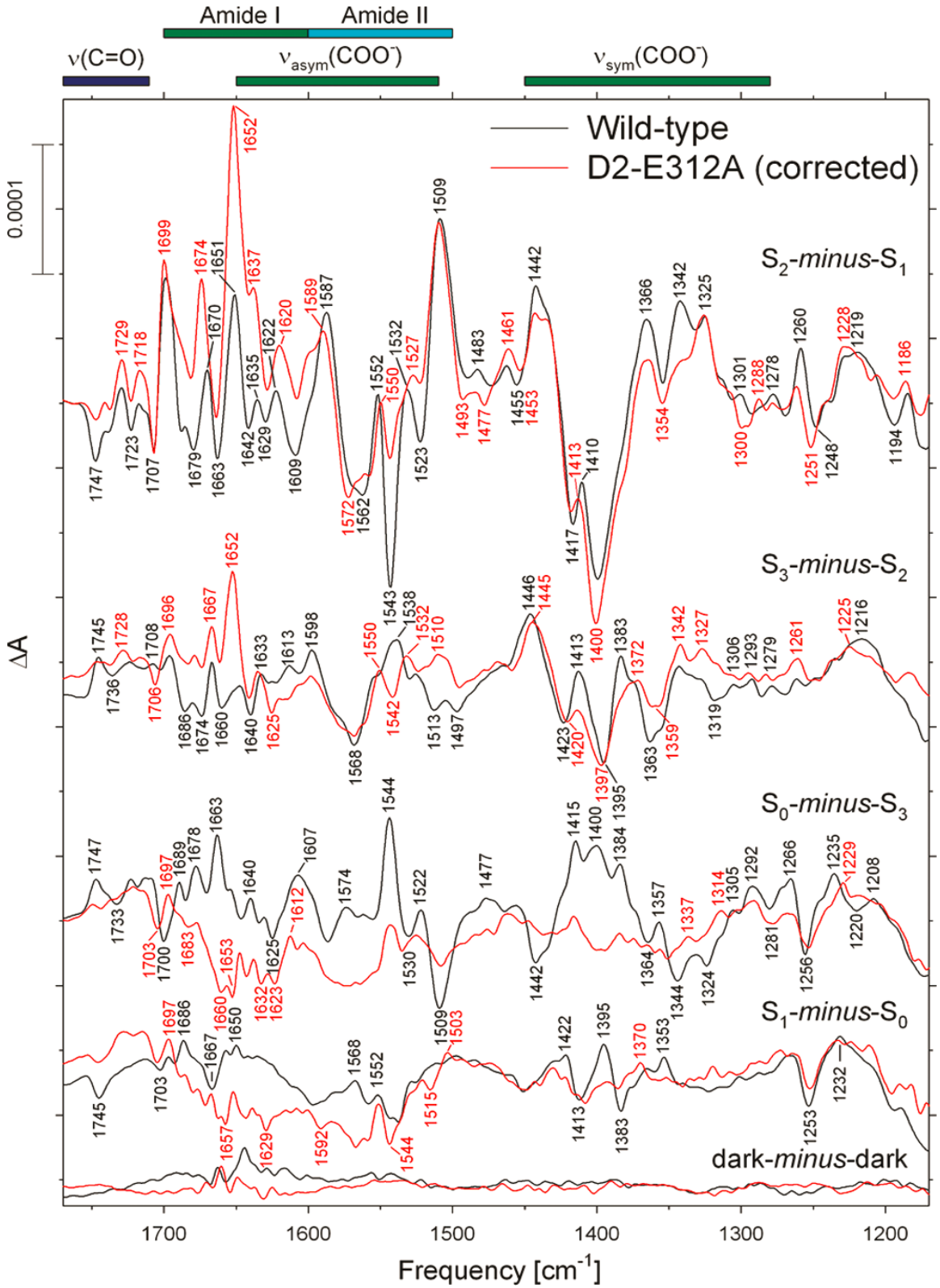
Amide I
Amide II
ν(C=O)
ν_asym(COO⁻)
ν_sym(COO⁻)
Wild-type
D2-E312A (corrected)
0.0001
ΔA
S2-minus-S1
S3-minus-S2
S0-minus-S3
S1-minus-S0
dark-minus-dark
1700
1600
1500
1400
1300
1200
Frequency [cm-1]

Figure 3.5

Figure 3.6 Comparison of the midfrequency FTIR difference spectra of wild-type (black) and D1-E329Q (red) PSII core complexes in response to four successive flash illuminations applied at 273 K. The data (plotted from 1770 to 1170 cm^{-1}) represent the averages of nine wild-type and four D1-D329Q samples (10800 and 4800 scans, respectively). The spectra have been normalized to the peak to peak amplitudes of the negative ferricyanide peak at 2115 cm^{-1} and the positive ferrocyanide peak at 2038 cm^{-1}. Dark-*minus*-dark control traces are included to show the noise level (bottom traces).

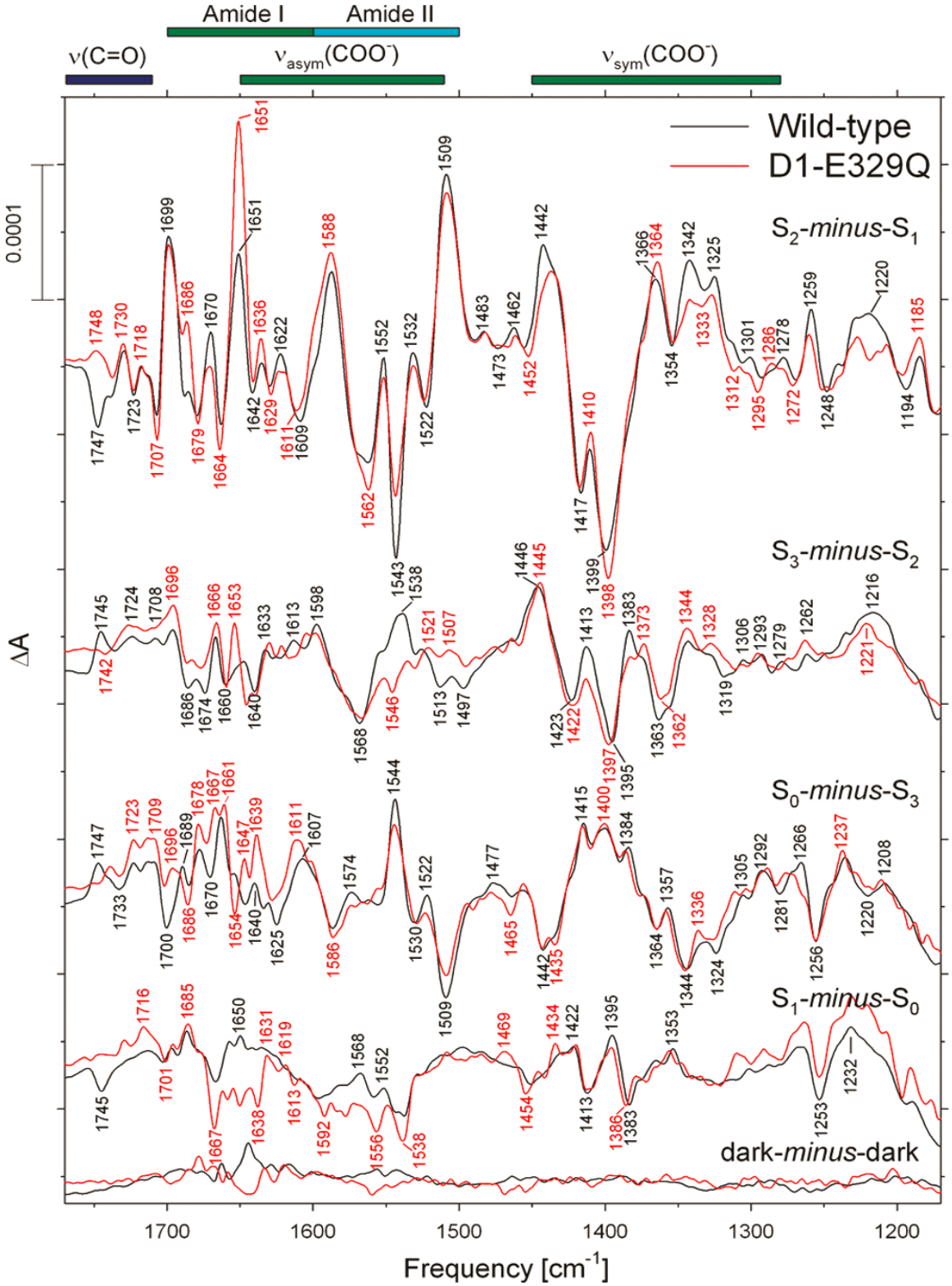
Amide I
Amide II
ν(C=O)
ν_asym(COO⁻)
ν_sym(COO⁻)
Wild-type
D1-E329Q
S2-minus-S1
S3-minus-S2
S0-minus-S3
S1-minus-S0
dark-minus-dark
0.0001
ΔA
Frequency [cm⁻¹]
1700
1600
1500
1400
1300
1200

Figure 3.6

Figure 3.7 Mn_4Ca cluster and its environment as depicted in the 2.9 Å crystallographic structural model of PSII from T. elongatus (PDB entry 3BZ1) (5). The four residues discussed in this panel are colored bright yellow (Asp61, Glu65, and Glu329 of the D1 polypeptide) or bright orange (Glu312 of the D2 polypeptide). The Mn, Ca, and Cl ions are depicted as red, orange, and green spheres, respectively. Tyrosine Y_Z and the protein ligands of the Mn_4Ca cluster are colored light yellow or orange (residues of D1 and CP43, respectively). Portions of water access, proton egress, and O_2 egress channels identified in the 2.9 Å structural model are colored blue, gray, and maroon, respectively (the channel coordinates from ref 35 were graciously provided by A. Zouni). In this model, the shortest distances between the carboxylate group and the nearest Mn ion are 4.6, 10.8, 11.3, and 7.5 Å for D1-Asp61, D1-Glu65, D2-Glu312, and D1-Glu329, respectively (5).

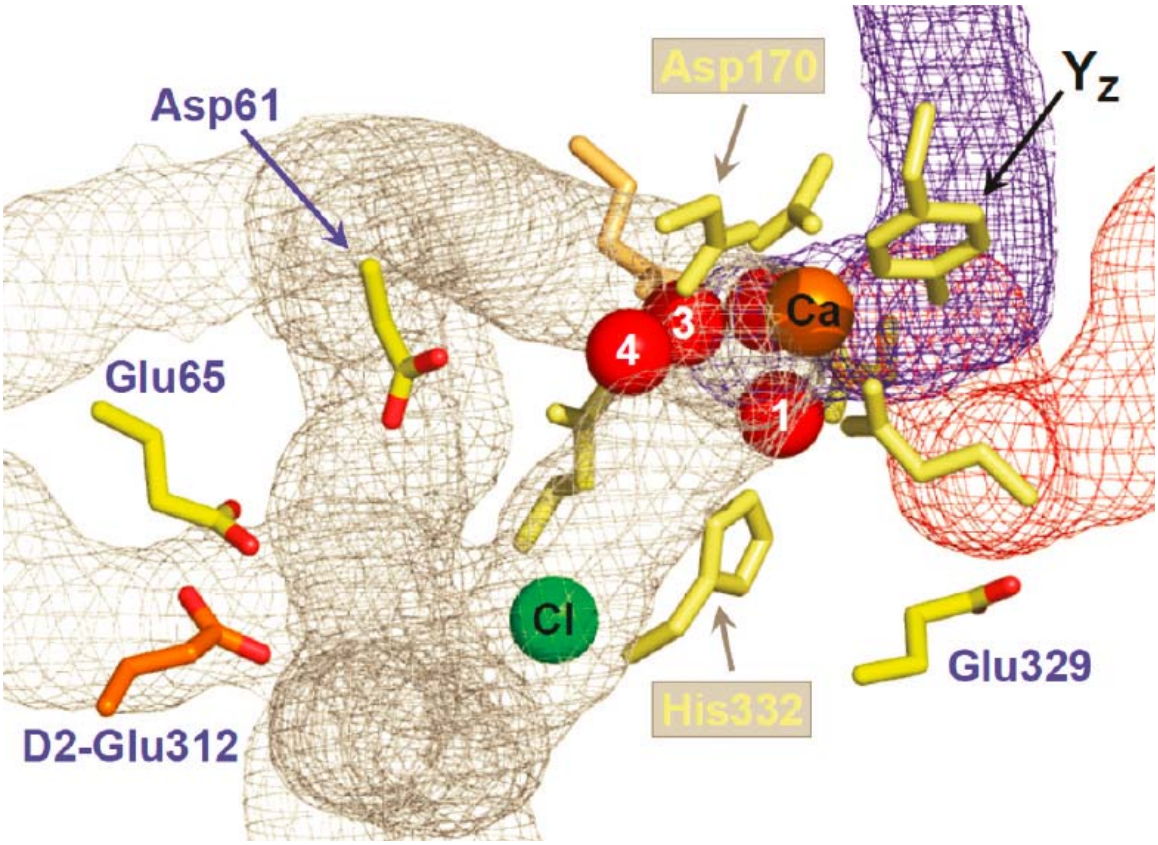

Figure 3.7

Figure 3.8. ν(C═O) region of the S_2-*minus*-S_1 FTIR difference spectra of (A) wild-type PSII core complexes maintained at a relative humidity of 99% (black) or 85% (blue) or as a dry film in the sample cell (red), (B) wild-type PSII core complexes exchanged into FTIR buffer containing H_2O (black) or D_2O (red), (C) wild-type (black) and D1-D61A (red) PSII core complexes, (D) wild-type (black) and D1-E65A (red) PSII core complexes, (E) wild-type (black) and D1-E312A (red) PSII core complexes [after correction of D2-E312A for the presence of Mn-depleted reaction centers (see the text for details)], and (F) wild-type (black) and D1-E329Q (red) PSII core complexes. The data have been reproduced from Figures 1A,B, 2, 3, 5, and 6, respectively.

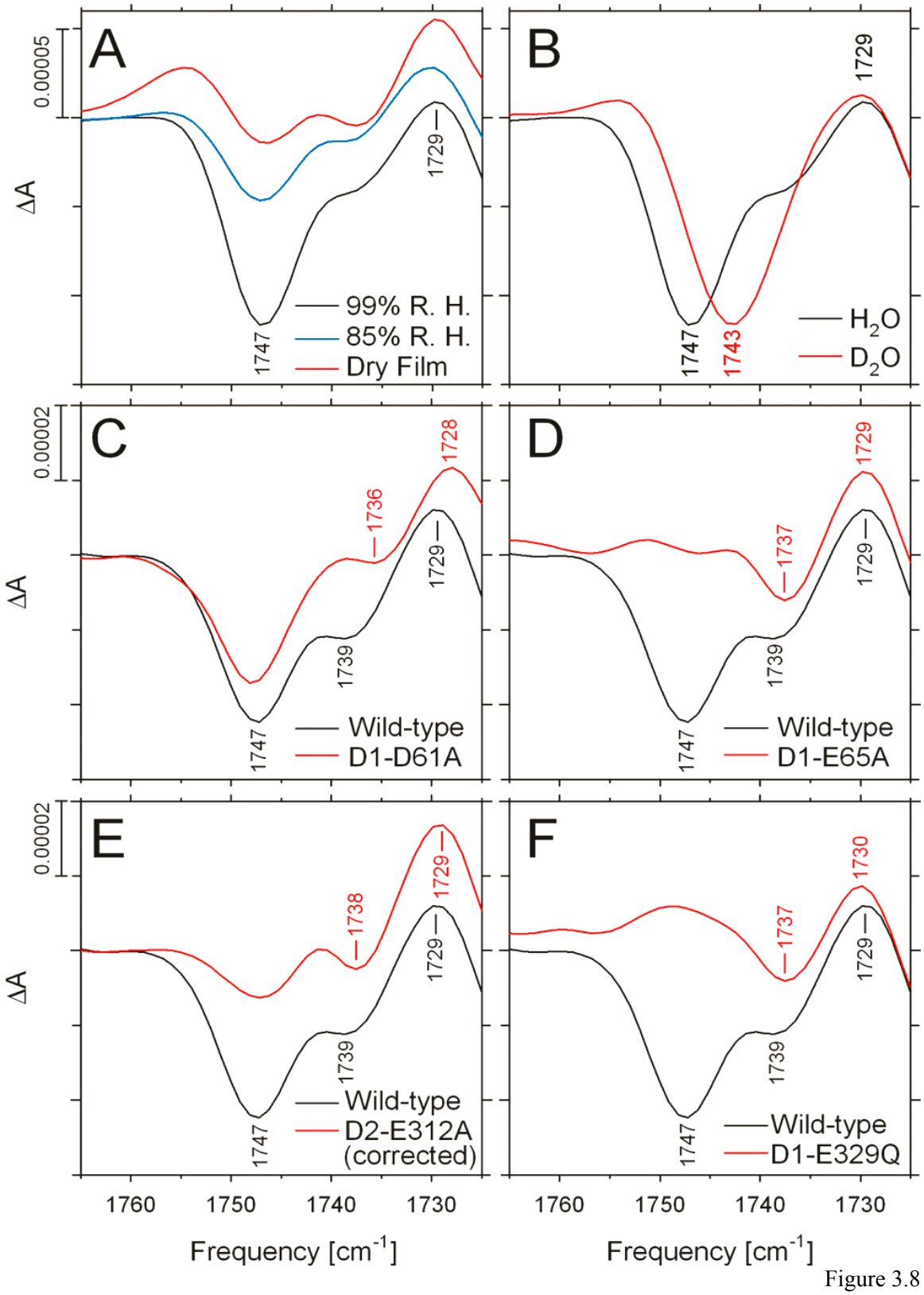
A
0.00005
ΔA
1729
1747
99% R. H.
85% R. H.
Dry Film
B
1729
1747
1743
H2O
D2O
C
0.00002
1728
1736
1729
1739
1747
Wild-type
D1-D61A
D
1729
1737
1729
1739
1747
Wild-type
D1-E65A
E
0.00002
1738
1729
1729
1739
1747
Wild-type
D2-E312A
(corrected)
F
1730
1737
1729
1739
1747
Wild-type
D1-E329Q
1760
1750
1740
1730
Frequency [cm-1]

Figure 3.8

CHAPTER 4

STUDY OF DEUTERIUM SUBSTITUTION AND THE MUTATION OF THREE POLAR RESIDUES OF THE BROAD CHANNEL ON HYDROGEN BONDING EFFECTS

4.1 Abstract

Thanks, in part, to the recent high resolution x-ray crystallographic structures, better guides exist for spectroscopic analysis. Different sized channels exist throughout PSII leading to and from the Mn_4Ca cluster and have been tentatively identified. Presence of polar groups, especially carboxylic acids, along the channels suggest a capacity for an interconnecting hydrogen bonding route, allowing dynamic bonding processes to occur during water oxidation. In an effort to examine this process, six mutations for three residues within the broad channel, a likely water or proton channel, were studied using FTIR difference spectroscopy. Careful inspection of the ν(C=O), particularly at the 1747 cm^{-1} band showed no effect by any of the mutants, D2-E323Q, D1-E333Q, D2-K317A, E, Q, and R. This indicates these residues are likely not involved in the hydrogen-bonding network. However, D1-E333Q did show many spectral variations, which can be attributed to heavy conformational change both at the Mn_4Ca cluster and a chloride ion to which its backbone nitrogen bonds. The D2-K317A, E, and Q mutants were unable to progress beyond S_2 storage state, suggesting D2-Lys317 serves as an important participant in a halogen bond to the chloride ion of the broad channel as well as a basis for structural integrity at the mouth of channel. D2-E323Q did not show evidence of any deviation from wild-type and is likely not directly involved in the extensive hydrogen-bonding network.

4.2 Introduction

The network of residues creating channels throughout PSII has a connection to an extending hydrogen-bonding network. As revealed in (1), a carboxylate within or at the edge of

this chain is shown to decrease its pK_a in response to the transition from S_1 to S_2 and can be monitored at the ν(C=O) region as previously discussed in Chapter 1.3. In an effort to identify this residue, carboxylates within purported water or proton egress channels are of particular interest, such as the broad channel (2 - 4). Such carboxylates do not have to be near the Mn_4Ca cluster as initially discovered with D2-Glu312, D1-Glu329, and D1-Glu65 to have an effect on the changing vibrational mode at 1747 cm^{-1} (1). A residue, D2-Glu323 was found in the broad channel, approximately 16 Å from the Mn_4Ca cluster and 10 Å from a chloride ion within the broad channel (3 - 5). In addition to a carboxylic acid residue, a free metal chloride ion, Cl^-, was located. Cl^- ions in PSII have been considered to play an important role in oxygen evolution (6 – 9). For decades, the role, benefit, and necessity of chloride has been studied with respect to photosynthesis and PSII, though the full spectrum of Cl^- participation with respect to the active site and protein channels is still not well understood (9).

Only now, with the recent x-ray crystallographic studies has the location of two Cl^- in two distinct areas been identified near the Mn_4Ca cluster using Br^- or I^- substitution (2 - 5). Location of Cl^-1 with respect to the OEC and broad channel can be seen in Figure 4.1. A residue which could contribute to an extensive hydrogen-bonding network within this channel is D2-Glu323 and is depicted within the channel in Figure 4.2. Cl^-1, greater than 6.5 Å from the Mn_4Ca cluster (5) is involved in a halogen bond with a nitrogen from the side-chain amine group of D2-Lys317 and backbone of D1-Glu333 which can be seen in Figures 4.3 and 4.4 respectively. Cl^-2, greater than 7 Å from the cluster, is between CP43-Glu354 and D1-Asn 338 backbone nitrogens. Both Cl^- are also surrounded by two water molecules.

Cl^-1 likely does not interact with the cluster directly. Based on evidence from similarly structured proteins such as α-amylase and angiotensin converting enzyme, the presence of Cl^-1 within the channel has been proposed to prevent a salt-bridge from forming between D2-Lys317

and/or D1-Glu333 with nearby D1-Asp61. The salt bridge would cause a conformational change resulting in shifted D1-Glu333, D1-His332, and lowering the pK_a of D1-Asp61 making proton egress a more difficult procedure, inhibiting the catalytic cycle (10). A Cl^- binding location exists within the broad channel, Cl^-1, and large channel, Cl^-2 (2, 3, 5). Cl^-1 exists near the opening of the broad channel, which contains two of the previously discussed hydrogen bonding network residues, D1-Glu65 and D2-Glu312 (1). In an effort to better comprehend the source of changes seen in the ν(C=O) region as well as the activity of Cl^-1, the residue D2-Glu323 as well as the two residues near Cl^-1, D2-Lys317 and D1-Glu333 all in the broad channel were examined using site directed mutagenesis and FTIR spectroscopy.

4.3 Materials and Methods

Sample Preparation

For wild-type tests prepared in D_2O, samples (approximately 70 μg of Chl a) were exchanged into deuterated water FTIR analysis buffer [40 mM sucrose, 10 mM MES-NaOH (pH 6.0), 5 mM $CaCl_2$, 5 mM NaCl, and 0.06% (w/v) n-dodecyl β-d-maltoside (11, 12)]. The FTIR analysis buffer and the potassium ferricyanide and glycerol solutions were prepared with 99.9% D_2O. The pD of the FTIR analysis buffer prepared in D_2O was adjusted with freshly opened 99.5% NaOD and the pD value was obtained by addition of 0.40 to the pH meter reading (13, 14). The sample passed through a 70 μL centrifugal gel filtration column at 27g (15). Samples concentrated to 10 μL were mixed with $^1/_{10}$ volume of fresh 100 mM potassium ferricyanide (dissolved in 99.9% deuterated water), spread to a diameter of ~10 mm on a 15 mm diameter BaF_2 window, and then dried lightly (until tacky) under a stream of dry nitrogen gas. Relative humidity of the sample in the FTIR cryostat was obtained by adding 20% (v/v) glycerol made with 99.9% deuterated water dropwise, away from but adjacent to the sample. A second IR

window with a 0.5mm Teflon spacer was placed between the windows and sealed with silicon-free high-vacuum grease. The sample was then loaded into the FTIR cryostat and equilibrated for 2 h at 273.0 K. Absorbance of the amide I band at 1657 cm^{-1} was no less than 0.8 and no greater than 1.2 for optimum spectral quality.

All mutant manipulations were conducted under dim green light at 4 °C. Samples of 30 µg of Chl *a* were exchanged into FTIR analysis buffer [40 mM sucrose, 10 mM MES-NaOH (pH 6.0), 5 mM $CaCl_2$, 5 mM NaCl, and 0.06% (w/v) *n*-dodecyl β-d-maltoside (11, 12)] passing through 70 µL centrifugal gel filtration column at 27*g* (15) and further concentrated to 10 µL in Microcon centrifugal filter units. Sample was pipetted onto a 25 mm diameter BaF_2 window in a 10 mm area with $^1/_{10}$ volume of fresh 100 mM potassium ferricyanide in water and dried under a gentle stream of nitrogen gas until tacky. Relative humidity of 99% was maintained using 1 µL x 4 drops of 20% (v/v) glycerol on the outer edge of the BaF_2 window, sealed with a rubber o-ring and additional BaF_2 window, creating a contained environment between the sandwiched windows (16). The sample was immediately loaded into the water-cooled FTIR cryostat and brought to ~ 273.0 K in darkness for 1½ h. Absorbance of the amide I band at 1657 cm^{-1} was no less than 0.8 and no greater than 1.2 for optimum spectral quality.

Measurement of FTIR Spectra

Deuterated water wild-type experiments were done on a Bruker Equinox 55, collecting midfrequency FTIR spectra at a spectral resolution of 4 cm^{-1} as described previously (12, 13, 17). Illumination by frequency-doubled Q-switched Nd:YAG laser was supplied at ~25 mJ/flash (~7 ns fwhm). One preflash was applied after dark adaptation and followed by 5 minutes of dark recovery time in order to oxidize Y_D. Six successive flashes occurred over an interval of 12 s each. Two single-beam spectra were recorded before the first flash, and one single-beam spectrum was recorded starting 0.33 s after the first and subsequent flashes to allow for the

oxidation of $Q_A^{\bullet -}$ by the ferricyanide added to the sample. Each spectrum consists of 100 scans and was collected over 12 series and averaged. Difference spectra were created by dividing the each preceding flash by its following flash, showing transitions between S-state. Each flash pushes the cycle to the next S-state which then loops after the fourth flash, S_2-*minus*-S_1 for the first flash and so on for S_3-*minus*-S_2, S_0-*minus*-S_3, and S_1-*minus*-S_0. After 30 minute dark adaptation back to the dark stable S_1, the process repeats.

Mutant experiments were tested similarly in a Bruker Vertex 70 spectrometer. Mutants studied in the Vertex 70 did not require a preflash. For the experiments, a series of 6 flashes were applied after initial 1½ h dark adaptation and 30 min dark adapting intervals 13 times after, each "series" consisting of 100 scans per single flash. Two single-beam spectra were recorded before the flash, and a single-beam spectrum was recorded starting 0.33 s after the flash. Difference spectra were obtained as explained above and averaged at 10,000 or greater scans.

Oxygen Rate

Light-saturated, steady state rates of O_2 evolution and chlorophyll a (Chl_a) concentrations were measured as described previously (18).

4.4 Results

4.4.1 Comparison of mutant to wild-type oxygen evolving rate

The O_2 evolving rates for D2-E323Q, D2-K317A, D2-K317E, D2-K317Q, D2-K317R, and D1-E333Q compared to that of the wild-type rate are provided in Table 1. Activity of mutants show D2-E323Q to have about half oxygen evolving rate of wild-type or O_2 μmol (mg of Chl)$^{-1}$ h^{-1}. The D2-Lys317 mutants vary between rates with D2-K317A being the highest at 81%, D2-K317E and D2-K317Q about 14%, and D2-K317R at 24%. The D1-E333Q mutant used for

these experiments has an unusually high rate of 21% that of wild-type compared to previous preparations of the same mutant, used in other studies.

4.4.2 Effect of 99.9% deuterated water on vibrational stretching modes in ν(C=O) of wild-type during the S_1 to S_2, S_2 to S_3, S_3 to S_0, and S_0 to S_1 transitions

Previously studied effects of relative humidity and deuterated water FTIR buffer showed a correlation of hydration to the vibrational mode at 1747 cm^{-1} of the ν(C=O) region (1). Only S_2-*minus*-S_1 were previously examined, though effects should be seen throughout all S-states. To show this, FTIR difference spectra were taken for wild-type samples prepared using 99.9% D_2O in FTIR buffer and compared to wild-type prepared in regular FTIR buffer. The spectra that were induced by the first, second, third, and fourth flashes correspond to the S_2-*minus*-S_1, S_3-*minus*-S_2, S_0-*minus*-S_3, and S_1-*minus*-S_0 FTIR difference spectra, respectively, in Figure 4.5.

4.4.3 Function of Glutamate-323 of the D2 polypeptide during the S_1 to S_2, S_2 to S_3, S_3 to S_0, and S_0 to S_1 transitions

The midfrequency difference spectra for the mutant D2-E323Q S-state cycle is shown against wild-type in Figure 4.6 followed by the S_2-*minus*-S_1 spectrum only in Figure 4.7 and the double difference wild-type-*minus*-D2-E323Q in Figure 4.8. The data are an average of 12,200 scans and normalized vertically at ferri/ferro peaks 2115 and 2038 cm^{-1} by a factor of 2.6 times wild-type, then at 1442 and 1400 cm^{-1} by 1.2 times wild-type and added 0.0000198 to baseline. The spectra of these figures show a mutant which can perform the four S-states very similarly to wild-type, with a S_2-*minus*-S_1 spectrum that is nearly identical to that of wild-type. Slight

difference occurs at amide I as well as a very slight shelf of 1385 cm^{-1} of the $\nu_{sym}(COO^{-})$, made more visible in the double difference spectrum. There is no significant change seen at the ν(C=O).

4.4.4 Function of Glutamate-333 of the D1 polypeptide during the S_1 to S_2, S_2 to S_3, S_3 to S_0, and S_0 to S_1 transitions

FTIR difference spectra for the mutant D2-E333Q were taken in four successive flash illuminations resulting in spectra corresponding to the S_2-*minus*-S_1, S_3-*minus*-S_2, S_0-*minus*-S_3, and S_1-*minus*-S_0, displayed in Figure 4.9. D1-E333Q spectra, shown in red, represent an average of 10,800 scans. It should be noted that the averaged data sets show characteristics of manganese depletion, consisting of a large negative peak at 1706 cm^{-1} and positive peaks at 1698 and 1512 cm^{-1}. For better spectral clarity, the manganese depleted spectrum was subtracted from S_2-*minus*-S_1, as seen in Figure 4.10. Resulting deviations from wild-type-*minus*-mutant D1-E333Q FTIR double difference spectra for the first flash are seen in Figure 4.11. Significant differences are seen in both amide and $\nu_{asym}(COO^{-})$ regions, mostly consisting of positive peaks. Additional changes, less pronounced, are located in the ν(C=O) and $\nu_{sym}(COO^{-})$ regions consisting of a small positive peak and small negative peak, respectively.

4.4.5 Function of Lysine-317 of the D2 polypeptide during the S_1 to S_2, S_2 to S_3, S_3 to S_0, and S_0 to S_1 transitions

FTIR difference spectra were taken for four D1-Lys317 mutants including alanine, glutamic acid, glutamine, and arginine. The first, D1-K317A was observed at all four transitions, S_2-*minus*-S_1, S_3-*minus*-S_2, S_0-*minus*-S_3, and S_1-*minus*-S_0. Difference spectra are an average of 11,200 scans and are normalized vertically at ferri/ferro peaks 2115 and 2038 cm^{-1} against wild-type by factor of 1.5, then normalized at 1442 and 1399 cm^{-1} by factor of 1.85 to the mutant data.

Though a full cycle program was used, the mutant did not show evidence of cycling (data not shown), so only S_2-*minus*-S_1 data are presented (Figure 4.12). The mutant D1-K317A as compared to wild-type show some variation in the amide I/II and symmetric/asymmetric carboxylate regions. There is little change in the carbonyl of the carboxylic acid stretching region. The double difference spectrum for wild-type-*minus*-D2-K317A is shown in Figure 4.13. A very large negative peak at 1526 cm^{-1} either belongs to amide II or $\nu_{asym}(COO^-)$. The lysine to alanine mutation could cause a rather large conformational change due to the missing side-chain nitrogen to Cl^-1 halogen bond. Since Cl^-1 is also bound to D1-Glu333, the change could effect the position of that residue, a bidentate ligand to Mn3 and Mn4, creating slight changes seen in the spectrum carboxylate regions. No apparent change is seen in the ν(C=O) region.

The second mutation, D2-K317E, was also done in four successive flash illuminations and is an average of 12,000 scans, presented against wild-type in Figure 4.14. Data is normalized vertically against wild-type by factor of 1.3 at ferri/ferro peaks 2115 and 2039 cm^{-1} then 1.5 times wild-type at 1442 and 1397 cm^{-1}, subtracting 0.00003 from baseline. As with the D2-K317A mutant, D2-K317E did not show evidence of cycling through any storage state beyond S_2. The mutant versus wild-type spectra show variation in both amide regions as well as $\nu_{asym}(COO^-)$. There are slight differences at the $\nu_{sym}(COO^-)$ region and very little change at ν(C=O) region as compared to wild-type, The double difference spectrum for wild-type-*minus*-D2 K317E is shown in Figure 4.15. As with D2-K317A mutant, D2-K317E has a very large negative peak at 1526 cm^{-1}. The lysine to glutamic acid mutation could act similar to alanine as it does not have a side-chain nitrogen for Cl^-1 halogen bond.

The third mutant, D2-K317Q, followed four successive flash illuminations and is an average of 11,000 scans, presented against wild-type in 4.16. Data is normalized vertically against wild-type by factor 2.27 at ferri/ferro, 2115 and 2039 cm^{-1} then 1.2 at 1433 and 1397 cm^{-1},

subtracting 0.00002 from baseline. As with the previous two mutants, D2-K317Q did not show evidence of cycling through any storage state beyond S_2. The double difference spectrum for wild-type-*minus*-D2-K317Q is shown in Figure 4.17. For the S_2-*minus*-S_1 spectrum, clear differences can be seen in amide I/II and asymmetric carboxylate. There is little change in $\nu_{sym}(COO^-)$ and only a small, positive difference at ν(C=O) regions. Additionally, like D2-K317A and D2-K317E, D2-K317Q has a large negative peak at 1526 cm^{-1}. The lysine to glutamine mutation does have a side-chain nitrogen, though is not charged and also, depending on the conformation, may not be positioned within range of Cl^-1. This could cause similarity of results as the previous two mutants described. In addition, it may create an environment for an addition hydrogen bond to be created at the channel, explaining the slight positive peak at 1747 cm^{-1} in the double difference spectrum.

The last mutant, D2-K317R, followed four successive flash illuminations and is an average of 13,200 scans, presented against wild-type in Figure 4.18 and closer inspection of the first flash is seen in Figure 4.19. The double difference S_2-*minus*-S_1 spectrum for wild-type-*minus*-D2-K317R is shown in Figure 4.20. Since the mutant had similar magnitude at the ferri/ferro peaks, mutant data was only normalized at 1431 and 1400 cm^{-1} vertically by factoring 1.6 times wild-type data.

Unlike the previous D2-Lys317 mutants, D2-K317R did show slight evidence of cycling through storage states. The mutant spectral magnitude is smaller than wild-type for S_2-*minus*-S_1, S_3-*minus*-S_2, S_0-*minus*-S_3, and S_1-*minus*-S_0, but is normalized for equivalency throughout the comparison. Characteristics of cycling through the S-states are apparent, suggesting a complete cycle is taking place. The mutant versus wild-type S_2-*minus*-S_1 spectrum shows numerous deviations throughout the 1800 – 1200 cm^{-1} range, a slight difference at the $\nu_{sym}(COO^-)$ and ν(C=O) regions while the majority in amide I/II and $\nu_{asym}(COO^-)$. Interesting deviations seen in

the double difference spectrum from the previous D2-K317 mutants are a positive peak at 1756 cm^{-1}, negative peak at 1510 cm^{-1} , and the lack of negative peak at 1526 cm^{-1}. The lysine to arginine mutation has a similar size as well as a positively charged side-chain nitrogen. Opportunity exists for arginine to have a similar interaction as lysine with $Cl^{-}1$.

4.5 Discussion

Comparison of the individual FTIR difference spectra of wild-type PSII core particles exchanged into 99.9% D_2O shows that the negative band at 1743 cm^{-1} in the S_2-*minus*-S_1 spectrum appear to correlate with a positive band at 1742 cm^{-1} in the S_0-*minus*-S_3 spectrum and that a positive band at 1740 cm^{-1} in the S_3-*minus*-S_2 spectrum appears to correlate with a negative band at 1740 cm^{-1} in the S_1-*minus*-S_0 spectrum. The H_2O wild-type behaves similarly with 1747 cm^{-1} 1st flash, 1746 cm^{-1} 3rd flash and then 1745 cm^{-1} 2nd flash, 1744 cm^{-1} 4th flash. Between D_2O and H_2O wild-type samples there is a consistent down shift of between 3 and 5 wavenumbers, through rounding (from decimal places not seen in figure) it is actually closer to a shift of 4 over the course of the cycle. The peaks do not stay aligned in a single frequency but wobble slightly, about 2 wavenumbers, between each S-state. This could be due to two different carboxylates acting oppositely. A carboxylate decreases its pK_a,, shown by the negative 1747 cm^{-1} band during the S_1 to S_2 transition, then reverses during the S_3 to S_0 transition. Then another carboxylate group increases its pK_a during the S_2 to S_3 transition and reverses during the S_0 to S_1 transition. Any effect of the hydrogen bonding network's influence on the carboxylate's environment would be difficult to determine since not all participants have been accounted for. Since the shifts are a characteristic of both D_2O and H_2O wild-type samples, they are likely not due to buffer interactions as both samples were made otherwise identically.

Further testing interactions within the ν(C=O) region, the D2-E323Q mutant was made and observed through FTIR difference spectra. Though the mutant exists within the broad channel

as D1-Glu65 and D2-Glu312 do, it does not show the same spectral features at 1747 cm^{-1} as these mutants do (3 - 5). In fact, the D2-E323Q mutant cycles as wild-type spectra do, though at at a magnitude factor of 2.6 less. Given the oxygen evolving rate is 50% less than that of wild-type, this is a reasonable result. The residue D2-Glu323 shows no evidence of participation within the hydrogen-bonding network.

Closer to the Mn_4Ca cluster yet still in the broad channel, the D1-Glu333 residue lies with its side chain oxygens coordinated to Mn3 and Mn4 and backbone nitrogen facing the Cl^-1 within the channel (5, 10). Mutation of this residue causes apparent manganese disruption as shown by the manganese depleted features in the first flash spectrum. However, enough features remain that activity can be observed, with some evidence of at least partial cycling. There are noticeable variations between mutant and wild-type spectra, mostly occurring within the amide I/II and $\nu_{asym}(COO^-)$ regions, but also less distinctly at $\nu(C=O)$ and $\nu_{sym}(COO^-)$. The D1-E333Q mutation seems to cause enough conformational changes within the structure that the oxygen evolving rate is, at best, only one-fifth that of wild-type and seems to struggle completing transitions through S-state cycling. This mutant regularly gives very low oxygen evolving rates as well as low magnitude FTIR difference spectra. Perhaps the conformational changes taken on by the D1-E333Q mutant are not always the same as it seems to be in a key location between the Mn_4Ca cluster and water/proton egress (broad) channel, immediately next to the Cl^-1 ion, thus giving regularly inconsistent activity and expressing "noise" observed in a lot of the spectra.

On the other side of Cl^-1 within the broad channel lies D2-Lys317. This residue is thought to participate in halogen bonding to Cl^-1. Considering the similarly structured α-amylase and angiotensin converting enzyme and lysine interactions, this seems to be a very likely case (10). Four mutations were performed with alanine, glutamic acid, glutamine, and arginine. D2-K317A showed no difference from wild-type in the $\nu(C=O)$ region. While some variation does

exist within the amide I/II and $\nu_{asym}(COO^-)$ regions, this is likely due to conformational change as a result of the mutation so near Cl^-1. However, the oxygen evolving rate for this mutant is rather good at 81% that of wild-type. This is counterintuitive to the FTIR difference spectra represented, which show no ability to pass beyond the S_2 state. It is possible that whatever structural perturbations occur as a result of the mutation briefly allow oxygen to evolve but cannot readapt to the S_1 state easily nor precisely pass through the S-states with much synchronicity. D2-K317E and D2-K317Q show very similar FTIR difference spectra between each other, particularly the large negative peak at 1526 cm^{-1} of the double difference spectra, which is shared by these three mutations. Both 317E and 317Q have a low oxygen evolving rate of 13-14% that of wild-type. In addition, FTIR difference spectra do not advance beyond the S_2 state. There many differences in the amide I/II and $\nu_{asym}(COO^-)$ regions and small changes at $\nu_{sym}(COO^-)$ region. Any change at ν(C=O) region, particularly 1747 cm^{-1}, is very slight. As with D2-K317A, these two mutants may be out of range to contribute to a halogen bond with Cl^-1, allowing a salt bridge to occur with D1-Asp61 and disrupting activity within the broad channel. The final mutant, D2-K317R, showed FTIR difference spectra very similar to that of wild-type. Though the oxygen evolving rate was approximately 25% that of wild-type, the mutant managed to successfully cycle through all S-states, though at a magnitude factor of 1.6 less. The double difference first flash spectrum for 317R does not have a large negative peak at 1526 cm^{-1} like the other three. It does, however, show some changes in all five regions under consideration. Many differences occur in amide I/II and $\nu_{asym}(COO^-)$ regions, but some noticeable changes occur as a positive peak at ν(C=O) and negative peak at $\nu_{sym}(COO^-)$ regions. Theoretically, the positively charged side-chain nitrogen could participate in a halogen bond with Cl^-1 as lysine does, retrieving some of the catalytic activity, but could also cause some structural perturbations in the process as there are still two other nitrogens jutting into the channel explaining the perturbed amide I/II region seen in the

difference spectra. None of the mutations for D2-Lys317 seem to affect first flash negative peak at 1747 cm^{-1} suggesting this residue, while important in the overall function of water oxidation, does not directly participate in the extensive hydrogen-bonding network as seen with D1-Glu65, D1-Glu329, and D2-Glu312.

4.6 References

1. Service, R. J., Hillier, W., and Debus, R. J. (2010) Evidence from FTIR Difference Spectroscopy of an Extensive Network of Hydrogen Bonds near the Oxygen-Evolving Mn_4Ca Cluster of PhotosystemII Involving D1-Glu65, D2-Glu312, and D1-Glu329, *Biochemistry 49*, 6655-6669.

2. Murray, J.W., Barber, J. (2007) Structural Characteristics of Channels and Pathways in Photosystem II including the Identification of an Oxygen Channel, *J. Struct. Biol*. *159* 228–237.

3. Ho, F, Styring, S (2008) Access Channels and Methanol Binding Site to the $CaMn_4$ Cluster in Photosystem II Based on Solvent Accessibility Simulations, with Implications for Substrate Water Access, *Biochimica et Biophysica Acta 1777* 140–153

4. Gabdulkhakov, A., Guskov, A., Broser, M., Kern, J., Müh, F., Saenger, W., Zouni, A., (2009) Probing the Accessibility of the Mn_4Ca Cluster in Photosystem II: Channels Calculation, Noble Gas Derivatization, and Cocrystallization with DMSO, *Structure 17*, 1223-1234.

5. Umena, Y., Kawakami, K., Shen, J.R., Kamiya, N. (2011) Crystal Structure of the Oxygen-Evolving Photosystem II at a Resolution of 1.9 Å, *Nature 473* 55-61.

6. Warburg, O., Luttgens, W. (1944) Weitere Experimente Zur Kohlensaureassimilation. *Naturwissenschaften 32*, 301.

7. Arnon, D., Whatley, F. (1949) Is Chloride a Coenzyme of Photosynthesis? *Science 110*, 554-556

8. Critchley, C. (1985) The Role of Chloride in Photosystem II, *Biochim. Biphys. Acta* 811, 33-46

9. Homann, P. (2002) Chloride and Calcium in Photosystem II: From Effects to Enigma, *Photosynthesis Research 7*, 169–175.

10. Pokhrel, R., McConnell, I., Brudvig, G. (2011) Chloride Regulation of Enzyme Turnover: Application to the Role of Chloride in Photosystem II. *Biochemistry 50* 2725-2734.

11. Yamanari, T., Kimura, Y., Mizusawa, N., Ishii, A., and Ono, T.-A. (2004) Mid- to Low-Frequency Fourier Transform Infrared Spectra of S-State Cycle for Photosynthetic Water Oxidation in *Synechocystis* sp. PCC 6803 *Biochemistry 43*, 7479– 7490.

12. Debus, R. J., Strickler, M. A., Walker, L. M., and Hillier, W. (2005) No Evidence from FTIR Difference Spectroscopy That Aspartate-170 of the D1 Polypeptide Ligates a Manganese Ion That Undergoes Oxidation during the S_0 to S_1, S_1 to S_2, or S_2 to S_3 Transitions in Photosystem II *Biochemistry 44*, 1367– 1374.

13. Glasoe, P. K., Long, F. A. (1960) Use of Glass Electrodes to Measure Acidities in Deuterium Oxide *J. Phys. Chem. 64*, 188– 191

14. Salomaa, P., Schaleger, L. L., and Long, F. A. (1964) Solvent Deuterium Isotope Effects on Acid-Base Equilibria *J. Am. Chem. Soc. 86*, 1– 7.

15. Strickler, M. A., Hillier, W., and Debus, R. J. (2006) No Evidence from FTIR Difference Spectroscopy that Glutamate-189 of the D1 Polypeptide Ligates a Mn Ion that Undergoes Oxidation During the S_0 to S_1, S_1 to S_2, or S_2 to S_3 Transitions in Photosystem II *Biochemistry 45*, 8801– 8811.

16. Noguchi, T. and Sugiura, M. (2002) Flash-Induced FTIR Difference Spectra of the Water Oxidizing Complex in Moderately Hydrated Photosystem II Core Films: Effect of Hydration Extent on S-State Transitions *Biochemistry 41*, 2322– 2330.

17. Strickler, M. A., Walker, L. M., Hillier, W., Britt, R. D., and Debus, R. J. (2007) No Evidence from FTIR Difference Spectroscopy That Aspartate-342 of the D1 Polypeptide Ligates a Mn Ion That Undergoes Oxidation during the S_0 to S_1, S_1 to S_2, or S_2 to S_3 Transitions in Photosystem II *Biochemistry 46*, 3151– 3160.

18. Chu, H.-A., Hillier, W., and Debus, R. J. (2004) Evidence that the C-Terminus of the D1 Polypeptide is Ligated to the Manganese Ion that Undergoes Oxidation During the S_1 to S_2 Transition: An Isotope-Edited FTIR Study *Biochemistry 43*, 3152– 3166.

4.7 Tables and Figures

Table 4.1: Comparison of PSII core complex particles for broad channel mutants D2-E323Q, D1-E333Q, D2-K317A, D2-K317E, D2-K317Q, and D2-K317R oxygen evolving rates against wild-type in O_2 μmol (mg of Chl)$^{-1}$ h^{-1}.

	Evolving Rate $\frac{O_2\ \mu mol}{(mg\ of\ Chl)\ h}$	Percent(%) Activity of Wild-type
D2-E323Q	2914	48
D1-E333Q	1312	21
D2-K317A	4955	81
D2-K317E	874	14
D2-K317Q	800	13
D2-K317R	1457	24
Wild-type	6120	

Table 4.1

Figure 4.1 Chloride-1 ion in broad channel at OEC. $Cl^{-}1$ green sphere, oxygen red sphere, manganese purple sphere, calcium yellow sphere. Channel residues in stick.

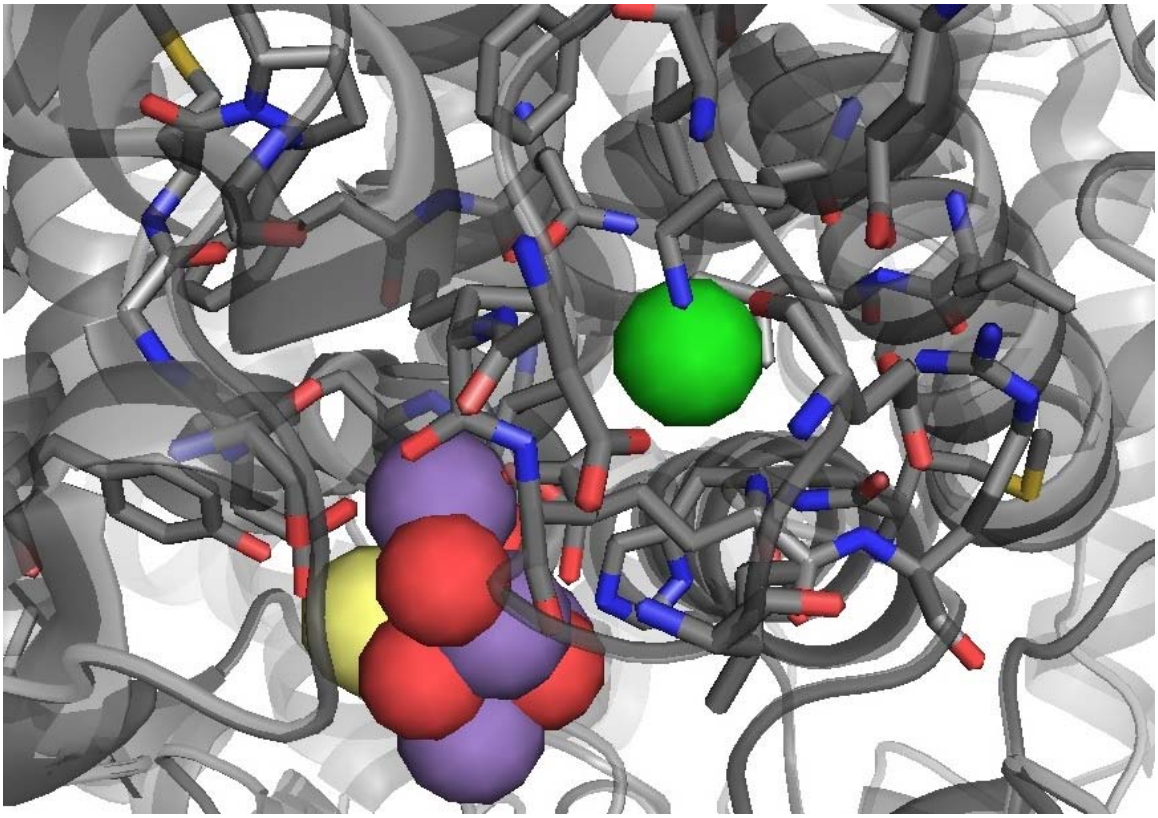

Figure 4.1

Figure 4.2 Chloride-1 ion in broad channel at OEC. $Cl^{-}1$ green sphere, oxygen red sphere, manganese purple sphere, calcium yellow sphere (not visible). Channel residues in stick, D1-Glu323 in yellow stick.

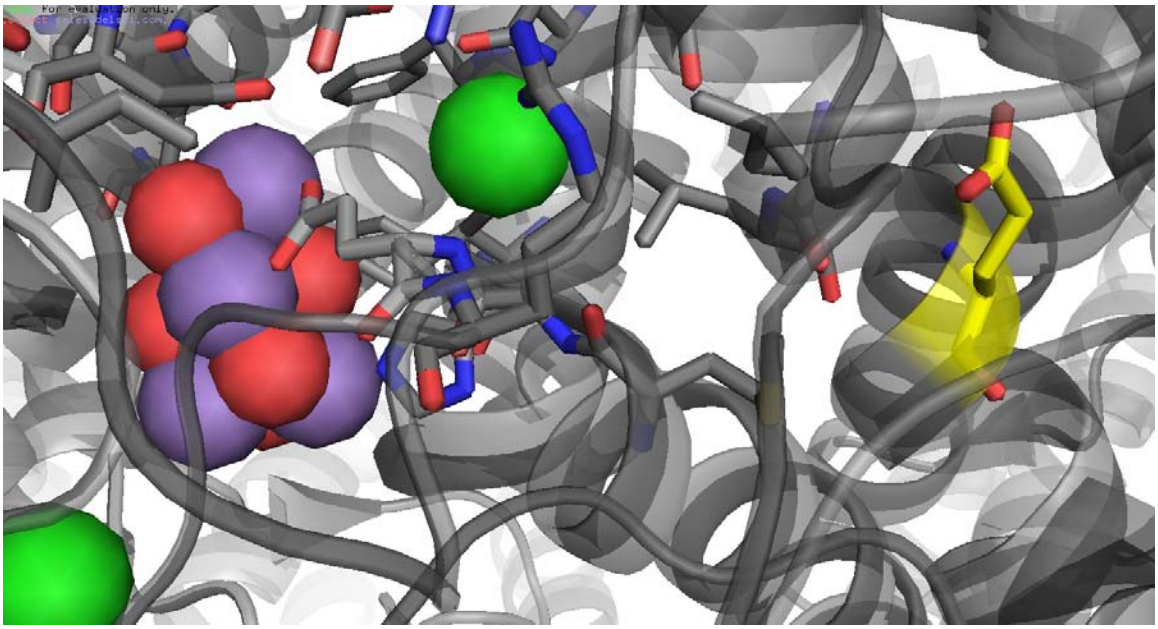

Figure 4.2

Figure 4.3 Chloride-1 ion in broad channel at OEC. $Cl^{-}1$ green sphere, oxygen red sphere, manganese purple sphere, calcium yellow sphere (not visible). Channel residues in stick, D1-Glu333 in yellow stick.

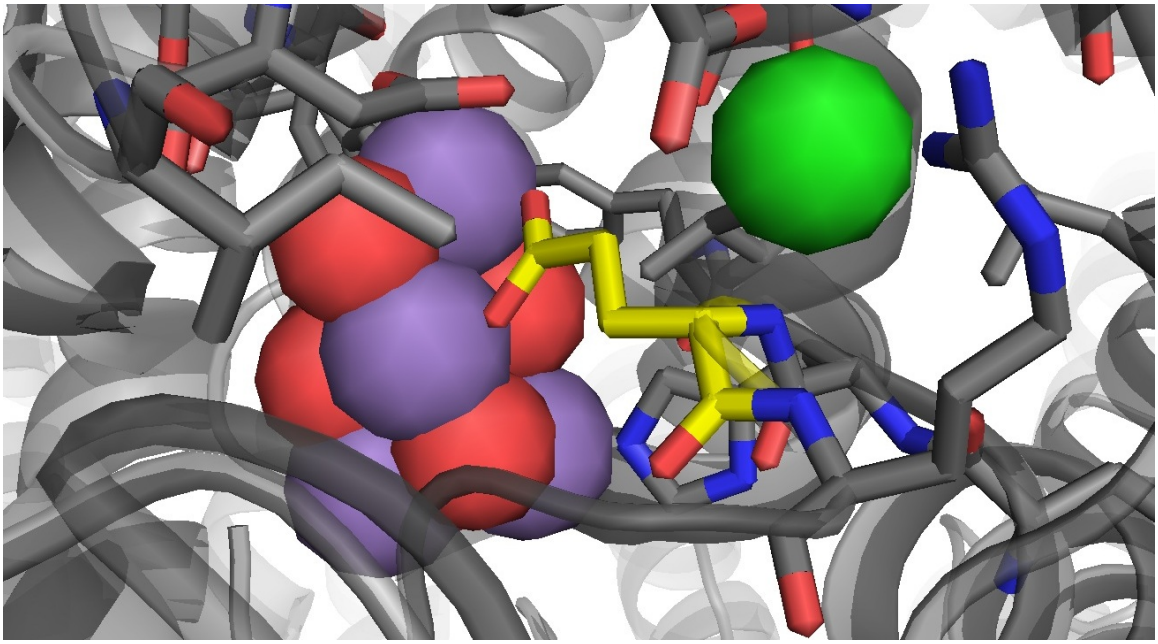

Figure 4.3

Figure 4.4 Chloride-1 ion in broad channel at OEC. $Cl^{-}1$ green sphere, oxygen red sphere, manganese purple sphere, calcium yellow sphere. Channel residues in stick, D2-Lys317 in yellow stick.

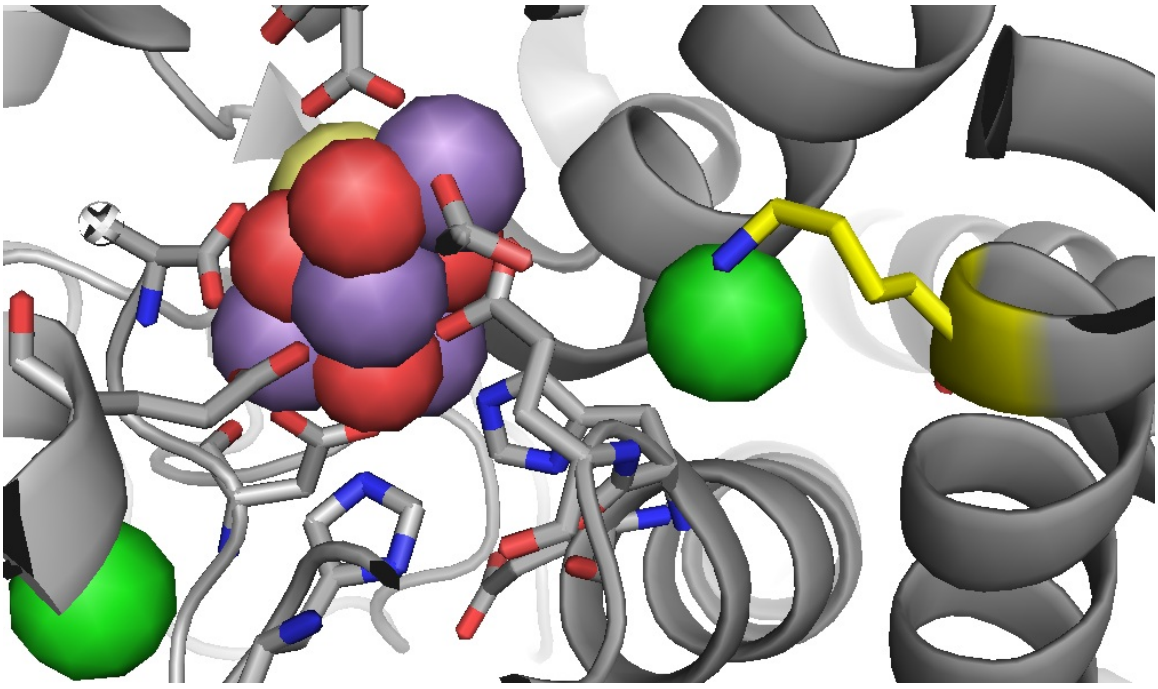

Figure 4.4

Figure 4.5 Comparison of the ν(C═O) region S-state FTIR difference spectra of wild-type sample prepared in (99.9%) deuterated FTIR buffer (red) compared to normally prepared wild-type sample (black).

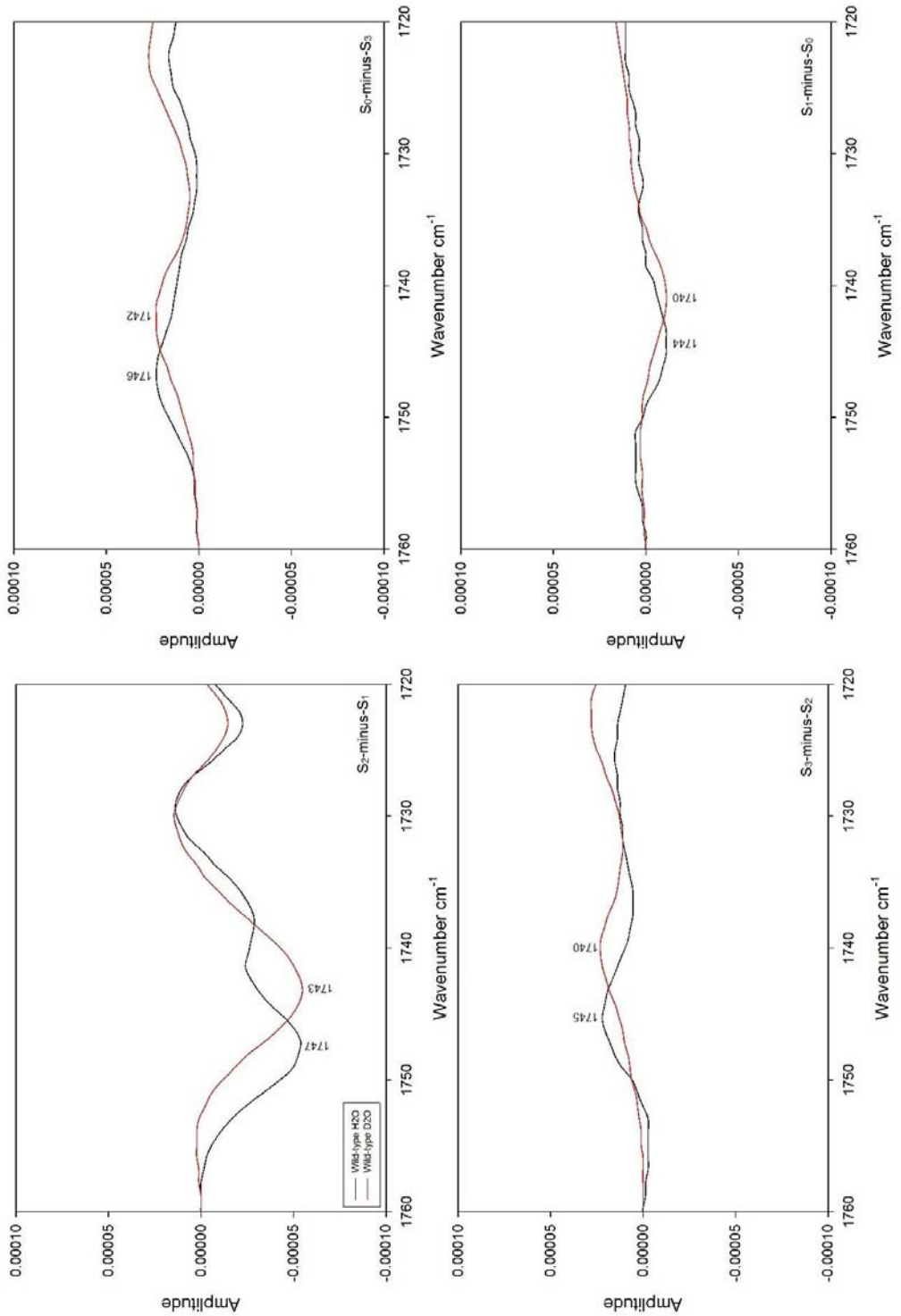
S0-minus-S1
S0-minus-S2
S0-minus-S8
S1-minus-S0
Amplitude
Wavenumber cm-1
0.00010
0.00005
0.00000
-0.00005
-0.00010
1720
1730
1740
1750
1760
1747
1743
1745
1740
1746
1742
1744
1740
Wild-type H2O
Wild-type D2O

Figure 4.5

Figure 4.6 Comparison of the midfrequency S_2-*minus*-S_1, S_3-*minus*-S_2, S_0-*minus*-S_3, and S_1-*minus*-S_0 D2-E323Q (red) versus wild-type (black) at 273K. Mutant spectra normalized to highlight cycling characteristics against wild-type.

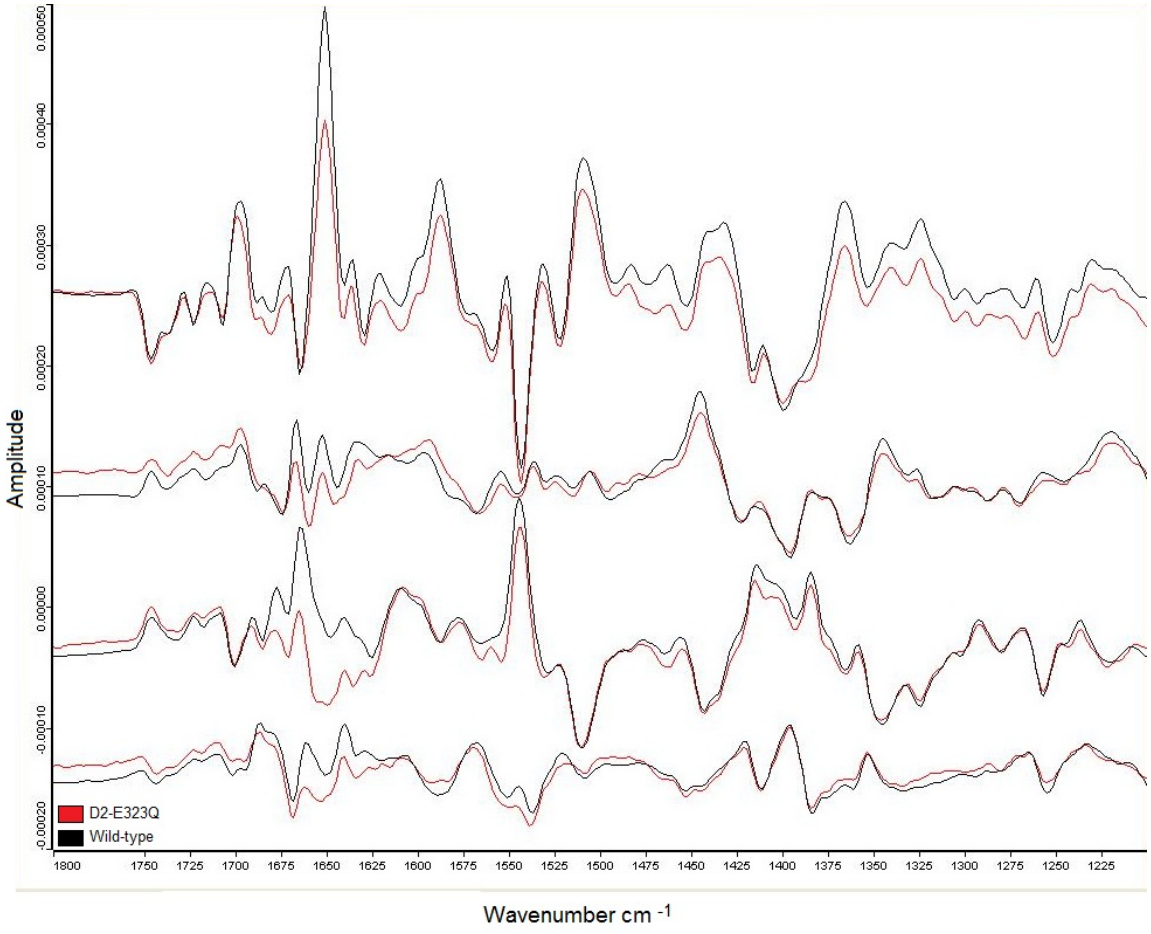
Amplitude
0.00050
0.00040
0.00030
0.00020
0.00010
0.00000
-0.00010
-0.00020
D2-E323Q
Wild-type
1800
1750
1725
1700
1675
1650
1625
1600
1575
1550
1525
1500
1475
1450
1425
1400
1375
1350
1325
1300
1275
1250
1225
Wavenumber cm -1

Figure 4.6

Figure 4.7 Comparison of the midfrequency S_2-*minus*-S_1 D2-E323Q (red) versus wild-type (black) at 273K. Mutant spectrum normalized against wild-type.

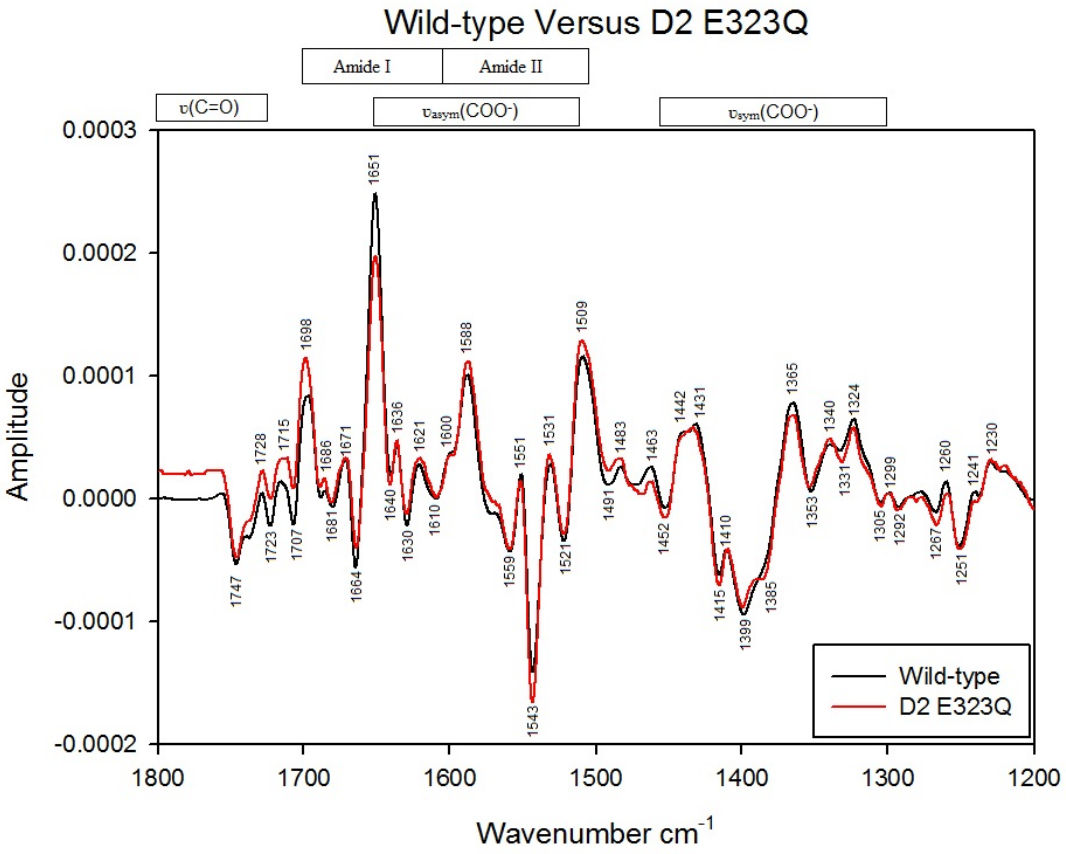
Wild-type Versus D2 E323Q
Amide I
Amide II
υ(C=O)
υasym(COO-)
υsym(COO-)
Amplitude
Wavenumber cm-1
Wild-type
D2 E323Q
0.0003
0.0002
0.0001
0.0000
-0.0001
-0.0002
1800
1700
1600
1500
1400
1300
1200
1747
1728
1723
1715
1707
1698
1686
1681
1671
1664
1651
1640
1636
1630
1621
1610
1600
1588
1559
1551
1543
1531
1521
1509
1491
1483
1463
1452
1442
1431
1415
1410
1399
1385
1365
1353
1340
1331
1324
1305
1299
1292
1267
1260
1251
1241
1230

Figure 4.7

Figure 4.8 S_2-*minus*-S_1 double difference spectrum of wild-type-*minus*-mutant D2-E323Q, subtracted 2.7 times.

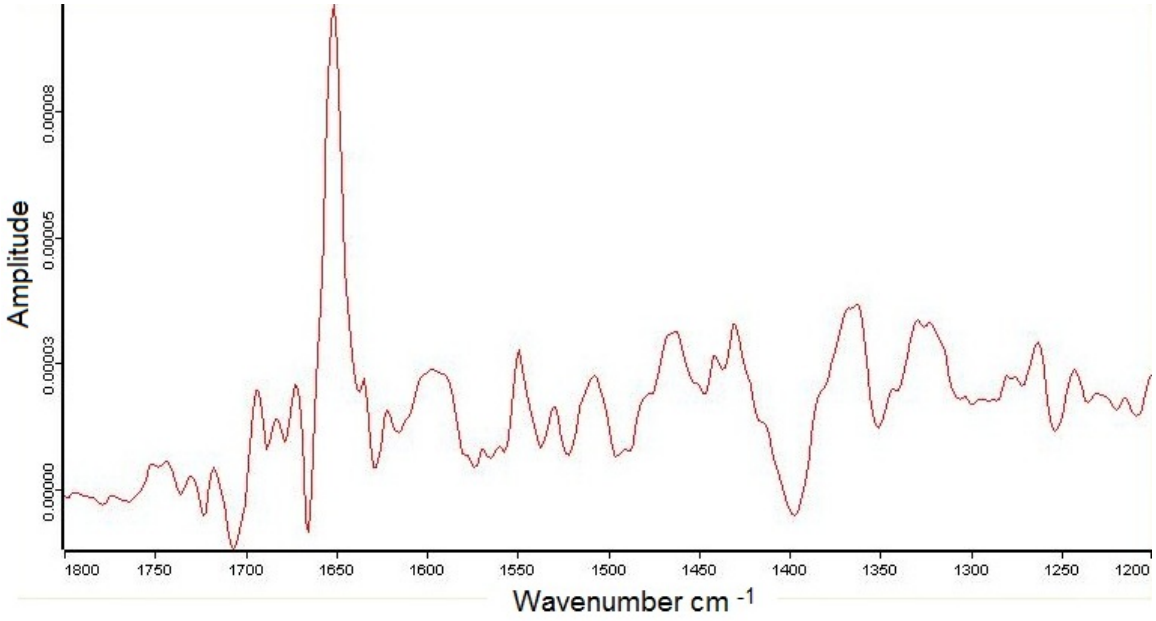
Amplitude
0.00008
0.00005
0.00003
0.00000
1800
1750
1700
1650
1600
1550
1500
1450
1400
1350
1300
1250
1200
Wavenumber cm -1

Figure 4.8

Figure 4.9 Comparison of the midfrequency 1st through 4th flash spectra D1-E333Q (red) versus wild-type (black) at 273K. Mutant spectrum normalized against wild-type.

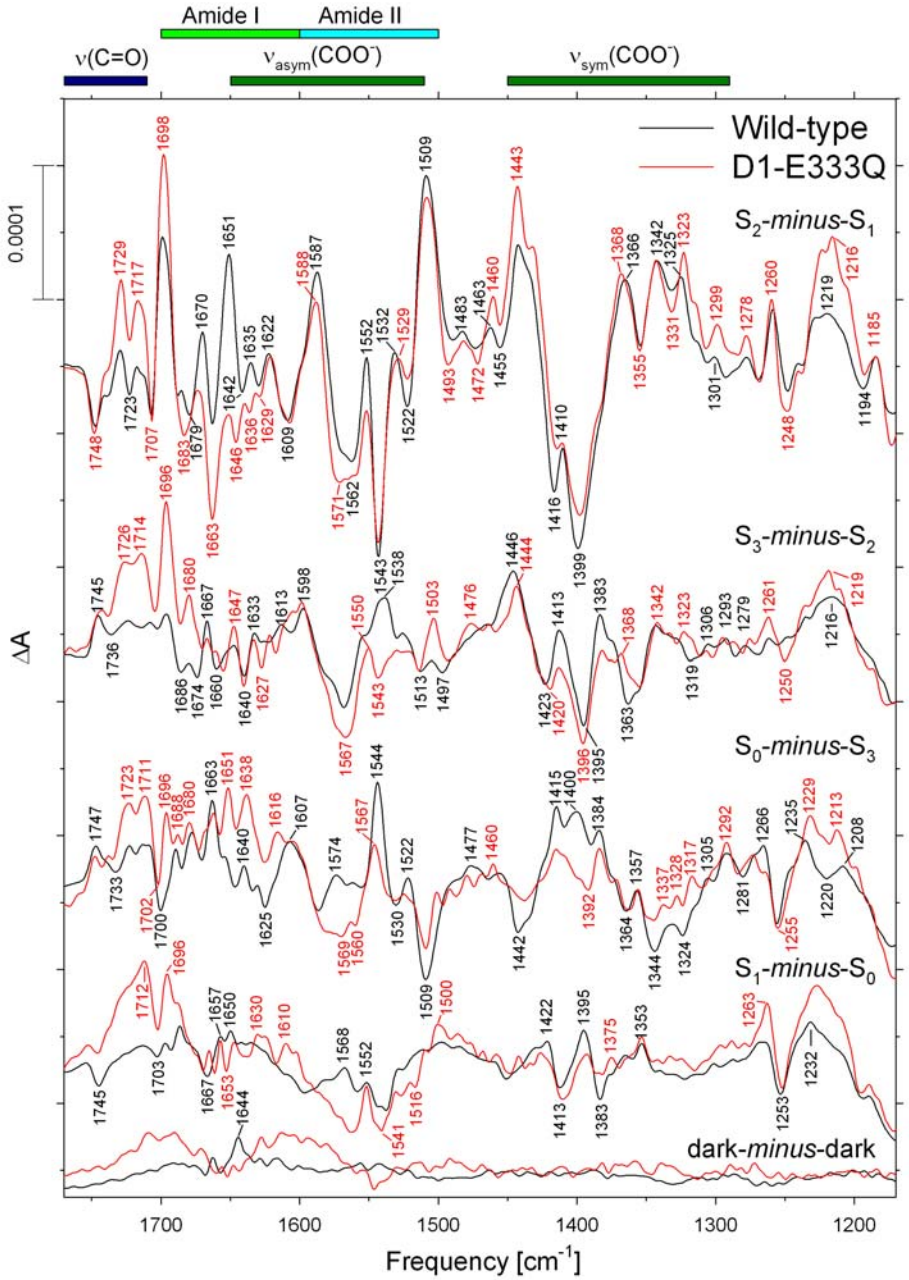
Amide I
Amide II
ν(C=O)
ν_asym(COO⁻)
ν_sym(COO⁻)
Wild-type
D1-E333Q
S2-minus-S1
S3-minus-S2
S0-minus-S3
S1-minus-S0
dark-minus-dark
0.0001
ΔA
1700
1600
1500
1400
1300
1200
Frequency [cm-1]

Figure 4.9

Figure 4.10 Comparison of the midfrequency S_2-*minus*-S_1 difference spectrum for D1-E333Q. First Flash (black) over Mn depleted spectrum (red). Mn depleted spectrum is subtracted from mutant to remove characteristics of manganese depletion. Taken at 273 K.

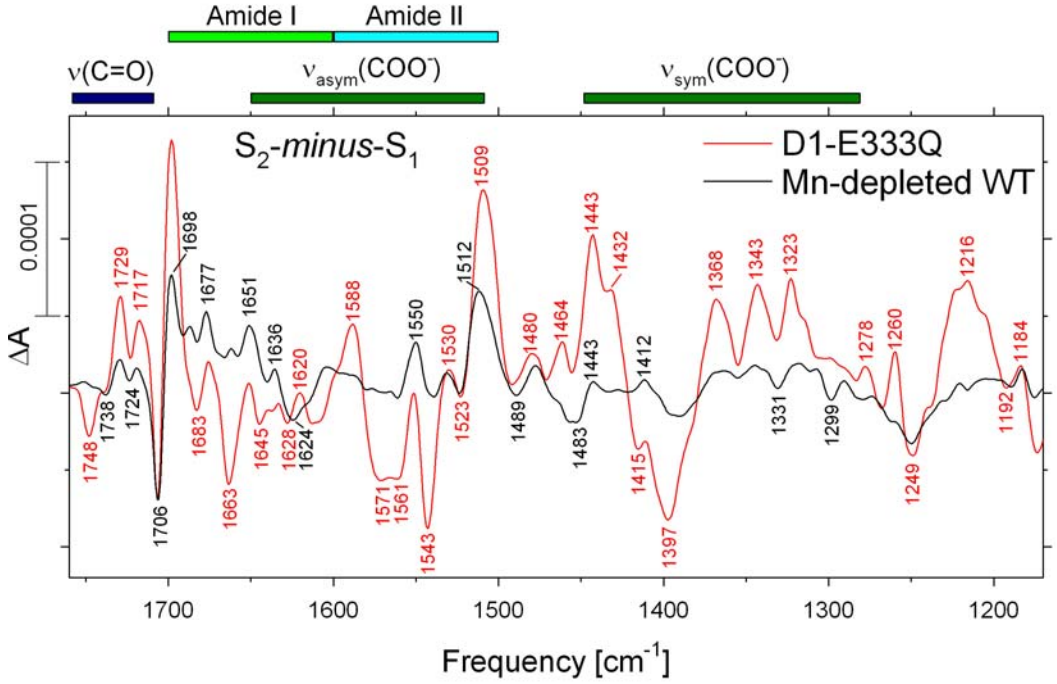
Amide I
Amide II
ν(C=O)
ν_asym(COO⁻)
ν_sym(COO⁻)
S2-minus-S1
D1-E333Q
Mn-depleted WT
0.0001
ΔA
1748
1738
1729
1724
1717
1706
1698
1683
1677
1663
1651
1645
1636
1628
1624
1620
1588
1571
1561
1550
1543
1530
1523
1512
1509
1489
1480
1464
1443
1443
1432
1415
1412
1397
1368
1343
1331
1323
1299
1278
1260
1249
1216
1192
1184
1700
1600
1500
1400
1300
1200
Frequency [cm-1]

Figure 4.10

Figure 4.11 S_2-*minus*-S_1 double difference spectrum of wild-type-*minus*-mutant D1-E333Q. Mn depleted spectrum subtracted 0.15 times from mutant first. Mutant subtracted from wild-type 1.9 times.

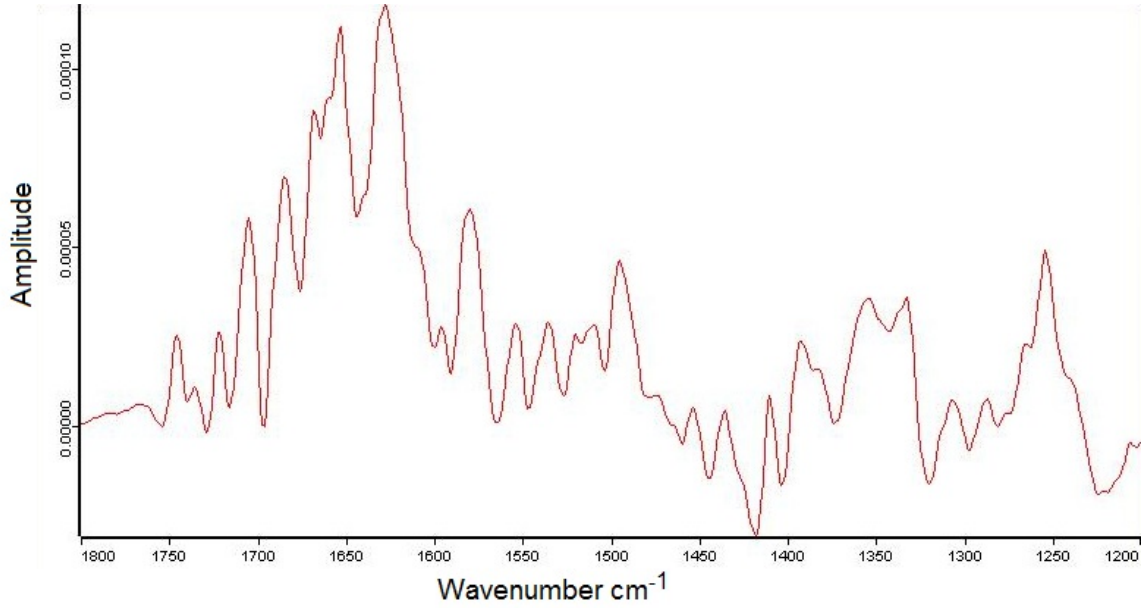
Amplitude
0.00010
0.00005
0.00000
1800
1750
1700
1650
1600
1550
1500
1450
1400
1350
1300
1250
1200
Wavenumber cm-1

Figure 4.11

Figure 4.12 Comparison of the midfrequency S_2-*minus*-S_1 FTIR difference spectra D2-K317A (red) versus wild-type (black) at 273K. Mutant spectrum normalized against wild-type.

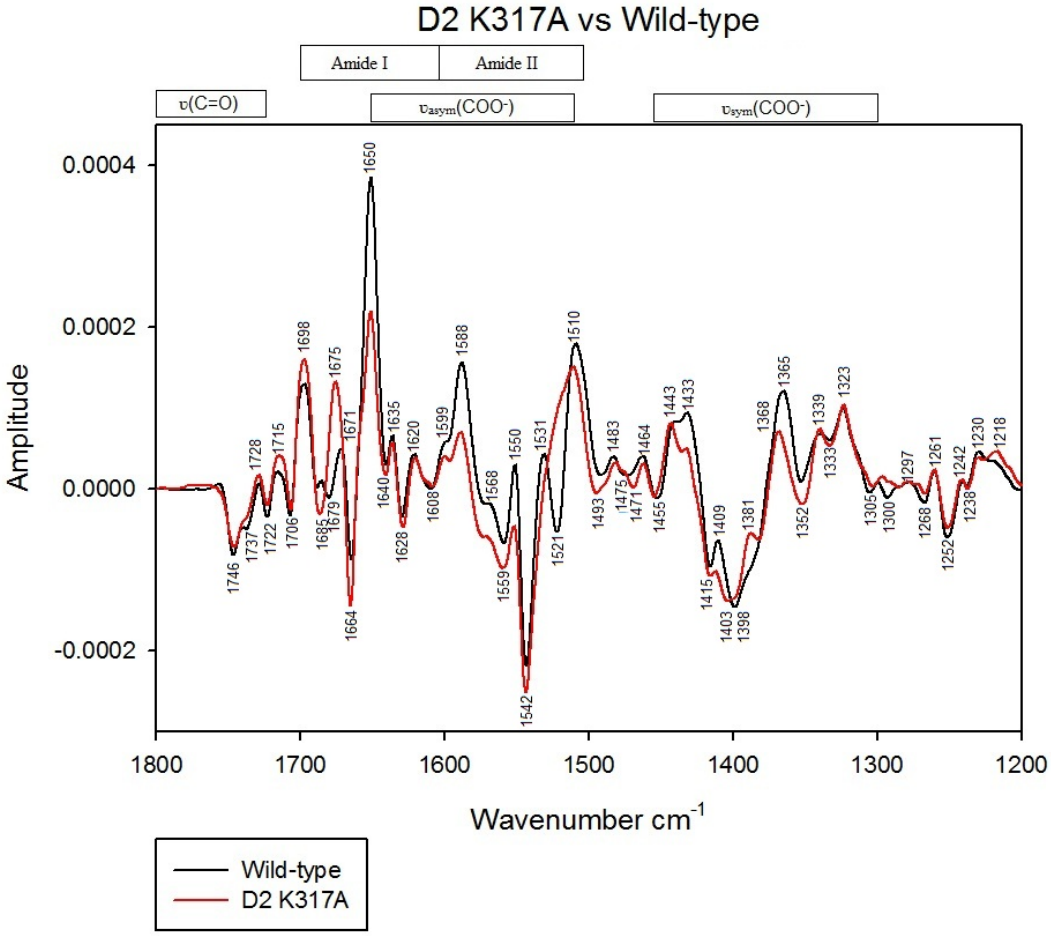
D2 K317A vs Wild-type
Amide I
Amide II
υ(C=O)
υasym(COO-)
υsym(COO-)
Amplitude
0.0004
0.0002
0.0000
-0.0002
1800
1700
1600
1500
1400
1300
1200
Wavenumber cm-1
Wild-type
D2 K317A

Figure 4.12

Figure 4.13 S_2-*minus*-S_1 double difference spectrum of wild-type-*minus*-mutant D2-K317A, subtracted 1.2 times.

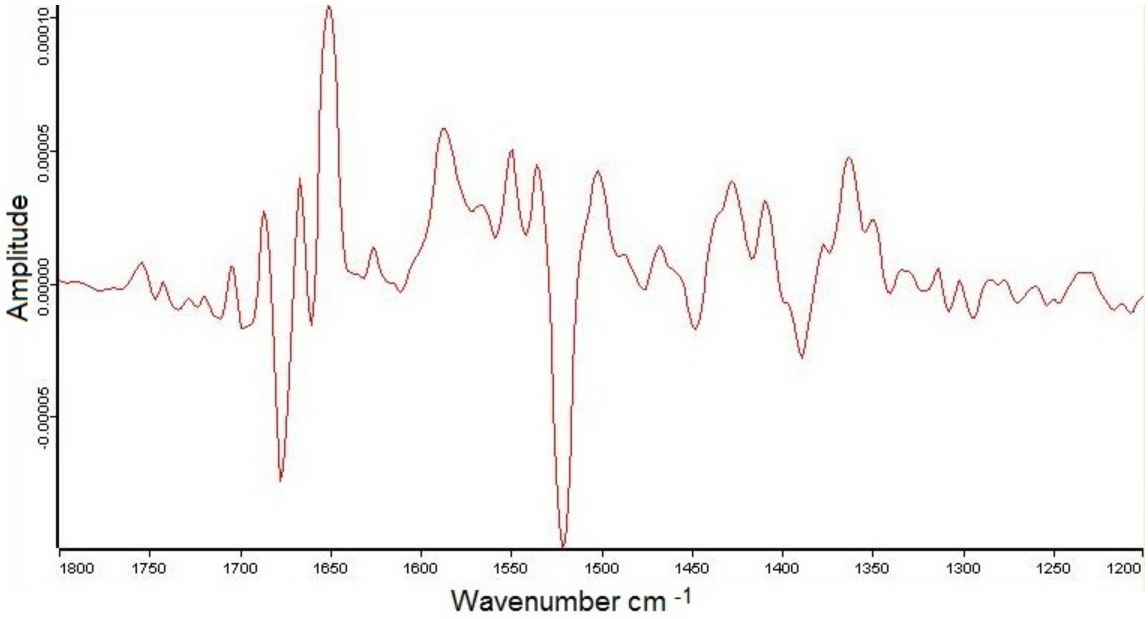
Amplitude
0.00010
0.00005
0.00000
-0.00005
1800
1750
1700
1650
1600
1550
1500
1450
1400
1350
1300
1250
1200
Wavenumber cm -1

Figure 4.13

Figure 4.14 Comparison of the midfrequency S_2-*minus*-S_1 FTIR difference spectra D2-K317E (red) versus wild-type (black) at 273K. Mutant spectrum normalized against wild-type.

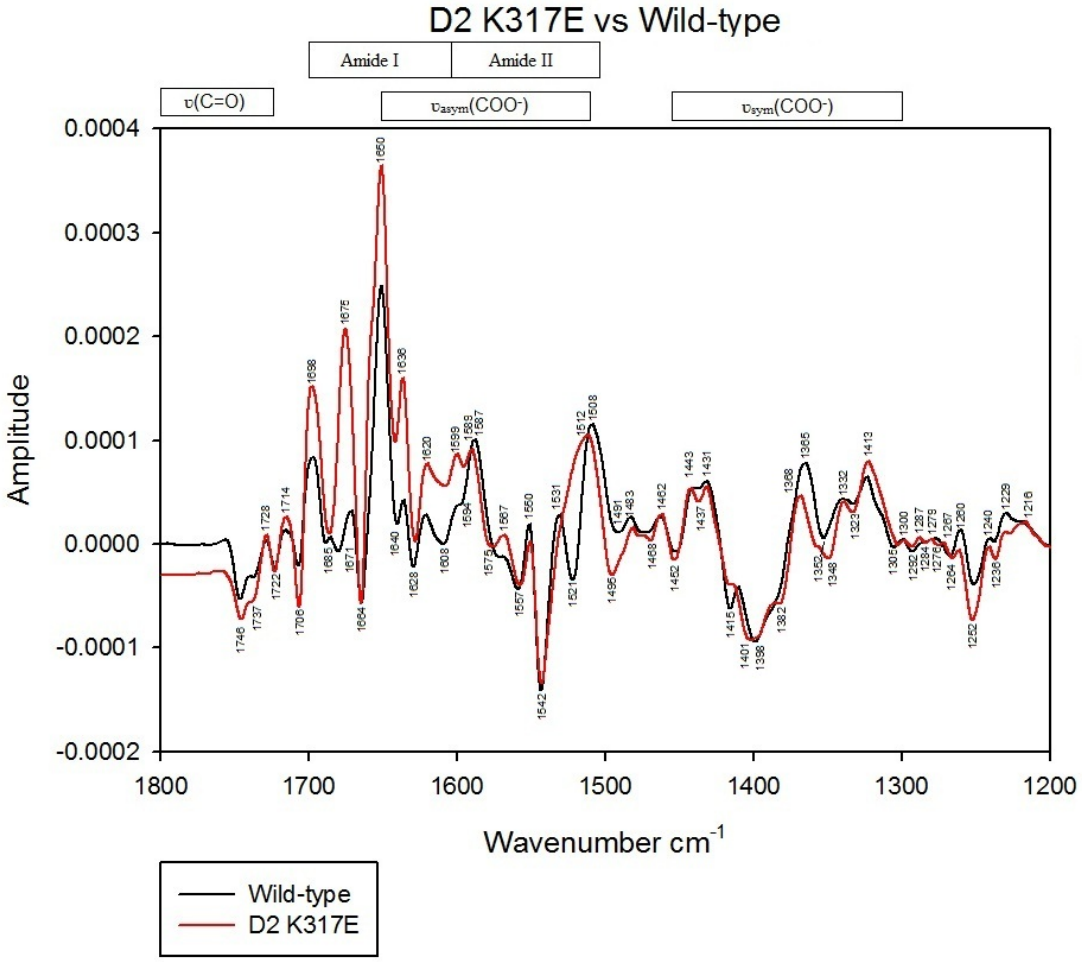
D2 K317E vs Wild-type
Amide I
Amide II
υ(C=O)
υasym(COO-)
υsym(COO-)
Amplitude
Wavenumber cm-1
Wild-type
D2 K317E

Figure 4.14

Figure 4.15 S_2-*minus*-S_1 double difference spectrum of wild-type-*minus*-mutant D2-K317E, subtracted 2 times.

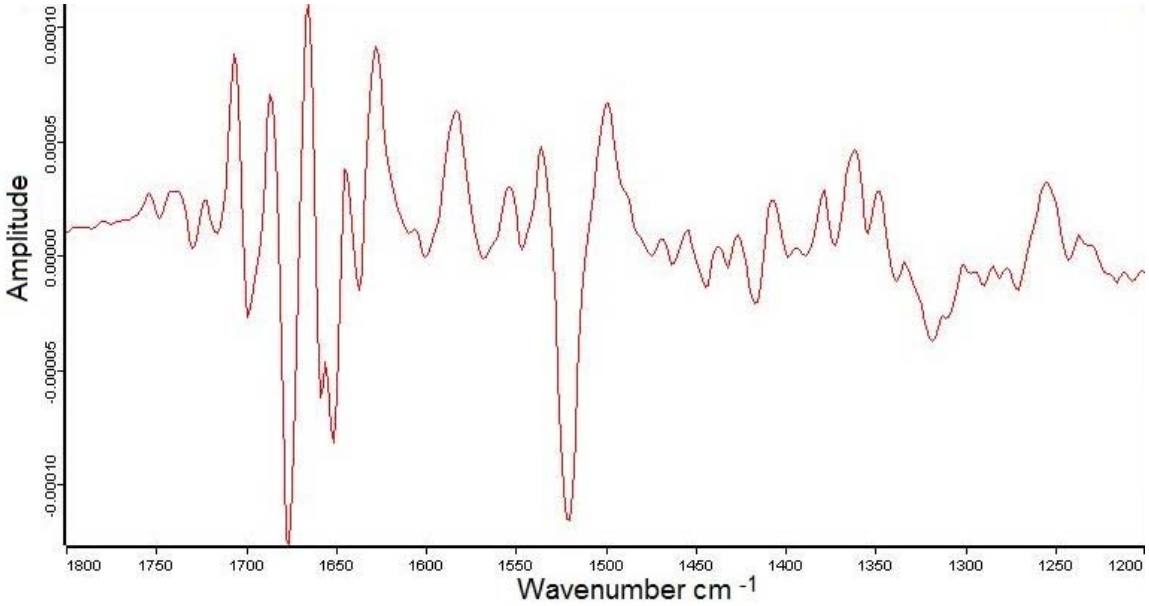
Amplitude
0.00010
0.00005
0.00000
-0.00005
-0.00010
1800
1750
1700
1650
1600
1550
1500
1450
1400
1350
1300
1250
1200
Wavenumber cm -1

Figure 4.15

Figure 4.16 Comparison of the midfrequency S_2-*minus*-S_1 FTIR difference spectra D2-K317Q (red) versus wild-type (black) at 273K. Mutant spectrum normalized against wild-type.

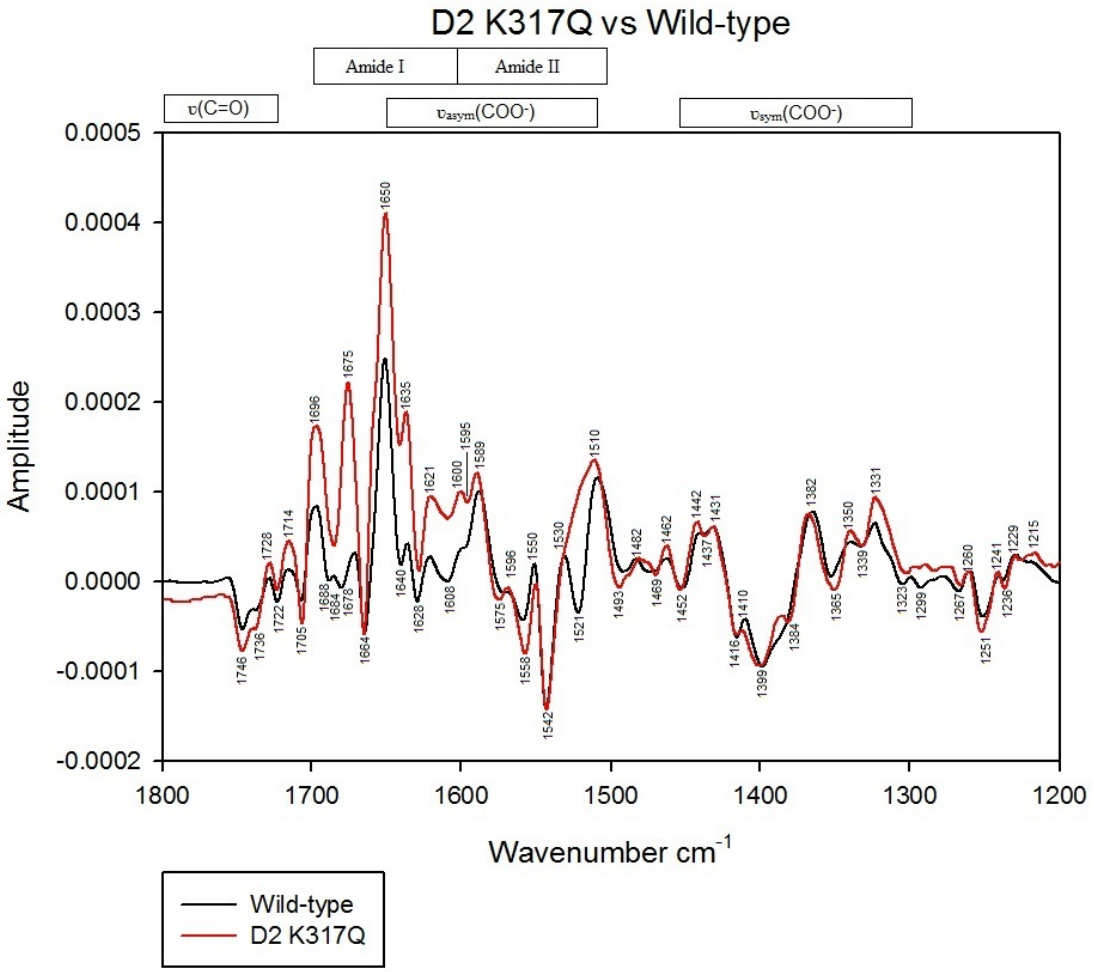
D2 K317Q vs Wild-type
Amide I
Amide II
υ(C=O)
υasym(COO-)
υsym(COO-)
Amplitude
Wavenumber cm-1
Wild-type
D2 K317Q

Figure 4.16

Figure 4.17 S_2-*minus*-S_1 double difference spectrum of wild-type-*minus*-mutant D2-K317Q, subtracted 2.9 times.

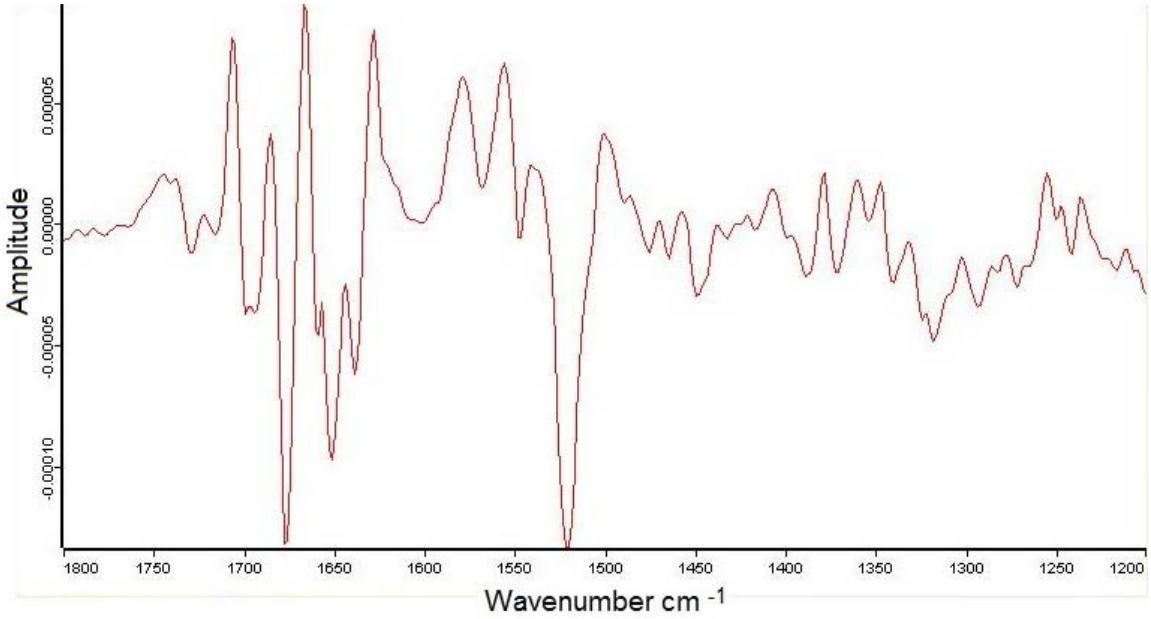
Amplitude
0.00005
0.00000
-0.00005
-0.00010
1800
1750
1700
1650
1600
1550
1500
1450
1400
1350
1300
1250
1200
Wavenumber cm -1

Figure 4.17

Figure 4.18 Comparison of the midfrequency S_2-*minus*-S_1, S_3-*minus*-S_2, S_0-*minus*-S_3, and S_1-*minus*-S_0 FTIR difference spectra of D2-K317R (red) versus wild-type (black) at 273K. Annotated points of interest include 1757 cm^{-1} of ν(C=O), 1511 cm^{-1} of either amide II or $\nu_{asym}(COO^-)$, 1404 and 1398 cm^{-1} of $\nu_{sym}(COO^-)$.

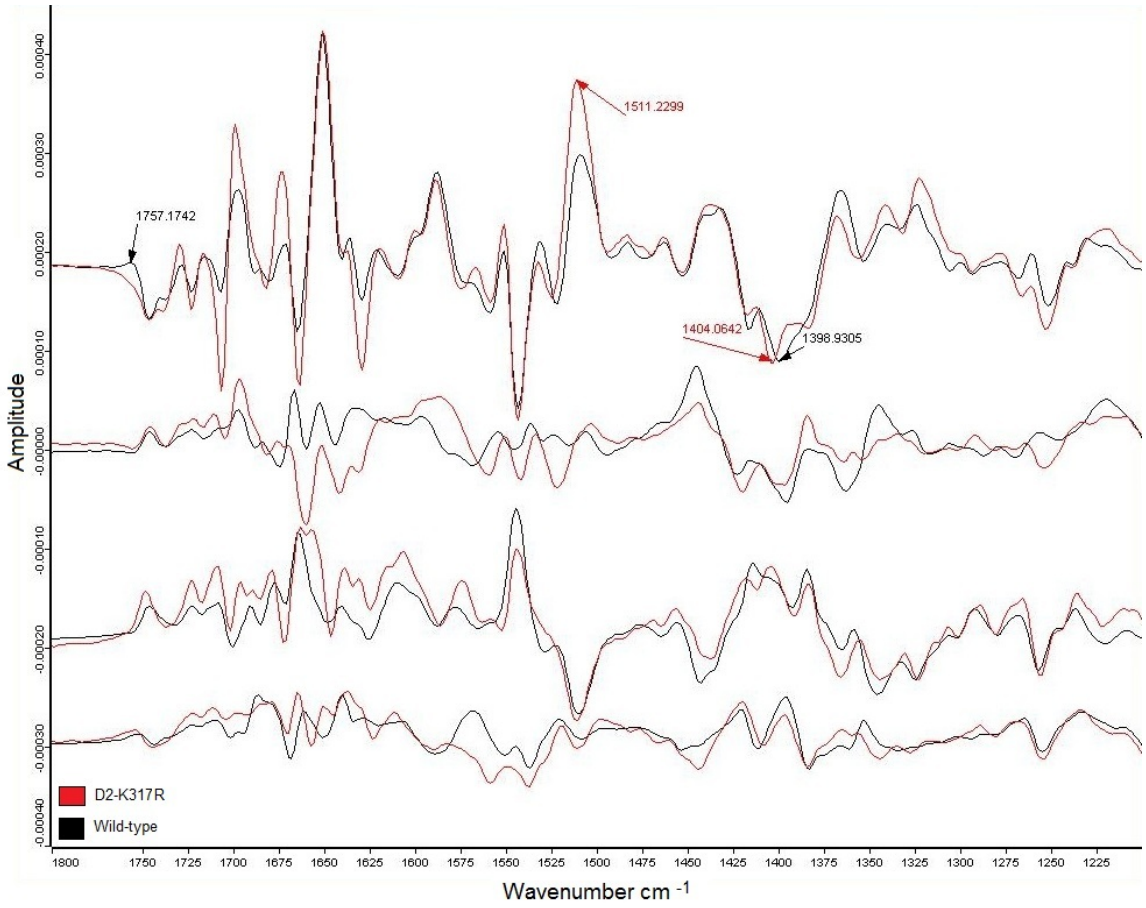
1511.2299
1757.1742
1404.0642
1398.9305
Amplitude
0.00040
0.00030
0.00020
0.00010
0.00000
-0.00010
-0.00020
-0.00030
-0.00040
D2-K317R
Wild-type
1800
1750
1725
1700
1675
1650
1625
1600
1575
1550
1525
1500
1475
1450
1425
1400
1375
1350
1325
1300
1275
1250
1225
Wavenumber cm -1

Figure 4.18

Figure 4.19 Comparison of the midfrequency S_2-*minus*-S_1 FTIR difference spectra of D2-K317R (red) versus wild-type (black) at 273K. Mutant spectrum normalized against wild-type.

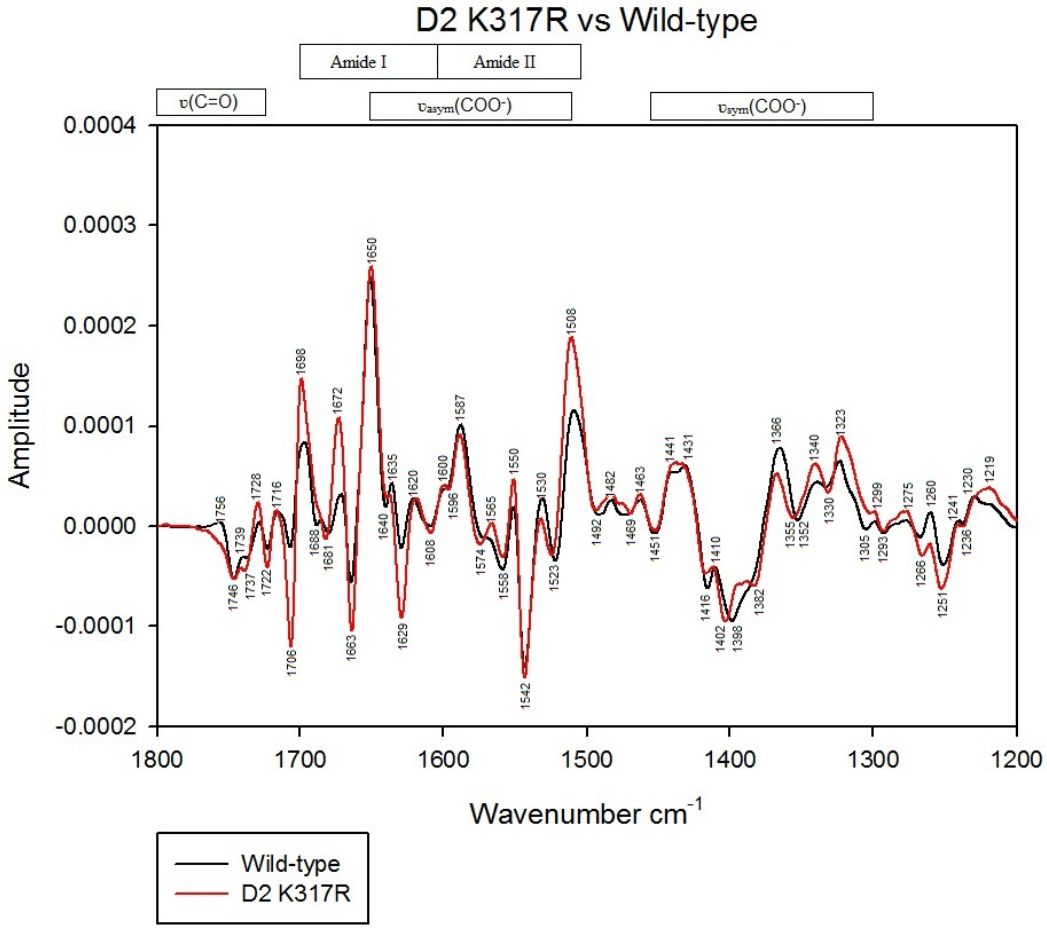
D2 K317R vs Wild-type
Amide I
Amide II
υ(C=O)
υasym(COO-)
υsym(COO-)
Amplitude
Wavenumber cm-1
Wild-type
D2 K317R

Figure 4.19

Figure 4.20 S_2-*minus*-S_1 double difference spectrum of wild-type-*minus*-mutant D2-K317R, subtracted 1.5 times.

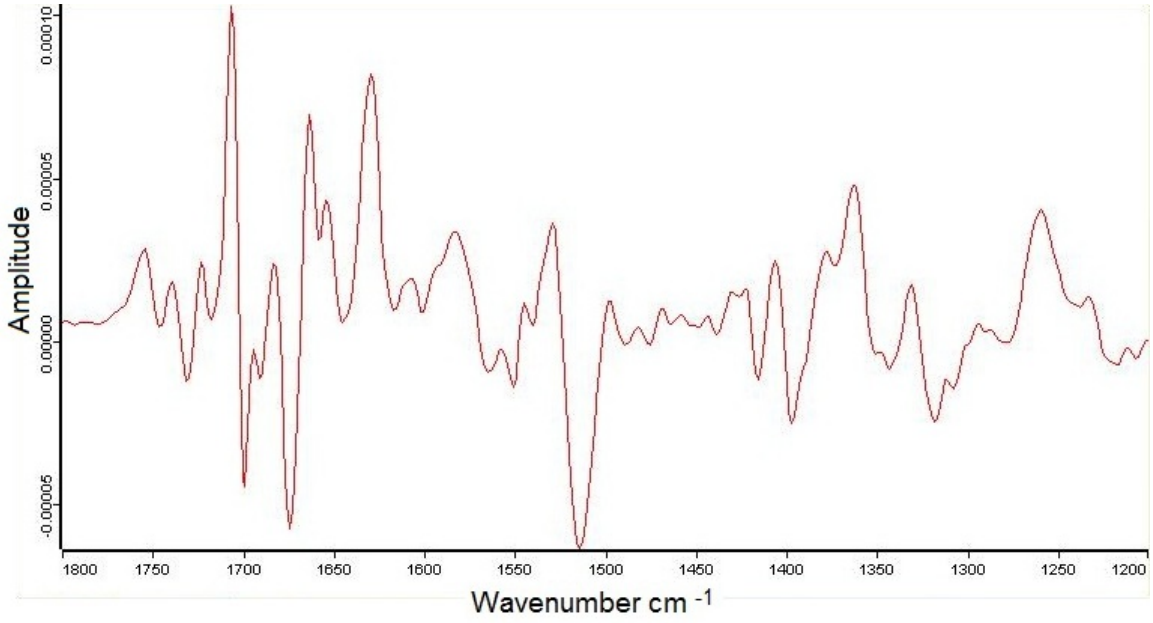
Amplitude
0.00010
0.00005
0.00000
-0.00005
1800
1750
1700
1650
1600
1550
1500
1450
1400
1350
1300
1250
1200
Wavenumber cm -1

Figure 4.20

CHAPTER 5

ROLES OF CHARGED AND CARBOXYLIC ACID RESIDUES NEAR THE MN_4CA CLUSTER AND WITHIN SURROUNDING WATER ENTRANCE OR PROTON EGRESS CHANNELS

5.1 The Role of CP43-Glu354 in Photosystem II

The unexpected findings of Debus et. al. (1 - 3) showed that three putative ligands to the Mn_4Ca cluster do not change coordination modes during S-state transitions. The FTIR difference spectra for mutations done on these three residues show no variation from wild-type in vibrational mode characteristics and progress through all S-states. This data is perplexing as wild-type FTIR difference spectra clearly and reproducibly show characteristic activity in amide and carboxylate vibrational modes for each S-state. Since the data do not represent activity from purported ligands around the cluster, the source of these vibrational modes is a mystery. In an effort to identify this source, expansion to residues of the second coordination sphere around the Mn_4Ca cluster as well as polar or charged belonging to water, proton, or oxygen channels were considered (4 - 6). Mutations for residues in these locations were monitored in the amide I/II, ν_{asym}(COO-), ν_{sym}(COO-), and ν(C=O) regions of FTIR difference spectra. Changes seen in these regions represent hydrogen bond creation or abolition in the carbonyl of carboxylic acid, effects on structure conformation in amide I or II, and possible coordination to a metal in symmetric or asymmetric carboxylate stretching region.

Two ligands to the Mn_4Ca cluster have demonstrated their participation in a coordinate bond with manganese. D1-Ala344 (7) and CP43-354 (8) both show evidence in FTIR difference spectra in the carboxylate stretching modes of a coordinate bond to a manganese that increases its charge in S_1 to S_2 transition. CP43-E354Q required a variety of spectroscopic analyses to

establish its role at the Mn_4Ca cluster including polarography, water exchange $H_2{}^{18}O$ mass spectrometry, x-ray absorption, electron paramagnetic resonance, and Fourier transform infrared spectroscopy (8). This residue was shown to be a ligand to Mn2 and Mn3 by Kamiya et. al. (9) in the 1.9 Å resolution x-ray crystallographic structure, as well as participating in the large channel leading to the Mn_4Ca cluster (5). Study of this mutant was complex, possibly because of its function in this location at the water splitting active site, Cl^-2, and mouth of the large channel. Preparation of the CP43-E354Q sample for FTIR spectroscopic study required a significantly longer period to dark adapt and inability to progress beyond the S_3 state. EPR showed evidence of unusually high S_2 stability as the S_2 decay half time was 2.5 hours. These are characteristics of unusually high S_2 stability. O2 flash yield polarography tests of the mutant showed similar signal patterns compared to wild-type data, though at a lower amplitude, corresponding to the 10% steady state oxygen evolving rate. X-ray absorption data for both near edge and fine structure showed a great likeness to that of wild-type, indicating the mutant has a similar overall energy and environment with only slight perturbations to the manganese. Water exchange data showed mutant slow and fast exchange rates were greater than wild-type rates in two water substrate sites. The fast rate, in particular, was a factor of 8.5 times greater than wild-type, indicating a weakly bound water. These data suggest the CP43-Glu354 residue interacts with Mn ion that ligates the substrate water undergoing rapid exchange in S_3. Also, the EPR data showed 76% of mutant PSII core complexes have photooxidizable Mn_4Ca clusters as compared to wild-type. FTIR difference spectra of this mutant show more perturbations than any other mutant made of the purported ligands of the cluster (1-3, 7). These data show deviations from wild-type spectra in the amide II, $\nu_{asym}(COO^-)$, and $\nu_{sym}(COO^-)$ regions. Specificity in vibrational modes, accomplished through ^{15}N labeling studies, showed that indeed, the CP43-E354Q mutant did create many structural perturbations. However, in the wild-type-*minus*-mutant double difference spectrum, there is a

negative peak at 1524 cm^{-1} which is not shifted as a result of the labeling and so can be assigned to $\nu_{asym}(COO^{-})$. The presence of this mode in the S_2-*minus*-S_1 difference spectrum of wild-type shows that the carboxylate group of CP43-Glu354 is perturbed by the electrostatic interactions of the positive charge developing on the Mn_4Ca cluster during the S_1 to S_2 transition. The removal of this mode by the CP43-E354Q mutation proposes the CP43-Glu354 does ligate the Mn_4Ca cluster by CP43-Glu354, likely that the residue ligates along the Jahn-Teller axis of a Mn(III) ion and that its $\nu_{asym}(COO^{-})$ mode shifts during the S_1 to S_2 transition (10, 11). Assignment of a correlating positive feature could not be accomplished, which seems to be a result of vibrational modes masking the $\nu_{asym}(COO^{-})$ frequency in with an amide II frequency, such as with the positive feature of 1506 – 1508 cm^{-1}. Also, a pair of positive and negative peaks in the wild-type-*minus*-mutant double difference spectra in the $\nu_{sym}(COO^{-})$ region at 1406(+), 1416(–), 1429(+), and 1395(–) cm^{-1} were detected but could not be assigned due to equal intensity of the peaks. Thus it cannot be confirmed that CP43-Glu354 residue changes its coordination mode to manganese during the S_1 to S_2 transition, only that it is a bridging ligand to Mn2 and Mn3. It should be noted that previously studied putative ligand mutants have not shown such sensitivity in preparation or testing methods as was the case with CP43-E354Q. The sensitivity expressed by this mutant suggests CP43-Glu354 plays an active, important role at the Mn_4Ca cluster, as well as maintaining structural integrity at Cl-2 and the large channel.

5.2 The Roles of Three Carboxylic Acid Residues in a Hydogen-Bonding Network

The structural perturbations caused by mutation at this residue are not only evident by the altered amide I/II vibrational modes but also in the ν(C=O) region at 1747 cm^{-1}. This region is associated with the carbonyl bond of carboxylic acids and is an indicator of changing pK_a of a carboxylic acid. This is useful in identifying groups which are involved in a hydrogen-bonding

network which extends at least 20 Å across the lumenal side of Photosystem II. To characterize the mode, wild-type PSII core complexes were exchanged into D_2O compared against wild-type prepared in normal buffer. The FTIR difference spectra for D_2O wild-type show evidence of a downshifted band in the ν(C=O) region of about approximately four wavenumbers over the entire S-state cycle. A shift of four wavenumbers is characteristic of a single carboxylic acid changing its pK_a. It is reasonable to suggest that this illustrates carboxylic acid proton interactions and possibly represents two carboxylates alternating decreasing and increasing pK_a activity as the positive and negative peaks alternate for the four states. In an attempt to identify the source of this vibrational mode, the residues CP43-Glu354 and D1-Glu329 of the large channel, and D1-Glu65, D1-Glu333, D2-Glu312, D2-Glu323 and D2-Lys317 of the broad channel, were observed. Evidence of residue interaction with a hydrogen-bonding network and/or the carboxylic acid changing its pKa would be evident in ν(C=O) region. Residues were chosen based on their position of polar side chains in either the large or broad channel (4-6, 9, 12). Since the CP43-Glu354 residue, at the mouth of large channel, interacts with this dynamic system, exploring the polar residues within these channels could better explain activity to/from/around the Mn_4Ca cluster during the catalytic cycle.

Starting with D1-Glu329 of the large channel, FTIR difference spectra for the D1-E329Q mutant show the abolition of the negative peak in the ν(C=O) region compared to wild-type. This indicates that the mutation of this residue to glutamine prevents the proton exchange from occurring. Thus, it is likely this residue belongs to the hydrogen-bonding network. D1-Glu65 and D2-Glu312, at the other side of the Mn_4Ca cluster, reside within the broad channel. FTIR difference spectra for mutants of both these residues show the same abolition of negative peak when compared to wild-type in the ν(C=O) region. Again, it is likely that mutations done at either of these residues prevents proton exchange, indicating D1-Glu65 and D2-Glu312 are both

members of the hydrogen bonding network. D1-Glu65, D2-Glu31, and D1-Glu329 are highly conserved and located greater than 5 but less than 12 Å from the nearest manganese atom (13 - 15). The side chain of D1-Glu329 has been proposed to participate in an O_2 exit (large) channel (15, 16), while the side chains of D1-Glu65, and D2-Glu312 have been proposed to participate in a water or proton egress (broad) channel (13, 15 -19) with D1-Glu65 and D2-Glu312 forming a potential gate in the broad channel (15, 16). FTIR difference spectra showed that the mutation of any of these three residues, or the partial dehydration caused by maintaining samples at a relative humidity of ≤85%, disrupts the network sufficiently that the structural perturbations associated with the S_1 to S_2 transition are no longer transmitted to this carboxylate, thereby eliminating the 1747 cm^{-1} band from the spectrum. This happens as a result of the altered environment of a carboxylate which decreases its pK_a value. These residues seem to all participate in the network. The carboxylate group that corresponds to the 1747 cm^{-1} band could be one of these three residues, but may also be another that has not yet been identified, such as either of the two carboxylate residues located at the other end of the broad channel, D2-Glu310 and D2-Asp308.

5.3 The Role of D1-Glu333 with Respect to Three Areas of Interest in Photosystem II

With recent x-ray crystallographic structures at 2.9 and 1.9 Å, the location of two chloride ions near the Mn_4Ca cluster have been identified (9, 15), one of the chloride ions, Cl^-1, located near two residues of interest within the broad channel, D1-Glu333 and D2-Lys317. These residues were observed for interactions with Cl^-1 as well as the hydrogen-bonding network, and for D1-Glu333, interactions with the Mn_4Ca cluster were also considered.

The D1-Glu333 residue lies in a crucial position, ligating Mn3 and Mn4 with side-chain oxygens while donating its backbone nitrogen to a range within halogen bonding distance to Cl^-1. It is also at the mouth of the broad channel. It is unsurprising, then, that the D1-E333Q mutation

shows significant deviations from wild-type in the FTIR difference spectra of the amide I/II region. Though there is some semblance of S-state transition characteristics, the overall spectra are noisy and difficult to reproduce with the same characteristics every time. There are many deviations throughout the amide, carboxylate, and carbonyl of carboxylate regions, suggesting structural conformation that also affects a carboxylate interaction with the Mn_4Ca cluster. While assignment of vibrational modes is dependent on isotopic labeling, it is clear in the S_2-*minus*-S_1 double difference spectrum for wild-type-*minus*-mutant that there are a vast number of deviations which may be difficult to pick apart from one another. As for interaction with the Cl^-1, specific interactions are difficult to identify, but it is clear that mutation of D1-Glu333 considerably changes structure conformation and this could be in part to the Cl^-1 displacement.

5.4 The Role of D2-Lys317 in the Broad Channel and at a Chloride Ion

The other residue in the immediate vicinity of Cl^-1, D2-Lys317, seems to play a role with it. Two similarly structured enzymes, α-amylase and angiotensin converting enzyme both have similar structures to PSII where a chloride ion is within halogen bonding distance to a lysine. Upon chloride removal, a salt-bridge can form between two charged residues (20). In this case, the D2-Lys317 could form a salt-bridge with nearby D1-Asp61 which could affect both structure as well as water oxidation dynamics due to its position at mouth of the broad channel. FTIR difference spectroscopy was performed on four mutations of D2-Lys317. Three of the mutations, alanine, glutamate, and glutamine, show difference spectra that are unable to advance beyond the S_2 state. There is a unique negative band at 1526 cm^{-1} evident in the S_2-*minus*-S_1 double difference spectrum for wild-type-*minus*-mutant whose vibrational mode could be identified with isotopic labeling but as of yet either belongs to amide II or $\nu_{asym}(COO^-)$. Some variations from wild-type occur in amide I/II, illustrating a structural change in PSII for all three mutants. This

could explain the inability of the three mutants to progress beyond S_2. However, a fourth mutation was performed, D2-K317R, which substitutes lysine with another positively charged side chain residue of similar length. This mutation could pass through all S-states, though with some variation from wild-type characteristics. The S_2-*minus*-S_1 double difference spectrum for wild-type-*minus*-mutant show variation in amide I/II, $\nu_{asym}(COO^-)$, $\nu_{sym}(COO^-)$, and $\nu(C=O)$, though smaller amplitudes compared to the other three mutations of this residue. It is possible that the D2-K317R mutation retrieves catalytic functionality but incurs structural rearrangement in the process. This corroborates Pokhrel et. al. in proposing the lysine Cl^-1 halide (20). However, as pertains to the hydrogen-bonding network, the FTIR difference spectra did not show the characteristic 1747 cm^{-1} mode elimination for any mutation in D2-Lys317, suggesting its role is more closely associated to the chloride ion and less to the network dynamics.

5.5 No Evidence of Interaction with a Hydrogen-Bonding Network by D2-Glu323

Finally, another broad channel carboxylate residue was observed with FTIR spectroscopy. D2-Glu323, which sits rather far from the Mn_4Ca cluster at 16 Å and 10 Å from Cl^-1, potentially could still interact within the broad channel. FTIR difference spectra for the D2-E323Q mutant did not show any significant variation from wild-type, though. Not only did it cycle through all S-states, the characteristics for each band were nearly identical to wild-type. Also, the spectra did not show the feature 1747 cm^{-1} abolition as with D1-Glu65, D2-Glu312, and D1-Glu329. It can be presumed that D1-Glu323 is not involved with the extensive network of hydrogen bonds.

5.6 Final Thoughts on Interplay Between the Mn_4Ca Cluster and Network Channels

In summation, through use of high resolution x-ray crystallographic structures, channel building programs, and spectroscopic analyses, the structure dynamics of Photosystem II

continues to gradually progress. Individual roles of residues can range from structure assembly, metal coordination, proton transfer, and halogen ligand. These features in FTIR difference spectra reflect more than activity at the Mn_4Ca cluster. Bands seen in amide I/II regions describe structural changes that occur during water oxidation for S-state transitions. The band seen in the ν(C=O) region in must reveal the response of the protein to the electrostatic influences arising from the positive charge developing on the cluster. It seems likely that a hydrogen bonding network consists of more residues than those uncovered in the data presented in this dissertation, determined by the sheer distance between the participants already detected. Also, carboxylates contributing vibrational modes to the wild-type FTIR difference spectra may not necessarily be within the primary coordination sphere of the Mn_4Ca cluster. The interactions of residues within water, oxygen, and proton egress channels to the network of hydrogen bonds and chloride ions show a complex, collective nature which may be difficult to isolate but are necessary to illustrate the intricate function of water oxidation in Photosystem II.

5.7 References

1. Strickler, M. A., Walker, L. M., Hillier, W., Britt, R. D., and Debus, R. J. (2007) No Evidence from FTIR Difference Spectroscopy That Aspartate-342 of the D1 Polypeptide Ligates a Mn Ion That Undergoes Oxidation during the S_0 to S_1, S_1 to S_2, or S_2 to S_3 Transitions in Photosystem II *Biochemistry 46*, 3151– 3160.

2. Debus, R. J., Strickler, M. A., Walker, L. M., and Hillier, W. (2005) No Evidence from FTIR Difference Spectroscopy That Aspartate-170 of the D1 Polypeptide Ligates a Manganese Ion That Undergoes Oxidation during the S_0 to S_1, S_1 to S_2, or S_2 to S_3 Transitions in Photosystem II *Biochemistry 44*, 1367– 1374.

3. Strickler, M. A., Hillier, W., and Debus, R. J. (2006) No Evidence from FTIR Difference Spectroscopy that Glutamate-189 of the D1 Polypeptide Ligates a Mn Ion that Undergoes Oxidation During the S_0 to S_1, S_1 to S_2, or S_2 to S_3 Transitions in Photosystem II *Biochemistry 45*, 8801– 8811.

4. Murray, J.W., Barber, J. (2007) Structural Characteristics of Channels and Pathways in Photosystem II including the Identification of an Oxygen Channel, *J. Struct. Biol. 159* 228–237.

5. Ho, F, Styring, S (2008) Access Channels and Methanol Binding Site to the $CaMn_4$ Cluster in Photosystem II Based on Solvent Accessibility Simulations, with Implications for Substrate Water Access, *Biochimica et Biophysica Acta 1777* 140–153.

6. Gabdulkhakov, A., Guskov, A., Broser, M., Kern, J., Müh, F., Saenger, W., Zouni, A., (2009) Probing the Accessibility of the Mn_4Ca Cluster in Photosystem II: Channels Calculation, Noble Gas Derivatization, and Cocrystallization with DMSO, *Structure 17*, 1223-1234.

7. Chu, H.-A., Hillier, W., and Debus, R. J. (2004) Evidence that the C-Terminus of the D1 Polypeptide is Ligated to the Manganese Ion that Undergoes Oxidation During the S_1 to S_2 Transition: An Isotope-Edited FTIR Study *Biochemistry 43*, 3152– 3166.

8. Service, R., Yano, J., McConnell, I., Hwang, H.J., Niks, D., Hille, R., Wydrzynski, T., Burnap, R., Hillier, W., Debus, R. (2011) Participation of Glutamate-354 of the CP43 Polypeptide in the Ligation of Manganese and the Binding of Substrate Water in Photosystem II, *Biochemistry 50*, 63-81

9. Umena, Y., Kawakami, K., Shen, J.R., Kamiya, N. (2011) Crystal Structure of the Oxygen-Evolving Photosystem II at a Resolution of 1.9 Å, *Nature 473* 55-61.

10. Sproviero, E. M., Gascón, J. A., McEvoy, J. P., Brudvig, G. W., and Batista, V. S. (2008) Computation Studies of the O_2-Evolving Complex of Photosystem II and Biomimetic Oxomanganese Complexes, *Coord. Chem. Rev. 252*, 395-415.

11. Sproviero, E. M., Gascón, J. A., McEvoy, J. P., Brudvig, G. W., and Batista, V. S. (2008) Quantum Mechanics/Molecular Mechanics Study of the Catalytic Cycle of Water Splitting In Photosystem II, *J. Am. Chem. Soc. 130*, 3428-3442.

12. Service, R. J., Hillier, W., and Debus, R. J. (2010) Evidence from FTIR Difference Spectroscopy of an Extensive Network of Hydrogen Bonds near the Oxygen-Evolving Mn_4Ca Cluster of Photosystem II Involving D1-Glu65, D2-Glu312, and D1-Glu329, *Biochemistry 49*, 6655-6669.

13. Ferreira, K. N., Iverson, T. M., Maghlaoui, K., Barber, J., and Iwata, S. (2004) Architecture of the Photosynthetic Oxygen-Evolving Center, *Science 303*, 1831-1838.

14. Loll, B., Kern, J., Saenger, W., Zouni, A., and Biesiadka, J. (2005) Towards Complete Cofactor Arrangement in the 3.0 Å Resolution Structure of Photosystem II, *Nature 438*, 1040-1044.

15. Guskov, A., Kern, J., Gabdulkhakov, A., Broser, M., Zouni, A., and Saenger, W. (2009) Cyanobacterial Photosystem II at 2.9-Å Resolution and the Role of Quinones, Lipids, Channels, and Chloride, *Nature Struct. & Mol. Biol. 16*, 334-342.

16. Chu, H.-A., Nguyen, A. P., and Debus, R. J. (1994) Site-Directed Photosystem II Mutants with Perturbed Oxygen Evolving Properties: 1. Instability or Inefficient Assembly of the Manganese Cluster *In Vivo*, *Biochemistry 33*, 6137-6149.

17. Yamanari, T., Kimura, Y., Mizusawa, N., Ishii, A., and Ono, T.-A. (2004) Mid- to Low-Frequency Fourier Transform Infrared Spectra of S-State Cycle for Photosynthetic Water Oxidation in *Synechocystis* sp. PCC 6803, *Biochemistry 43*, 7479-7490.

18. Chu, H.-A., Hillier, W., and Debus, R. J. (2004) Evidence that the C-Terminus of the D1 Polypeptide is Ligated to the Manganese Ion that Undergoes Oxidation During the S_1 to S_2 Transition: An Isotope-Edited FTIR Study, *Biochemistry 43*, 3152-3166.

19. Strickler, M. A., Walker, L. M., Hillier, W., and Debus, R. J. (2005) Evidence from Biosynthetically Incorporated Strontium and FTIR Difference Spectroscopy that the C-Terminus of the D1 Polypeptide of Photosystem II Does Not Ligate Calcium, *Biochemistry 44*, 8571-8577.

20. Pokhrel, R., McConnell, I., Brudvig, G. (2011) Chloride Regulation of Enzyme Turnover: Application to the Role of Chloride in Photosystem II. *Biochemistry 50* 2725-2734.